ALMA MATER STUDIORUM
UNIVERSITÀ DI BOLOGNA

Facoltà di Scienze Matematiche Fisiche e Naturali
Dipartimento di Astronomia

DOTTORATO DI RICERCA IN ASTRONOMIA
CICLO XXIV (2009-2011)

SOLVING THE COOLING FLOW PROBLEM THROUGH MECHANICAL AGN FEEDBACK

Tesi di Dottorato
di
MASSIMO GASPARI

COORDINATORE:
Chiar.mo Prof.
Lauro MOSCARDINI

RELATORE:
Chiar.mo Prof.
Fabrizio BRIGHENTI

Esame Finale Anno 2012

SCUOLA DI DOTTORATO IN SCIENZE MATEMATICHE, FISICHE E ASTRONOMICHE
Settore Concorsuale: 02/C1 – Astronomia, Astrofisica, Fisica della Terra e dei Pianeti
Settore Scientifico-Disciplinare: FIS/05 – Astronomia e Astrofisica

To the people who believed in me

Alle persone che hanno creduto in me

Contents

Introduction **3**

1 The Cooling Flow Problem **5**

1.1 Hot Gas 5

1.2 Cooling Time 8

1.3 Pure Cooling Flows 8

1.4 Quenched Cooling Flows 10

1.4.1 X-ray Surface Brightness 11

1.4.2 Temperature Profiles 11

1.4.3 Cooling Rates 12

1.4.4 Cold Gas 12

1.4.5 Star Formation 14

2 Heating Mechanisms **17**

2.1 AGN Bubbles 18

2.2 AGN Shocks 21

2.3 AGN Jets and Outflows 24

2.4 Self-regulation and Thermal Balance 26

2.5 Transport: Conduction and Turbulence 28

3 Numerical Methods **31**

3.1 FLASH code 31

3.2 Hydrodynamics 32

3.3 The Eulerian AMR grid 34

3.4 Numerical Solver: PPM 37

3.5 Radiative Cooling . . . 41
3.5.1 Cold Gas Dropout . . . 43
3.6 AGN Outflows . . . 44
3.7 Accretion and Self-regulation . . . 46
3.8 Stellar Winds and Supernovae . . . 48
3.9 Initial Conditions and Gravity . . . 50
3.9.1 Gaussian Perturbations . . . 51

4 AGN Feedback in Galaxy Clusters 53
4.1 Galaxy Clusters Overview . . . 53
4.2 Simulation Setup . . . 58
4.2.1 Template: Abell 1795 . . . 59
4.3 Results . . . 61
4.3.1 Pure Cooling Flow [cl-CF] . . . 61
4.3.2 Cold Feedback: $\epsilon = 5 \times 10^{-4}$ [cl-C5m4] . . . 61
4.3.3 Cold Feedback: $\epsilon = 10^{-3}$ [cl-C1m3] . . . 64
4.3.4 Cold Feedback: $\epsilon = 5 \times 10^{-3}$ [cl-C5m3] . . . 64
4.3.5 Cold Feedback: $\epsilon = 10^{-2}$ [cl-C1m2] . . . 66
4.3.6 Cold Feedback: $\epsilon = 5 \times 10^{-2}$ [cl-C5m2] . . . 67
4.3.7 Cold Feedback: $\epsilon = 10^{-1}$ [cl-C1m1] . . . 67
4.3.8 Summary of Cold Feedback . . . 68
4.3.9 Intermittent or Continuous Feedback . . . 68
4.3.10 Role of the Jet Size . . . 70
4.3.11 Bondi Feedback: $\epsilon = 10^{-1}$ [cl-B1m1S] . . . 71
4.4 Dynamics of Best Model [cl-C5m3] . . . 73
4.5 X-ray Observables . . . 78
4.5.1 Cavities and Shocks . . . 79
4.5.2 Iron Enrichment and Mixing . . . 80
4.5.3 Hydrostatic Equilibrium . . . 81
4.6 Discussion . . . 83
4.6.1 Comparison with other Feedback Models . . . 83
4.6.2 Cold Feedback . . . 85
4.6.3 Hot Bondi-like Feedback . . . 87
4.6.4 Best Models Comparison . . . 88

5 AGN Feedback in Galaxy Groups **89**
5.1 Galaxy Groups Overview . . . 89
5.2 Simulation Setup . . . 94
5.2.1 Template: NGC 5044 . . . 94
5.3 Results . . . 95
5.3.1 Pure Cooling Flow [gr-CF] . . . 95
5.3.2 Bondi Feedback: $\epsilon = 5 \times 10^{-2}$ [gr-Bc5m2] . . . 97
5.3.3 Hybrid Feedback: $\epsilon = 5 \times 10^{-2}$ [gr-Bi5m2] . . . 99
5.3.4 Bondi Feedback: $\epsilon = 10^{-1}$ [gr-Bc1m1] . . . 101
5.3.5 Hybrid Feedback: $\epsilon = 10^{-1}$ [gr-Bi1m1] . . . 102
5.3.6 Bondi and Hybrid Feedback: $\epsilon = 10^{-2}$ [gr-Bc1m2; gr-Bi1m2] . . . 102
5.3.7 Bondi and Hybrid Feedback: $\epsilon = 10^{-3}$ [gr-Bc1m3; gr-Bi1m3] . . . 103
5.3.8 Cold Feedback: $\epsilon = 5 \times 10^{-5}$ [gr-C5m5] . . . 103
5.3.9 Cold Feedback: $\epsilon = 10^{-4}$ [gr-C1m4] . . . 103
5.3.10 Cold Feedback: $\epsilon = 5 \times 10^{-4}$ [gr-C5m4] . . . 104
5.3.11 Cold Feedback: $\epsilon = 10^{-3}$ [gr-C1m3] . . . 106
5.3.12 Intermittent Feedback . . . 107
5.3.13 Thermal Feedback . . . 109
5.3.14 Inflow-Outflow Feedback . . . 110
5.4 Dynamics and Observables of Best Models . . . 111
5.5 Discussion . . . 117
5.5.1 Hot Bondi-like Feedback . . . 117
5.5.2 Cold Feedback . . . 118
5.5.3 Hybrid feedback . . . 119
5.5.4 Rejected Models . . . 120
5.5.5 Comparison with other Works . . . 120
5.5.6 Comparison with Galaxy Clusters . . . 121

6 AGN Feedback in Elliptical Galaxies **123**
6.1 Elliptical Galaxies Overview . . . 123
6.2 Simulation Setup . . . 129
6.2.1 Isolated Elliptical . . . 129
6.2.2 Elliptical with Circumgalactic Gas . . . 130
6.3 Results: Isolated Elliptical . . . 130
6.3.1 Pure Cooling Flow . . . 131

6.3.2 Cold Feedback: $\epsilon = 10^{-4}$ [iso-C1m4] . . . 133
6.3.3 Cold Feedback: $\epsilon = 10^{-3}$ [iso-C1m3] . . . 135
6.3.4 Cold Feedback: $\epsilon = 3.3 \times 10^{-4}$ [iso-C3m4] . . . 136
6.3.5 X-ray Observables . . . 136
6.4 Results: Elliptical with Circumgalactic Gas . . . 141
6.4.1 Cold Feedback: $\epsilon = 8 \times 10^{-4}$ [cgg-C8m4] . . . 141
6.4.2 X-ray Observables . . . 143
6.5 Discussion . . . 150
6.5.1 Comparison with other Feedback Models . . . 150
6.5.2 AGN Turbulence . . . 151
6.5.3 Concluding Remarks . . . 152

7 Multiphase Gas 155
7.1 Cold Gas Overview . . . 155
7.2 Simulation Setup . . . 159
7.2.1 Initial Conditions . . . 161
7.3 Results . . . 161
7.3.1 Pure Cooling Flow [r7-CF] . . . 162
7.3.2 AGN Feedback: $t_{\rm cool}/t_{\rm ff} = 7$ and $\epsilon = 6 \times 10^{-3}$ [r7-i6m3] . . . 164
7.3.3 AGN Feedback: $t_{\rm cool}/t_{\rm ff} = 7$ and $\epsilon = 10^{-2}$ [r7-i1m2] . . . 168
7.3.4 AGN Feedback: Wobbling Outflows [r7-i6m3w] . . . 170
7.3.5 AGN Feedback: $t_{\rm cool}/t_{\rm ff} = 21$ and $\epsilon = 6 \times 10^{-3}$ [r21-i6m3] . . . 171
7.3.6 AGN Feedback: $t_{\rm cool}/t_{\rm ff} = 21$ and $\epsilon = 10^{-2}$ [r21-i1m2] . . . 171
7.4 Discussion: the Detailed Thermal State . . . 173

8 Conclusions 181
8.1 Consistency with Observations . . . 182
8.2 Successful Feedback Characteristics . . . 184
8.3 Limitations and Future Developments . . . 187
8.4 Finale . . . 190

Bibliography 191

PhD Production 204

Acknowledgments 206

Introduction

One of the most crucial problems of present-day astrophysics concerns the thermodynamical evolution of the baryonic, ordinary matter. Heating processes play a fundamental role in galaxies, groups and clusters, struggling in an intricate but fascinating dance with its antagonist, cooling. The majority of baryons in the universe appears to reside in the form of an almost fully ionised gas, a plasma with temperatures over ten million degrees and densities below one particle per cm^3. Quantum mechanics tells us that such plasma looses thermal energy, emitting photons, mainly due to bremsstrahlung, recombination and line excitation. Unopposed radiative cooling would lead to the cooling catastrophe; the denser, central regions of virialised systems cool faster, loosing partial pressure support and inducing a subsonic inflow of gas from the peripheral zones toward the nucleus. The increment of gas density causes a further increase of radiative cooling. This vicious circle leads to unobserved cooling rates up to hundreds solar masses per year, in the most massive systems. At the centre of galaxies, groups and clusters, the huge accumulation of monolithically condensed cold gas would produce unrealistic surface brightness peaks and star formation rates. This is *the cooling flow problem*. Since every important baryonic structure, like molecular clouds, stars, dust and planets, will later rise from the hot plasma crucible, it is crucial to find and understand the counterbalancing process, i.e. heating.

The last-generation (X-ray) telescopes, *Chandra* and *XMM-Newton*, have provided a striking hint to the solution of the cooling flow problem. We now see the spectacular and powerful interactions of the supermassive black hole, residing at the centre of the active galactic nucleus (AGN), with the surrounding medium, in the form of buoyant bubbles, shock cocoons, metals dredge-up, turbulence, jets and nuclear outflows. Even if from an energetic point of view the AGN is capable to balance radiative losses, numerous questions are far to be settled. In primis, what is dominant engine of heating? How can the AGN energy couple to the interstellar/intracluster plasma? How can the galaxy, group or cluster maintain a state of quasi thermal equilibrium for several Gyr? What is the original feedback process that generates the wealth of observational features? Why do we observe extended (filamentary) and nuclear cold gas, even in the presence of strong heating?

With the present Thesis, I intend to deeply investigate the previous questions, focusing on the solution of the cooling flow problem, i.e. dramatically quenching the cooling rates for several Gyr without destroying the cool-core structure. The main theoretical

hypothesis is that the dominant feedback process should be mechanical and anisotropic, originated from massive subrelativistic AGN outflows. The natural self-regulation may be provided by linking the property of the cooling gas to the injection of feedback energy. This central idea will be severely tested via three-dimensional hydrodynamic simulations, carried out via the state-of-the-art Eulerian code FLASH, substantially modified and upgraded to study astrophysical phenomena, as outflows, shocks, cooling, turbulence, thermal instabilities, and multiphase gas.

The Thesis is organised as follows.

- In Chapter 1, I first review the key properties of the hot plasma, residing in the majority of the cosmic virialised structures, as clusters, groups and ellipticals. I focus on the theoretical background essential to understand what is a classic cooling flow. The second part describes instead the observational evidences of real, *quenched* cooling flows.

- In Chapter 2, I present an essential review on the cooling counterpart, heating. The attention is mainly given to the various manifestation of AGN feedback in hot halo systems, including buoyant bubbles, shocks, jets/outflows, but also transport processes as conduction and turbulence.

- In Chapter 3, I describe the entire numerical methods, necessary to carry out the simulations via the FLASH code. After a brief introduction on hydrodynamics, I introduce the AMR grid structure and how the Euler equations are solved (PPM scheme). I discuss then, in detail, the key implementation of radiative cooling, AGN outflows, the self-regulation, stellar evolution and the initial condition setup.

- In Chapter 4, I begin to present the results of the simulations on (mechanical) AGN feedback in galaxy clusters, after a brief overview of these systems. The ultimate aim of the investigation is to solve the cooling flow problem, at the same time avoiding overheating and reproducing fundamental features, as cavities, shocks and metal inhomogeneities. As in the next Chapters, I present an in-depth discussion of the merits and flaws of all models, with a critical eye toward observational concordance.

- In Chapter 5, I continue to analyse the 3D simulations on massive AGN outflows, self-regulated by cold and and hot accretion, this time in a typical galaxy group. I present the best models dynamics and observables, thoroughly discussing the properties of the feedback self-regulation.

- In Chapter 6, I close the range of tested hot halo systems, studying the self-regulated AGN outflows also in (isolated and massive) elliptical galaxies. It is important to solve the cooling flow problem on every scale. In fact, in less bound objects, the feedback seems to have more dramatic consequences. Particular attention is given to the generated X-ray features.

- In Chapter 7, I test the idea that multiphase gas is the direct consequence of the AGN feedback. The recurrent outflows may induce substantial turbulence, leading to nonlinear thermal instabilities, with the condensation of the hot phase into cold

filaments and clouds (as suggested by observations). The cold phase may become later the fuel for the feedback engine, explaining the previously assumed (and preferred) cold accretion mode.

- In Chapter 8, I conclude the Thesis, highlighting the key findings on solving the cooling flow problem through mechanical AGN feedback. I focus, in particular, on the consistency with the latest observations, the fundamental characteristics of a successful feedback and the limitations of my models. Finally, I lay the bases for future developments.

Chapter 1

The Cooling Flow Problem

A FUNDAMENTAL gap in the current understanding of the formation and evolution of virialised cosmic systems, such as galaxies, groups and clusters, concerns the thermal and dynamical evolution of the baryonic component.

In the standard ΛCDM cosmological scenario the ordinary, baryonic matter, in the form of gas, collapses in the dark matter potential wells (see also Chapter 4). The adiabatic compression due to the gravitational infall heats the gas to temperatures up to $10^7 - 10^8$ K, near the virial temperature, forming a hot atmosphere of ionised gas in quasi hydrostatic equilibrium, with densities around $10^{-4} - 10^{-2}$ cm^{-3}. This simple mechanism, driven only by gravity, applies to the massive halos of galaxy clusters down to the scales of isolated galaxies. However, in a later stage, the process known as cooling determines the final state of the baryons. The interstellar, intergalactic or intracluster medium (ISM, IGM, ICM) represents in the end the crucible where several fundamental astrophysical structures emerge and continue to form: cold and molecular clouds, small and giant stars, and tiny planets like the Earth.

In the present Chapter, I review the key properties of the hot gas, fundamental requirement in order to understand the theoretical novel work presented in Chapters 4-7. In the following Sections, generality will be pursued as much as possible, with emphasis on the understanding of pure and quenched *cooling flows*. Hot plasma is in fact a common characteristic among cosmic systems, dominating in clusters, groups and massive ellipticals. Each introduction in Chapters 4-6 serves, instead, to highlight the differences between these systems.

1.1 Hot Gas

The hot atmosphere of cosmic systems - hereafter implying clusters, groups and massive ellipticals - is constituted of a nearly fully ionised plasma, mostly hydrogen and helium fully stripped of their electrons; heavier elements have retained only a few of their electrons. Electromagnetic radiation plays a key role: in such hot medium quantum mechanical interactions induce the plasma to emit X-ray photons, thus reducing the internal energy and temperature; in one simple word: cooling. Cooling is one of the

two main actors at the centre of this work, together with its antagonist, heating.

As a good general approximation, the hot plasma can be considered optically thin, i.e. the radiation escapes without interacting with the gas. We are thus allowed, on large scales, to study the plasma with magneto-hydrodynamics (e.g. through numerical simulations), avoiding the complex radiative transfer equations. On small scales, the radiative processes can be studied separately.

The X-ray emission from ionised atoms can be very complex. Fortunately, it is well described by the coronal approximation (Elwert 1952; Mewe 1999), i.e. when an optically-thin plasma is in collisional equilibrium (as in the solar corona). This means that recombinations precisely balance collisional ionisations, a condition which is eventually achieved if a plasma remains undisturbed for a long enough period of time. Once the balance is determined, the X-ray spectrum can be calculated considering the single radiative processes.

Over 10^7 K the main emission mechanism in the hot gas is thermal bremsstrahlung, the deceleration of the free electrons in the Coulomb field of an ion. The total power per volume (or emissivity) radiated by bremsstrahlung is given by $\epsilon_{\rm br} \approx 10^{-27}\, n_{\rm e}\, n_{\rm i}\, T^{1/2}$ erg cm^{-3} s^{-1}, where $n_{\rm e}$ and $n_{\rm i}$ are the electron and ion (hydrogen) number density, and T is the electron temperature. Note the strong dependence of this emission on the gas density ($\propto n^2$), a crucial factor in cooling flows. In addition to bremsstrahlung, bound-free and two-photon emission are also a significant source of continuum radiation.

Below 10^7 K ($\approx$ 1 keV) the dominant radiative mechanism is discrete line emission by several atomic processes: collisional excitation, radiative recombination, dielectric recombination and resonant excitation. Several codes have been developed to calculate the resultant spectrum, considering all the relevant elements (e.g. MEKAL – Liedahl et al. 1995; APEC – Smith et al. 2001). Despite the complexity of transitions, there are only a few prominent features in the emission (see Figure 1.1), such as hydrogen and helium bumps ($T \approx 10^4$ and $\approx 10^5$ K), or the $K\alpha$ line of the Fe XXVI at 6.9 keV and Fe XXV at 6.7 keV. Other hot gas elements worth mentioning are O (VII and VIII), C (VI), S (XXVI and XXV), Si (XIII and XIV), Mg (XI and XII), Ne (X and IX), and N (VII).

The total radiative emissivity can be finally reduced to a very convenient form:

$$\epsilon_{\rm tot} = n_{\rm e}\, n_{\rm i}\, \Lambda(T, Z)\,, \tag{1.1}$$

adopting an analytical cooling function $\Lambda(T, Z)$ (erg cm^3 s^{-1}), which depends both on gas temperature and abundance, as shown in Figures 1.1 and 1.2. Typical values of metal (iron) abundances are $\sim$ 0.3 $Z_\odot$ in the ICM/IGM, raising to about a solar value at the centre of galaxies. The metal enrichment indicates that the gas is not totally primordial, but it has been reprocessed probably through an early population of stars (via supernovae and stellar winds).

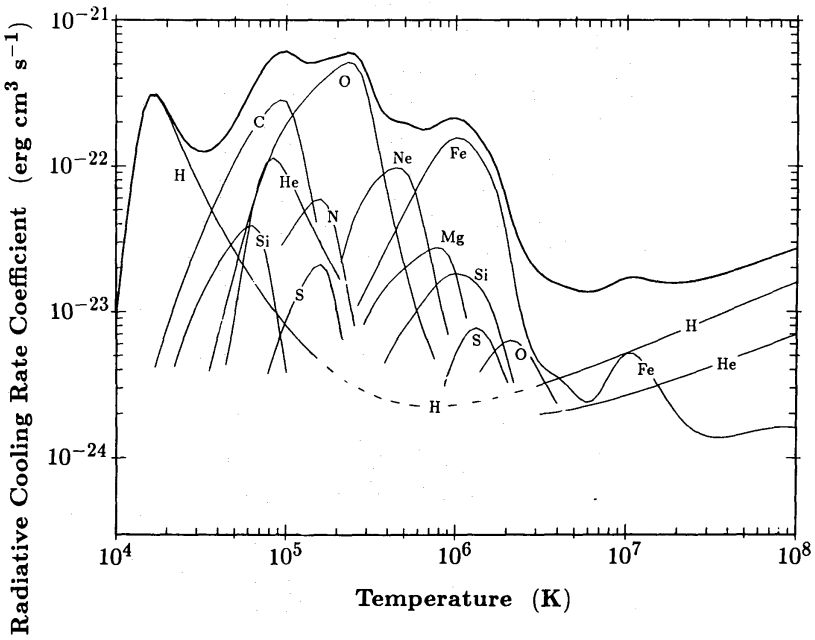

Figure 1.1. Contribution of the different elements to the total radiative cooling function for solar abundance elements (from Boehringer & Hensler 1989).

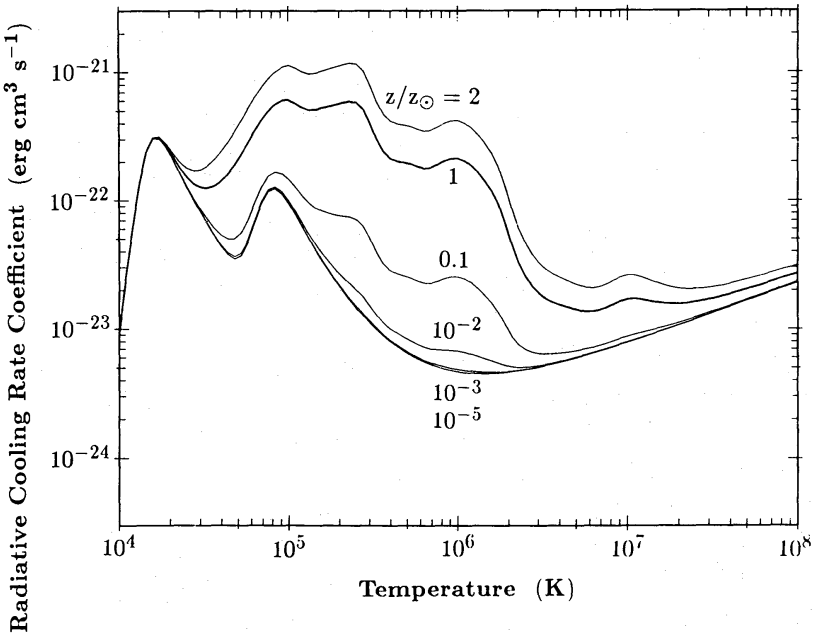

Figure 1.2. Total radiative cooling function for an optically thin plasma in ionisation equilibrium, varying the metallicity ($Z/Z_\odot$; from Boehringer & Hensler 1989).

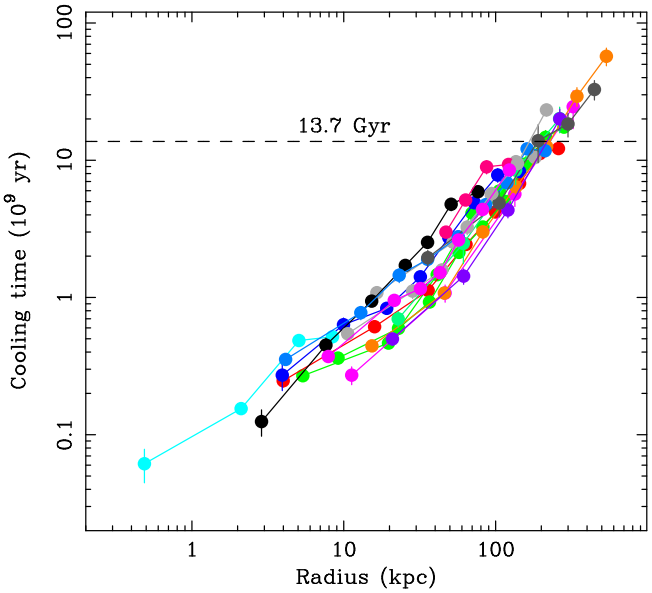

Figure 1.3. Radial profiles of the cooling time for a sample of 16 typical cool-core clusters (from Voigt & Fabian 2004).

1.2 Cooling Time

The fundamental scale in order to understand the thermal evolution of the plasma is the cooling time, defined as the enthalpy[1] divided by the energy lost per unit volume:

$$t_{\rm cool} \equiv \frac{5/2\, n k_{\rm b} T}{n^2 \Lambda} \approx \frac{T_8}{\Lambda_{-23}\, n_{-2}}\, t_H\,, \tag{1.2}$$

where t_H is the age of the universe (13.7 Gyr), $k_{\rm b}$ the Boltzmann constant, T_8 is the gas temperature expressed in units of 10^8 K, Λ_{-23} the cooling function in units of 10^{-23} erg cm^3 s^{-1}, and n_{-2} the gas number density in units of 10^{-2} cm^{-3}. The densest gas at the centre of virialised systems has thus sufficient time to cool. In galaxy clusters $t_{\rm cool}$ can be less than 500 Gyr, while in groups or elliptical galaxies it can drop even below 10 Myr.

We can also define a cooling radius, such as the radius at which the cooling time equals the Hubble time: $t_{\rm cool}(r_{\rm cool}) = H_0^{-1}$. Typical values approach a few 100 kpc for 'cool-core' clusters, as shown in Figure 1.3. It is interesting to note that the profiles display the same radial dependence, suggesting there may be no trend in terms of old and young cooling flows.

1.3 Pure Cooling Flows

At this point, we possess all the elements to properly define a classic pure cooling flow (see also Sections 4.3.1, 5.3.1, 6.3.1 and 7.3.1, for the detailed dynamics). Inside the cooling radius ($\sim 10-100$ kpc), the hot gas is able to cool in a short time compared to the age of the system, if not balanced by some kind of heating. The loss of thermal energy

[1]It is more appropriate to use the enthalpy over thermal energy, because the gas is also compressed as it cools, effectively raising the heat capacity, $c_{\rm v} \approx 3/2$, by a factor 5/3.

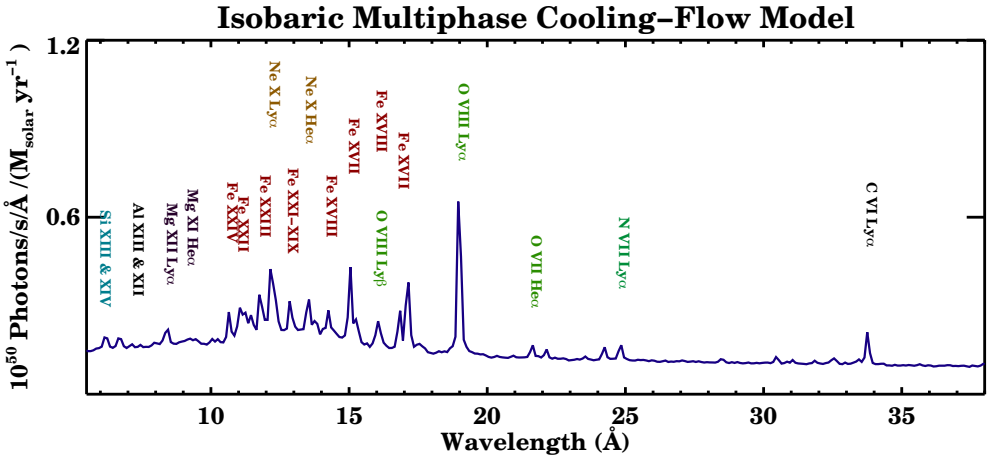

Figure 1.4. The standard multiphase cooling flow model (from Peterson & Fabian 2006).

reduces the gas pressure ($E_{\rm th} = c_{\rm v}P$), leading to a slow inflow. Given the subsonic nature of this so-called *cooling flow* ($t_{\rm cool}$ is always longer than the free-fall time), the process can be considered in quasi hydrostatic, pressure equilibrium. Therefore, the cooling gas drops in temperature and rises in density, further decreasing the cooling time (Equation 1.2; $t_{\rm cool} \propto T^{\beta}/n$, where $-1/2 \lesssim \beta \lesssim 1/2$).

The vicious circle induces huge mass cooling rates, reaching a saturated steady-state after a few cooling times (when the adiabatic compressional heating of the inflow starts to have a relevant impact). The mass deposition rate[2] $\dot{M}$, due to cooling, can be roughly estimated from the X-ray luminosity, assuming the energy lost in time is given by the variation of thermal energy plus the PV work done on the gas as it enters $r_{\rm cool}$ (i.e. the variation of enthalpy[3], when the process is isobaric):

$$\dot{M} = \frac{2}{5}\frac{\mu m_p}{k_{\rm b}T} L_{\rm c} \simeq 118\,\frac{L_{\rm c,44}}{T_{7.6}}\ \ [M_{\odot}\ {\rm yr}^{-1}]\,, \tag{1.3}$$

where $L_{\rm c}$ is the X-ray luminosity[4] within $r_{\rm cool}$ (in units of 10^{44} erg s^{-1}), and T the gas temperature at $r_{\rm cool}$ (in units of $4{\times}10^{7}$ K). Predicted values of $\dot{M}$ range from a few $M_{\odot}$ yr^{-1}, for massive elliptical galaxies, to several hundreds $M_{\odot}$ yr^{-1} for rich clusters (Fabian 1994; Peres et al. 1998). Even without relying on deep observations, we can already suspect that rates of 1000 $M_{\odot}$ yr^{-1} are likely unrealistic and overestimated.

A more accurate modelling of a pure cooling flow includes matter cooling out over a range of radii, with a spectrum of densities and temperatures. Such more advanced model is known as isobaric multiphase cooling flow (e.g. Peterson & Fabian 2006). From Equation 1.3 it is straightforward to infer that the variation of the X-ray luminosity in respect of temperature is

$$\frac{dL}{dT} = \frac{5}{2}\frac{k_{\rm b}\dot{M}}{\mu m_{\rm p}}\,. \tag{1.4}$$

Since for a spectral line $dL(\nu) = n_{\rm e}n_{\rm i}\Lambda_{\nu}(T)\,dV$, the line contribution to the X-ray

[2] Accretion rate is a misleading term given that not all the gas flows in the nuclear region far from $r_{\rm cool}$.

[3] $H \equiv E_{\rm th}V + PV = \frac{1}{\gamma-1}\frac{k_{\rm b}TM}{\mu m_{\rm p}} + \frac{k_{\rm b}TM}{\mu m_{\rm p}} = \frac{5}{2}\frac{k_{\rm b}TM}{\mu m_{\rm p}}$, where μ is the gas molecular weight (≈ 0.61), M the gas mass (density times volume, $\rho V = n\,\mu m_{\rm p} V$), $m_{\rm p}$ the proton mass, and γ is the adiabatic index (= 5/3 for a monoatomic gas).

[4] Typical values are $\sim 10\%$ of the total luminosity: $\sim 10^{42} - 10^{44}$ erg s^{-1}.

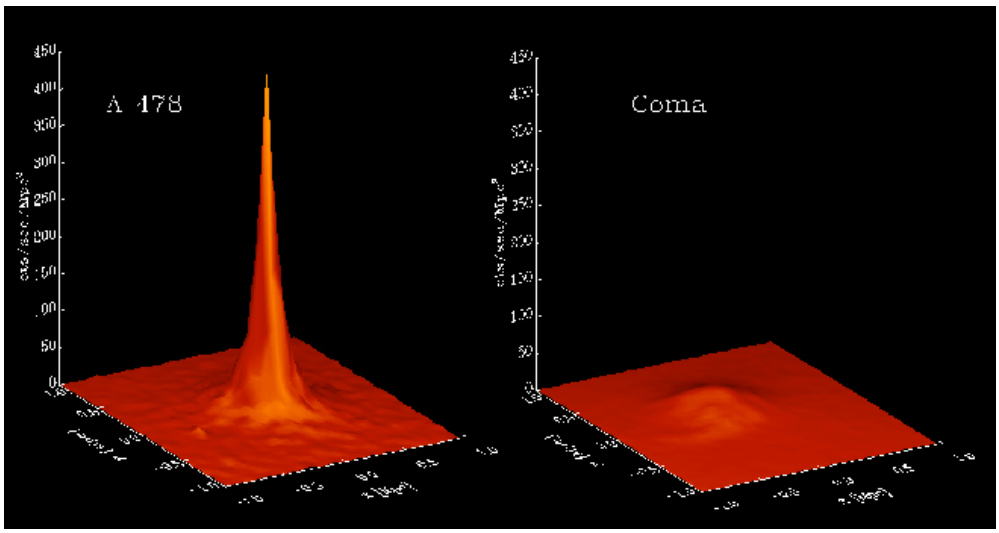

Figure 1.5. X-ray surface brightness distribution of a typical cool-core (A478; left) and non-cool-core cluster (Coma; right). The two systems have comparable total X-ray luminosity, rescaled to be viewed at the same redshift (from Allen & Fabian 1997).

luminosity is

$$L(\nu) = \frac{5}{2}\frac{k_{\rm b}\dot{M}}{\mu m_{\rm p}} \int_0^{T_{\rm i}} \frac{\Lambda_\nu(T)}{\Lambda(T)}\, dT\,, \tag{1.5}$$

where $T_{\rm i}$ is the initial temperature. The previous Equation, in conjunction with atomic physics, allows to reproduce the global X-ray spectrum, as shown for instance in Figure 1.4. However, the recent spectral observations (Section 1.4.3) have demolished the classic cooling flow model, which fails to predict several low-energy X-ray lines of the hot gas in clusters, groups and galaxies.

The multiphase cooling flow was historically introduced to solve the problem of too sharply peaked surface brightness profiles predicted by the single-phase model, due to the strong central gas mass accumulation (emissivity is $\propto n^2$). To obtain the best-fitting $\rm SB_x$ profiles (see Figure 1.5), an inhomogeneous multiphase cooling flow with $\dot{M}(r) \propto r$ is required (Fabian et al. 1984). Nevertheless, distributed cooling can not alter the total - huge - cooling rates. Moreover, the observed spatial distribution of cold gas and star formation is more consistent with the single-phase model, but at levels that fall orders of magnitude below the predictions.

1.4 Quenched Cooling Flows

The previous pure cooling flow scenario, although simple and elegant, is wrong. The problems related to the classic cooling flow are numerous, and can be summarised in one basic statement: the hot plasma is allowed to cool too much. In this Section, I focus on the general appearance of *real* hot atmospheres in cosmic systems.

What we actually observe in the universe are *quenched* cooling flows, tightly associated with cool-core systems. The majority of observed cosmic systems (e.g. Sarazin 1986; Fabian et al. 1991; Peres et al. 1998; Bauer et al. 2002) resides in this category,

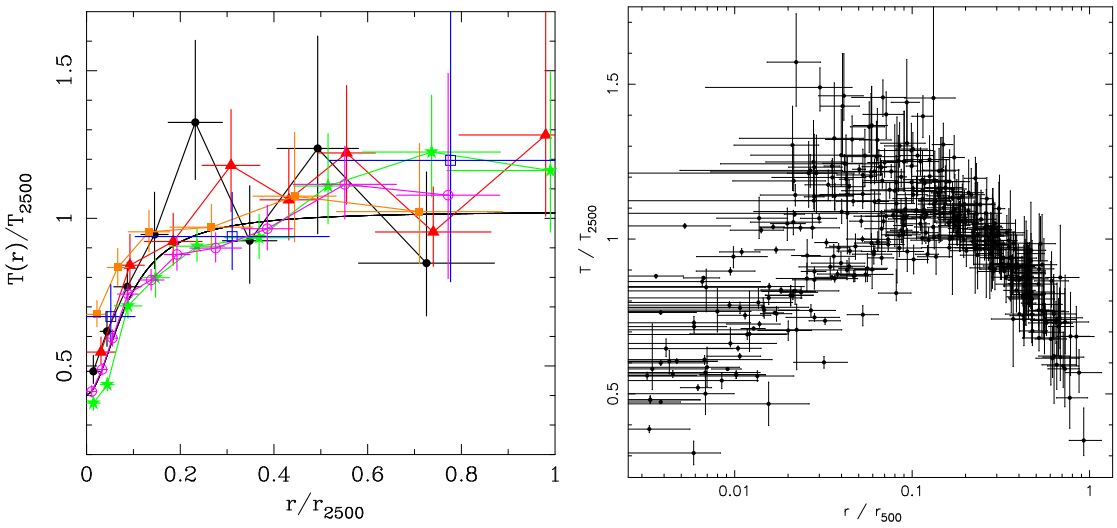

Figure 1.6. Azimuthally averaged temperature (in keV), normalised to r_{2500}, for a sample of galaxy clusters (left; from Allen et al. 2001) and groups (right; from Sun et al. 2009), observed with *Chandra*. See also Figure 6.2, for the profiles of elliptical galaxies.

meaning that (reduced) cooling flows must be common and long-lived.

1.4.1 X-ray Surface Brightness

The first indicator of an active moderate cooling flow is the peaked surface brightness profile, where the cooling time is usually very low (10 – 100 Myr; see Figure 1.5). As previously noticed real density profiles do not present the dramatic cusp predicted by the classic cooling flow model, retaining a moderate slope especially in the inner few kpc ($\log n \gtrsim -1$; Fig. 4.4). A minority of systems, named non-cool-core objects, does not even show the peaked SB_x, suggesting that cooling is in great measure shut off by some kind of violent process (likely cosmological merging).

It is worth noting that at the centre of the group or cluster potential well typically resides a massive elliptical galaxy (BCG, cD), probably due to dynamical friction. The gravity of these galaxies can marginally increase the influence of the cooling flow, and thus the peak of SB_x, in the inner $\sim$ 10 kpc.

1.4.2 Temperature Profiles

The second key characteristic of gas cooling is the central positive gradient in the temperature profiles[5]. Inside r_{cool}, where the cooling time is less than the age of the system, the temperature declines[6], flattening around $1/2 - 1/3$ of the virial temperature, T_{vir} (see Figure 1.6). A pure cooling flow model would instead show central temperatures collapsing well below this floor (Chapters 4-7). Again, plasma cooling

[5]This observational (projected) temperature is extracted from the observed X-ray spectrum, in circular annuli centred on the emission peak.

[6]The decline at intermediate radii is also caused by the flattening of the gravitational potential, and thus a reduced adiabatic compressional heating.

seems substantially quenched for several Gyr by some kind of process; at the same time the cool core must remain intact, as shown by the majority of observed cosmic systems, especially in the nearby universe.

1.4.3 Cooling Rates

The third systematic evidence for severely quenched cooling flows is the aforementioned spectroscopic analysis, mainly carried out by Peterson and collaborators (2001, 2003, 2006). If the gas cools from $T_{\rm vir}$ down to zero K, then the isobaric multiphase cooling flow spectrum (Fig. 1.4 and Eq. 1.5) would show prominent iron L-shell transitions between 10 and 17 Å, in particular Fe XVII (15 – 17 Å) which traces the cold gas with temperatures between $3.5-8\times10^6$ K (at the boundary of the soft X-ray band). Other important cooling-flow lines worth mentioning are Fe XXV, tracing the gas with $T \lesssim 1-5\times10^7$ K, O VIII ($T\sim2\times10^7$ K), and O VI ($T\sim5\times10^5-10^6$ K, in the UV band).

The great resolution of the Reflection Grating Spectrometer (*RGS*) of *XMM-Newton* has provided striking data in the last decade, clearly confuting the classic cooling flow model (Sec. 1.3). As shown in Figure 1.7, there is a strong deficit of observed emission lines (blue curve) linked to the cold gas, especially with temperatures below $1/3\ T_{\rm vir}$. The absence of cold gas at $T < 1$ keV was even reported by lower resolution instruments (David et al. 2001; Molendi & Pizzolato 2001).

Based on all these observations (Peterson et al. 2001, 2003; Oegerle & Hill 2001; Bregman et al. 2001, 2005, 2006; Xu et al. 2002; Tamura et al. 2003), it is nowadays clear that cooling flows in clusters, groups and massive galaxies must be reduced by at least one order of magnitude with respect to the simple classic expectation.

This can be regarded as the fundamental *cooling flow problem*.

There is no reason to differentiate all the single cooling flow problems in different bands (soft X-ray, optical, etc.), as historically done. The cause of the problem is simply one: the hot gas is allowed to cool excessively, at least 10 – 20 times more than observed!

1.4.4 Cold Gas

Another spectacular evidence of quenched cooling flows are the observations of cold gas and star formation, both deeply interwoven (see Chapter 7 for further details).

A distinguishing characteristic of cool-core systems is the presence of warm, optical line-emitting gas (Hu et al. 1985; Heckman et al. 1989; Crawford et al. 1999; Jaffe et al. 2005; Hatch et al. 2007), typically observed at Hα (6563 Å; other relevant lines are Si VI, S XI, O VI). Such warm gas exhibits either a nuclear or filamentary morphology, extending up to tens kpc from the centre (see third column in Figure 1.8), in several clusters, groups and ellipticals. The filaments are often filled with dust, injected by stellar evolution and highly emitting in the IR band (O'Dea et al. 2008). The Hα gas correlates with several properties of the cool core, as the cooling rate and entropy (McDonald et al. 2010, 2011a), strongly suggesting that its origin is tied to the cooling flow and thermal instabilities (Chapter 7), over alternative ram-pressure stripping and galaxy interaction

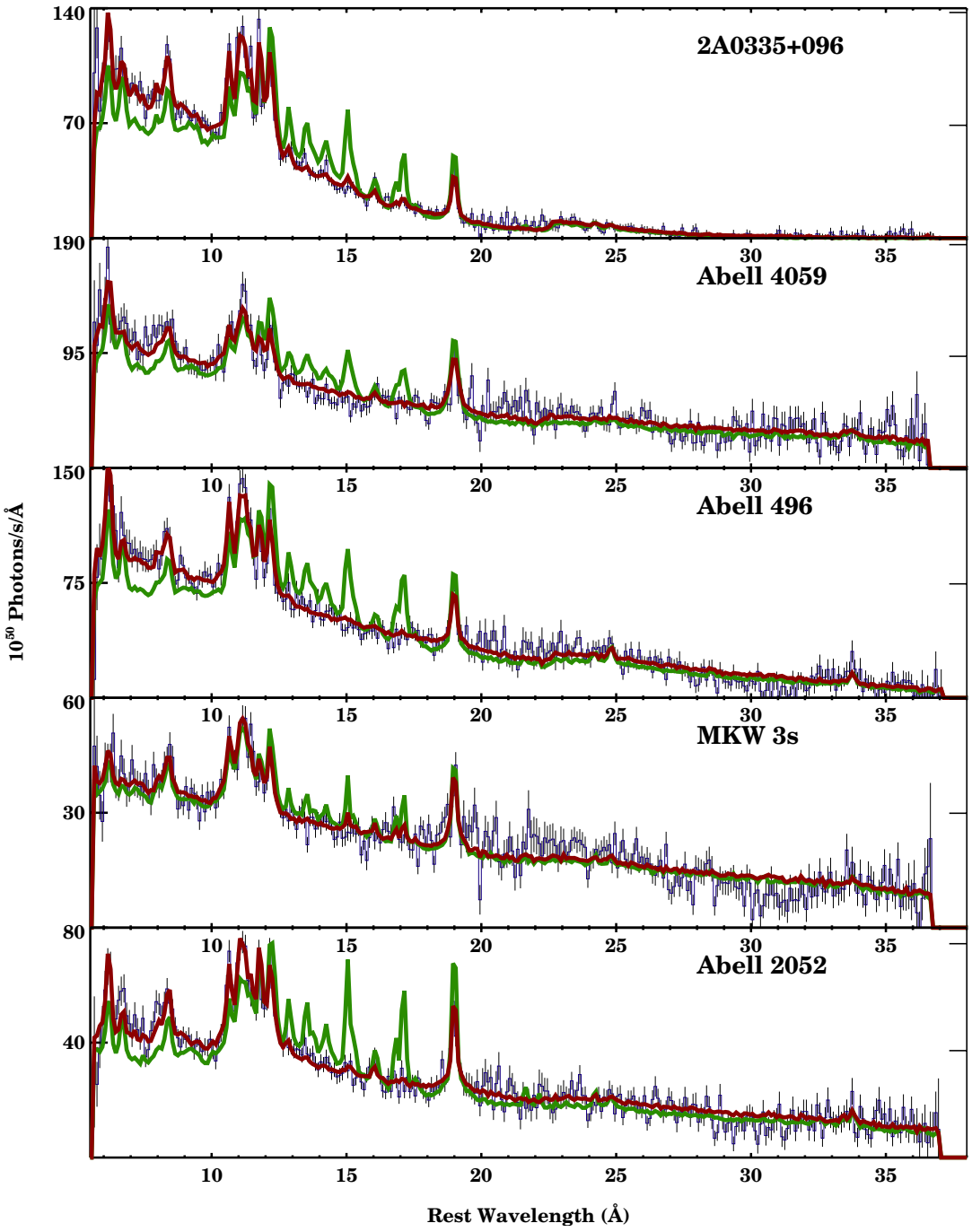

Figure 1.7. Real observed spectra (blue curves; *RGS-XMM*) versus the standard cooling flow model (green); the red curve is an empirical model where emission from the standard cooling flow model is allowed to be adjusted in specific temperature ranges. Clearly, some of the cooling-flow predicted lines (e.g. Fe XVII at $\approx$ 15 Å) are missing from the observed spectrum, in particular the emission associated with the cold gas ($T < 1/3\ T_{\rm vir}$). From Peterson & Fabian (2006).

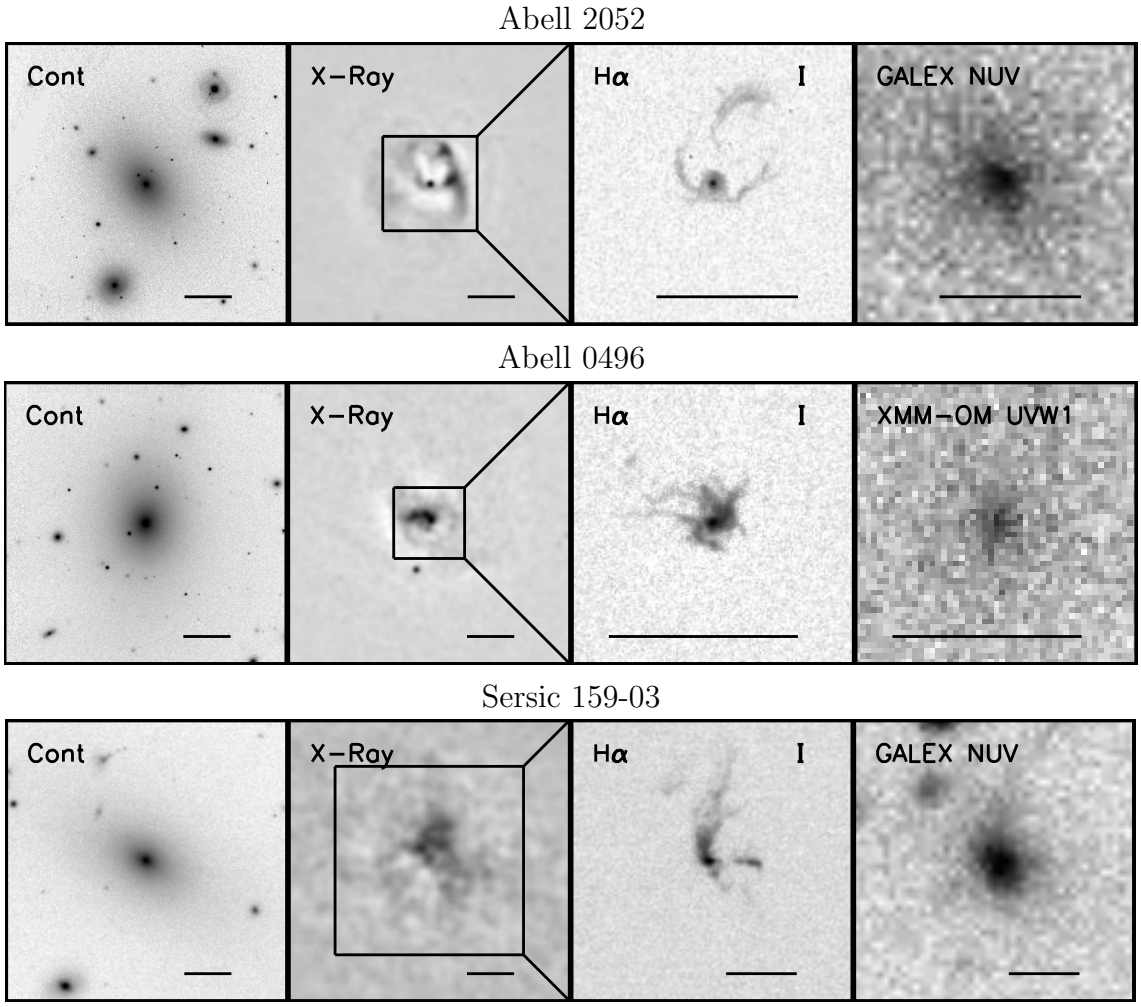

Figure 1.8. Multi-wavelength data for a sample of cool-core clusters (from left to right column): red continuum (MMTF), unsharp mask X-ray image (CXO), Hα (MMTF), and NUV (GALEX). The horizontal scale bar represents 20 kpc. Note the extended filamentary cold/warm gas in the third column. From McDonald et al. (2010).

models.

The Hα gas probably represents the tip of the iceberg, tracer of the actual cold gas at $T \lesssim 10^4$ K, in the form of molecular hydrogen. The latter is quite difficult to estimate, indirectly revealed through CO emission (which is typically calibrated in our Galaxy). For instance, molecular masses in cool-core clusters are in the range $10^9 - 3 \times 10^{11}\ M_\odot$ (Edge 2001; Salomé & Combes 2003). If we naively apply the pure cooling flow model, we obtain cold molecular masses well over several $10^{12}\ M_\odot$ (for clusters; see Chapter 7), essentially forming a new massive elliptical galaxy!

1.4.5 Star Formation

Another piece of evidence for the reduced cooling rates comes from the lack of star formation, which is strongly tied to the evolution of the cold (molecular) gas. This phenomenon is more evident in massive elliptical galaxies at the centre of clusters and

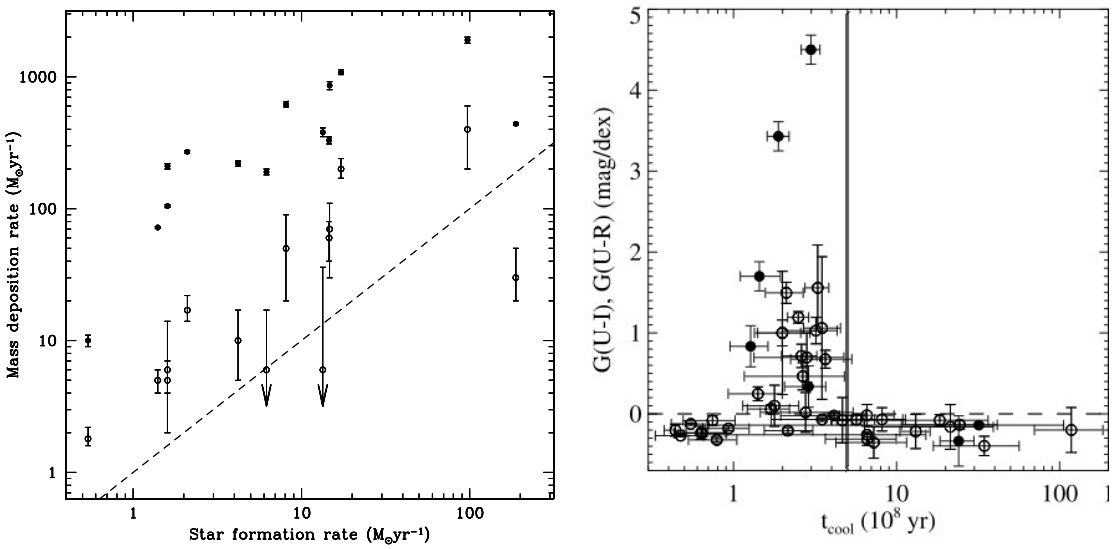

Figure 1.9. Left: cooling rate upper limits versus estimated SFRs (from O'Dea et al. 2008). The filled circles (higher points) correspond to the pure cooling flow rates, while open circles are the cooling rates consistent with the X-ray spectroscopic analysis. The dashed line indicates equal SF and cooling rates. Right: colour versus cooling time (at 12 kpc) for a sample of 46 BCGs (from Rafferty et al. 2008).

groups – BCGs (Johnstone et al. 1987; McNamara & O'Connell 1989; O'Dea et al. 2008). Common results indicate that SFRs are about 30-100 times smaller than the mass deposition rates inferred from the pure cooling flow model, and 3-10 times the cooling rates consistent with the X-ray spectra (SFR $\sim 1 - 20\ M_\odot\ \mathrm{yr}^{-1}$; O'Dea et al. 2008), as shown in Figure 1.9 (left). The previous fact implies also that only a fraction of cold gas transforms into stars (SFR efficiency $\sim 10 - 30\%$).

Star formation, like cold gas, is almost certainly being fuelled by cooling flows. A strong relationship between the X-ray cooling times and SFRs has been resolved by *Chandra*, discovering a clear sharp threshold (Rafferty et al. 2008; Cavagnolo et al. 2008): whenever $t_{\rm cool} \lesssim 50$ Myr massive elliptical galaxies (BCGs) show a UV/blue-light excess (Fig. 1.9, right), a sign of substantial star formation. This demarcation also corresponds to an entropy threshold of about 30 keV cm^2, where the onset of Hα emission and radio activity strikingly appears (see Fig. 7.2; Cavagnolo et al. 2008). The simulations presented in Chapter 7 provide a natural explanation for this threshold.

Note that galaxies in a less dense environment suffer a more severe cooling flow/star formation quenching (e.g. Ferreras & Silk 2000; Trager et al. 2000; Graves et al. 2009; Jeong et al. 2009), moving the system to the quiescent red part of the colour-colour diagram (Temi et al. 2009).

As a concluding remark, the stifled cooling and star formation rates are also particularly manifest in the sharp exponential cut-off of the galaxy luminosity function at the bright end (Benson et al. 2003; Balogh et al. 2006; Croton et al. 2006; Faber et al. 2007; Cattaneo et al. 2008, 2009; see also Section 4.1).

This Section concludes the description of the key properties of idealised and real cooling flows, without pretending to be totally comprehensive. For further insights, I suggest the excellent reviews provided by Fabian (1994), Peterson & Fabian (2006), McNamara & Nulsen (2007), and Böhringer & Werner (2010). The next logical step is to find out why we do not observe classical cooling flows in the universe.

Chapter 2

Heating Mechanisms

WHAT is the main antagonist of cooling flows?

"Although in principle the cooling could instead be balanced by sources of heat, we show below that this is neither physically nor astrophysically plausible, nor it is consistent with observations of cooler, X-ray line-emitting gas" (Fabian 1994).

As inferred from this quote (from the seminal article on cooling flows), during the 90s and before, cooling was considered the central protagonist in the thermodynamical evolution of cosmic systems. Besides the lack of direct evidences, the known heating mechanisms (e.g. conduction, cosmic rays, star formation) would cause the gas to become thermally unstable, leading to overcooling or overheating. A key missing element was the idea of a feedback self-regulation. In contrast to the above statement, I believe that heating *is* physically plausible. In fact, as nature teaches us every day, cooling is always balanced by some kind of heating process on certain spatial and temporal scales, restoring a stable (quasi) thermal equilibrium. The second law of thermodynamics - entropy can never decrease - even indicates that heating is favoured over cooling[1].

It may be possible for non-radiative cooling to proceed near the canonical rates without revealing X-ray line emission through gas-phase mixing, differential photoelectric absorption, or high metallicity inclusions in the hot gas, leading to rapidly unresolved cooling (Fabian et al. 2001a). Sensitive searches, in optical, infrared, and radio bands, for the permanent repository of the cooling material have severely restricted this possibility, if not ruled it out entirely. Nowadays, it is also clear that stellar supernova heating alone is insufficient to prevent the gas from cooling and forming stars (Borgani et al. 2002, 2004; Tornatore et al. 2003; Piontek & Steinmetz 2011). Thus, the massive black hole lurking at the centre of galaxies, groups and clusters becomes the natural suspect to provide the heating required to quench cooling flows (Binney & Tabor 1995).

In this Chapter, I review the main heating mechanisms, with emphasis on the feedback due to the active galactic nucleus (AGN) and its key observational evidences, which seem ubiquitous among all virialised systems (differences are instead explored in Chapters 4-6).

[1] Based on energy conservation, we can write $\rho T\, dS/dt = \mathcal{H} - \mathcal{L}$, where S is the gas specific entropy (erg K^{-1} g^{-1}), $\mathcal{H}$ and $\mathcal{L}$ are the heating and cooling rate per unit volume, respectively. If $dS \geq 0$ (isolated system), then $\mathcal{H} \geq \mathcal{L}$.

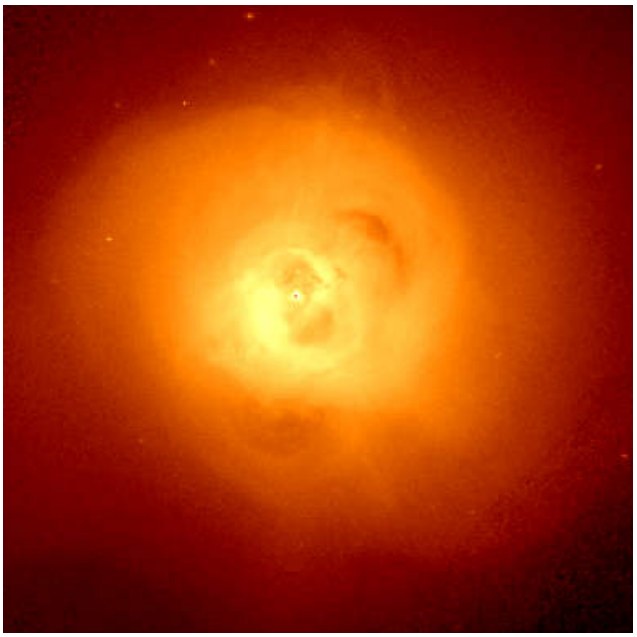

Figure 2.1. *Chandra* composite image in the 0.5-7.0 keV band of NGC 1275 (1.4 Ms; from Fabian et al. 2011), the galaxy at the centre of the Perseus cluster.

2.1 AGN Bubbles

In the last decade, the new generation *XMM-Newton* and *Chandra* telescopes have radically changed the panorama of the evolution of hot gas in cosmic systems. High resolution X-ray images show clear evidence of the interaction between the hot gas and the active galactic nucleus in galaxy clusters (e.g. Perseus; Fig. 2.1), groups (e.g. NGC 5044; Fig. 2.2) and ellipticals (e.g. Cygnus A; Fig. 2.3). Other spectacular examples are Hydra A, M87, A2052, A2597 and Centaurus.

The supermassive black hole, residing at the centre of AGNs, can easily provide enough energy to offset the radiative losses. For a typical black hole mass of $M_{\rm BH} \approx 10^9\ M_\odot$ (e.g. Ferrarese & Merritt 2000; Gebhardt et al. 2000[2]), an amount of energy $E_{\rm BH} \approx 0.1\, M_{\rm BH} c^2 \approx 2 \times 10^{62}$ erg could in principle be injected in the surrounding gas. This is a sizeable fraction of the whole energy radiated away by the intracluster medium in a massive cluster lifetime, and is significantly larger than the binding energy of the interstellar medium in a typical elliptical galaxy or group ($E_{\rm gal} \approx M_{\rm gal}\, \sigma^2$, where $M_{\rm gal}$ and σ are the galaxy mass and velocity dispersion, respectively):

$$\frac{E_{\rm BH}}{E_{\rm gal}} \approx 2 \times 10^{-4} \left(\frac{c}{\sigma} \right)^2 \gtrsim 100\,, \tag{2.1}$$

using the common relation $M_{\rm BH} \approx 2 \times 10^{-3} M_{\rm gal}$ (Häring & Rix 2004), and assuming $\sigma \lesssim 400$ km s^{-1}.

The most visible manifestation of AGN heating are certainly underdense bubbles (e.g. Boehringer et al. 1993; Blanton et al. 2001; Finoguenov & Jones 2001; Jones et al. 2002; Rafferty et al. 2006; McNamara & Nulsen 2007; Finoguenov et al. 2008; Rafferty

[2]The current record is held by NGC 4889, with $M_{\rm BH} \sim 2 \times 10^{10}\ M_\odot$; McConnell et al. 2011.

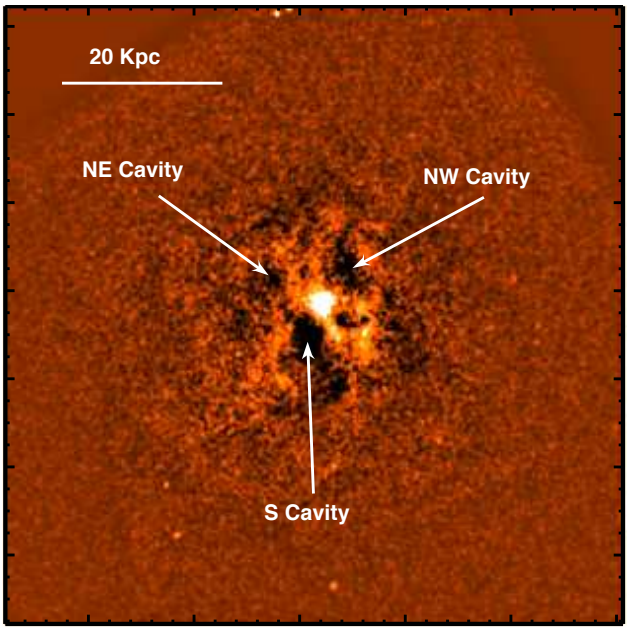

Figure 2.2. *Chandra* ACIS-S unsharp masked image of the galaxy group NGC 5044 in the 0.3-2.0 keV band (from David et al. 2009).

et al. 2008), which rise buoyantly in the hot atmosphere, dissipating their mechanical energy via weak shocks and turbulent wakes. The fairly common presence of X-ray cavities with bright cold rims, often coincident with lobes of radio emission connected to the core by a radio jet (e.g. Figure 2.3), indicates that AGNs inject energy in the hot atmosphere in kinetic form and as relativistic particles, although the quantitative significance of the latter is difficult to estimate (Dunn et al. 2005; Gitti et al. 2010).

The mechanical energy output of the AGN outburst can be *roughly* estimated through its enthalpy (assuming a reversible process), the sum of internal energy and the work required to inflate it (Dunn & Fabian 2006):

$$E_{\rm cav} = H = \frac{\gamma}{\gamma - 1} PV \approx 2.5 - 4\, PV, \tag{2.2}$$

where P and V are the pressure and volume of the bubble, while the adiabatic index ranges from $4/3$ (relativistic plasma) to $5/3$ (non-relativistic plasma). Since the pressure confining an expanding cavity decreases as it expands, Eq. 2.2 is generally an underestimate. The cavity power is then given by $P_{\rm cav} = E_{\rm cav}/t_{\rm age}$, where the bubble age can be associated either with the local sound speed ($t_{\rm age} = R/c_{\rm s}$, at a distance R from the system centre) or the buoyancy velocity[3] ($t_{\rm age} = R/v_{\rm b}$, when the bubble is old and detached from the core).

Several investigations (Bîrzan et al. 2004; Dunn & Fabian 2006; Rafferty et al. 2006) have shown that the AGN power associated with the cavity formation (Eq. 2.2) is comparable to the the core X-ray luminosity, in a large sample of cool-core systems (e.g. Figure 2.4). Although this energetic balance is only a necessary, but not sufficient,

[3]The buoyancy velocity is $v_{\rm b} \approx \left(\frac{2gV}{D\pi r^2}\right)^{1/2}$, where g is the gravitational acceleration, r the bubble radius, and $D = 0.75$ the drag coefficient. This velocity is retrieved equaling the buoyancy force, $F_{\rm b} = gV\,(\rho_{\rm amb} - \rho_{\rm cav})$, with the ram pressure (drag), $F_{\rm d} = 1/2\, D\, \pi r^2\, \rho_{\rm amb}\, v_{\rm b}^2$, where $\rho_{\rm amb}$ and $\rho_{\rm cav}$ are the ambient and bubble density (Churazov et al. 2001).

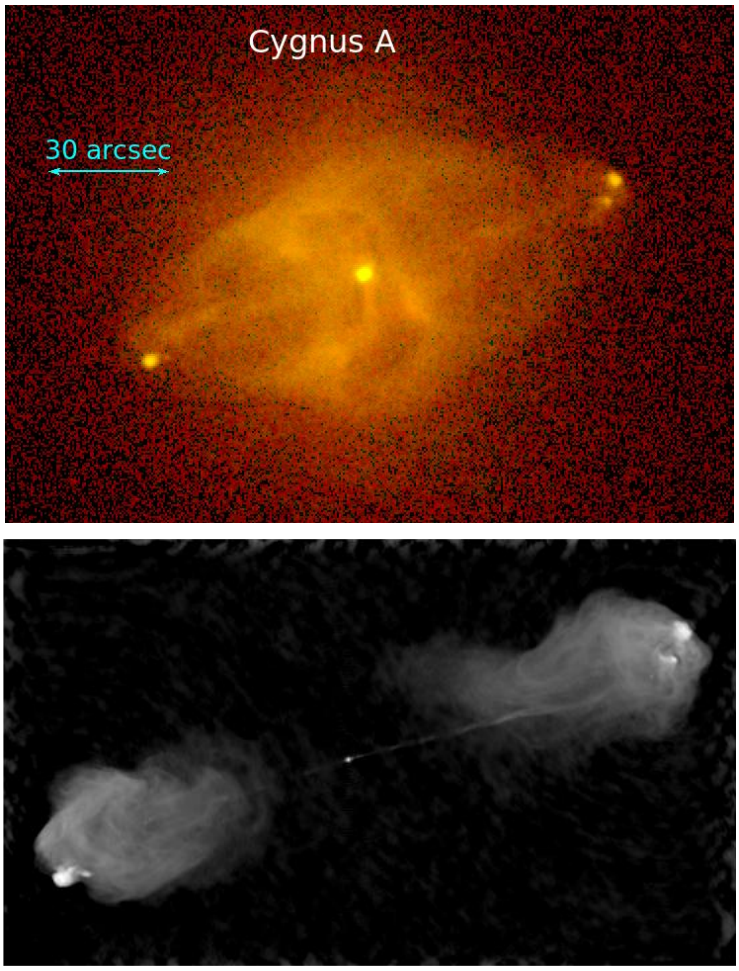

Figure 2.3. Top: *Chandra* X-ray image of the elliptical galaxy Cygnus A (Smith et al. 2002). Bottom: 6 cm VLA radio image of Cygnus A (Perley et al. 1984).

requirement for a heating scenario to be successful, it strongly suggests that the heating process often manifests itself generating bubbles in the hot medium. Cavities can be easily created by directional input of energy, such as jets or collimated outflows, making spherically symmetric form of heating less appealing as major players in solving the cooling flow problem. The relationship between the jet radio luminosity and the cavity power, although with large scatter, further supports this scenario ($P_{\rm cav} \propto L_{\rm radio}^{0.7}$; O'Sullivan et al. 2011a). It is worth noting that not all the bubbles are filled with radio emission ('ghost' cavities), a possible sign of electron ageing or simply indicating a different origin linked to non-relativistic outflows (as assumed in this Thesis).

Cavities are difficult to detect, thus we are biased towards young and powerful systems. Typical surface brightness depressions are 20-40% compared to the level of the surrounding gas. The zoology of cavities is extremely variegated. They are usually found in pairs of elliptical shape, vary enormously in size: from radii smaller than a few kpc in elliptical galaxies (M87; Forman et al. 2007) to the giant bubbles of radius 100 kpc found in the galaxy cluster MS0735.6+7421 (McNamara et al. 2005). Energies can vary from $\sim 10^{55}$ to 10^{61} erg in rich clusters. Cavity systems are often surrounded by cold rims, open arms, filaments and sheets (e.g. Forman et al. 2005, 2007; Fabian et al. 2006;

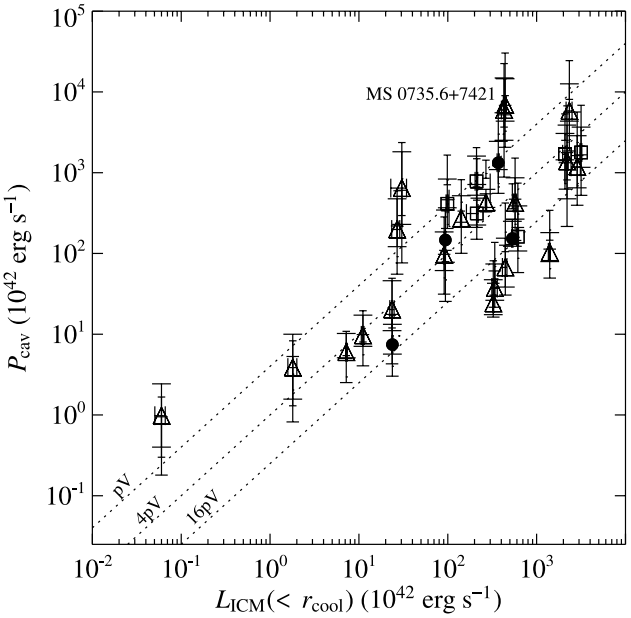

Figure 2.4. Cavity power versus X-ray power radiated within the cooling radius, for 33 galaxies at the centre of quenched cooling flows (from Rafferty et al. 2006).

Baldi et al. 2009), possibly linked to uplifted gas and thermal instabilities (Chapter 7).

With deeper observations, the frequency of observed cavities increases, suggesting that the AGN cycle (called 'duty cycle') shall be very short or almost continuous (see also the simulations in Chapters 5-7). For instance, the detailed analysis of Dunn & Fabian (2006) indicates an AGN cycle greater than 0.7. Some rare system displays small radio lobes without the presence of X-ray cavities (e.g. A2063, A2204).

Note that the bubble generation is just one part of the actual heating, but not the whole feedback story, including the jet/outflow mechanical source, and subsequent shocks and turbulence propagation (as tackled in the next Sections). In fact, in some system, the cavity $P_{\rm mech}$ alone is not able to balance radiative losses. Furthermore, simple bubbles thermally inflated ex abrupto (Churazov et al. 2001; Brüggen & Kaiser 2002; Dalla Vecchia et al. 2004; Omma et al. 2004) tend to quickly fragment, due to Kelvin-Helmoltz and Rayleigh-Taylor instabilities, unlike observed ones. On the contrary, bubbles inflated by outflows are more stable and similar to observations (see Chapters 4-6), a signal that cavities may be just one of the side effects of the feedback process.

2.2 AGN Shocks

Whenever the AGN feedback injects a large amount of energy in the surrounding cooling plasma, especially through outflows or jets, a typical hydrodynamic feature appears: a shock. A shock is simply the transition layer where the plasma properties vary dramatically, forming a clear discontinuity, both in density and temperature, given by the famous Rankine-Hugoniot conditions:

$$\frac{T_2}{T_1} = \frac{(\gamma+1)-(\gamma-1)\,\rho_1/\rho_2}{(\gamma+1)-(\gamma-1)\,\rho_2/\rho_1}\,, \tag{2.3}$$

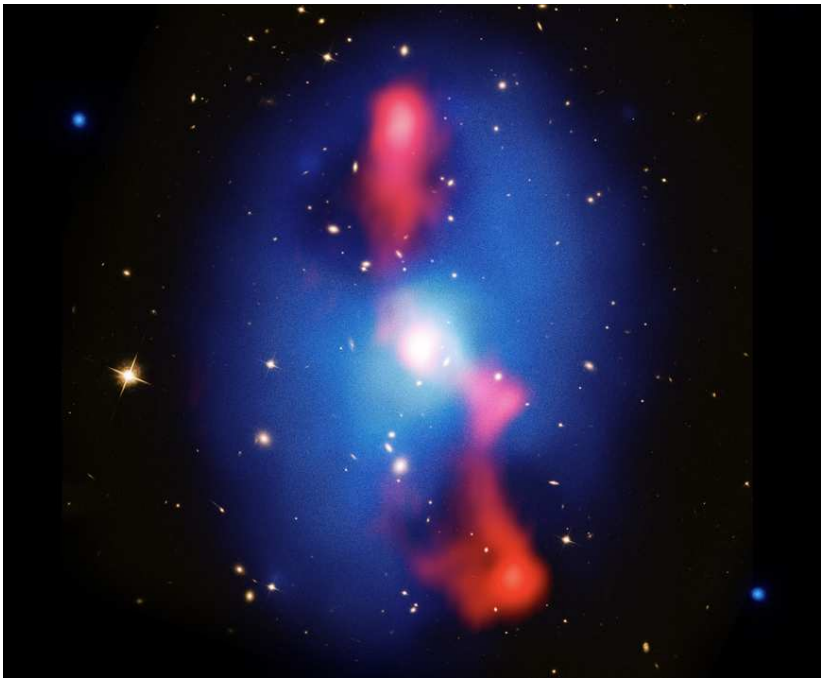

Figure 2.5. Deep *Chandra* X-ray image (blue) and VLA 330 MHz radio image (red), superposed to the HST optical image of the galaxy cluster MS0735.6+7421 (from McNamara et al. 2005); the box is large 800 kpc.

with typical temperature jumps $T_2/T_1 \sim 20-30\%$. At this layer, the entropy shows also a positive jump, meaning that a shock is always associated with irreversible heating: $\Delta Q \simeq T\Delta S$, where the entropy jump ΔS is proportional to the cube of the shock strength ($\delta P/P$; Landau & Lifshitz 1959). Therefore, the role of shocks can not be neglected in the AGN feedback cycle.

AGN shocks expand almost isotropically, with typical elliptical cocoons enveloping the radio-lobe cavities. Radiative losses are negligible on the short shock timescales (see below), while magnetic fields are dynamically insignificant in the ISM/ICM. Surface brightness discontinuities are very difficult to detect, since the observed shocks are seen in projection and only slightly supersonic, with Mach number ($v/c_s \sim 1.1-1.8$), except for rare cases (like Centaurus A with Mach 8 and NGC 3801 with Mach 4). A beautiful example of cocoon shock has been found in MS0735.6+7421 (McNamara et al. 2005; see Fig. 2.5), with Mach ~ 1.3. The shock energy corresponds to several PV per cavity, meaning that Eq. 2.2 is just a lower limit of the feedback energy input.

The fact that we do not observe strong shocks in the majority of systems, even when the AGN outburst is powerful, should not be a surprise. Let us consider a simple spherical thermal explosion in a singular point, also known as Sedov problem. Using only the laws of Newton, we can write $d(M\dot{R})/dt = 4\pi R^2 P$, where $M = \rho V$ and R are the mass and radius of the shocked expanding shell and P the pressure generated by the feedback explosion ($P = E/(\gamma-1)V$, with $V = 4/3\,\pi R^3$ and $\gamma = 5/3$). Solving the differential equation through a power-law function and knowing that the medium sound speed is $c_s \approx 1.5\times10^4\,T^{1/2}$, we obtain the Mach number of the shocked shell as a function of time,

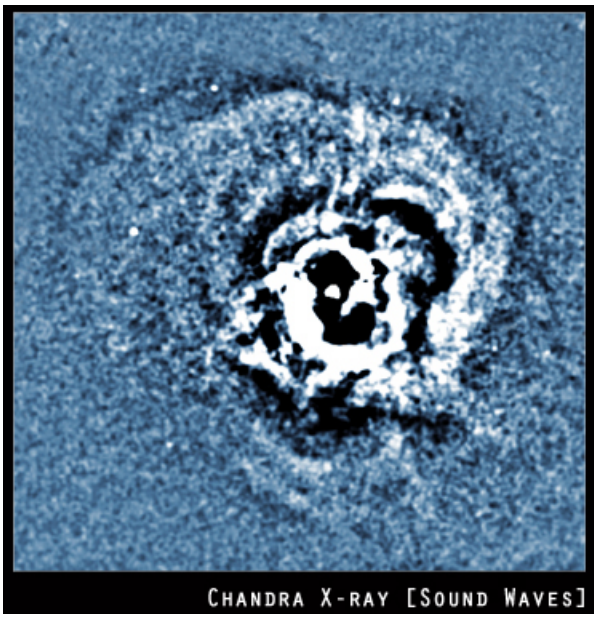

Figure 2.6. Unsharp mask image of the Perseus cluster; 0.3-7.0 keV *Chandra* band (from Fabian et al. 2006). Buoyant bubbles, weak shocks and ripples are clearly visible.

after a few algebraic steps[4]:

$$\text{Mach} \simeq 3.6 \times 10^{-5} \left(\frac{E}{\rho}\right)^{1/5} T^{-1/2}\, t^{-3/5}\,. \tag{2.4}$$

For typical values of the ICM ($T \sim 10^8$ K, $n \sim 10^{-3}$ cm^{-3}) and a range of injection energy of $\sim 10^{55} - 10^{58}$ erg, the Mach number drops below 2 (weak shock regime) in just $\sim 0.1 - 1$ Myr. Most of the observed bubbles have an age $\sim 10 - 100$ Myr, implying the associated Mach should be always very mildly supersonic (a similar argument applies to the bubble rims, explaining why they do not usually appear hotter than the surrounding medium). In conclusion, it is statistically difficult to observe very young and thus strong shocks (or bubbles). The previous simple calculation, even without including the PV work, demonstrates that AGN shocks are an essential - even primary - ingredient of the feedback heating required to quench cooling flows (Chapters 4-7).

Together with shock cocoons (e.g. McNamara et al. 2005; Nulsen et al. 2005a,b; Blanton et al. 2009; Randall et al. 2011), in a few deeply observed systems (like Perseus; Fabian et al. 2006) several disturbances are detected in the surface brightness, interpreted as concentric sound waves (or very weak shocks). These sonic ripples (Figure 2.6) have pressure amplitudes $\sim 5 - 10\%$, with a period 10^7 yr. The dissipation of the sound waves could generate in principle additional heating in order to sustain the cooling flow (Ruszkowski et al. 2004a,b). Whereas weak shock heating depends on the cube of the shock strength (pressure amplitude), sound wave heating is proportional to the square of the wave amplitude (Landau & Lifshitz 1959), making it more effective on larger scales. Unfortunately, the dissipation process is poorly understood (Sec. 2.5), because the amount of viscosity (and associated conduction) is yet unknown[5], although its presence

[4]The differential equation to solve is: $3R^3\dot{R} + \ddot{R}R^4 = 9E/4\pi(\gamma - 1)\rho$, which has a power-law solution $R = At^{\alpha}$, with $\alpha = 2/5$ and $A = (225\,E/16\pi\rho)^{1/5}$. Differentiating $R(t)$ leads to the shell velocity and thus Mach number.

[5]For example, the viscosity coefficient for an unmagnetised plasma is on the order of the Spitzer value: $\mu \approx$

may be suggested by the stability of bubbles and filamentary structures. Nevertheless, sonic ripples in the temperature and density profiles are again a typical phenomenon of AGN activity, probably originated from the repeated (or altered) bipolar jets/outflows.

2.3 AGN Jets and Outflows

Although the most visible features of AGN heating are buoyant bubbles and shocks, the real origin of the feedback is probably the mechanical input associated with jets and/or outflows. This is also the fundamental thesis of the present work, that I will confute or validate through several hydrodynamic simulations.

From an observational point of view, there is widespread evidence for the existence of jets and outflows originating from the galactic nuclei, possessing a great amount of mechanical energy on kpc scale. Most of the AGN cavities appear inflated by two bipolar jets, which are strongly visible in the radio band due to synchrotron radiation (see Fig. 2.3). The anisotropic dredge-up of cold metal-rich gas via entrainment also support the AGN outflow scenario (Kirkpatrick et al. 2009; Gitti et al. 2012).

The formation and original composition of jets/outflows near the black hole is still matter of extensive debate. The most popular mechanism was proposed by Blandford & Payne (1982). Energy and angular momentum are magnetically extracted from the accretion disc, by the $\boldsymbol{B}$-field lines anchored to the disc. The ejected mass removes angular momentum and allows material to fuel the black hole, independently of viscosity; the flow radial velocity can in fact be written as $\boldsymbol{v} = f\,\boldsymbol{B}/4\pi\rho + \boldsymbol{\omega} \times \boldsymbol{r}$, where the second term is the rotational velocity (f is the ratio of the constant mass flux to magnetic flux). At large distances from the disc, the toroidal component of the magnetic field accelerates the light particles (the so-called 'magnetic tower'; Figure 2.7, left), forming two collimated relativistic jets.

MHD outflows may be dominated initially by relativistic electrons or Poynting flux (e.g. Nakamura et al. 2008), however the large ratio between mechanical jet power and synchrotron luminosity ($> 100 - 1000$) implies that jets are governed on large kpc scales by heavy particles. This is another reason why our feedback simulations are based on *massive* outflows (see Binney 2004; Soker & Pizzolato 2005 for related insights). Moreover, relativistic radio jets strongly decelerate within a few kpc from the AGN, due to the entrainment of ambient gas (especially in Fanaroff-Riley I sources; e.g. Giovannini 2004; Croston 2008).

AGN radiation may be the other (complementary?) mechanism able to generate massive subrelativistic outflows. One of the main radiative processes may be Compton heating, given by (per unit volume)

$$\mathcal{H}_{\rm C} = C\,\frac{\rho\,(T_{\rm C} - T)\,L_{\rm AGN}}{4\pi r^2}\,, \tag{2.5}$$

where $L_{\rm AGN}$ is the radiative AGN luminosity (with radiative efficiency typically $\eta \gtrsim 0.1$), with a Compton temperature $T_{\rm C} \approx 2 \times 10^7$ K (Sazonov et al. 2004), and C the

$1.8 \times 10^3\,(kT/5\ {\rm keV})^{5/2}$ g cm^{-1} s^{-1} (Braginskii 1958).

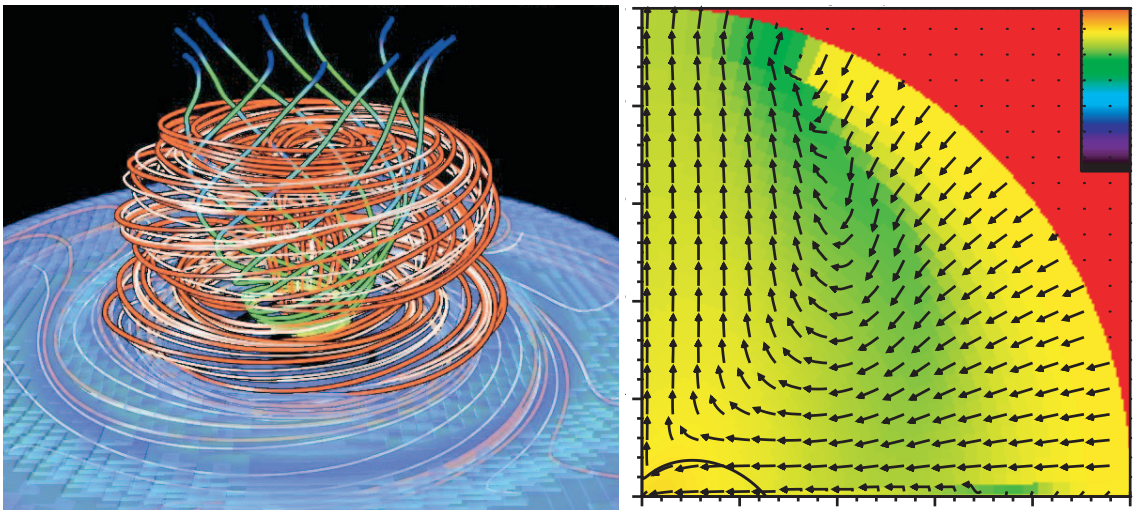

Figure 2.7. Left: accumulated magnetic field lines (red and white), emerging from the accretion disc, produce a magnetic tower; the toroidal field component is able to accelerate a collimated jet (from Kato et al. 2004). Right: radiatively-driven outflow; temperature map (10^3 – 10^7 K) with the velocity field overlaid, in a box of ≈ 7 pc (from Proga 2007).

process constant[6]. Even without using the radiative transfer equations, through which $L_{\rm AGN}$ decreases due to absorption, I note that this type of feedback requires very high luminosities ($> 10^{45}$ – 10^{46} erg s^{-1}, typical of quasars), plus a very dense impacting medium ($n > 10^4$ cm^{-3}). Another flaw of the model is that it produces a thermal isotropic blast, usually overheating the core of the system. Finally, where $T > T_{\rm C}$ (like in galaxy clusters), the Compton process induces cooling, and not heating.

A more appealing outflow mechanism is associated with radiation pressure, linked to electron scattering and dusty gas (with some large opacity κ; cm^2 g^{-1}). In fact, the wind shock will likely lose energy due to cooling, conserving only ram pressure (King & Pringle 2007). The generated pressure gradient can be written as

$$\nabla P_{\rm rad} = \frac{\kappa \rho}{4\pi r^2} \frac{L_{\rm AGN}}{c}. \tag{2.6}$$

The geometry of these outflows is controlled largely by the radiation field: a brighter disc/central object produces a more polar/equatorial wind (e.g. Proga 2007; Figure 2.7, right), driven vertically by the disc radiation and radially by the central source photons. Nevertheless, on large kpc scales the outcome is again the production of subrelativistic massive bipolar outflows. Therefore, our analysis does not require to distinguish between the entrained (radio) jet and radiative wind scenario, as long as both produce a mechanical anisotropic feedback. In future, I plan to focus on the detailed accretion and entrainment process (Chap. 8).

It is worth noting that the radiative mode could likely play an important role at high redshift[7] ($z \gtrsim 2$), given the increasing number of quasars; on the contrary, in the local

[6] $C = (4\sigma_T/3m_e c^2)(3k_b/2\mu m_p)$ cm^2 g^{-1} K^{-1}, where σ_T is the Thomson cross section, c the speed of light, m_e and m_p the electron and proton mass, k_b the Boltzmann constant, $\mu \approx 0.61$ the gas molecular weight.

[7] Assuming momentum balance, $L_{\rm Edd}/c = GM_{\rm gal}M_{\rm gas}/r^2$, it is easy to show that Eddington-limited quasars may reproduce the Magorrian relation: $L_{\rm Edd} \propto M_{\rm BH} \propto (\sigma^2 r)\,(\sigma^2 r)/r^2$, thus $M_{\rm BH} \propto \sigma^4$. This fact suggests that the radiative mode may have a fundamental role at early times in shaping the primordial galaxy.

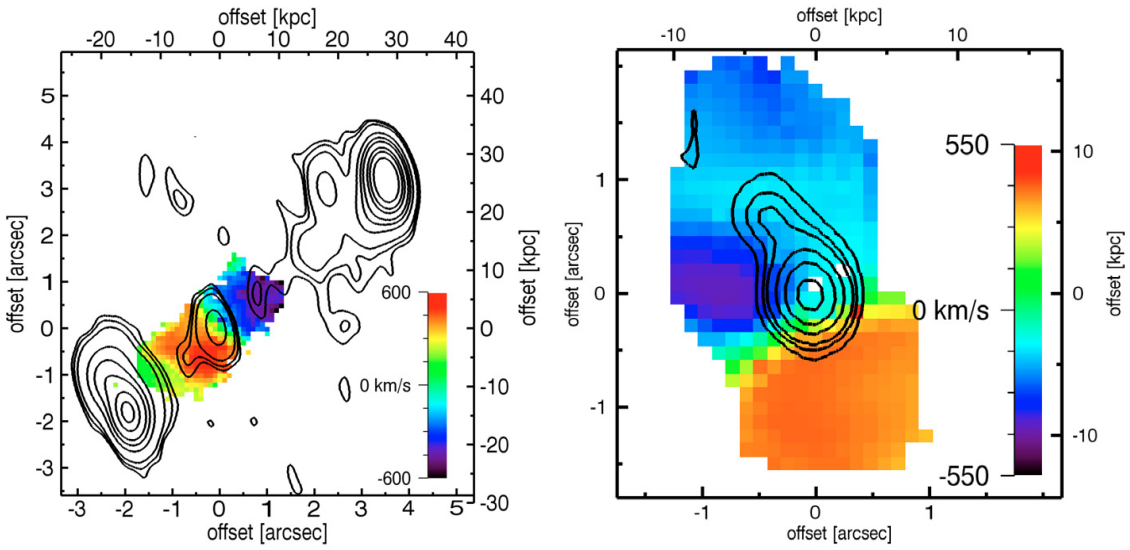

Figure 2.8. Velocity map of MRC0406-244 (left) and TSX0828+193 (right), retrieved from [O III] lines (from Nesvadba et al. 2008).

universe mechanical feedback is probably driven by entrained (magnetically-driven) radio jets, with radiatively inefficient AGN sources (see Merloni & Heinz 2008). Another possibility is that they may be complementary processes. For instance, we do not observe a clear correlation between the AGN radio core luminosity and X-ray losses, implying that the radio jet is not a necessary requirement for the mechanical feedback process.

In the last decade of observations several research teams have provided an increasing number of evidences that support the existence of mechanical massive AGN outflows. Unfortunately, most of the times we can not directly resolve the central pc/kpc region, where the core of the outflows resides. The best available method in order to study AGN outflows is via blueshifted absorption lines in different bands: UV and X-ray (e.g. George et al. 1998; Crenshaw et al. 1999, 2003; Kriss et al. 2003; Risaliti et al. 2005; McKernan et al. 2007; Cappi et al. 2009, 2011; Pounds & Reeves 2009; Tombesi et al. 2010a,b, 2012), optical (Nesvadba et al. 2008, 2011), and 21-cm microwave (Morganti et al. 2005, 2007). High-energy bands tend to capture the fast and light component of the outflow, with velocities up to $0.1c$ and mass rates around a fraction or few $M_\odot$ yr^{-1}. On the contrary, in low-energy bands, like in optical, is observed the slower molecular component, with $v \lesssim 1000$ km s^{-1} and high outflow mass rates over $10-100\ M_\odot$ yr^{-1} (see Figure 2.8), a strong indication of substantial entrainment. These lines usually originate at pc/kpc distance from the nucleus, showing conical outflows with narrow opening angles, sometimes consistent with precession.

2.4 Self-regulation and Thermal Balance

A healthy heating model must be tightly entangled with the cooling of the hot atmosphere, in the so-called feedback loop. Failure to meet this key requirement implies overcooling or overheating of the core at some point of the evolution, besides accidental coincidences (like mergers). In fact, for most of the heating mechanisms without feedback, the effect

of excess heating is to increase its dominance over cooling, and vice versa, making the balance unstable.

In order to prevent significant gas cooling, the feedback process must be activated with a frequency not greatly different from $1/t_{\rm cool}$, where the central cooling time usually remains below few 10^8 yr for clusters (Voigt & Fabian 2004; Sanderson et al. 2006; Mittal et al. 2009) and even lower for elliptical galaxies or groups; $t_{\rm cool} \sim 1.5 \times 10^7$ yr for NGC 4636 (Baldi et al. 2009). Another evidence for the self-regulation is that atmospheres with larger X-ray cooling luminosities host more powerful AGNs (Fig. 2.4).

On the other hand, the presence of central temperature drops, abundance gradients[8], low cooling times, and the observations of modest cold gas reservoir in the core (Chapter 1), suggest that heating should not exceed cooling by more than $\sim 10\%$, even in the most powerful outbursts (e.g. MS0735.6+7421, with 10^{62} erg). This (quasi) thermal balance appears rather strict, continuing over several Gyr of evolution[9].

The previous two requirements for a successful heating are the foundations of my theoretical investigation. In several works the thermostat assumption is often considered as a one-way process. However, the feedback heating must preserve the cool-core appearance in the majority of clusters (e.g. Peres et al. 1998; Mittal et al. 2009), groups and ellipticals (Sun et al. 2005, 2007). A spatially concentrated heating, while very efficient in stopping the cooling process, often generates negative temperature gradients, contrary to the observations (Brighenti & Mathews 2002b, 2003). Instead, the heating process is surprisingly 'gentle', as remarked by the soft flattening of the central entropy profiles (Voit & Donahue 2005), and by the survival of negative metallicity gradients. Note that, in less bound objects, the AGN feedback seems to have a stronger impact on the previous properties (possibly inducing the deviation in the self-similar scaling relations).

The best candidate for a feedback loop is certainly the central supermassive black hole. For instance, since the buoyancy timescale of the inflated bubbles is usually lower than the cooling times (Rafferty et al. 2008), the rapid AGN activity seems capable to avoid runaway cooling. Although the dynamics is certainly complex, cooling and infalling cold gas may drastically increase the accretion rate in a few dynamical times (< 1 Myr), boosting the AGN heating and restoring the thermal balance, until a new moderate cooling flow occurs again. Such idealised 1D loop is very efficient, however, the coupling of the AGN energy with the surrounding medium and the degree of thermalisation is far more complicated, as also shown by the feedback simulations in Chapters 4-7.

As a concluding remark, it is quite astonishing how the thermal balance is strictly maintained in the majority[10] of cosmic systems, considering that the feedback energy comes from a nuclear region smaller than a needle compared to the whole Earth!

[8] Cool cores usually present a negative metallicity gradient, implying that there should be no rapid mixing between the central and external regions (> 100 kpc).

[9] At higher redshift, strong (Perseus-like) cooling flows appear even more quenched, showing a declining cold gas nebular emission (Samuele et al. 2011); see also Chapter 7.

[10] A minority of systems, $\lesssim 30\%$, displays a non-cool core, with a flat temperature gradient; they are usually very perturbed, associated with a merger event. We can not exclude, however, that an extreme AGN outburst has recently modified the radial profiles.

2.5 Transport: Conduction and Turbulence

Transport properties in the plasma of cosmic systems are currently very difficult both to model and to estimate. In the absence of magnetic fields, the transport properties would be governed by Coulomb collisions, with electron mean free path[11] $\lambda_{\rm e} \approx 0.2\,(T/10^7\ {\rm K})^2\,n_{\rm e}^{-1}$ pc (and very similar for the ions). The mean free path determines the thermal conduction of the plasma, i.e. the natural transport of heat from the reservoir of hot gas toward the cold gas regions. The heat flux can be written as

$$q = -\,\kappa\,\nabla T\,, \tag{2.7}$$

where the thermal conductivity κ for a plasma is usually given by the Spitzer (1962) value, which can be expressed in terms of the electron number density $n_{\rm e}$, mass $m_{\rm e}$ and temperature $T_{\rm e}$ (Cowie & McKee 1977):

$$\kappa_{\rm S} = 1.31\,n_{\rm e}\,\lambda_{\rm e}\left(\frac{k_{\rm b}T_{\rm e}}{m_{\rm e}}\right)^{1/2} \approx 5\times10^{-7}\,T^{5/2}\ \ [{\rm erg\ s^{-1}cm^{-1}\,K^{-1}}]\,. \tag{2.8}$$

Thermal conduction in very hot clusters may play a significant role in preventing gas from cooling (e.g. Voigt & Fabian 2004), assuming that the conductivity occurs at or near the Spitzer value (Eq. 2.8). However, for the inner cooler parts of clusters and in the regime of groups (below 5×10^7 K), the effective conductivity required to halt cooling is certainly insufficient (see Figure 2.9). Another fundamental problem is that thermal conduction is drastically reduced in the presence of a magnetic field: $\kappa = f\,\kappa_{\rm S}$, where f can easily drop below $0.1 - 0.01$ when the magnetic field is tangled on the very small scales (thus conduction depends only on the coherence length scale of the field; Chandran & Cowley 1998). The suppression factor f is yet very poorly determined.

Turbulent motions in the interstellar/intergalactic medium can certainly help conduction, raising the level of gas mixing. The turbulent conductivity can be expressed as $\kappa_{\rm turb} = n_e k_{\rm b}\,(C_{\rm dyn}\,L\,v_L)$, where $C_{\rm dyn}$ is a constant of order unity (Cho & Lazarian 2003). Assuming a reasonable turbulent scalelength $L \sim 20$ kpc, plus a subsonic turbulent velocity $v_L \sim 0.1 - 0.5\ c_{\rm s}$, and fixing the cooling time to 1 Gyr, a rough estimate of the turbulent conductivity in galaxy clusters is (Voigt & Fabian 2004)

$$\kappa_{\rm turb} \sim 4\times10^{13}\,T_{7.7} \sim 5\,\kappa_{\rm S}\,(T_{7.7}^{-3/2})\,, \tag{2.9}$$

where the temperature is expressed in units of 5×10^7 K. Therefore, as also pointed out in Figure 2.9, turbulence may considerably increase the thermal conductivity, or at least sustain the conductivity with $f \gtrsim 0.3$ (Narayan & Medvedev 2001). Similar reasonings apply also to the degree of viscosity, tightly associated with conduction.

The transport processes may be far more complex[12]. The ratio of the (electron) Larmor radius is incredibly small compared to the electron mean free path: $r_{\rm L}/\lambda_{\rm e} \simeq 10^{-10}\,n_{\rm e}\,T_7^{-3/2}\,B_{\mu{\rm G}}^{-1}$, where the temperature is expressed in units of 10^7 K and the magnetic field in μG[13]. This means that the plasma particles are tightly tied to the magnetic

[11] The logarithm of the associated impact parameter has an average value $\ln\Lambda = 29.7 + \ln n^{-1/2}(T/10^6\ {\rm K}) \sim 38$.

[12] Plasma instabilities, like firehose, mirror and gyrothermal, may additionally alter the heat flux; in future the ISM/IGM may prove to be as complex as the solar wind!

[13] The typical magnetic field strength in the IGM/ICM is a few μG (e.g. Bonafede et al. 2011).

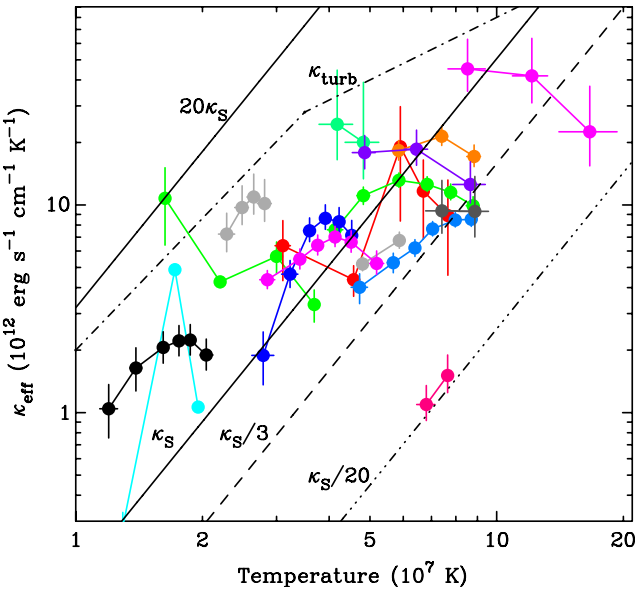

Figure 2.9. The effective conductivity required to halt X-ray cooling in a sample of cluster cores, based on the observed density and temperature profiles (from Voigt & Fabian 2004). Each colour is a different cluster, with measurements at several radii. The black lines denote either the Spitzer, κ_S, or the turbulent conductivity, κ_{turb}.

field lines, making transport extremely anisotropic and temperature gradients unstable. When temperature increases in the direction of gravity, as in the cluster outskirts, the magnetothermal instability (MTI; Balbus 2000) tends to make the $\boldsymbol{B}$-lines radial, promoting the radial heat flux. On the other hand, in cool cores, where the temperature gradient is positive, anisotropic conduction makes the atmosphere subject to the heat flux driven buoyancy instability (HBI; Quataert 2008). HBI reorients the $\boldsymbol{B}$-lines in the direction perpendicular to gravity (and ∇T), thus suppressing thermal conduction. However, turbulent motions seem again to play a key role in randomising the magnetic fields and restoring high levels of conduction (Ruszkowski & Oh 2010, 2011).

The exact strength of turbulence is yet poorly known and is expected to vary throughout the evolution of the cosmic system. In general, turbulence should not be so strong to cancel typical observed structures, such as radio lobes, optical cold filaments, and metallicity gradients (Rebusco et al. 2005). Recent attempts have been made to put constraints on the turbulent velocities from the width of the lines in *RGS* spectra (Sanders et al. 2011). Upper limits ranging from 200 km s^{-1} up to 1500 km s^{-1} were found in a sample of 62 clusters, groups and elliptical galaxies. Turbulence seems therefore typically sonic or subsonic. The origin of turbulence is linked to galaxy motions[14] and minor/major mergers at large radii[15]. In the core, turbulence is very likely driven by AGN outbursts, as shown in the next Chapters. Very recently, de Plaa et al. (2012) have measured the turbulence through line widths and resonant scattering in two famous groups with evident

[14]The gas behind galaxies, moving at supersonic velocities, forms a wake, which may heat the surrounding cooling plasma via dynamical friction and weak shocks. However, the efficiency of conversion is usually very low (see Faltenbacher et al. 2005), unless adopting a large viscosity.

[15]A major merger can release up to 10^{64} erg, however the tiny cool core, with high central pressure, is usually shielded from such huge disturbances.

AGN outbursts, placing rather stringent constraints: $320 < v_{\rm turb} < 720$ km s^{-1} (NGC 5044) and $140 < v_{\rm turb} < 540$ km s^{-1} (NGC 5813). Overall, turbulence represents another interesting observational test for AGN feedback models.

Given all the previous uncertainties and strong assumptions, the heating linked to thermal conduction will be neglected in the present work. There are two other fundamental reasons to believe that conduction is not the key process governing the heating of cooling flows (although it may help the dissipation of energy in the hotter systems; Brighenti & Mathews 2002b). First, thermal conduction and turbulent heat diffusion involve no evident feedback mechanism, without a clear link between heating and radiative cooling rates[16]. Second, conduction presents a serious fine tuning problem. If the primordial gas starts out isothermal, then either the gas cools in which conduction is not able to stop it ($T^{5/2}$ dominates over ∇T), or conduction is efficient and there is no cold gas ($\nabla T \sim 0$). Thus, how are initially generated the positive temperature gradients of cool cores? Why are rich clusters so 'smart' to fix the conductivity to $0.3\,\kappa_{\rm S}$, while poor ones over $0.9\,\kappa_{\rm S}$? Future specialised investigations are required to assess the detailed (secondary?) role of conduction.

This Section concludes the description of the main properties of the heating processes, the majority of them linked to the central active galactic nucleus. In this work, I intend to test the idea that the massive mechanical outflows are the original source of the feedback mechanism, capable to stifle cooling flows. In order to accomplish this task, my method of investigation is based on three-dimensional hydrodynamic simulations, with a large spatial and temporal range.

[16]The absence of feedback applies also to several past unsuccessful heating models, such as mergers and dynamical friction.

Chapter 3

Numerical Methods

THE PRESENT Chapter is entirely dedicated to the computational engine, which allowed to properly carry out the astrophysical investigation on AGN feedback. The main purpose of the code is to solve the equations of hydrodynamics, with the required astrophysical source and sink terms, employing various advanced numerical methods.

The numerical implementation, testing and development of the code represent a key and massive part of the present Thesis. In the following Sections, I intend to tackle and explain only the major properties of the developed numerical structure. I foresee in fact that the usual reader should be more interested in the physical and astronomical results (Chapters 4-8), rather then pure computational complexities. Although a substructure of the investigation, numerics remains the hearth of this work. Thus, I recommend to assimilate the basics of computational fluid dynamics through the following exemplary text books: in first place Toro (1997) and LeVeque (1998), but also Fletcher (1991), Laney (1998) and Roache (1998).

My preferred method of investigation is to entirely avoid using the basic code as a black box. After learning all the details of the basic modules, I have tested and upgraded them, plus I have developed several new physical modules, such as: astrophysical initial conditions, plasma radiative cooling, self-regulated AGN outflows, supernovae and stellar winds, static gravity, black hole accretion, cold mass dropout, and Gaussian perturbations.

3.1 FLASH code

The original code, chosen for the present research, is FLASH (version 3 and 4, which are very similar[1]). FLASH is a modular code, designed to allow users to configure their initial and boundary conditions, change algorithms, and implement new physics. It is based on a block-structured adaptive grid, placing resolution elements only in the regions of interest. In addition, FLASH uses the Message-Passing Interface (MPI) library to achieve portability and very high scalability on a variety of high-performance parallel computers (HPC).

[1] FLASH was first developed by the DOE NNSA-ASC OASCR Flash Center at the University of Chicago.

FLASH was originally designed to attack some of the most challenging computational astrophysical problems, namely type Ia supernovae, classical novae and X-ray bursts (first described in Fryxell et al. 2000). The code solves the fully compressible, reactive hydrodynamic equations, using an advanced Godunov-type solver (PPM). State-of-the-art modules for the equations of state and thermonuclear reaction networks are also included. It is beyond the scope of the work to describe the entire FLASH capabilities (e.g. magnetic fields, particles, cosmology, conductivity, self-gravity). We will thus focus on the key numerical pillars, i.e. hydrodynamics, the Eulerian grid and the novel implemented physics.

3.2 Hydrodynamics

It is really amazing that most of the conventional matter in the Universe can be treated as a *fluid*. On some spatial or temporal magnification level the fluid approximation seems to perfectly describe the dynamics of the system: hot diffuse medium, cold clouds, stars, dust, even the universe (see the Friedmann equations) and ... traffic jam!

A fluid is simply an idealised concept to model complex reality, in which the matter is described as a continuous medium, with some macroscopic properties that vary as a function of position, $\boldsymbol{x}$, and time, t (like density, velocity, energy). More precisely, we can adopt the continuum approximation only when the system is collisional. That is, one assumes that the scale over which these quantities are defined is much larger than the mean free path of the individual particles, λ. At the same time, the control volume (Δx) must be much smaller than the macroscopic lengthscale L on which fluid properties vary:

$$\lambda << \Delta x << L\,. \tag{3.1}$$

The case we want to study involves one of the most common astrophysical conditions, i.e. a very hot and diffuse gas, almost fully ionised, also known as plasma (locally charged, but globally quasi neutral). The mean free path for the plasma electrons (very similar for the ions), due to Coulomb collisions, can be written as $\lambda_{\rm e} \approx 0.2\,(T/10^7\ {\rm K})^2\, n_{\rm e}^{-1}$ pc (Spitzer 1962). For ISM/ICM conditions, $\lambda_{\rm e}$ is on the order of the pc/kpc scale. Typical simulations consider a box of few Mpc, thus allowing the usage of the hydrodynamic equations. The common presence of typical hydrodynamical features in the ISM/ICM, such as shocks, indicate that the mean free path may be even lower due to the strong interactions of the charged plasma particles with the magnetic field (instabilities, trapping, etc.; the solar wind is a striking example). A non-collisional gas system, e.g. in very hot and rarefied regions, must instead be treated via the general collisionless Boltzmann equation, following the evolution of the particles distribution function in the phase-space, $f(\boldsymbol{x}, \boldsymbol{p}, t)\, d\boldsymbol{x}\, d\boldsymbol{p}$, similarly to galaxies dynamics (Binney & Tremaine 1988).

The three equations of hydrodynamics simply represent the conservation of the fundamental flow quantities (per unit volume), i.e. mass, momentum and total energy. In conservative form, the equations for an inviscid flow, without any source term (right hand side), are known as the Euler equations:

$$\frac{\partial \rho}{\partial t} + \boldsymbol{\nabla} \cdot (\rho \boldsymbol{v}) = 0 \tag{3.2}$$

$$\frac{\partial \rho \boldsymbol{v}}{\partial t} + \boldsymbol{\nabla} \cdot (\rho \boldsymbol{v} \otimes \boldsymbol{v}) + \boldsymbol{\nabla} P = 0 \tag{3.3}$$

$$\frac{\partial \rho E}{\partial t} + \boldsymbol{\nabla} \cdot \left[(\rho E + P)\, \boldsymbol{v} \right] = 0 \tag{3.4}$$

where ρ is the gas density, $\boldsymbol{v}$ the total velocity, E the specific total energy (internal and kinetic, $E = e + 1/2\, v^2$), and P the pressure. The three conservation equations can be retrieved by using basic principles and the Gauss theorem[2]. They can also be written in compact form as

$$\frac{\partial \boldsymbol{U}}{\partial t} + \frac{\partial \boldsymbol{F}(\boldsymbol{U})}{\partial \boldsymbol{x}} = 0\,, \tag{3.5}$$

where $\boldsymbol{U} = (\rho, \rho \boldsymbol{v}, \rho E)$ are the so-called conserved flow quantities - adopted also by FLASH - and $\boldsymbol{F}(\boldsymbol{U})$ the fluxes along the three directions. A more rigorous derivation should involve taking the moments of the collisional Boltzmann equation (the gas is made of particles, but we can actually observe only macroscopic average quantities).

Using the Lagrangian derivative, $D/Dt = \partial/\partial t + (\boldsymbol{v} \cdot \boldsymbol{\nabla})$, we can notice that these equations express the amount of advection $(\boldsymbol{v} \cdot \boldsymbol{\nabla})$ and compression $(\boldsymbol{\nabla} \cdot \boldsymbol{v})$ in the three flow quantities. In fluid dynamics, the system feels an additional (isotropic) force, due the gradient of pressure, which modifies the momentum and energy Equation (3.3 and 3.4, respectively).

In order to close the system of equations, the pressure is obtained from the internal energy and density through an equation of state (EoS). The adopted case in the present work is the common and simple gamma-law EoS given by

$$P = (\gamma - 1)\, \rho e\,, \tag{3.6}$$

where the adiabatic index is $\gamma = (1 + c_\mathrm{v})/c_\mathrm{v}$ (with c_v the specific heat at constant volume), hereafter assumed equal to 5/3 (non-relativistic monoatomic gas). In the more general case, the specific heat, and thus γ, should depend on the degrees of freedom and composition of the gas.

The temperature T is finally computed from $P = \rho e/c_\mathrm{v} = \rho\, kT/\mu m_\mathrm{p}$ (ideal gas), using the previous EoS and a fixed mean atomic weight. In this work I usually[3] assume a composition of the plasma given by solar mass fractions: H $\approx$ 0.71, He $\approx$ 0.265, and metals $Z_\mathrm{tot} \approx 0.025$. Therefore, the mean atomic weight of the entire simulated plasma is $\mu \simeq (2\,\mathrm{H} + 0.75\,\mathrm{He} + 0.5\,Z_\mathrm{tot})^{-1} \approx 0.61$. The gas number density is then $n = \rho/\mu m_\mathrm{p} = n_\mathrm{e} + n_\mathrm{p} \sim 2.2\, n_\mathrm{p}$, where n_e and n_p are the electron and ion number densities ($\mu_\mathrm{p} \sim 1.35$ and $\mu_\mathrm{e} \sim 1.13$).

The Euler equations are impossible to solve analytically, even in the simple 1D case. They are in fact highly nonlinear partial differential equations (PDEs). The hydrodynamic PDEs are hyperbolic, meaning that they possess only real eigenvalues and thus wave-like solutions. If a disturbance is made in the initial data of a hyperbolic system, then not

[2] To obtain the first equation: $M = \int \rho dV \Rightarrow \frac{\partial M}{\partial t} = \int \frac{\partial \rho}{\partial t}\, dV = \int \rho \boldsymbol{v} \cdot d\boldsymbol{S} = -\int \boldsymbol{\nabla} \cdot (\rho \boldsymbol{v})\, dV$.

[3] Slightly altering μ, e.g. diminishing Z, does not change the results.

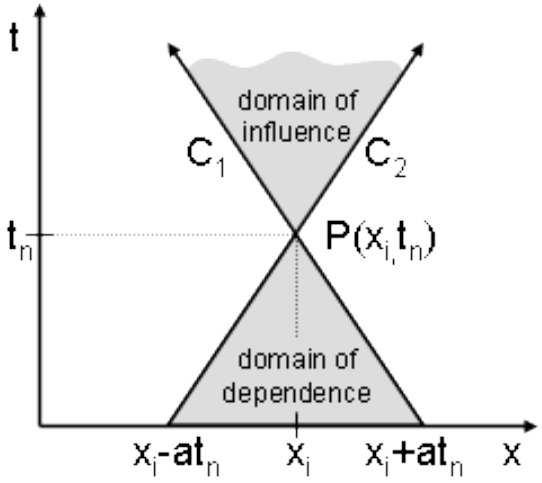

Figure 3.1. Hydrodynamic equations are hyperbolic partial differential equations: two characteristics (in one spatial dimension), C_1 and C_2, delimit the subdomains of dependance and influence of a point P in the space-time (using the Lagrangian approach). For fluids, the characteristic speed a is the sound speed, c_s.

every point of space feels the disturbance at once (perturbations have a finite propagation speed[4], i.e. the sound speed[5] c_s; see Figure 3.1). They travel along the characteristics of the equation, which are curves along which the PDE becomes an ordinary differential equation (ODE), in the $\boldsymbol{x}$ - t plane. On the contrary, a perturbation in the initial or boundary data of an elliptic (like the Poisson equation) or parabolic PDE (like the heat equation) is felt at once by essentially all points in the domain.

The next step is therefore finding a numerical discretisation, constructing a convergent[6] and stable[7] numerical solver and, through the raw power of (parallel) high-performance computing, retrieving the numerical solutions. The only additional data required are values at the boundaries of the domain and at the initial time ($t = 0$).

3.3 The Eulerian AMR grid

Since we want to tackle complex astrophysical high-energy problems, such as AGN outflows, shocks, turbulence, mixing, and instabilities in the plasma properties, the most accurate numerical approach is the Eulerian discretisation. In the Eulerian approach we consider the flow quantities U at fixed locations, or more precisely, over control volumes (the domain is discretised like a grid; see Figure 3.2, left). In the Lagrangian approach we follow instead U flowing with a fluid element, i.e. a particle (the numerical particle usually represents an ensemble of real particles, like in SPH[8] codes; see Figure 3.2, right). The

[4]This property is extremely useful for the numerical integration and discretisation, since we can divide the system in several subdomains of influence.

[5]The sound speed is defined as $c_s^2 = \partial P/\partial\rho$ (with respect to adiabatic change); for an ideal gas the adiabatic sound speed results $c_s^2 = \gamma P/\rho = \gamma k_b T/\mu m_p$, thus $c_s \approx 1.5 \times 10^4\, T^{1/2}$.

[6]Convergence implies that the numerical solution approaches the exact solution, as the step $\Delta x \to 0$.

[7]Stability means that the numerical solution is robust against numerical noise, avoiding spurious oscillations.

[8]Smoothed-particle hydrodynamics.

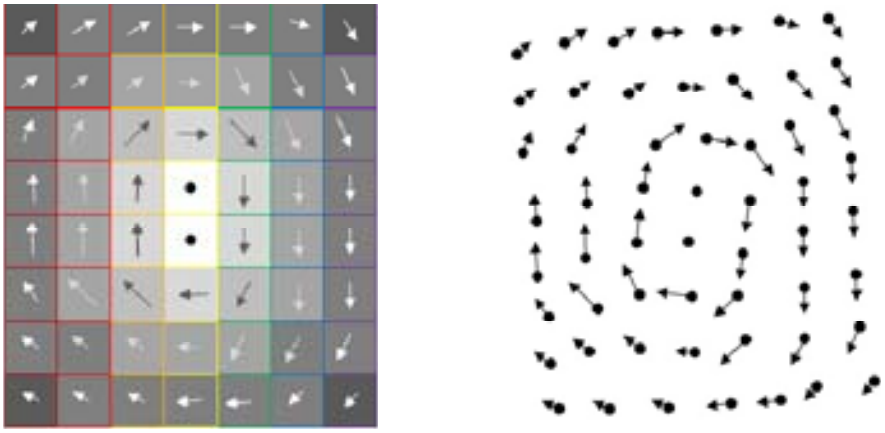

Figure 3.2. Left: in the Eulerian approach we consider the flow quantities U at fixed locations, or more precisely, over control volumes. Right: in the Lagrangian approach we follow U flowing with a fluid element, i.e. a particle.

Eulerian approach seems to be better to describe supersonic flows, because it can naturally follow discontinuities, taking advantage of the integral formulation of the Euler equations applied to several control volumes (Equation 3.7).

The FLASH code adopts the Eulerian - grid - discretisation. It is practically impossible, however, to obtain a very high resolution, $\Delta \boldsymbol{x}$, and large dynamical range in the three-dimensional (3D) case. The Millennium simulation, one of the biggest (N-body) computations, used 10 billion elements, with a computational time of a couple of months (using the entire Garching Supercomputing Center). This means that along one direction the relative grid resolution would be just ~ 2000. Even assuming 256^3, we count already 17 millions of elements, which is substantial for HPC computations. For all the previous reasons, the entire 3D domain can not be entirely resolved, in order to achieve a dynamical range of 10^3 or more. The solution to this problem is simply zooming only in the region of interest, for example where the gradient of a flow quantity (density, pressure) varies substantially. The zooming method is called adaptive mesh refinement (AMR).

The default AMR method of FLASH is based on PARAMESH (MacNeice et al. 2000), which uses a block-structured AMR scheme similar to others in the literature (see the classic article of Berger & Colella 1989). The fundamental data structure is a block of cells arranged in a logically Cartesian fashion, implying that each cell can be specified using a block identifier (processor number and local block number) and a coordinate triple (i, j, k), where $i = 1 \ldots \mathrm{nxb}$, $j = 1 \ldots \mathrm{nyb}$, and $k = 1 \ldots \mathrm{nzb}$ refer to the x, y, and z-directions, respectively. Although a spherical grid can be indexed in the same manner, in the present work I preferred to use rectangular blocks with typical size: $\mathrm{nxb} = \mathrm{nyb} = 8$ or 16, and $\mathrm{nzb} = \mathrm{nxb}/2$. Having fixed blocks, instead of refining on a cell-by-cell manner (like ENZO or RAMSES code), drastically increases the performance of the load distribution on parallel processors (using also the Morton space-filling curve; Warren & Salmon 1993), although the global domain tends to be slightly more refined.

The complete computational grid consists of a collection of blocks with different physical cell sizes, which are related to each other in a hierarchical fashion using a tree data structure (Figure 3.3). The blocks at the root of the tree have the largest cells, while

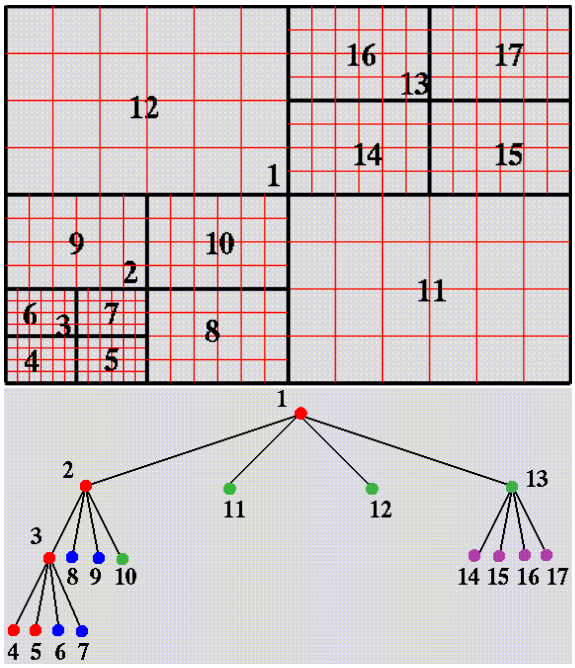

Figure 3.3. The block-structured adaptive mesh of FLASH (in two dimensions: nxb = 8, nyb = 4). Block children can be refined only by a factor 2, compared to the parent block.

their children have smaller - refined - cells. Three rules govern the establishment of refined child blocks. First, a refined child block must be 0.5 as large as its parent block in each spatial dimension. Second, a block children must be nested, i.e. the child blocks must fit within their parent block and can not overlap one another. Therefore, in d dimensions a given block has either zero or 2^d children (in 3D it is called octree, $2^3 = 8$). Third, blocks which share a common boundary may not differ from each other by more than one level of refinement (see Fig. 3.3). Whenever a block is marked for refinement or derefinement, the adaptive grid executes (monotonic) interpolation or averaging of the data, respectively.

Each block contains nxb $\times$ nyb $\times$ nzb interior cells and a set of guard cells. The guard cells contain boundary informations needed to update the interior cells, obtained from physically neighbouring blocks, externally specified boundary conditions, or both. The number of guard cells depends on the interpolation schemes and the differencing stencils used by the various physics units (usually hydrodynamics). For our adopted hydro-algorithm, the PPM (see Section 3.3), four guard cells are required in each direction. PARAMESH also enforces flux conservation at jumps in refinement, as described by Berger & Colella (1989), thus conserving U at machine precision.

In most of the simulations we decided to use a number of concentric fixed grids in cartesian coordinates, centred[9] on the supermassive black hole (SMBH). In fact, we require often a dynamical range of 4096 - 8192, simulating scales from hundreds pc to few Mpc. Since we are more interested in the cool core of the cluster, group or isolated elliptical galaxy, the resolution in this region needs to be the highest possible. Typical numbers of refinement levels are $l_{\rm max} = 10$ (the minimum level is instead 4 or 5). Note that the grid resolution is simply given by $h =$ nxb $\times\ 2^{l_{\rm max}-1}$ (typically $h = 8 \times 2^{10-1} = 4096$); thus, the spatial resolution in one of the three directions is $\Delta x = L_x/h$, where L_x is

[9]The exact location of the system centre is in the cell corner.

the box size along the x-direction. The finest, inner grid has a resolution in the range $\Delta x = \Delta y = \Delta z \sim 0.1 - 2$ kpc (specified in each Chapter). In general, grids of every level extend radially for about 40-50 cells, with the (cubical) shell linear size doubling among adjacent levels. This ensures a proper resolution of shocks, waves, cavities and turbulence generated in the core by the AGN outflows.

The previous refining method is arguably the best strategy in order to cover the huge spatial scales (pc to Mpc) and at the same time integrating the system for seven or more Gyr. With this method the few millions of grid cells are usually integrated in 'reasonable' massively-parallel HPC times (a high-resolution production run[10] can take up to 50,000 total hours, over 1024 CPUs).

Finally, the 3D box in the majority of the simulations extends slightly beyond the virial radius, R_{104} (for the cluster ~ 2.6 Mpc and for the group ~ 870 kpc), or the galaxy outskirts (~ 150 kpc). I usually simulate the $z \geq 0$ half-space with reflecting boundary condition at $z = 0$, setting elsewhere outflow conditions ($\nabla U = 0$) with inflow prohibited (the box is big enough that boundary disturbances do not interfere with the cool-core dynamics).

3.4 Numerical Solver: PPM

The pure hydrodynamic equations (with no source terms; Eq. 3.2-3.4) are solved via a finite-volume scheme, named the piecewise parabolic method (PPM; first described by Colella & Woodward 1984). Classical numerical schemes usually rely on simple finite-difference methods, i.e. taking advantage of the Taylor expansion[11]. For instance, the simple linear advection equation ($\partial \boldsymbol{U}/\partial t + c'_{\rm s}\, \partial \boldsymbol{U}/\partial x = 0$, with $c'_{\rm s} > 0$ a constant sound speed) can be solved in a stable way using a forward time derivative and a backward space derivative: $(\boldsymbol{U}_i^{n+1} - \boldsymbol{U}_i^n)/\Delta t + c'_{\rm s}(\boldsymbol{U}_i^n - \boldsymbol{U}_{i-1}^n)/\Delta x = 0$, where the upper/lower indexes indicate as usual the temporal/spatial states.

On the contrary, finite-volume methods do not try to discretise the Euler differential equation (Eq. 3.5) at given points in space, but they take advantage of the more rigorous integral form over some control volume ($[x_1, x_2] \times [t_1, t_2]$, in one spatial dimension):

$$\int_{x_1}^{x_2} \boldsymbol{U}(x, t_2)\, dx = \int_{x_1}^{x_2} \boldsymbol{U}(x, t_1)\, dx + \int_{t_1}^{t_2} \boldsymbol{F}(\boldsymbol{U}(x_1, t))\, dt - \int_{t_1}^{t_2} \boldsymbol{F}(\boldsymbol{U}(x_2, t))\, dt\,. \qquad (3.7)$$

Therefore, the flow quantities represent now *cell-averaged* values[12], over each volume $V = \Delta x\, \Delta y\, \Delta z$.

A fully detailed description of the PPM, even adopting just the present direct Euler approach, is clearly beyond the scope of this work (I refer the reader to the seminal article of Colella & Woodward 1984). Nevertheless, it is worth to understand the main

[10] The simulations were run mainly on the IBM P575 Power 6 (SP6) at CINECA supercomputing centre, and on the Pleiades supercluster at the NASA-Ames base; see also PhD Production.

[11] The Taylor expansion of a function f around a point a is: $f(x \to a) = f(a) + f'(a)\,(x - a)/1! + f''(a)\,(x - a)^2/2! + \mathrm{O}(x^3)$, where the last term is the order of approximation.

[12] The (1D) spatial average is given by $\langle \boldsymbol{U} \rangle_i = \frac{1}{\Delta x_i} \int_{x_i - 1/2}^{x_i + 1/2} \boldsymbol{U}(x)\, dx$.

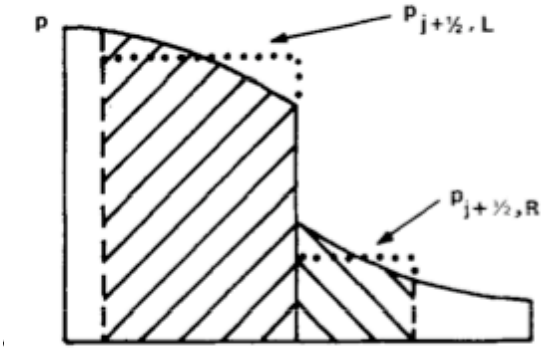

Figure 3.4. An example of parabolic approximation within discrete cells. The left and right states will serve as input values for the Riemann problem (see next Figure).

methodological steps, in order to get a solid overview of the key numerical properties of this famous solver.

The procedure for updating the initial conditions can be divided into two separate parts: the reconstruction step and the solution step. Since the values of the flow variables are not known at any given point in space, it is necessary to reconstruct the requisite point values at the zone interfaces from the zone average values. Therefore, the code performs an interpolation based on a cubic polynomial (fourth-order), with the correct average values, in order to obtain the right and left interface quantities. For instance, in the case of uniform zoning, the interpolated density at the right interface is $\rho^n_{i+1/2} = (-\langle\rho\rangle^n_{i+2} + 7\langle\rho\rangle^n_{i+1} + 7\langle\rho\rangle^n_i - \langle\rho\rangle^n_{i-1})/12$. Any non-monotonic behaviour in the interpolation can lead to unphysical oscillations in the solution and it must be prevented by modifying the slope via the classic van Leer (1979) monotonicity constraint. It is now possible to construct a parabola which passes through the two interface values and the single zone average value (e.g. Figure 3.4).

The interface values and parabolae calculated above are only preliminary, because they need to be modified in the regions where the flow is not smooth. The first modification is performed in regions near contact discontinuities. In order to prevent these sharp structures from spreading diffusively as they propagate across the grid, the interface values are altered to provide steeper slopes within the relevant zones. Second, because of the self-steepening mechanism in shocks and the low dissipation in PPM, shock fronts tend to become too narrow, frequently less than a zone wide. When this situation arises, unphysical oscillations develop behind the shock, and a procedure, know as flattening, is used to provide a sort of extra dissipation[13].

After the reconstruction stage, the second main procedure is the solution step, which updates the conserved variables to the new time step, via the time-averaged interface fluxes (see Equation 3.7). One of the major difficulties is certainly finding the most accurate fluxes. The fluxes are thus computed by solving the Riemann (or shock tube) problem at each zone interface. The PPM is in fact a higher order version of the method

[13]This method is much more effective in stabilising shock waves than the more traditional approach of using an artificial viscosity (see ZEUS code; Stone & Norman 1992). Typically, shocks are spread over only one to two grid points, and in most cases, post-shock oscillations are virtually nonexistent.

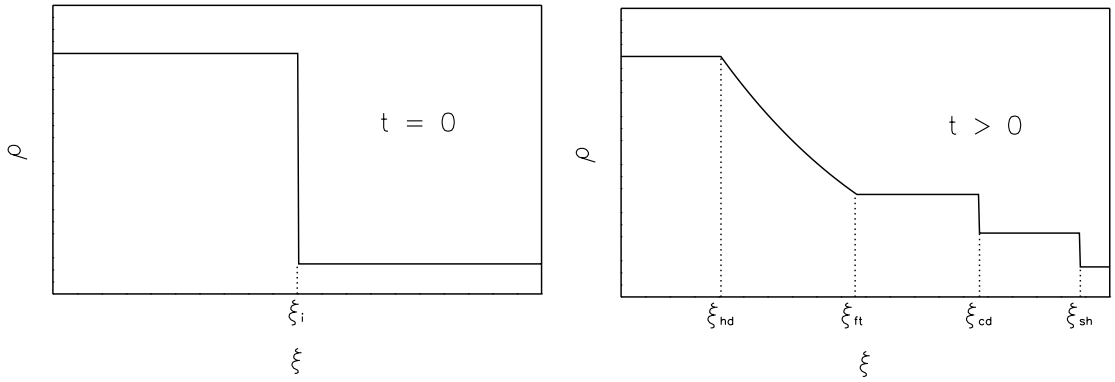

Figure 3.5. The Riemann problem starting from a shock tube data. Left: initial density discontinuity at $t = 0$. Right: self-similar solution of the problem, showing a rarefaction ($\xi_{\rm ft} \rightarrow \xi_{\rm hd}$), a contact discontinuity ($\xi_{\rm cd}$), and a shock wave ($\xi_{\rm sh}$). From Fryxell et al. (2000).

developed by Godunov (1959), which originally represented the variables as piecewise constant within each zone (first order accuracy).

The previously calculated zone interface and average values are essential for defining the effective left and right input states of the Riemann problem (see Figure 3.5). In the simple first-order Godunov method the left and right states are the zone average values (i and $i + 1$). PPM has instead reconstructed a parabolic distribution of the flow quantities. By tracing back the domain of dependence via the characteristics (Fig. 3.1), it is possible to find where the parabolic distribution should be integrated, and finally retrieve the left and right state for the Riemann problem.

Solving the Riemann problem is then straightforward, because it exists an analytical solution. The general solution consists of one wave (shock or rarefaction[14]) moving to the left, a second wave traveling to the right (shock or rarefaction), and a contact discontinuity in between. A typical example of the Riemann problem is shown in Figure 3.5. The previous three hydrodynamical features appear only in nonlinear problems and are fundamental elements of all astrophysical (highly compressible) plasmas.

The piecewise parabolic method is ideally third order accurate in space, however the practical implementation reduces slightly its accuracy. Nevertheless, PPM is still considerably more accurate and efficient than most second-order algorithms. The PPM hydro-solver is finally executed along each separate three-dimensional direction, also known as dimensional splitting (Strang 1968). Reversing the order of the integration ($x - y - z$ and then $z - y - x$) provides second-order accuracy in time. I preferred the split method, over the unsplit formulation, because it is rather faster and still very robust.

The (necessary) stability condition of PPM is analogous to most explicit hydrodynamical solver, also known as Courant-Friedrichs-Lewy condition (CFL; Courant et al. 1928). In three dimensions, the CFL limiter on the numerical time step is given by

[14]A rarefaction is a smooth nonlinear transition between the left and right state (with infinite solutions). In a rarefaction, the characteristic curves diverge from a single point in the space-time. On the contrary, shock waves (jumps in density and entropy) are described by convergent characteristics.

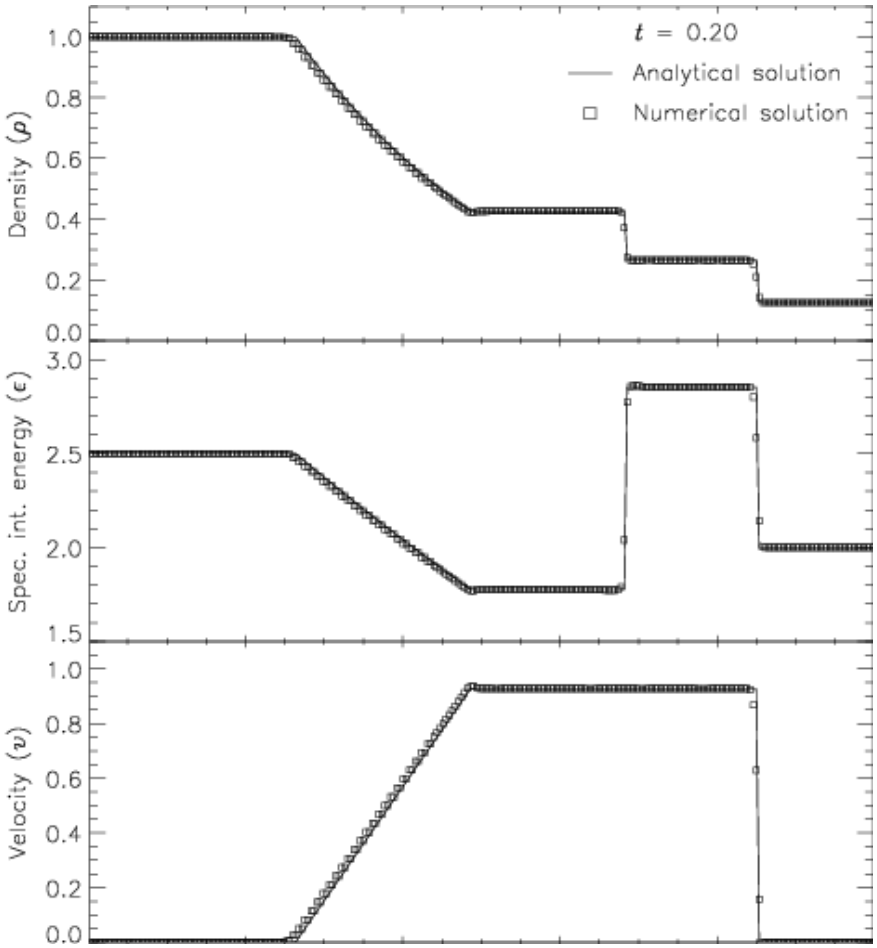

Figure 3.6. Comparison of the numerical (points) and analytical (line) solutions to the shock tube (Riemann) problem. The 2D grid has six levels of refinement. Note the high accuracy and stability of the hydrodynamic solver of FLASH, the PPM. From Fryxell et al. (2000).

the minimum among all points of

$$\Delta t_{\rm cfl} = C \, \min\left(\frac{\Delta x}{|v_x| + c_{\rm s}}, \frac{\Delta y}{|v_y| + c_{\rm s}}, \frac{\Delta z}{|v_z| + c_{\rm s}}\right), \tag{3.8}$$

where $C < 1$ is the Courant number (typically $\sim 0.2 - 0.3$ or less, with strong flow perturbations). The simple foundation of this condition is that informations have a finite travelling speed. If a wave is moving across a discrete spatial grid and we want to compute its amplitude at discrete time steps of equal length, then this length must be less than the time for the wave to travel to adjacent grid points. In essence, the numerical domain of dependence must include the analytical domain of dependence (defined by the characteristic curves; see Fig. 3.1).

Overall, the high resolution and accuracy of PPM are obtained by the explicit nonlinearity of the scheme (and through the use of the previous smart dissipation algorithms). For all these reasons PPM is particularly well suited to describe discontinuities, such as shocks and contact discontinuities, at the same time properly following the smooth flow regions (check the numerical shock tube test of FLASH in Figure 3.6 compared to the analytical solution).

The Roe and Lax-Friedrichs solvers were also tested, with various slope limiters (van

Leer, minmod, MC, Toro). They perform rather well for smooth flows, but not for a powerful jet ignition, producing unstable results also with low CFL numbers ($C < 0.1$). On the contrary, the HLLC solver (Toro 1997) is very stable also for higher CFL numbers (~ 0.5), with a decent description of shocks and contact discontinuities (second order). In the end, results with both methods are comparable, with PPM being more accurate, while HLLC faster and more manageable. In the present investigation I preferred nevertheless accuracy over speed.

3.5 Radiative Cooling

In the next Sections I describe the entirely new implemented modules, which add fundamental physical capabilities to FLASH. The Equations 3.2-3.4 do not possess any source or sink term (right hand side), and they include only the pure advection and compression of the gas. The usual computational strategy to include source/sink terms is known as splitting technique. First, we integrate the Euler partial differential equations with the PPM, and then we integrate the ordinary differential equation linked to the source term (using the flow quantities found in the PPM step). This method is only first order accurate. In order to further improve the coupling, I implemented a second order accurate temporal evolution in the splitting scheme, alternating the order of the integration of the hydrodynamical (H) and source terms (S) as follows: H-S-S-H.

The main physical module, in order to study cooling flows, is certainly radiative cooling (sink term added to the energy Equation 3.4). The interstellar, intergalactic or intracluster medium emits radiation mainly in the X-ray band due to Bremsstrahlung ($T \gtrsim 10^7$ K) and line emission ($10^4 - 10^7$ K; see Section 1.1 for more details). Assuming collisional ionisation equilibrium, the cooling sink term can be modelled with a defined cooling function $\Lambda(T, Z)$. It is computationally efficient to use an analytical fit to the Sutherland & Dopita (1993) tabulated values for a fully ionised plasma (Fig. 3.7). The temperature floor is set at 10^4 K, justified by the reionisation from stars. The total radiative losses are also proportional to the electron and ion number densities (Sec. 1.1):

$$\mathcal{L} = -\, n_{\rm e}\, n_{\rm i}\, \Lambda(T, Z) = -\, \frac{\rho^2}{\mu_e \mu_i m_{\rm p}^2}\, \Lambda(T, Z)\,. \tag{3.9}$$

The cooling function depends also on the gas metallicity. Hereafter, we assume that the abundance of all the heavy elements in solar units is the same as the iron one[15]. Although not strictly true, this has a negligible effect on the cooling process. In most runs we set a fixed metallicity of $Z = 0.3\ Z_\odot$ for clusters (Tamura et al. 2004) and $Z = 1\ Z_\odot$ for groups/ellipticals (Rasmussen & Ponman 2009). In the more advanced models, we follow self-consistently, via an advection tracer, the variable abundance linked to stellar evolution (Section 3.8).

In most of the simulations, in particular when the cold gas dropout is enabled (Sec. 3.5.1), a second-order Runge-Kutta (RK2) explicit solver is enough[16] to properly

[15] As customary, the iron abundance is calculated with respect to hydrogen mass: [Fe/H] = $\log Z$, in solar units.

[16] I tested also the fourth-order explicit Runge-Kutta scheme, without finding any significant improvement. Implicit schemes, like Crank-Nicholson, are instead very inaccurate, although 'allowing' a larger Δt.

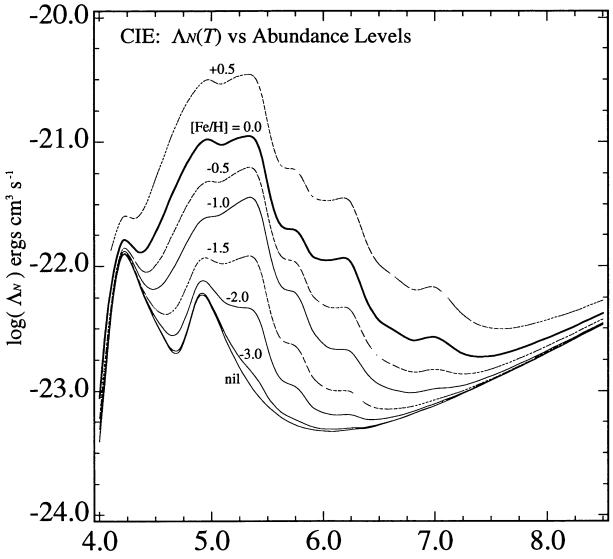

Figure 3.7. Implemented radiative cooling function $\Lambda(T, Z)$ for an astrophysical plasma in collisional ionisation equilibrium, as a function of (iron) metallicity [Fe/H] $= \log Z$, in solar units. From Sutherland & Dopita 1993.

integrate the cooling ODE at each spatial point:

$$E_{\rm th}^{n+1/2} = E_{\rm th}^{n} + \frac{\Delta t}{2}\mathcal{L}(E_{\rm th}^{n})\,,$$

$$E_{\rm th}^{n+1} = E_{\rm th}^{n} + \Delta t\,\mathcal{L}(E_{\rm th}^{n+1/2})\,, \tag{3.10}$$

where $E_{\rm th} = \rho e = c_{\rm v}\, k_{\rm b}\rho T/\mu m_{\rm p}$ is the thermal energy density, and $\mathcal{L}^{n+1/2}$ is the emissivity retrieved from the first half time step (note that the density ρ is constant during this integration). In order to properly couple the hydrodynamics with the cooling term we need to add another time step limiter, $\Delta t_{\rm c} \lesssim t_{\rm cool} = 2.5\, P/\,|\mathcal{L}|$, which can significantly slow down the computation (it is usually a few times lower than $\Delta t_{\rm cfl}$).

When studying the entire multiphase gas without any dropout term (Chapter 7), a more rigorous prescription for the cooling solver is required. This is especially important in order to follow the formation and growth of thermal instabilities, producing cold clumps and filaments in the ICM. In the splitting framework, it is actually possible to avoid the use of implicit or explicit solvers (for the ODE step associated with cooling). The new temperature T^{n+1} can be computed from the old temperature T^{n} by *exactly* evaluating the following integral (at each grid point):

$$\int_{T^n}^{T^{n+1}} \frac{dT'}{\Lambda(T')} = -\frac{(\gamma-1)\,\mu}{k_{\rm b}\mu_{\rm e}\mu_{\rm i}m_p}\,\rho\,\Delta t\,. \tag{3.11}$$

A practical way to compute the integral is to split the integration interval into two parts: one from T^n to $T_{\rm ref}$ and the other one from $T_{\rm ref}$ to T^{n+1}, using an arbitrary reference value (see Townsend 2009). This leads, after few mathematical steps, to

$$T^{n+1} = Y^{-1}\left[Y(T^n) + \frac{T^n}{T_{\rm ref}}\frac{\Lambda(T_{\rm ref})}{\Lambda(T^n)}\frac{\Delta t}{t_{\rm cool}}\right], \tag{3.12}$$

where $t_{\rm cool}$ is the cooling time[17], and Y is an evolution function defined as

$$Y(T) \equiv \frac{\Lambda(T_{\rm ref})}{T_{\rm ref}} \int_{T}^{T_{\rm ref}} \frac{dT'}{\Lambda(T')}. \tag{3.13}$$

The temperature T^{n+1} can be exactly computed if the reciprocal of the cooling function is analytically integrable. Thus, we decompose the cooling function into a large number of piecewise power-laws in logarithmic temperature intervals

$$\Lambda(T) = \Lambda_k \left(\frac{T}{T_k} \right)^{\alpha_k}, \qquad T_k \leq T \leq T_{k+1}\,, \tag{3.14}$$

and precompute at initialisation the constants of integration for each interval. The integral in Eq. 3.13 can be computed analytically using this power-law decomposition of the cooling function. The only effort in retrieving T^{n+1} comes from finding the correct interval in which the argument of Y^{-1} resides (Eq. 3.12).

Besides being exact (only in the ODE step) and thus very accurate, this method is also slightly faster than either explicit or implicit methods[18]. Finally, the error from the piecewise power-law approximation is negligible, because the number of the temperature intervals can be made very large (matching the tabulated Sutherland & Dopita values), without large memory requirements.

3.5.1 Cold Gas Dropout

When interested only in the hot gas dynamics (adopting the simple Runge-Kutta solver), we numerically handle the very cold clouds by using a dropout mass sink term (added to Equation 3.2): $S_{\rm drop} = -\,q(T)\,\rho/t_{\rm cool}$. This is a convenient scheme to remove the cold gas ($T \lesssim 10^5$ K) from the numerical grid, at constant pressure, without altering the calculated cooling rate (Brighenti & Mathews 2002b). The dimensionless coefficient $q(T)$ is defined as $q = 2\exp[-(T/T_{\rm q})^2]$, thus dropout becomes significant[19] when $T \lesssim T_q \simeq 10^5$ K. On the other hand, the physical evolution of the entire multiphase gas, without dropout, requires at least a better solver, like the exact method, plus high resolution in the regions of hot gas condensation.

As previously done, we are always using the splitting method for adding the sink terms, i.e. first solving the homogeneous PDE hydro-equations and then integrating the ODE associated with the dropout term: $d\rho/dt = S_{\rm drop}$. Expanding the cooling time, $t_{\rm cool}$, and properly centring the variables, leads to the the following discretisation for the dropout ODE (using the second-order centred derivative):

$$\rho^{n+1} = \rho^{n} \left(1 + \frac{\mu}{2.5\,k_{\rm b}\mu_{\rm e}\mu_{\rm i}m_{\rm p}} \frac{q^{n+1/2}\,\Lambda^{n+1/2}\rho^{n}}{T^{n+1/2}}\,\Delta t \right)^{-1}. \tag{3.15}$$

[17] Here using just the internal thermal energy, instead of the enthalpy $2.5P$.

[18] We have compared explicit calculations, setting a *strong* limiter ($< 0.1\ t_{\rm cool}$), with runs based on the 'exact' solver. Tests were carried out in idealised conditions (e.g. an isolated cooling cylinder or sphere) and simulating a short pure cooling flow evolution. We obtained similar results (like the cold mass and time of collapse).

[19] In our tests, we do not see any significant difference in the hot gas evolution or in the total cooling rates, as long as $T_q \lesssim 10^6$ K. The warm gas below 10^7 K is in fact very unstable and tends to rapidly cool toward the floor temperature, due to the strong line emission.

The dropout term, as any source step, has a time limiter condition associated. Using the dropout ODE equation, we find that the relative density decrement, $D = 1 - \rho^{n+1}/\rho^n$, is linked to the following timescale: $t_{\rm drop} = [D/(q\,(1-D))]\,t_{\rm cool}$. It is evident that the dropout limiter is tightly correlated with the cooling limiter, $\eta\,t_{\rm cool}$. Limiting the variation of internal energy has the consequence to directly reduce the dropped mass, quantitatively: $D = \eta\,q/(1+\eta\,q)$. In order to smoothly couple the hydro-solver to the sink terms, a reasonable limiter is $\eta = 0.4$; since the maximum value of q is 2, the dropout decrement will never exceed $\approx 45\%$ per time step (it is usually much lower).

In passing, I note that the numerical cooling rates ($\dot{M}_{\rm cool}$) are simply given by the dropped cold gas. When the dropout is disabled, the cold gas ($T \leq 5\times10^5$ K) is tracked inside the domain at each time step, providing $\dot{M}^n_{\rm cool} = (M^n_{\rm cold} - M^{n-1}_{\rm cold})/\Delta t$.

3.6 AGN Outflows

Motivated by the widespread observational evidences found in different bands (see Section 2.3 and references therein), I intend to understand, through the present work, the exact role of AGN outflows in solving the cooling flow problem. More specifically, I will adopt purely mechanical AGN outflows, which are considerably massive, subrelativistic and collimated. In considering massive slow outflows, we are implicitly assuming that the relativistic radio jet entrains some mass ($M_{\rm act}$), or in a similar way, that the jet is highly relativistic on pc scale, but rapidly decreases to subrelativistic velocities within few kpc from the black hole (Giovannini 2004; Croston 2008). Another possibility, highlighted in the previous Chapter, is the generation of mechanical massive outflows via the radiation emitted by the AGN (Proga 2007). The latter scenario, more likely happens at higher redshifts ($z \sim 2$), due to the increasing number of quasar-like objects in the universe.

The AGN injection can be carried out in two different ways, which nevertheless produce similar results. In both models the kinetic power of the jet[20] is given only by the mass outflow rate and jet velocity:

$$P_{\rm jet} = \frac{1}{2}\dot{M}_{\rm jet} v^2_{\rm jet}\,. \tag{3.16}$$

For most of the presented runs I apply injection of purely kinetic energy and associated momentum ($M_{\rm jet} v_{\rm jet}$; added to Eqs. 3.3-3.4) directly in the domain, i.e. in the active outflow region with mass $M_{\rm act}$, motivated by the entrainment scenario. The size of this region will be specified in each Chapter (4-7); typical values are $d_{\rm jet} \sim 1$ kpc (width) and $z_{\rm jet} \sim 1$ kpc (height), in line with observations of the more massive outflow component. Note that a slightly smaller or larger active region does not drastically alter the global feedback evolution[21]. The mass outflow rate, per each time step Δt, is then roughly estimated as

$$\dot{M}_{\rm jet} \sim \frac{M_{\rm act}}{\Delta t}\,. \tag{3.17}$$

[20] Hereafter, I use the term 'jet' and 'outflow' interchangeably, meaning a central anisotropic ejection of mass, without referring specifically to the relativistic radio jet.

[21] The same can be said for more sophisticated implementations, like smoothing the injection region with a truncated Gaussian.

Using the jet power (Eq. 3.16), it is straightforward to retrieve the outflow velocity:

$$v_{\rm jet} = \left(\frac{2 P_{\rm jet}\, \Delta t}{M_{\rm act}} \right)^{1/2} . \tag{3.18}$$

Apart from few computations, the jet velocity is usually aligned with the z-axis (cylindrical jets). Simulations with conical outflows (with half-opening angle up to 25 degrees; see also Sternberg et al. 2007) have a similar impact on the global properties of the flow. In fact, the pressure of the surrounding plasma collimates the outflows within few tens kpc (see Brighenti & Mathews 2006). Larger outflows become instead almost isotropic, leading to a bad self-regulation (inhibiting accretion; Sec. 7.3.4).

The second (less used) method is based on the physical assumption that the original AGN jet is not resolved by the grid. We thus inject flux of momentum, mechanical energy[22], and also mass via the numerical boundaries at $z = 0$ (or taking advantage of the block guard cells). The total cross-sectional area of this 'nozzle' is typically $A_{\rm noz} = (2\Delta x)^2$, where Δx is the highest resolution. This injection method tends to evacuate less easily the regions perpendicular to the jets, however, it requires the specification of one of the two key jet parameters, either $\dot{M}_{\rm jet}$ or $v_{\rm jet}$. Note that it is also very important to limit the time step according to the jet velocity, in addition to the CFL condition.

In the first case, the outflow mass rate is assumed $\dot{M}_{\rm jet} = \rho_{\rm jet}\, A_{\rm noz}\, v_{\rm jet}$, with jet density $\rho_{\rm jet}$ about $1/10$ of the initial central gas density, and therefore

$$v_{\rm jet} = \left(\frac{2 P_{\rm jet}}{\rho_{\rm jet} A_{\rm noz}} \right)^{1/3} . \tag{3.19}$$

In the second case, $v_{\rm jet} \sim$ few 10^4 km s^{-1}, consistently with absorption-line observations (e.g. Crenshaw et al. 2003; Tombesi et al. 2012), and thus $\dot{M}_{\rm jet} = 2\, P_{\rm jet}/v_{\rm jet}^2$. This choice of the velocity usually generates reasonable mass outflow rate values, around few $M_\odot$ yr^{-1}. It is worth noting that very massive (and slower) outflows tend to carve a more visible channel in the medium, while relatively lighter (and faster) jets release most of their energy in the central region, producing strong shocks and bigger bubbles.

The jet fluxes are again parallel to the z-direction (and opposite when simulating the two bipolar outflows). In a couple of models (Section 7.3.4) I tested also jet wobbling, with variable inclination (θ) and azimuthal angle (ϕ): the location of the nozzle remains fixed in space, but all three velocity components (e.g. $v_x = v_{\rm jet} \sin\theta \cos\phi$) vary randomly with time, within a specified solid angle.

For the sake of completeness, I tested runs where the outflows are continuously generated or possess a fixed frequency and duration. This type of heating usually returns wrong results, due to the several artificial parameters and lacking any kind of self-regulation. Finally, I note that injecting only thermal energy at the centre of the system typically leads to the destruction of the cool core (see also Brighenti & Mathews 2002b).

[22] The thermal energy of the jet is set to be negligible.

3.7 Accretion and Self-regulation

The AGN outflow injection, previously described, is deeply interwoven with the accretion model, which provides the self-regulated feedback mechanism. It is beyond the scope of this work to study the detailed accretion very near the black hole. The goal of our study is instead to study the effects of (large-scale) outflows on the ISM/ICM evolution. Massive black holes in nearby X-ray bright ellipticals likely accrete gas through a radiatively inefficient mechanism. ADAF models naturally predict outflows and jets (Narayan & McClintock 2008), which might provide the mechanical feedback I study here.

Ideally, we would like to numerically resolve a region with size a few Schwarzschild radii, $R_S \approx 3 \times 10^{14}\,(M/10^9 M_\odot)$ cm $\sim 10^{-5}\,R_B$ (where R_B is the usual Bondi radius; see below). This is currently not feasible for 3D simulations aimed to investigate the effect of the feedback on kpc and Mpc scales. Because the direct calculation is impractical, we are left to rely on a sub-grid prescription to estimate the accretion rate. Therefore, the exact quantitative of material that is considered 'accreted' must be taken with caution and only as a rough approximation.

Because of the previous (not easily quantifiable) uncertainties I prefer to not assume any sophisticated subgrid modelling for the accretion process. As customary done in accretion theory, the jet power is taken proportional to the accretion rate $\dot{M}_{\rm acc}$ (or better, to the accreted rest mass energy per unit time):

$$P_{\rm jet} = \epsilon\, \dot{M}_{\rm acc}\, c^2\,, \tag{3.20}$$

where ϵ is the mechanical efficiency[23], which is a free parameter of our models in the range $\sim 10^{-4} - 10^{-1}$. The frequency and strength of the feedback events will strongly depend on ϵ. It is likely that the efficiency depends on the ratio between the actual accretion rate and the Eddington rate, i.e. $\dot{M}_{\rm Edd} \approx 22\,(M_{\rm BH}/10^9 M_\odot)\ M_\odot\,{\rm yr}^{-1}$ (Churazov et al. 2005; Merloni & Heinz 2008). However, given the uncertainties in estimating the accretion rate, I prefer to assume a constant ϵ. It is worth noting that we can absorb the uncertainty in the actual accretion rate into the efficiency parameter ϵ. If only a fraction f of the gas considered accreted in the simulation falls into the black hole, the real efficiency could be indeed rescaled to ϵ/f.

The next step is to find the feedback. The best self-regulation, as shown in the next Chapters, is achieved when the accretion rate is linked to the cooling rate, usually in a spherical region near[24] the AGN ($r_0 \sim 5 - 10$ kpc). We call this model *cold feedback*:

$$\dot{M}_{\rm acc} = \dot{M}_{\rm cool}(r < r_0). \tag{3.21}$$

In the more advanced simulations r_0 is discarded, assuming that the cooled gas (dropped at radius $r_{\rm i}$) goes into free fall and accretes onto the black hole in a free-fall time, given by

$$t_{\rm ff} = \int_{r_{\rm i}}^{0} \frac{{\rm d}r}{\sqrt{2\,|\phi(r) - \phi(r_{\rm i})|}}\,, \tag{3.22}$$

[23] Note that the mechanical efficiency is different from the usual radiative efficiency ($\eta \sim 0.1$), and typically a few orders of magnitude lower.

[24] The majority of the cold gas is in any case generated at the very centre.

where ϕ is the gravitational potential (see Section 3.9). I also impose that the infalling gas must have a low angular momentum, less than $v_c(\Delta r)\,\Delta r$ (circular velocity times the minimum radial grid size), even if most of the cooling gas does not present a large angular momentum, also during a typical AGN simulation. The cold mass reaching the centre at a given time step defines the new accretion rate, which triggers as usual the AGN outflow.

The second self-regulated accretion model is called *hot feedback*, which is based on the theory of Bondi (1952). Any strong gravitational field, in particular linked to SMBH, can attract large amount of surrounding gas, mostly hot. In 1952, Bondi found an analytical solution to the steady radial accretion problem of the gas on a central attractor at rest:

$$\dot{M}_{\rm acc} = \dot{M}_{\rm B} \equiv 4\pi\,(G M_{\rm BH})^2\,\frac{\rho_0}{c_{\rm s,0}^3}\,, \tag{3.23}$$

where ρ_0 and $c_{\rm s,\,0}$ are the constant density and sound speed at the boundaries (infinity), respectively. In practice, the boundary conditions can be taken at a few Bondi radii, the region of BH influence: $R_{\rm B} = G M_{\rm BH}/c_{\rm s,\,0}^2 \approx 19\,M_{\rm BH,9}/T_{0,7}$ pc, where the black hole mass is expressed in units of $10^9\ M_\odot$ and the temperature in 10^7 K. The first problem with the Bondi formula is that the profiles of the system vary with the radius. A reasonable choice seems to take ρ_0 as the volume-weighted (hot) gas density calculated within $r \lesssim 5$ kpc, and $c_{\rm s,0}$ as the mass-weighted sound speed in the same region. Our assumed SMBH has a mass of $3 \times 10^9\ M_\odot$.

The Bondi radius (~ 50 pc for cluster or ~ 80 pc for groups), is usually smaller than our resolution limit, so I refrain to attach a strict physical meaning to $\dot{M}_{\rm B}$. Moreover, the Bondi theory requires rather strict assumptions: the flow must in fact be steady, adiabatic and without angular momentum. Although almost all feedback studies employ the Bondi theory to estimate the instantaneous BH accretion rate (e.g. Springel et al. 2005; Cattaneo & Teyssier 2007; Sijacki et al. 2007; Puchwein et al. 2008; Booth & Schaye 2009; Dubois et al. 2010), I believe that it does not represent properly the complex reality. Beside complications such as turbulence, (slow) rotation and magnetic fields (see Krumholz et al. 2005, 2006; Mościbrodzka & Proga 2008, 2009; Narayan & Fabian 2011), which can easily change the accretion rate by a factor of a few with respect to the classic value, the central ISM can be prone to thermal instabilities. The dusty multiphase gas can drastically change the nature of the accretion process. In fact, in the presence of a cooling flow the mass inflow rate at some small radius should be determined by the gas cooling process, rather than the BH gravity.

The third model for the accretion rate, used only in the multiphase gas simulations (Chapter 7), is based on the central *inflow* rate. Without discriminating between hot and cold gas, the quantity of accreted material is estimated as the inflow through a 'spherical'[25] surface very near the centre ($r \sim 500$ pc). Each cubical cell i containing a piece A_i of the spherical surface, contributes $\dot{M}_{{\rm acc}_i} = \rho_i v_{r_i} A_i$ to the accretion rate only if the radial velocity v_{r_i} is negative (inflow). The accreted gas mass, $\dot{M}_{{\rm acc}_i}\Delta t$, is then removed from the same zone[26], along with the related momentum and total energy (BH sink terms).

[25] More specifically, this region corresponds to the cells surrounding the very central 8 zones, where the bipolar outflows are injected.

[26] This method has the advantage to prevent unphysical voids; the accretion and sink terms are tightly linked on a cell-by-cell basis, as we do not compute spherical averages of these terms.

3.8 Stellar Winds and Supernovae

The core of the system needs to be modelled in the more realistic way possible, in order to study the competition of heating versus cooling. At the centre of clusters and groups often resides a large massive elliptical galaxy (the BCG or cD galaxy), whose SMBH should be the dominant thermostat of the whole feedback process. From a historic point of view, the heating linked to stellar evolution - via stellar winds (SW) and supernovae Ia (SNIa) - was considered the first possible candidate to halt the cooling flow. It became soon clear that this process is too weak, orders of magnitude lower than the radiative losses (e.g. Borgani et al. 2002, 2004; Tornatore et al. 2003; Piontek & Steinmetz 2011). Moreover, stellar heating does not present any kind of evident feedback loop, required for a proper self-regulation.

We decided to include stellar evolution, first, to check if it is totally negligible or has a marginal influence in the heating process. More importantly, it pollutes the ISM/ICM with metals (mainly iron), incidentally a great tracer of the anisotropic outflow activity. In addition, it is an essential element in driving the evolution of the isolated galaxy, governed only by internal processes. Studying the exact local star formation mechanism will be not investigated here. In fact its study requires, not only very high resolution (at least a fraction of the Jeans length) and self-gravity, but also sophisticated numerical techniques to follow the dynamics of single stars, like sink particles (see Federrath et al. 2010). It thus sufficient here to adopt a smooth injection of mass, metals and energy, directly linked to the stellar density ρ_*, since our resolution will be always greater than 150 pc, reaching ~ 2 kpc in the cluster runs (a mature SNIa remnant has typically a size of $\lesssim 40$ pc).

The stellar density profile, ρ_*, is retrieved from a de Vaucouleurs' surface brightness distribution, $\mathrm{SB} = \mathrm{SB}_0 \exp[-7.67\,(r/r_\mathrm{e}^{1/4} - 1)]$, which fits well the profile of ellipticals and bulges. An excellent analytical approximation is given by Mellier & Mathez (1987):

$$\rho_* = \rho_0\, r^{-0.855} \exp\left(-r^{1/4}\right), \tag{3.24}$$

where the central density is $\rho_0 = M_0/16\pi a^3$, with $a = r_\mathrm{e}/7.67^4$ and $M_0 \simeq 1.65 \times 10^4\, M_{*,t}$. The total stellar mass $M_{*,t}$ and the effective radius r_e of our typical simulated elliptical are $\sim 3.4 \times 10^{11}\, M_\odot$ and ~ 10 kpc, respectively (similar to NGC 5044; Buote et al. 2004).

The mass source term, added to Eq. 3.2, is simply governed by the stellar density and the specific rate of mass loss:

$$S_{\mathrm{stellar},\rho} = \alpha\, \rho_*. \tag{3.25}$$

In the coefficient α (s^{-1}) resides the entire physics of stellar evolution, based on stellar winds and SNIa (Brighenti & Mathews 2002a; Mathews & Brighenti 2003): $\alpha = \alpha_* + \alpha_\mathrm{sn}$. The mass loss source term is governed mainly by the evolving stars, α_* (e.g. the current mass loss for NGC 4472 is $\sim 0.15\, M_{*,t}/(10^{11}\, M_\odot)\, M_\odot\ \mathrm{yr}^{-1}$). The basic assumption is that gas ejected from evolving giant stars as winds or planetary nebulae eventually becomes part of the hot phase. We consider a mass loss rate from a single burst stellar population with Salpeter initial mass function (IMF) and age t, varying as (Mathews 1989)

$$\alpha_* \simeq 4.7 \times 10^{-20}\, (t/t_\mathrm{n})^{-1.3}\,, \tag{3.26}$$

where $t_\mathrm{n} \approx 13$ Gyr is the galaxy age (results are not sensitive to the adopted t_n). For other power-law IMFs, α_* varies inversely with the stellar mass-to-light ratio.

The specific mass loss rate from SNIa is given by

$$\alpha_{\rm sn} \simeq 3.17 \times 10^{-20}\, {\rm r_{Ia}}(t)\, (M_{\rm sn}/M_\odot)\, \gamma_{\rm B}\,, \tag{3.27}$$

where $M_{\rm sn} \approx 1.4\ M_\odot$ (the Chandrasekhar mass) and the mass-to-light ratio in the B band $\gamma_{\rm B}$ is typically around 8. The supernova rate (in SNu[27]) is a critical parameter for the chemical enrichment of the system. The current rate of SNIa has become more defined thanks to recent observations, placing it on a level of $r_{\rm Ia} \sim 0.06\,(t/t_n)^{-s}$ SNu (Mannucci et al. 2005; Greggio 2005; Greggio et al. 2008). Unfortunately, the past evolution of this rate is not well constrained, and a reasonable value appears $s \sim 1.1$; the adopted $r_{\rm Ia}$ results in iron abundances consistent with observations ($\sim 1-2$ the solar value; Humphrey & Buote 2006). Evolutionary flow solutions with $s > 1.3$, although granting a substantial heating at high redshift (Ciotti et al. 1991), produce iron abundances far in excess of those observed today, unless the iron is preferentially removed by selective cooling.

The second key term linked to stellar evolution is the energy source (added to Eq. 3.4), assuming that the entire SW and SNIa energy becomes thermalised on subgrid level:

$$S_{\,{\rm stellar},\,e} = \alpha\rho_* \left(e_0 + \frac{1}{2}\,|\boldsymbol{v} - \boldsymbol{v}_*|^2 \right), \tag{3.28}$$

where the mean gas injection energy is $e_0 = 3k_{\rm b}T_0/2\mu m_{\rm p}$, with $T_0 = (\alpha_* T_* + \alpha_{\rm sn} T_{\rm sn})/\alpha$. The SN temperature is simply retrieved from the injected total thermal energy by a SNIa, $E_{\rm sn} \approx 10^{51}$ erg. The stellar temperature is instead proportional to the stellar velocity dispersion σ_*, i.e. $T_* = (\mu m_{\rm p}/k_{\rm b})\,\sigma_*^2$. The stellar velocity dispersion is calculated by solving the Jeans equation for a spherically symmetric, isotropic stellar system. It is worth noting that, while the mass loss is governed by the stellar losses, the heating is dominated by the energy injection of SNIa, $T_{\rm sn} > T_*$. Finally, the last term in Equation 3.28, $\propto |\boldsymbol{v} - \boldsymbol{v}_*|$, represents a drag on the flow, which is generally negligible if the flow is subsonic (the mean stellar velocity is $\boldsymbol{v}_* \sim 0$ for non-rotating galaxies).

As previously mentioned, stellar feedback will result insufficient to quench cooling flows in groups and clusters, and only marginally relevant in an isolated galaxy. On the other hand, it is extremely interesting to follow the metal enrichment and evolution (in some simulations it is used also for computing the cooling function). Again, we take as reference for the metallicity the iron content (Sec. 3.5), which is consistently calculated by solving a passive density advection equation:

$$\frac{\partial \rho_{\rm Fe}}{\partial t} + \boldsymbol{\nabla}\cdot(\rho_{\rm Fe}\boldsymbol{v}) = \left(\frac{Z_{\rm Fe,\odot}}{1.4}\,\alpha_* + \frac{y_{\rm Ia}}{M_{\rm sn}}\,\alpha_{\rm sn} \right) \rho_*\,, \tag{3.29}$$

where $y_{\rm Ia} = 0.744\ M_\odot$ is the supernova iron yield and the stellar wind ejecta are assumed to have solar abundance $Z_{\rm Fe,\odot} \simeq 1.83 \times 10^{-3}$ (by mass). In the diagnostic maps, I prefer to plot the usual fractional abundance $Z_{\rm Fe} = 1.4\ \rho_{\rm Fe}/\rho$, in solar units (1.4 is the ratio of the total mass to hydrogen mass at solar abundance).

As a concluding remark, note that the assumption of smooth injection made for the previous stellar source terms (see also Mathews & Baker 1971; Loewenstein & Mathews 1987), clearly breaks down within the very nuclear region. A mature SNIa remnant would

[27] The number of supernovae in 100 years, expected from stars of total luminosity (in the B band) $10^{10}\ L_{\odot,\,\rm B}$.

have a size of $\sim$ 40 pc, if the external medium has number density $\sim$ 0.1 cm^{-1} and temperature $\sim 10^7$ K. Stellar winds from orbiting stars likely generate long tails of warm gas, several tens of pc in size (Mathews 1990; Parriott & Bregman 2008; Bregman & Parriott 2009), giving rise to inhomogeneities. These intrinsic complexities, along with the lack of merging as possible source of gas, hamper a proper semi-analytical modelling of the ISM in the central $\lesssim$ 100 pc.

3.9 Initial Conditions and Gravity

In the present work we study the effect of feedback on the 100s pc − few Mpc scales, integrating the system for 7-10 Gyr. Several feedback schemes are only able to delay excessive gas cooling for 1-2 Gyr before failing, and therefore it is fundamental to investigate the very long-term behaviour of heated flows. On the other hand, it is extremely expensive to carry out fully cosmological simulations with such high dynamical range. Fortunately, major mergers, which can drive additional turbulence and heating, are also rare with timescales much longer than the core cooling times (e.g. Fakhouri et al. 2010). Overall, I preferred to focus on the physics of the AGN feedback, assuming a totally relaxed system, while leaving the study of secondary[28] effects, linked to more realistic environments, to later works.

In Sec. 3.2, we examined the setup of the grid and the whole computational box. I now explain the setup of the physical initial conditions. Assuming a relaxed system, with static potential, we use spherical hydrostatic equilibrium as the approximated initial state:

$$\frac{1}{\rho}\frac{dP}{dr} = g_{\rm dm}(r) + g_{\rm cD}(r)\,, \tag{3.30}$$

where the total gravitational acceleration $g_{\rm tot}$ is due the dark matter halo and the cD galaxy potential (dominating in the central $\lesssim$ 20 kpc). The self-gravity of the gas is negligible, compared to the previous contributions. There are two ways to retrieve the initial conditions. In the first one (used mainly for the cluster runs), we take advantage of the known gravitational potential, i.e. the famous NFW dark matter profile (Navarro, Frenk & White 1996):

$$\phi_{\rm dm} = -\frac{GM_{\rm vir}}{r_{\rm s} f(c_{102})}\frac{\ln(1+r/r_{\rm s})}{r/r_{\rm s}}\,, \tag{3.31}$$

where $c_{102} = R_{\rm vir}/r_{\rm s}$ is the concentration at overdensity 102 ($\approx$ 6.6 for the cluster; $\approx$ 8.7 for the group), and $f(c_{102}) = \ln(1+c_{102}) - c_{102}/(1+c_{102})$. We always adopt a ΛCDM cosmological universe with density parameters $\Omega_{\rm M} = 0.27$, $\Omega_\Lambda = 0.73$, and Hubble constant $H_0 = 71$ km s^{-1} Mpc^{-1}. The virial mass is taken $M_{\rm vir} = 10^{15}\ M_\odot$ (for the cluster) and $M_{\rm vir} = 4\times10^{13}\ M_\odot$ (for the group/elliptical). The gravitational acceleration is obviously $g_{\rm dm} = -\,d\phi_{\rm dm}/dr$. The gravity of the massive elliptical is provided instead by

$$g_{\rm cD} = -\frac{GM_*(<r)}{r^2}, \tag{3.32}$$

[28] Cool cores may survive major mergers (e.g. Burns et al. 2008), implying that the central AGN feedback is needed regardless of the cosmological evolution.

where $M_*(< r) = M_{*,t}\,\gamma(8.58, w)$ and $w = 7.67(r/r_\mathrm{e})^{1/4}$ (γ is the incomplete Gamma function; see Mellier & Mathez 1987). Note that gravity requires two additional source terms in the momentum and energy Euler equations, i.e. $\rho \boldsymbol{g}_\mathrm{tot}$ and $\rho \boldsymbol{g}_\mathrm{tot} \boldsymbol{v}$, respectively.

The next step is finding a convenient fit to the observed temperature profile (K). For a typical galaxy cluster (A1795; see Figure 4.4, black dotted line):

$$T_\mathrm{cluster} = 2\,\frac{T_0}{1 + [r_\mathrm{a}/(r + r_\mathrm{b})]}\,, \tag{3.33}$$

where $T_0 = 4.3{\times}10^7$ K, $r_\mathrm{a} = 35$ kpc, and $r_\mathrm{b} = 10$ kpc. For a typical galaxy group/elliptical (NGC 5044; see Figure 5.3, black dotted line), a good empirical fit is

$$T_\mathrm{group} = \left[\left(\frac{1}{0.78 + 1.02\,r_\mathrm{kpc}^{1.5}} + \frac{r_\mathrm{kpc}^{1/3}}{1.8}\right)^{-1/3} + T_\mathrm{cut}\right] 10^7\,, \tag{3.34}$$

where the radius is expressed in kpc and $T_\mathrm{cut} = -0.12\exp(-r_\mathrm{kpc}/1.5)$. The T fit and the total gravitational potential allow to finally retrieve the gas density profile, integrating numerically the hydrostatic Equation 3.30:

$$\rho_\mathrm{i} = \rho_\mathrm{i-1}\exp\left[-\frac{T_\mathrm{i} - T_\mathrm{i-1}}{T_\mathrm{i-1/2}} + \frac{\mu m_\mathrm{p}}{k_\mathrm{b} T_\mathrm{i-1/2}}\,g_\mathrm{tot,\,i-1/2}\;(r_\mathrm{i} - r_\mathrm{i-1})\right], \tag{3.35}$$

with $\rho_{i=0}$ the density normalisation fixed by the baryon fraction at the virial radius, $f_\mathrm{b} \sim 0.15$ (for clusters) or $f_\mathrm{b} \sim 0.11$ (for groups).

The second method consists instead in adopting both the observed temperature and density fit, calculating then the pressure ($P = nk_\mathrm{b}T$), to finally obtain the gravitational potential via Eq. 3.30. For instance, I use several times the following electron number density (cm^{-3}) fit for the elliptical/group NGC 5044 (Figure 5.3):

$$n_{e,\,\mathrm{group}} = \frac{0.09}{r_\mathrm{kpc}^{0.55}}\frac{1}{1 + (r_\mathrm{kpc}/9.5)^{1.05}} + \frac{0.0025}{1 + (r_\mathrm{kpc}/30.5)^3}. \tag{3.36}$$

Once we obtained all the initial radial profiles of temperature, density and gravitational acceleration, it is straightforward to linearly interpolate the profiles in the numerical 3D box, and then to compute the derived quantities, such as pressure and internal energy. Finally, the initial total velocity is set to zero in the entire domain.

3.9.1 Gaussian Perturbations

When studying the details of the flow, such as the thermal instabilities and filamentary multiphase gas, spherically symmetric initial conditions are too idealised. To start the system in a more natural configuration, in the more advanced simulations (Chap. 7), I perturbed the initial density and temperature profiles, initiating the formation of cold filaments and clouds. Depending on the model parameters, such features can develop even in the early stages of evolution, before the AGN has become very powerful.

The fluctuations leading to the thermal instability can be produced by the turbulence associated with cosmological mergers. It is beyond the scope of this work to study such

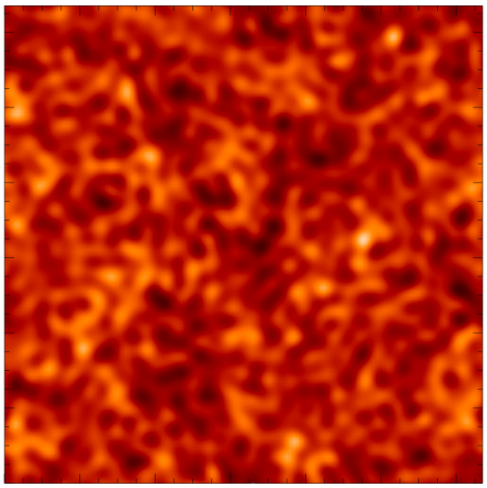

Figure 3.8. Example of a Gaussian random field with white noise power spectrum (here only 128^3), which is used to perturb the initial density and temperature profiles.

effects. Here, it is sufficient to adopt a simple Gaussian random field with a white noise power spectrum of gas density. Using dispersion relation and direct simulation, McCourt et al. (2012) and Sharma et al. (2012) demonstrated that thermal instability does not depend on the range of the driving modes in Fourier space. Moreover, in the late stage of the evolution, the density fluctuations are governed by the AGN jets and associated turbulence, losing memory of the initial imprint.

I generate initial conditions using IDL. First, I initialise a complex stochastic field (1024^3) in the **k**-space, with amplitude of each mode given by

$$W \propto k^{-1}, \tag{3.37}$$

where $k = (k_x^2 + k_y^2 + k_z^2)^{1/2}$. The above prescription ensures that the '3D' power spectrum, which is $\propto W^2\, k^2$, remains constant, i.e. is described by a white noise spectrum. Second, the above amplitude is combined with a Gaussian random field:

$$[\mathrm{Re}(W(\mathbf{k})),\ \mathrm{Im}(W(\mathbf{k}))] = [G(u_1)W,\ G(u_2)W] \tag{3.38}$$

where G is a function of a uniform random deviate u_1 or u_2 that returns Gaussian-distributed values. This method guarantees that the phases are random. I also impose cutoffs at $k_{\mathrm{max}} = 1024/4$ and $k_{\mathrm{min}} = 3$ (in units of $2\pi/L$, with L the box size). The high-k cutoff is introduced in order to avoid spurious numerical effects. Third, I compute inverse Fourier transform of $W(\mathbf{k})$ to obtain $W(x, y, z)$, and normalise it by the mean of its absolute value $\langle|W(x, y, z)|\rangle$. Finally, I superpose the normalised fluctuations (e.g. Figure 3.8) onto the initial density distribution ρ_{unp}:

$$\rho(x, y, z) = \rho_{\mathrm{unp}}(x, y, z)\left(1 + \xi\frac{W(x, y, z)}{\langle|W(x, y, z)|\rangle}\right), \tag{3.39}$$

where $\xi = 0.3$ is the chosen amplitude of the initial perturbations. The new temperature distribution is computed from the new density assuming isobaric fluctuations.

Chapter 4

AGN Feedback in Galaxy Clusters

THE PRESENT Chapter opens the second part of the Thesis, i.e. the presentation of the theoretical and numerical results on the mechanical AGN feedback, which is supposed to quench cooling flows in every virialised system with a hot gas halo. In the first two Chapters, I reviewed and commented the current state of the general cooling flow problem and the observational evidences for a self-regulated heating, tightly linked to the central active galactic nucleus. In the third Chapter, I explained the numerical setup, methods and implemented physics, required to study the complex thermodynamical competition between heating and cooling.

This Chapter is entirely dedicated to the role of massive AGN outflows in controlling the evolution of the plasma in the environment of galaxy clusters. In the previous Chapters, we did not focus extensively on the differences between cosmic systems. Therefore, before analysing in depth the numerical results, it is worth to define better the main properties of the chosen system for the first set of simulations, i.e. a cluster of galaxies. For more details on the subject, I refer the reader to the excellent reviews of Sarazin (1986), Rosati et al. (2002), Voit (2005), Borgani & Kravtsov (2009), and Böhringer & Werner (2010). The results of this Chapter are also presented in Gaspari et al. (2011a).

4.1 Galaxy Clusters Overview

Modern cosmology has reached fundamental milestones. A wide range of observations support one evolutionary scenario, the 'concordance model'. The universe appears geometrically flat, implying that its total energy density is very close to the critical density ($\Omega \approx 1$), needed to close the universe. The cosmos appears governed mainly by two components. About 23% of the energy resides in the form of non-baryonic non-collisional matter, also known as dark matter (DM). Since it does not emit any kind of electromagnetic radiation, the presence of dark matter is revealed only by gravitational interactions (via dynamical and lensing studies). The second, more dominant ($\Omega_\Lambda \approx 0.73$) component, dark energy, is even more mysterious: its negative pressure is responsible for the current acceleration of the expanding universe. Only a minor fraction of the whole

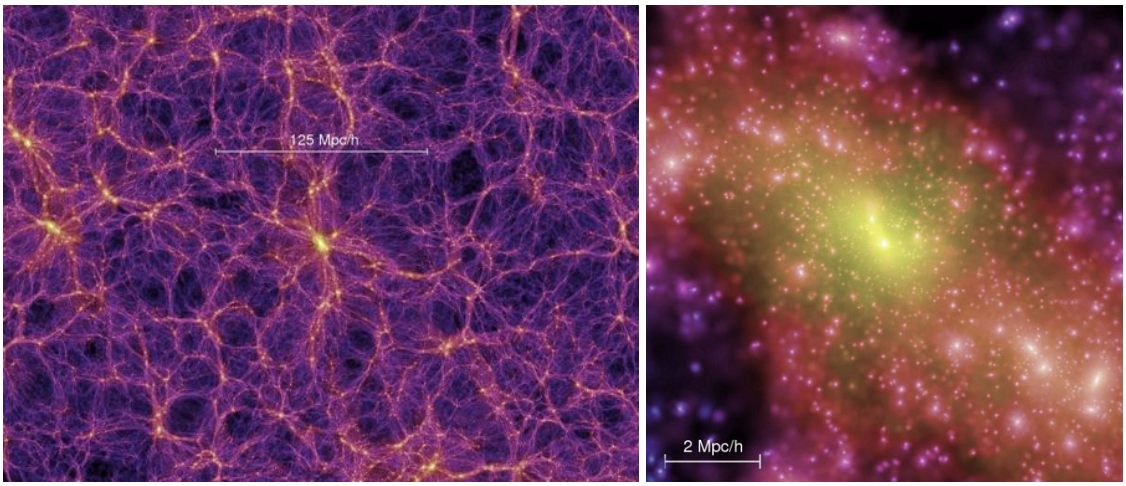

Figure 4.1. Large scale structure of the universe (dark matter only), recreated via the massive N-body Millenium simulation (from Springel et al. 2005). Left: the filamentary cosmic web over several 100s Mpc, containing galaxies, groups and clusters, separated by void regions. Right: a zoom of the central heavily clustered region.

universe ($\Omega_b \approx 0.045$) is in the form of ordinary, baryonic matter. This mere 15% of the total amount of matter (Ettori & Fabian 1999) is extremely variegated, mainly composed by the hot diffuse plasma, and to a lesser extent by the colder gas and stars (see references in the reviews quoted above).

Clusters of galaxies have a special place in the previous ΛCDM cosmological framework. They are the largest matter aggregates within the large-scale structure that have collapsed under their own gravity. A step back. When the universe was still young, 360,000 years after the supposed Big Bang ($z \sim 1100$), at the recombination of hydrogen, the cosmos is overall homogeneous and isotropic. Very small perturbations are present, probably due to quantum effects linked to a strong inflationary period. After the recombination, these small linear perturbations are amplified via gravitational instability and the dominant matter component, dark matter, starts to collapse in nonlinear overdensities. Assuming that the DM is non-relativistic (cold), the first structure to form, due to larger perturbation amplitudes, reside on the smallest scales. Larger structures, such as groups and clusters, form in a later stage, via merging of smaller halos (known as hierarchical clustering; see Figure 4.1). The ordinary, baryonic matter follows the evolution of the dark matter: the primordial gas falls in the deep DM potential well (well described by a NFW profile – Eq. 3.31), is gravitationally shock-heated and thus forms the ubiquitous hot plasma, studied in this work. The cold gas and stars of the galaxies condense, in general, from this hot cauldron, albeit the process is complex and variegated.

Galaxy clusters, on the top of the cosmological hierarchy, are therefore a precious source of information about the cosmological scenario (Borgani & Guzzo 2001). Since they are also the most luminous objects, due to the massive gas radiative emission in the X-ray band ($L_x \sim 10^{44} - 10^{45}$ erg s^{-1}), they are optimal laboratory to observe and to study the baryonic physics, including AGN feedback.

The marked characteristic of clusters is that they are the largest gravitationally bound objects in the universe, which are closely approaching dynamical equilibrium. In fact, the

crossing time for a galaxy in a cluster with radius R is rather short compared to the cluster age:

$$t_{\rm cr} = \frac{R}{\sigma_{\rm v}} \approx 1 \left(\frac{R}{1\ {\rm Mpc}} \right) \left(\frac{\sigma_{\rm v}}{10^3\ {\rm kms^{-1}}} \right)^{-1}\ [{\rm Gyr}]\,, \tag{4.1}$$

where $\sigma_{\rm v}$ is the velocity dispersion of galaxies (from the virial theorem, typically $\sim 10^3$ km s^{-1}). Thus, for clusters that formed at $z \sim 1$, galaxies may have experienced a few orbits, in particular in the inner regions (< 1 Mpc). A rich cluster typically contains hundreds of galaxies, which contributes only to few percent to the total mass, $M_{\rm tot} \sim 10^{14} - 10^{15}\ M_{\odot}$. The baryon fraction ($\sim 0.16$, down to ~ 0.14 for poor clusters) is instead dominated by the intracluster medium (ICM), which shines copiously in the X-ray band. Another key property of clusters is that they are relatively young. The observations indicate that clusters formed relatively recently compared to the single galaxies ($z \sim 1$, i.e. $\sim 7 - 8$ Gyr). Therefore, they allow to determine several fundamental cosmological parameters, such as the density parameters, the baryon fraction and the amplitude of the mass fluctuations, σ_8 (see the review of Borgani 2006). However, it is worth noting that rich clusters are relatively rare, with a spatial number density of $\sim 10^{-5}$ Mpc^{-3}. Poor clusters and groups are instead the most common building blocks of the universe (see next Chapters); the number density of galaxies is in fact $\sim 10^{-2}$ Mpc^{-3}.

The fraction of elliptical, S0 and spiral galaxies depends on the cluster density and classification[1]. Nevertheless, near the centre of the cluster the fraction of elliptical and spheroidal galaxies increases (culminating with the central BCG), while spiral galaxies tend to disappear. The luminosity function of galaxies $n(L)$ (the number of galaxies in the luminosity range $[L, L + dL]$) is well approximated by the Schechter functional form, i.e. $n(L) = N^*/L^*\,(L/L^*)^{-\alpha} \exp(-L/L^*)$, where $L^* \simeq 2 \times 10^{10}\ L_{\odot}$, $\alpha \simeq 5/4$, and N^* is the number of galaxies with $L > L^*$. This function has a theoretical interpretation based on the simple self-similar collapse of structure formation (Press & Schechter 1974).

Galaxy clusters shine also in the radio band, with the source either linked to single galaxies (e.g. Fanaroff-Riley I and II) or to a more diffuse halo. Regarding the former, we already know that the radio and X-ray emission are often correlated (Chapter 2), with the AGN cavities often filled by the radio emission produced by the collimated relativistic jet (see Figure 4.2). The extended radio sources, although rather uncommon, present instead various morphologies: very wide (~ 1 Mpc) and regular, decentralised and irregular (relic), or a mini halo surrounding the central massive elliptical. The radio emission is associated with the synchrotron process, due to the interaction of relativistic electrons with the magnetic field (few μG). Its power spectrum is well represented by a power-law distribution. In the ICM, the lifetime of the relativistic electrons is relatively short, mainly due to synchrotron and inverse Compton emission: $\tau \sim 10^8$ yr (Sarazin 1999). Therefore, assuming an effective speed (random walk with Alfvén speed) of ~ 100 km s^{-1}, the previous time is not sufficient for the particle to travel Mpc distances (reaching at most ~ 10 kpc), and some kind of reaccelerating mechanism is required (AGNs, mergers?).

The ICM can be observed also through its effects on the cosmic microwave background (CMB). This is possible via the thermal SZ effect (Sunyaev & Zeldovich

[1]The most common is the richness classification by Abell (in 1958), i.e. the count of galaxies brighter than $m_3 + 2$ (where m_3 is the magnitude of the third brightest member). Other classifications involve the morphological type of the members (e.g. Rood-Sastry).

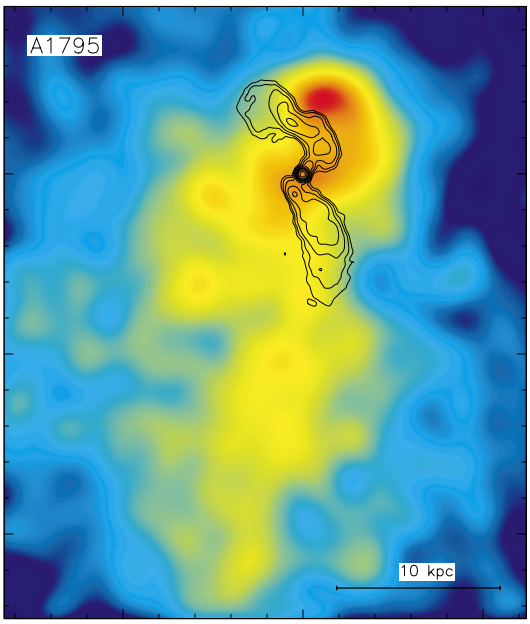

Figure 4.2. The massive galaxy cluster A1795, observed by *Chandra*, with the 3.6-cm radio emission overlaid (from Fabian et al. 2001b).

1972), i.e. the distortion of the CMB black body spectrum due to the inverse Compton on the photons that travels the hot plasma. The magnitude of the temperature distortion is proportional to the Compton parameter:

$$\frac{\Delta T}{T_{\rm CMB}} \propto y = \int \frac{k_{\rm b} T_{\rm e}}{m_e c^2} n_{\rm e} \sigma_{\rm T} \, dl \,, \tag{4.2}$$

where $T_{\rm e}$ and $n_{\rm e}$ are the electron temperature and number density, $\sigma_{\rm T}$ is the Thomson cross section and l is the line of sight. The SZ effect, which is independent of redshift, is a valuable tool to retrieve several cluster properties, such as the mass and distance (combined with the X-ray emission analysis).

The X-ray properties of the ICM have been amply highlighted in Section 1.1. Here I just recall that the ICM is a typical astrophysical collisional plasma, very hot ($T \sim T_{\rm vir} \approx 2 - 10 \times 10^7$ K) and diffuse ($n \sim 10^{-4} - 10^{-2}$ cm^{-3}). In this energy interval the radiative cooling is mainly due to free-free bremsstrahlung emission ($\epsilon \propto n^2 T^{1/2}$), with the plasma being fully ionised. On average abundances in the ICM are $\sim 0.3\, Z_\odot$ (Tamura et al. 2004), slightly increasing at the centre[2]. The most commonly detected lines are Fe, O, Si, S, Mg, Ne, N and C.

The sound crossing time in the ICM is about

$$t_{\rm s} \approx 6 \times 10^8 \left(\frac{D}{1 \text{ Mpc}} \right) \left(\frac{T}{10^8 \text{ K}} \right)^{-1/2} \text{ [yr]} \tag{4.3}$$

where D is the cluster diameter. This time is particularly short compared to the age of the cluster, thus, only as a first-order approximation (neglecting the cool-core turbulent region), the ICM may be assumed in hydrostatic equilibrium. The total mass can therefore

[2]Non-cool-core clusters, usually associated with mergers, tend instead to show a flat abundance gradient.

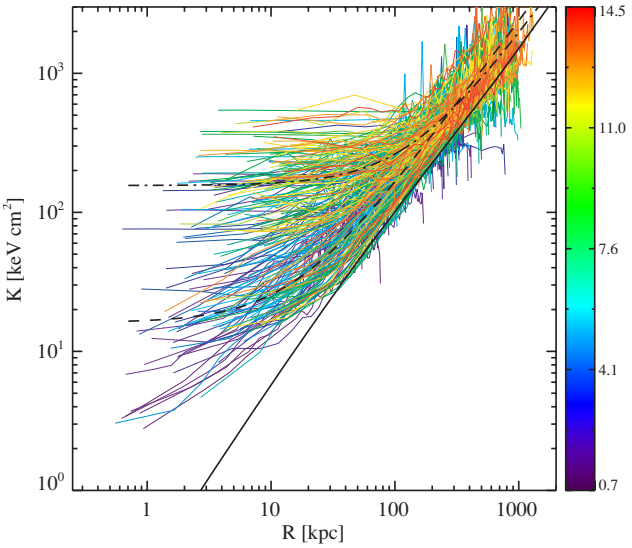

Figure 4.3. Observed entropy profiles for varying cluster temperature ranges (see colour bar, in keV unit – from Cavagnolo et al. 2009), compared to a pure cooling model (solid line; note that at larger radii this profile coincide with the self-similar scaling, i.e. $K \propto r^{1.1}$ – Voit et al. 2002).

be retrieved by the density, $\rho(r)$, and temperature, $T(r)$, profiles of the ICM:

$$M_{\rm tot}(r) = -\frac{k_{\rm b} T r}{G\mu m_{\rm p}} \left(\frac{d\log\rho}{d\log r} + \frac{d\log T}{d\log r} \right) . \tag{4.4}$$

providing a typical cluster mass estimate in the range $10^{14} - 10^{15}\ M_{\odot}$.

A commonly used fit to the gas surface brightness (and thus density) profile is known as the β-model (Cavaliere & Fusco-Femiano 1978):

$$\mathrm{SB_x} \propto \left[1 + \left(\frac{b}{r_{\rm c}} \right)^2 \right]^{-3\beta+1/2} , \tag{4.5}$$

where b is the projected distance from the centre, $r_{\rm c}$ is the core radius, and $\beta = \mu m_{\rm p} \sigma_r^2 / k_{\rm b} T$, with σ_r the one dimensional velocity dispersion of galaxies[3]. Except for the central cool-core peak, the β-model is rather consistent with observations[4]. Finally, the ICM temperature profiles show in the majority of cases (cool-core clusters) the typical positive gradient, with central cooler temperatures about 1/3 of the virial one (see Section 1.4 for further insights). At large radii, the temperature appears also to decline by more than 50%, although measurements are quite uncertain in very low-density regions.

I conclude this overview by noting that, assuming a self-similar cosmological collapse governed only by gravity (see Kaiser 1986), all cosmological systems should follow specific scaling relations[5], among the most notable ones: $L_{\rm x} \propto T^2$, $M_{\rm tot} \propto T^{3/2}$, $L_{\rm x} \propto M_{\rm tot}^{4/3}$, and $K \propto T$ (with $K = k_{\rm b} T n_{\rm e}^{-2/3}$ the entropy parameter). The self-similar relations can be simply understood through the virial theorem: $E_{\rm kinetic} = -2E_{\rm potential} \propto G M_{\rm tot}/R$. During

[3]The gas and galaxies densities are related as $\rho \propto \rho_{\rm gal}^{\beta}$.

[4]However, note that the β-model is derived under the strong assumptions that the gas is isothermal, plus the underlying cluster potential follows a King model (King 1962).

[5]The fiducial scaling radius is usually taken as the radius where the overdensity factor is $\delta \sim 200 - 500$ the critical density, which is always smaller than the virial radius.

the collapse the potential energy of the ICM is converted into internal heat, and thus $T \propto M_{\rm tot}/R \propto M_{\rm tot}^{2/3}$. In reality, other key physical processes, as cooling and heating, cause the thermodynamical properties to deviate from a pure gravitational self-similar collapse (Borgani et al. 2008 for a review), in particular within $r \lesssim 0.1\ R_{\rm vir}$. For instance, Figure 4.3 shows the clear excess of entropy in the core, which can not be explained by gravity (and cooling) alone, requiring again a substantial underlaying heating process. As tackled in Chapter 5, lower mass halos tend to break more evidently the self-similarity (Fig. 5.2), possibly due to the relatively stronger effect of AGN feedback and cooling.

4.2 Simulation Setup

We are now ready to investigate via 3D hydrodynamic simulations the role of self-regulated AGN outflows in quenching the cooling flows. I recall briefly the main motivations and goals (Chapters 1-2).

Active galactic nuclei can easily provide enough energy to the gas to offset the energy lost by radiation. High resolution X-ray images show indeed clear evidence of AGN-gas interaction in several clusters (e.g. Boehringer et al. 1993; Blanton et al. 2001; Finoguenov & Jones 2001; Jones et al. 2002; McNamara & Nulsen 2007), especially in the form of cavities and weak shocks. Moreover, there is widespread observational evidence, based on blueshifted absorption lines, for massive mechanical outflows originating from the galactic nuclei (Crenshaw et al. 1999, 2003; Kriss et al. 2003; Morganti et al. 2005, 2007; Risaliti et al. 2005; McKernan et al. 2007; Nesvadba et al. 2008; Pounds & Reeves 2009; Cappi et al. 2011; Tombesi et al. 2012). Motivated by these investigations, I argue that a realistic feedback should possess the following key characteristics.

- Mechanical, because most of the outflow internal energy is quickly radiated away on sub-pc scales (high-density regions).
- Anisotropic, in the form of bipolar and highly collimated outflows.
- Subrelativistic, the outflow/jet has decelerated on kpc scales due to substantial mass loading (entrainment).
- Self-regulated, the AGN should react to the environmental conditions, either via hot or cold accretion, at least on scales of a cooling time.

The main objectives of the computed AGN feedback models are the following.

- Quenching cooling rates, at least $\lesssim 10\%$ of the classic cooling flow (no overcooling).
- Preserving the cool-core structure, without destroying the observed temperature and density profiles (no overheating).
- Resembling quasi thermal equilibrium for 7 or more Gyr (galaxy clusters formed in relatively recent times).
- Reproducing the main observational X-ray cluster features, such as buoyant bubbles, shocks, metals uplift, and turbulence.

It is worth noting that we adopt multigrid, 3D hydrodynamic simulations to fully capturing the intrinsically chaotic and turbulent nature of cooling flows. It is in fact essential to allow a realistic description of all instabilities, which in turn strongly influence the outflow evolution. 1D or 2D axisymmetric simulations may provide instead very different and biased results, due to the imposed geometry.

I emphasise that the scheme for the generation of jets and their connection with the black hole accretion (Chap. 3) is kept, on purpose, as simple as possible, due to numerical limitations. The attempt to investigate in depth subjects like the BH growth is beyond the scope of the work. Here, we focus on the large scale effects of feedback, with the aim of solving the cooling flow problem for several Gyr. The computed models and results will be critically tested, highlighting the positive and problematic aspects of the proposed feedback, with particular attention to the comparison with observational constraints.

In Table 4.1 are summarised all the numerical details of the simulations carried out with FLASH, including the type of feedback (Sec. 3.7), the efficiency, the jet width and height ($d_{\rm jet} \times z_{\rm jet}$), and other relevant properties (see Chapter 3 for the details of implementation). As usual, the hydrodynamic equations are solved via the split PPM solver (Sec. 3.2). All galaxy cluster computations use the RK2 solver for radiative cooling ($Z = 0.3\ Z_{\odot}$), with cold gas dropout enabled (Sec. 3.5). The outflows are always cylindrical, usually injected inside the domain, according to the entrainment scheme (Equation 3.18). When $z_{\rm jet} = 0$, the jet is instead injected through the internal boundaries, assuming $\rho_{\rm jet}$ about $1/10$ of the initial central gas density (Sec. 3.6).

4.2.1 Template: Abell 1795

In order to study the feedback in a realistic environment, I adopt the well-observed cluster Abell 1795 (Tamura et al. 2001; Ettori et al. 2002), as template for the simulations. Being A1795 a rather typical, relaxed (Buote & Tsai 1996), cool-core massive ($M_{\rm vir} \sim 10^{15}\ {\rm M}_{\odot}$) cluster, all the presented results should be relevant for any object in this category. The short central cooling time, $t_{\rm cool} \sim 4 \times 10^8$ yr (Ettori et al. 2002), assures that this cluster should host a strong cooling flow in absence of feedback. Recent X-ray observations place an upper limit to the radiative cooling rate $\dot{M}_{\rm cool} \lesssim 30\ {\rm M}_{\odot}\ {\rm yr}^{-1}$ (Peterson et al. 2003; Bregman et al. 2006), which is a key constraint for the success of a heating model.

As usual, we start the calculations with the hot gas in spherical hydrostatic equilibrium in the potential well mainly dominated by the dark matter halo. The cD galaxy does not provide sufficient heating, via SNIa and stellar winds, and does not change the results of the cooling flow in a cluster environment. It is nevertheless important for the metal enrichment, tracer of the AGN outflows. Using the fit to the observed temperature profile (see Eq. 3.33), we recover the density radial profile $\rho(r)$, assuming a gas fraction of 0.15 at virial radius (Sec. 3.9; dotted lines in Figure 4.4). The initial conditions are not perturbed.

The computational rectangular box extends slightly beyond the cluster virial radius, $R_{\rm vir} \sim 2.6$ Mpc. We simulate only half cluster with symmetric boundary condition at $z = 0$, setting elsewhere outflow conditions with inflow prohibited. The maximum number of refinement levels is 9 (with basic blocks of $8 \times 8 \times 4$ points). The finest, inner grid has a resolution of ~ 2.7 kpc (see Section 3.3 for further details).

Table 4.1. Parameters and properties of the most relevant galaxy cluster simulations.

Model	Feedback	Efficiency ϵ	Jet width × height (kpc)	Injection	Notes
cl-CF	no AGN heating	-	-	-	-
cl-C5m4	cold	5×10^{-4}	2.7×6.8	entrainment	self-regulated
cl-C1m3	cold	10^{-3}	2.7×6.8	entrainment	self-regulated
cl-C1m3L	cold	10^{-3}	2.7×17	entrainment	self-regulated
cl-C5m3	cold	5×10^{-3}	2.7×6.8	entrainment	self-regulated
cl-C5m3L	cold	5×10^{-3}	2.7×17	entrainment	self-regulated
cl-C5m3S	cold	5×10^{-3}	2.7×0	nozzle	self-regulated
cl-C1m2	cold	10^{-2}	2.7×6.8	entrainment	self-regulated
cl-C1m2L	cold	10^{-2}	2.7×17	entrainment	self-regulated
cl-C5m2	cold	5×10^{-2}	2.7×6.8	entrainment	self-regulated
cl-I20	intermittent	-	2.7×6.8	10^4 km s^{-1}	cycle 20/200 Myr
cl-I10	intermittent	-	2.7×6.8	10^4 km s^{-1}	cycle 10/100 Myr
cl-I01	intermittent	-	2.7×6.8	10^4 km s^{-1}	cycle 1/10 Myr
cl-v2e3	continuous	-	2.7×6.8	2×10^3 km s^{-1}	continuous
cl-v6e3	continuous	-	2.7×6.8	6×10^3 km s^{-1}	continuous
cl-v1e4	continuous	-	2.7×6.8	10^4 km s^{-1}	continuous
cl-B1m1S	Bondi	10^{-1}	2.7×0	nozzle	self-regulated

Radiative cooling ($Z = 0.3\ Z_\odot$): Runge-Kutta (2nd), plus cold mass dropout ($T \lesssim 5 \times 10^5$ K; $r_0 \sim 10$ kpc).

Supernovae Ia & stellar winds: cD galaxy ($M_* \approx 6 \times 10^{11}\ M_\odot$; $r_e \approx 8.5$ kpc).

4.3 Results

I start describing the results for various flows, exploring a large set of feedback parameters. The suite of simulations described here is used to thoroughly explore the outflows parameter space in order to bound the region of successful models.

4.3.1 Pure Cooling Flow [cl-CF]

As a reference flow, I first calculated a pure cooling flow (cl-CF), with no AGN feedback, shown in Figure 4.4. As expected, both density and (mass-weighted) temperature profiles steepen in the central region, an effect caused by radiative losses and the consequent subsonic gas inflow. In ~ 1 Gyr the calculated profiles disagree with the observations of A1795, although not by a great extent. It is interesting, however, that the logarithmic slope in the core region of the model temperature profiles at late times is very close to 0.4, which Sanderson et al. (2006) found to be typical in the central region of cool-core clusters. The (partial) similarity between the temperature distribution in the cooling flow run and real clusters, where heating is currently preventing gas cooling, put severe constraints on the feedback process: it should not greatly perturb the T profile shaped by radiative cooling. This is a demanding requirement (Brighenti & Mathews 2002b, 2003).

After few Gyr, the flow reaches an approximate steady state. The bolometric X-ray luminosity slowly increases with time, from $L_x \sim 1.5 \times 10^{45}$ erg s^{-1} at $t = 0$, up to $\sim 2.3 \times 10^{45}$ erg s^{-1} at $t = 7$ Gyr. The growth of the gas density in the cluster core is responsible for the increase of L_x.

It is interesting to investigate the global energetic budget. The internal energy within $R_{\rm vir}$ decreases by $\sim 5 \times 10^{61}$ erg (that is, of about 1%), while the potential energy drops by $\sim 4 \times 10^{62}$ erg, considering both the hot gas remaining in the grid and the cooled gas at the centre of the cluster. The kinetic energy is $\sim 2 \times 10^{58}$ erg and is therefore negligible. Thus, energy is radiated away ($E_{\rm rad} \sim 4.5 \times 10^{62}$ erg in 7 Gyr) mainly at the expense of the potential energy.

The gas cools in the very centre and is removed from the computational grid by the dropout term. The cooling rate increases with time, reaching ~ 250 M$_\odot$ yr^{-1} at the end of the calculation, a blatant discrepancy with observations (Tamura et al. 2001; Ettori et al. 2002). This is the main cooling flow problem (Chapter 1), the focus of this work.

4.3.2 Cold Feedback: $\epsilon = 5 \times 10^{-4}$ [cl-C5m4]

I start now illustrating the results for the outflow feedback models, where the mechanical energy of the jet is linked to the cooled gas mass (within $r \sim 10$ kpc). In Figure 4.5, I show the relevant properties for the model named[6] cl-C5m4, with mechanical efficiency $\epsilon = 5 \times 10^{-4}$. The width and length of the active region are 2.7 and 6.8 kpc, respectively.

The cooling rate, although reduced with respect to the cooling flow model cl-CF, is still too high ($\dot{M}_{\rm cool} \sim 75$ M$_\odot$ yr^{-1} at the end of the simulation, 7 Gyr). The mass-weighted

[6]The codename of each run follows in general this logic: system-feedback-parameter.

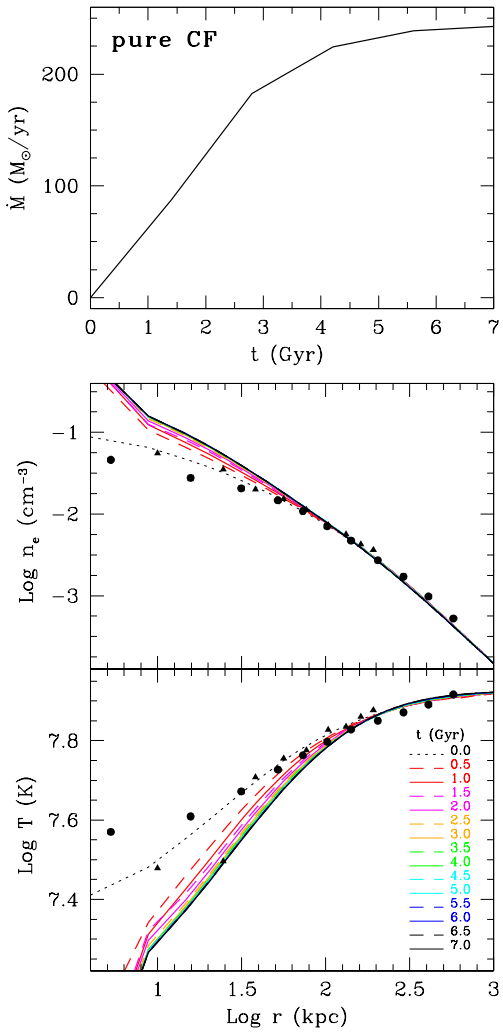

Figure 4.4. Evolution of the cooling flow model (cl-CF; no AGN feedback). Top panel: gas cooling rate versus time. Middle and bottom panels: temporal evolution of the gas (electron) number density and mass-weighted temperature profiles. The profiles are displayed at 15 different times, as indicated in the lowermost panel. Observational data of A1795 is shown with filled circles (Tamura et al. 2001, *XMM-Newton*) and filled triangles (Ettori et al. 2002, *Chandra*).

temperature and density profiles (in spherical shells) are similar to those of model cl-CF, with only a little temporal variation; the weak outflows perturb only slightly the T profiles.

In the right column of Figure 4.5 are shown the physical characteristics of all jet events; the quantities refer to the half-space $z \geq 0$ considered in our simulations. In this model, the outflows are activated frequently, because their relatively low mechanical power can not prevent the cooling for a long time.

In the top panel of the right column is plotted the cumulative (mechanical) energy injected by the jets. At $t = 7$ Gyr, $E_{\rm jet} \sim 1.5 \times 10^{62}$ erg has been injected in the ICM. Jets become more frequent at late times, because of the slow secular decrease of the central cooling time, a result of the slight predominance of radiative losses over heating. At the end of the simulation, more than 2×10^{11} $M_\odot$ have cooled and dropped out of the hot phase. Clearly, if all the cooled gas were accreted on the central black hole, as we have assumed in our simple feedback scheme, the final black hole mass would result far in

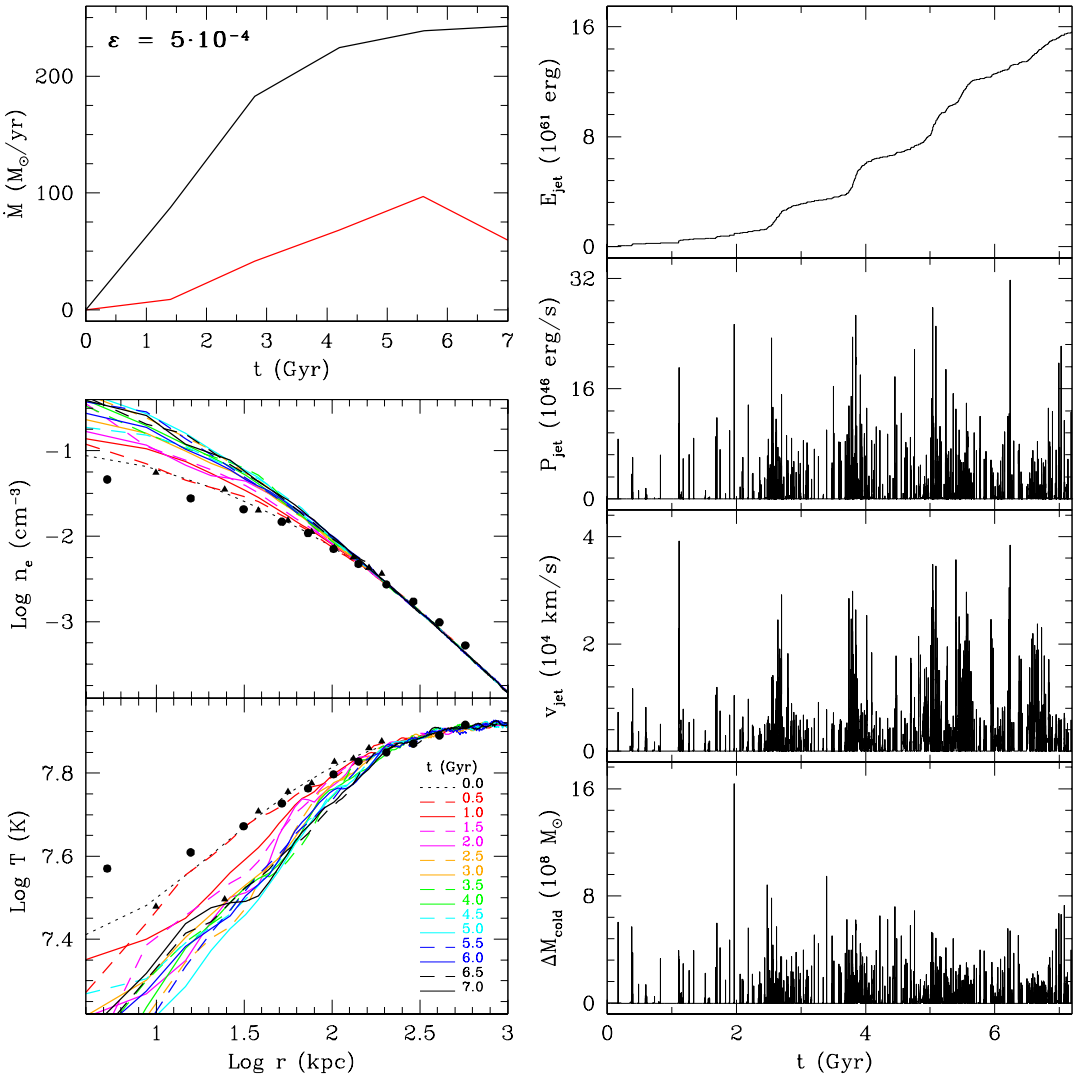

Figure 4.5. Evolution of AGN feedback model cl-C5m4 ($\epsilon = 5 \times 10^{-4}$). The plots in the left column are analogous to those in Figure 4.4. In the right column are shown the temporal evolution of the total kinetic energy injected by the outflows, the instantaneous outflow power and velocity, and the mass cooled in a single time step. These quantities are calculated for the half-space $z \geq 0$.

excess to that of real black holes. We could formally avoid the problem of the excessive black hole mass by assuming that only a fraction of the cooled gas actually accretes on it with a higher heating efficiency. For instance, this model would be identical if we assume that only 1% of the cooled gas is accreted by the central black hole and the efficiency is increased to 5×10^{-2}. This degeneracy means that the present model is too simple to allow a proper investigation of the black hole growth.

In the remaining panels are displayed the power, velocity and mass cooled (within 10 kpc) during each jet event. Typically, the gas is ejected with $v_{\rm jet} \approx 10^4$ km s^{-1} and power $P_{\rm jet} = 0.5\, M_{\rm act} v_{\rm jet}^2 / \Delta t \approx 10^{46} - 10^{47}$ erg s^{-1}. The quantity $\Delta M_{\rm cool}$, shown in the bottom right panel (Fig. 4.5), represents the mass cooled within 10 kpc during a given time step, and it has typical values few 10^8 M$_\odot$. We note that the Eddington luminosity, $L_{\rm Edd} \approx 1.5 \times 10^{38} (M_{\rm BH}/M_\odot) \approx 1.5 \times 10^{47}$ erg s^{-1} for a 10^9 M$_\odot$ black hole, is close to the mechanical power of a typical outflow.

In summary, model cl-C5m4 ($\epsilon = 5\times10^{-4}$) resembles a pure cooling flow model, with a cooling rate still too large and must therefore be rejected. The next logical step is to increase the mechanical efficiency ϵ, in order to reduce the mass of the cooled gas and check if more powerful outflows perturb the variable profiles in an acceptable way.

4.3.3 Cold Feedback: $\epsilon = 10^{-3}$ [cl-C1m3]

Model cl-C1m3, with $\epsilon = 10^{-3}$, is not shown here and the results are just briefly described. This run shows good temperature profiles, moderately peaked density, and a cooling rate of ~ 30 $M_\odot$ yr^{-1} at $t = 7$ Gyr, marginally acceptable. The cooling rate for $t \lesssim 2$ Gyr, however, is < 10 $M_\odot$ yr^{-1}. Evidently, a low efficiency feedback is able to suffocate the cooling flow for several Gyr. Only at late times ($t \gtrsim 6$ Gyr) the cooling rate becomes too high. This result emphasises the importance of calculating a model for many Gyr to check the long-term thermal evolution. With respect to model cl-C5m4, the jet events are more separated in time, especially at early times, consistently with the low cooling rate at that epoch. The total amount of the energy transferred to the ICM is similar to that for model cl-C5m4, being the whole feedback process self-regulated.

4.3.4 Cold Feedback: $\epsilon = 5\times10^{-3}$ [cl-C5m3]

Increasing the efficiency to $\epsilon = 5\times10^{-3}$ generates a successful model (cl-C5m3), which I discuss in more length (see also Section 4.4 for the detailed analysis of the flow dynamics). The cooling rate (Fig. 4.6) is very low at any time, $\dot{M}_{\rm cool} \sim 5$ $M_\odot$ yr^{-1}, a value fully compatible with the current observations ($\dot{M}_{\rm cool} \lesssim 30$ $M_\odot$ yr^{-1}; Peterson et al. 2003; Bregman et al. 2006).

The density and temperature radial profiles for $t \geq 1-2$ Gyr are always in good agreement with those observed in A1795. Both the ICM density and temperature vary with time, following the outflow cycles as expected, but the cluster always conserves the status of 'cool-core cluster', even though gas is essentially not cooling. The shock waves generated by the outflows (Sec. 4.4) are not strong enough to significantly heat the gas and perturb the global T positive gradient, although small amplitude ripples are seen in the profile, corresponding to weak shocks associated with the jet propagation. These waves are visible up to a distance of ~ 400 kpc.

In this model the AGN feedback is triggered less frequently, and only about 50 jet events occur. The duty cycle is $\sim 6\%$ (of total time). The total energy injected, $\sim 1.25\times10^{62}$ erg is again of the same order as in the previous simulations, and the average outflow power and velocity are thus larger. This energy must be compared with the total energy radiated away, $\sim 1.1\times10^{62}$ erg (again calculated in the half-space). Not surprisingly, the two energies are on the same order. In fact, if the gas density distribution is similar to that of the standard cooling flow model, then the energy radiated away is also similar. Thus, the energetic balance to stop cooling requires that the AGN provides an energy $\sim 10^{62}$ erg. In the strong events the power of the outflows often exceeds the Eddington luminosity. While the latter is not strictly relevant in this context, the large power might indicate that we are overestimating accretion, due to limited resolution.

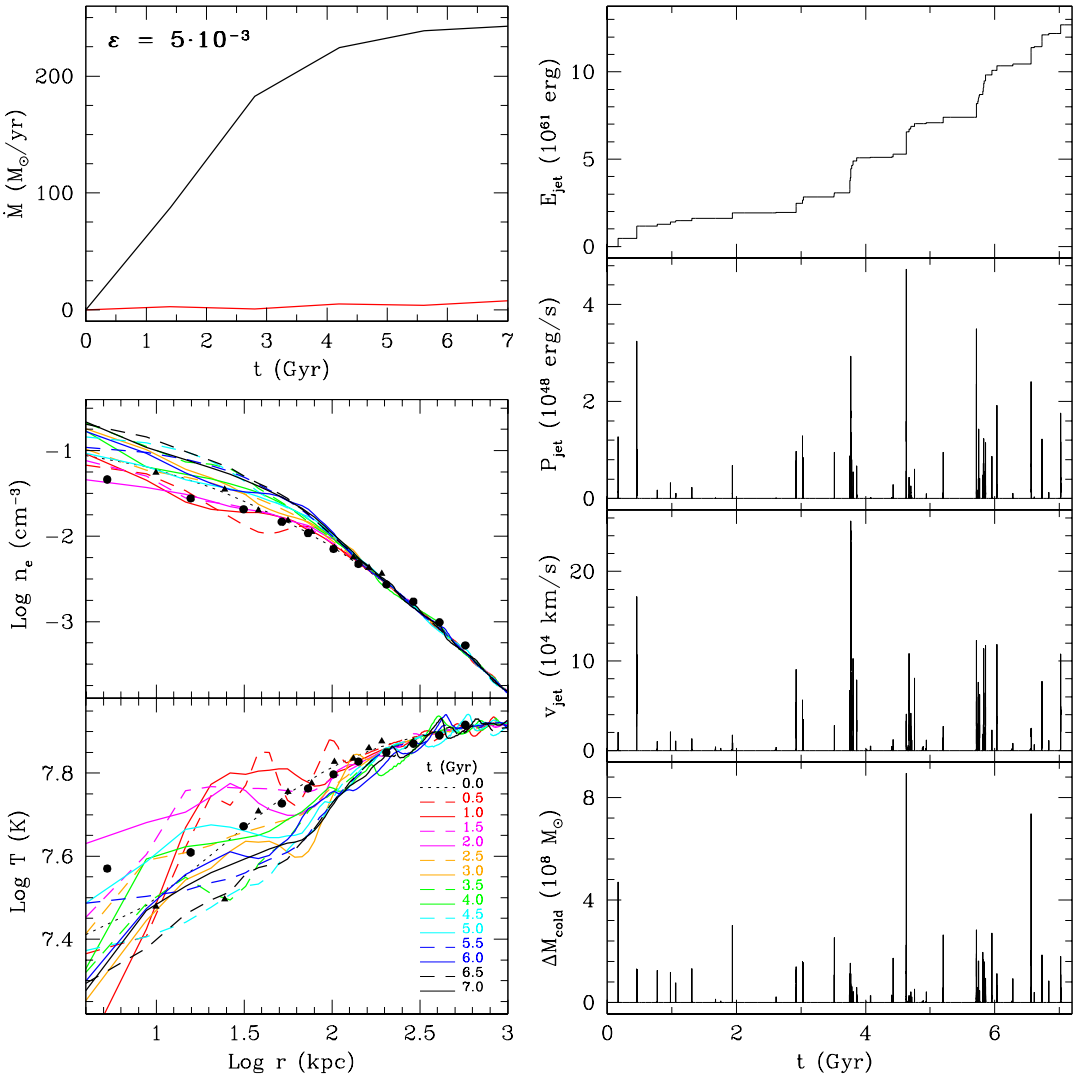

Figure 4.6. Evolution of model cl-C5m3 ($\epsilon = 5 \times 10^{-3}$). Plot description same as for Figure 4.5.

It is instructive to examine the evolution of the energetics in the cluster core region ($r \leq 50$ kpc), the most perturbed by the AGN feedback. After each AGN outburst, the core kinetic energy increases on average by $\approx 8 \times 10^{60}$ erg (with the most powerful outbursts depositing $\gtrsim 2 \times 10^{61}$ erg), which is comparable to the thermal energy content in the core region ($\sim 1.5 \times 10^{61}$ erg). However, the kinetic energy generated by an outflow is dissipated in only $\sim$ few $\times 10^7$ yr. Thus, most of the time the thermal energy dominates over the kinetic energy. Following the dissipation of the kinetic energy, the thermal energy also rises, because of shock heating. Finally, a large fraction of the thermal energy gained by the AGN outburst is transformed in potential energy, as a consequence of the quasi-adiabatic cooling due to the ICM expansion.

In order to understand the effect of the cD galaxy (gravity and heating), I have run model cl-C5m3 with and without its contribution. As expected, being the galactic gravity dominant only in the inner $\sim$ 20 kpc, the basic results (cooling rate, variable profiles and injected energy) are similar to Figure 4.6.

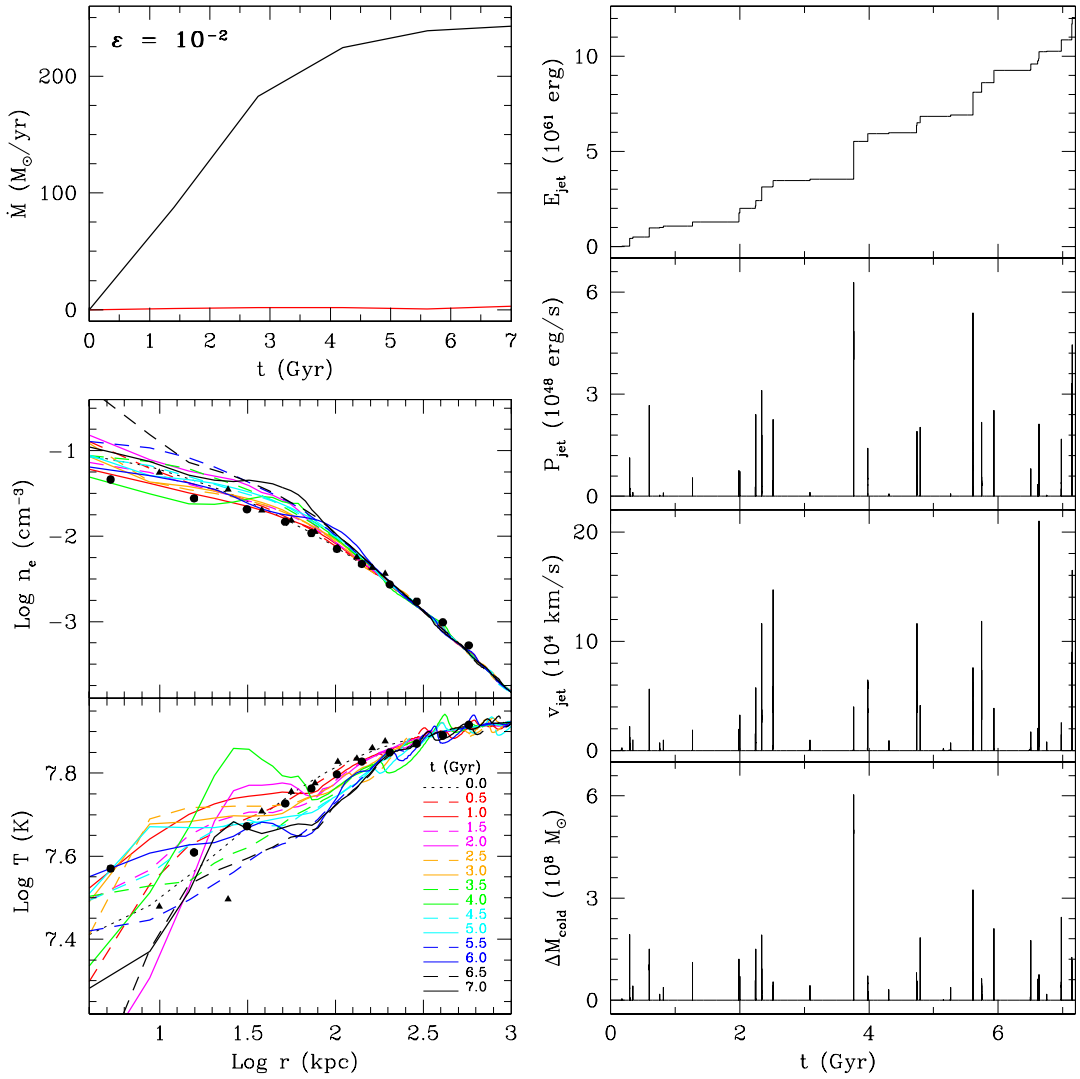

Figure 4.7. Evolution of model cl-C1m2 ($\epsilon = 10^{-2}$). Plot description same as for Figure 4.5.

4.3.5 Cold Feedback: $\epsilon = 10^{-2}$ [cl-C1m2]

When the efficiency is further increased ($\epsilon = 10^{-2}$, model cl-C1m2 in Figure 4.7), the overall results are very similar to those of cl-C5m3. Again, the jet heating generates fluctuations in the temperature which seem to exceed those observed now in A1795. The time-averaged profiles (not shown), however, agree very well with the observations. At almost any time this model would be classified as a cool-core cluster.

The number of jet activations during the 7 Gyr of evolution is further reduced, with only a few bursts occurring within the first several Gyr. The total energy generated by the feedback is $\sim 1.5 \times 10^{62}$ erg, again an acceptable value considering that the total 'available' BH energy is around 1.8×10^{62} erg ($E_{\rm BH} \sim 0.1\, M_{\rm BH}\, c^2$, with $M_{\rm BH} \sim 10^9$).

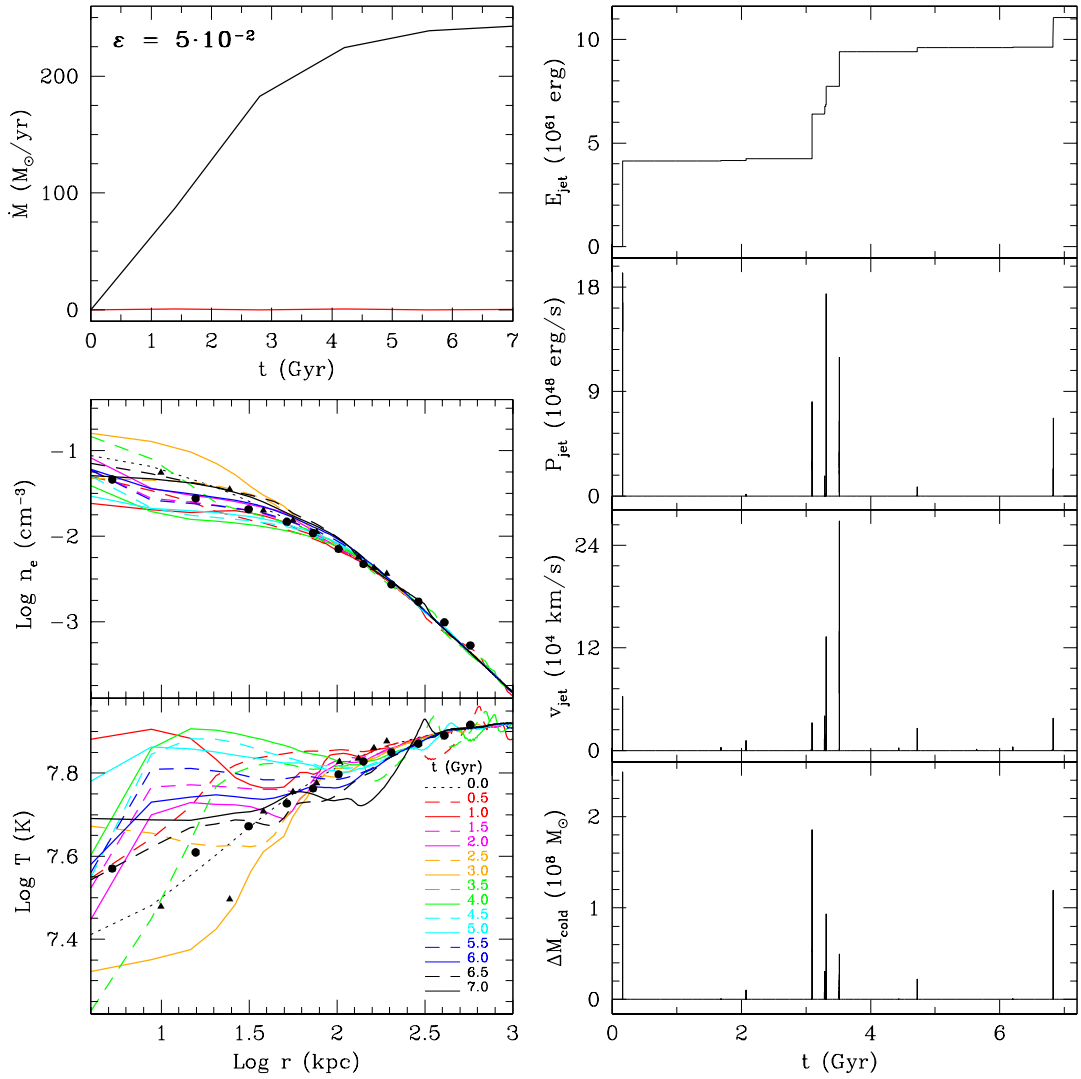

Figure 4.8. Evolution of model cl-C5m2 ($\epsilon = 5 \times 10^{-2}$). Plot description same as for Figure 4.5.

4.3.6 Cold Feedback: $\epsilon = 5 \times 10^{-2}$ [cl-C5m2]

The present model (cl-C5m2, $\epsilon = 5 \times 10^{-2}$; Fig. 4.8) clearly demonstrates the flaws of a too powerful feedback, albeit the total energy generated by the AGN is, once more, approximately the same as in all other models. The mere 11 AGN outbursts, occurring during the 7 Gyr evolution, are now very violent, with powers typically larger than 10^{49} erg s^{-1}, and velocities approaching the relativistic regime (right column in Fig. 4.8). As expected, the gas cooling is essentially zero, but the shock heating is too strong and the central temperature too high for most of the time (overheating). With such an efficient feedback, cool-core clusters would be a rarity, in contrast to the observational evidences.

4.3.7 Cold Feedback: $\epsilon = 10^{-1}$ [cl-C1m1]

A mechanical feedback with $\epsilon = 10^{-1}$ (an implausibly large efficiency, but cl-C1m1 has been calculated for pedagogical reasons) soon erases the initial cool core and the system would show a flat temperature profile thereafter (apart an intermittent mini cool core,

$\sim$ 10 kpc in size, associated with the central galaxy and expected also in non-cool-core clusters; Brighenti & Mathews 2002a; Sun et al. 2007; Sun 2009). In passing, I note that the ubiquitous presence of these galactic-scale cool cores poses very strict constraints on the nature of the AGN feedback, which can not deposit a large amount of energy in the region near the central black hole.

4.3.8 Summary of Cold Feedback

In Sections 4.3.2-4.3.7 I have illustrated the global features of the cold feedback models, in order to check whether and when non-relativistic outflows are a tenable mechanism for AGN feedback, able to shut off the gas cooling and at the same time preserving the cool-core appearance, i.e. $T(r)$ and $n(r)$. To summarise the main results, I find that the efficiency must be in the range $10^{-3} - 10^{-2}$ in order to generate successful models. Outflows must be relatively infrequent and powerful. The total energy necessary to considerably quench gas cooling for 7 Gyr of evolution is about 1.5×10^{62} erg, not surprisingly on the same order as the energy radiated away. However, the energetic balance *feedback energy* $\approx$ *energy radiated away* does not guarantee the success of a particular model (see models cl-C5m4 and cl-C5m2, for instance). Instead, it is crucial how this energy is communicated to the ICM, with the appropriate time-scales and power.

4.3.9 Intermittent or Continuous Feedback

I now illustrate the results when the jets are intermittently activated at predetermined times (cl-I...) or by assuming a continuous outflow (cl-v...).

In run cl-I20, outflows are generated every 200 Myr by setting $v_{\rm jet} = 10^4$ km s^{-1} inside the active region, for a time of 20 Myr each. The results are shown in Figure 4.9, rightmost column. The general features of this model are similar to those of run cl-C1m3. The cooling rate is very low for the first $\sim$ 3 Gyr and then increases slowly up to $\sim$ 80 $M_\odot$ yr^{-1} at $t = 7$ Gyr. The variable profiles remind those of a pure cooling flow calculation, especially at late times. This model is acceptable for the first few Gyr. However, the central gas density slowly grows with time until radiative cooling prevails over heating, causing the cooling rate to surpass the threshold of acceptability. The total energy injected by the outflows is $\gtrsim 2 \times 10^{63}$ erg, a much larger value than in successful simulations adopting the cold feedback, like cl-C5m3. This huge amount of energy can not come from a single black hole of typical mass $\approx 10^9$ $M_\odot$.

Some of the problems of model cl-I20 can be cured increasing the frequency of the jet events as shown in run cl-I10 (third column in Fig. 4.9). This model generates outflows every 100 Myr, each one lasting 10 Myr. Their velocity is the same as in run cl-I20. Although the gas cooling rate is much reduced up to $t = 5$ Gyr, it rapidly increases in the last 2 Gyr. The temperature and density profile gradients become too steep after $\sim 1 - 2$ Gyr, becoming very similar to those of model cl-CF. While these global properties would make this model acceptable, the required total energy is again $\sim 2 \times 10^{63}$ erg, a value difficult to justify.

A better model can be obtained increasing the frequency of the AGN feedback even

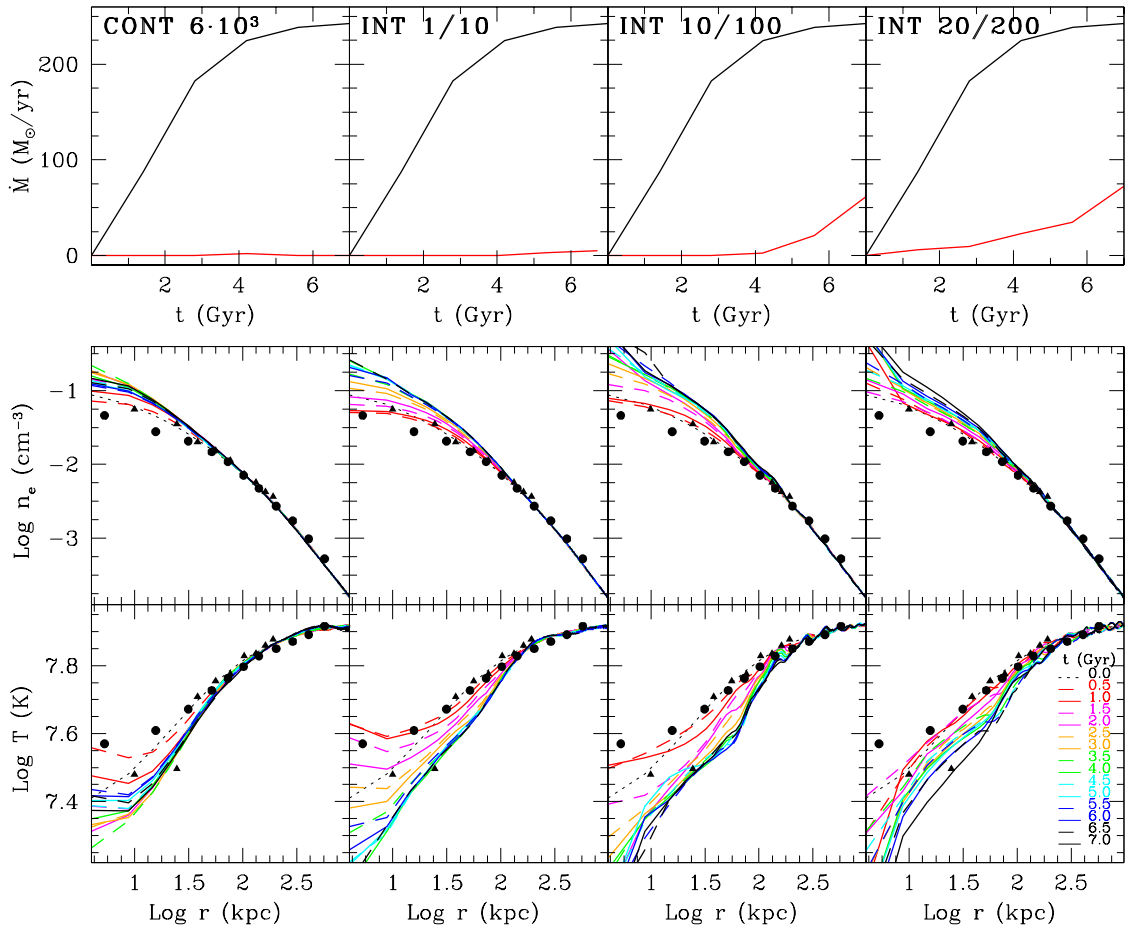

Figure 4.9. Evolution of continuous and intermittent models cl-v6e3, cl-I01, cl-I10 and cl-I20, from left to right. Plot description same as for Figure 4.4.

further. Model cl-I01, second column from the left in Figure 4.9, illustrates a run with outflows activated every 10 Myr (similar to the outbursts frequency estimated in the Perseus cluster; Fabian et al. 2006), each one persisting for just 1 Myr. As in models cl-I10 and cl-I20, the velocity is fixed to 10^4 km s^{-1}. Only a very small amount of gas cools, and the variable profiles resemble again those of a classic cooling flow. The total feedback energy, $\sim 1.6 \times 10^{63}$ erg, is still inconveniently large.

The first column of Figure 4.9 shows the outcome of a simulation in which the feedback is always active. Here the outflow velocity is set $v_{\rm jet} = 6000$ km s^{-1} (model cl-v6e3). This is clearly an extreme model, calculated mainly for pedagogical reasons. The ICM in the centre is continuously heated and transported to large radii, and almost no gas is able to cool. The central density rises secularly and it is possible that some cooling would occur, had we evolved the cluster for a longer time. The temperature profiles agree very well with the observations, with a flattening due to shock heating visible in the inner $\sim$ 10 kpc. Another unpleasant feature of model cl-v6e3, besides the excessive injected energy, is that the continuous outflow forms a very long tunnel in the ICM, where it propagates without inflating any cavity.

We have experimented the effect of varying the outflow velocity in continuous feedback simulations (not shown here). Increasing the outflow velocity to $v_{\rm jet}$ =

10^4 km s^{-1} (model cl-v1e4) leads to a negative temperature gradient in the inner $\sim$ 10 kpc, with $T(0) \sim 5 \times 10^7$ K, which may be in contrast with the observations of Sun (2009). Conversely, with a reduced jet velocity $v_{\rm jet} = 2 \times 10^3$ km s^{-1} (model cl-v2e3; not shown) the gas cooling can not be halted and the model resembles a pure cooling flow.

In summary, it is possible to find partially successful models using a continuous or intermittent feedback, but it is difficult to justify the large amount of outflow energy required or the extreme character of a continuous jet, when we clearly see the signature of intermittent/variable jets in the different generations of X-ray cavities (Fabian et al. 2000; McNamara & Nulsen 2007; Wise et al. 2007).

4.3.10 Role of the Jet Size

Finally, I address how the results depend on the size of the jet active region. I increased its length to $\sim$ 17 kpc (the width being the same as before, 2.7 kpc) and calculated several models varying the efficiency. I do not show figures for these runs, but only briefly discuss their essential properties. Overall, the results are very similar to those described in the previous Sections dedicated to cold feedback. When the efficiency is $\epsilon = 10^{-3}$ (cl-C1m3L), the cooling rate grows steadily with time, reaching $\dot{M}_{\rm cool} \sim 80$ $M_\odot$ yr^{-1} at $t = 7$ Gyr. The temperature and density profiles resemble those for run cl-C1m3 (shorter jet), although they are slightly smoother for $r \lesssim 20$ kpc, as expected, since the outflow shocks are generated at the tip of the source region ($z \sim 17$ kpc). The run with $\epsilon = 5 \times 10^{-3}$ (cl-C5m3L) has excellent attributes, with very low $\dot{M}_{\rm cool} \lesssim 10$ $M_\odot$ yr^{-1} at any time, and smooth profiles in very good agreement with those observed for A1795. Finally, we find that high efficiency $\epsilon = 10^{-2}$ still generates an excellent model (cl-C1m2L), with very little cooling and very consistent density and temperature profiles, where a small temperature bump at $r \sim 30$ kpc, due to the jet shock, is sometimes visible in the mass-weighted radial profile.

At the other extreme, we run a model (cl-C5m3S) in which the jets are generated by imposing a mass, momentum and kinetic energy flux through a small nozzle (2.7×2.7 kpc^2) at the centre of the boundary plane $z = 0$. This scheme, does not directly change the ICM velocity, but the hot gas is pushed from below by the outflow, which enters the grid at $z = 0$ (see Sec. 3.6). With efficiency $\epsilon = 5 \times 10^{-3}$, the same as model cl-C5m3, we find that the cooling rate is again acceptable ($\dot{M}_{\rm cool} \lesssim 10$ $M_\odot$ yr^{-1}), with a moderate increase near the end of the evolution. The temperature profiles often show a positive central gradient in agreement with the observations of A1795, although sometimes with a sharper central temperature peak in the inner $\sim$ 10 kpc. Given the similar results to cl-C5m3, we did not pursue the search of the best model using this outflow generation method, by fine tuning the efficiency or other parameters.

We conclude that moderately varying the size of the source region or the method of injection does not drastically alter the previous results (Sections 4.3.2-4.3.7), in particular when the feedback is driven by cold gas accretion.

4.3.11 Bondi Feedback: $\epsilon = 10^{-1}$ [cl-B1m1S]

Given the uncertainties in the real accretion mechanism, it is worth to investigate a more gentle feedback. As previously discussed, the cold feedback mechanism in galaxy clusters tends to show a rather explosive behaviour, with super-Eddington peaks, perhaps due to the excessive accretion rates. For instance, in model cl-C1m2 the most powerful jets imply accretion rates of ten times or more the Eddington rate $\dot{M}_{\rm Edd} \sim 60$ M$_\odot$ yr^{-1} (assuming $M_{\rm BH} \approx 3\times10^9\ M_\odot$). The outbursts with super-Eddington values may not be very common for AGN (see the theoretical arguments of King 2009) and yet, according to the results based on cold feedback, we *need* fast and energetic outflows, which imply accretion of large gas masses, to shut down the gas cooling.

Therefore, at this point it is worth trying a different approach to mitigate this too explosive behaviour. The Bondi accretion theory (Bondi 1952), although highly idealised with respect to the complexity expected in real accretion systems (thin or thick discs, ADAF, etc.), has been widely used to estimate accretion rates onto SMBH. However, in presence of a standard cooling flow the 'unperturbed' gas is not at rest as in Bondi theory. The accretion rate on the central black hole should then be determined by the ICM inflow rate and should be proportional to the cooling rate, which in turn is determined by the global physical conditions of the ISM/ICM. Thus, the Bondi rate should not be particularly relevant if the gas cooling rate is large.

Despite this theoretical considerations, our resolution is still very far from capturing the real central accretion engine (few tens of Schwarzschild radius) and we have to base the triggering mechanism on mean large-scale values. In this sense, it is interesting to calculate a model in which the AGN feedback is linked to the accretion rate estimated via the Bondi's formula: $\dot{M}_{\rm B} = 4\pi\,(G M_{\rm BH})^2\,\rho_0/c^3_{\rm s,0}$ (Sec. 3.7). Note that the accretion increases when temperature drops and density grows, or better when the entropy ($\propto T/\rho^{2/3}$) is falling off. Therefore, also Bondi models are sensitive to gas cooling, but in a more gentle and moderate manner. If such a small accretion rate is sufficient to halt the cooling, then this model is self-consistent.

In a sample of nine X-ray bright elliptical galaxies Allen et al. (2006) estimated typical Bondi accretion rates $\dot{M}_{\rm B} \approx 0.01$ M$_\odot$ yr^{-1}. For galaxies at the centre of rich clusters the Bondi rates are not expected to greatly exceed these values. Therefore, the Bondi feedback model should operate in an opposite regime compared to the previous cold feedback models. In particular, we expect a quasi-continuous AGN activity of moderate intensity.

There is no clear way how to choose the averaging region in order to calculate the Bondi boundary conditions (ρ_0 and $c_{\rm s,0}$). From a numerical point view, it seems better to take the average over several cells, at the same time avoiding a too extended[7] region ($\gtrsim 10$ kpc), choosing therefore a radius of ~ 5 kpc.

The results for the Bondi model (cl-B1m1S) are shown in Figure 4.10. The T profiles and the cooling rate are consistent, the latter exceeding the observational limits only after ~ 6 Gyr. The density profile seems instead slightly too peaked, but only in the central 10 kpc. The activity of the AGN is continuous and moderately weak, with a quite steady jet

[7]This way the feedback loses the proper self-regulation and the runs show at some point the cooling catastrophe.

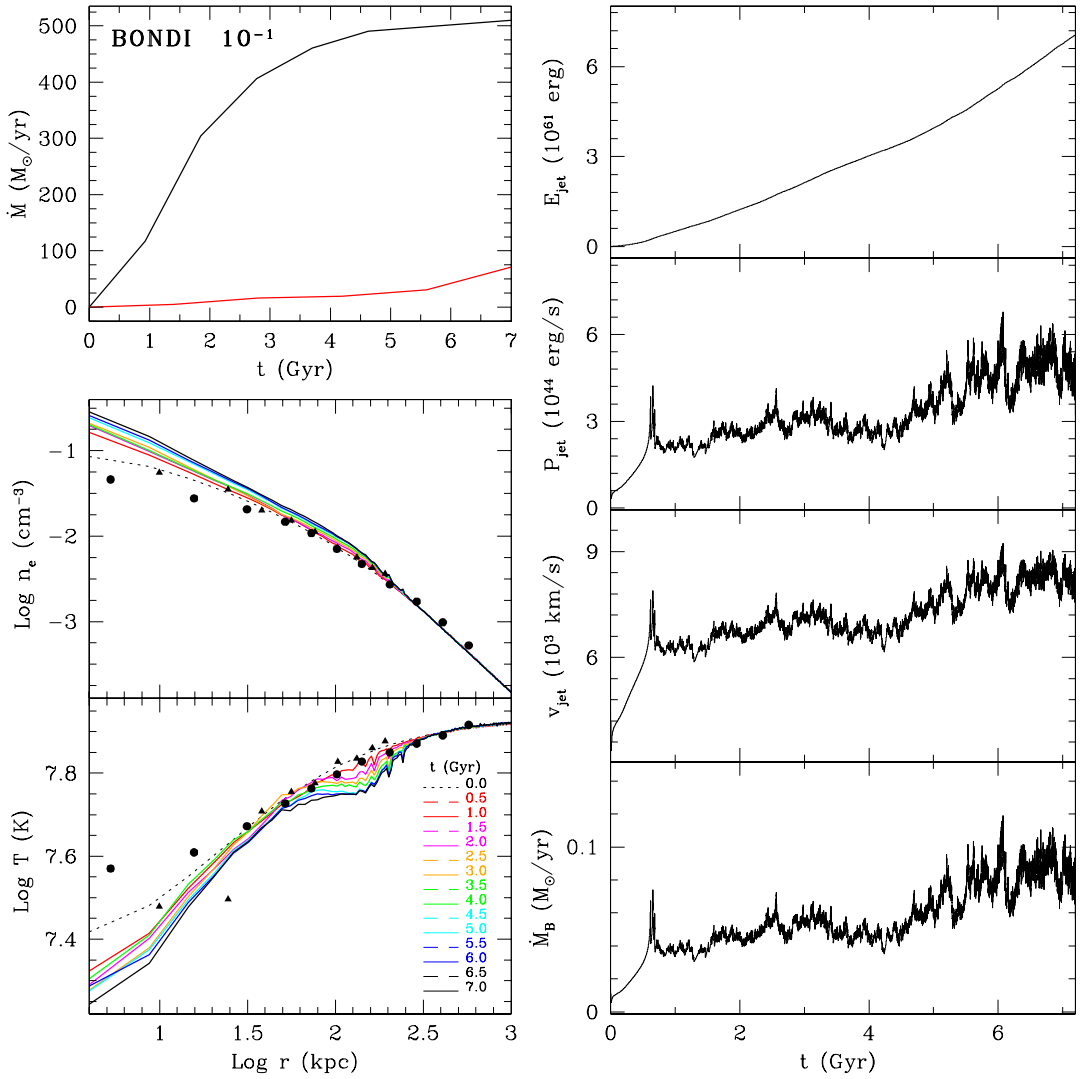

Figure 4.10. Evolution of the Bondi model ($\epsilon = 0.1$; cl-B1m1S), with the outflows injected from the grid boundary at $z = 0$. The panels description is the same as for Figure 4.5, except for bottom right panel showing the Bondi accretion rate.

power, in the range $2 - 3 \times 10^{44}$ erg s^{-1}. The total injected energy is $\sim 7 \times 10^{61}$ erg. In fact, the Bondi accretion rate does not vary much, $\dot{M}_{\rm B} \sim 4 - 8 \times 10^{-2}$ M$_\odot$ yr^{-1}, slightly larger than the estimates by Allen et al. (2006). It is important to note that the mechanical efficiency, producing this rather acceptable model, is very high $\epsilon = 0.1$, and thus difficult to justify. Typical values are in fact lower than 0.01 (Merloni & Heinz 2008; La Franca et al. 2010).

Another relevant riddle for Bondi models is the absence of frequent jet-inflated spherical cavities (similar to previous continuous models). The continuous AGN activity (with mean velocity $v_{\rm jet} \sim 7000$ km s^{-1}) carves a narrow tunnel of about 50 kpc in length, although its density contrast with the environment is large only for $z \lesssim 20$ kpc (and not particularly evident in the X-ray surface brightness maps).

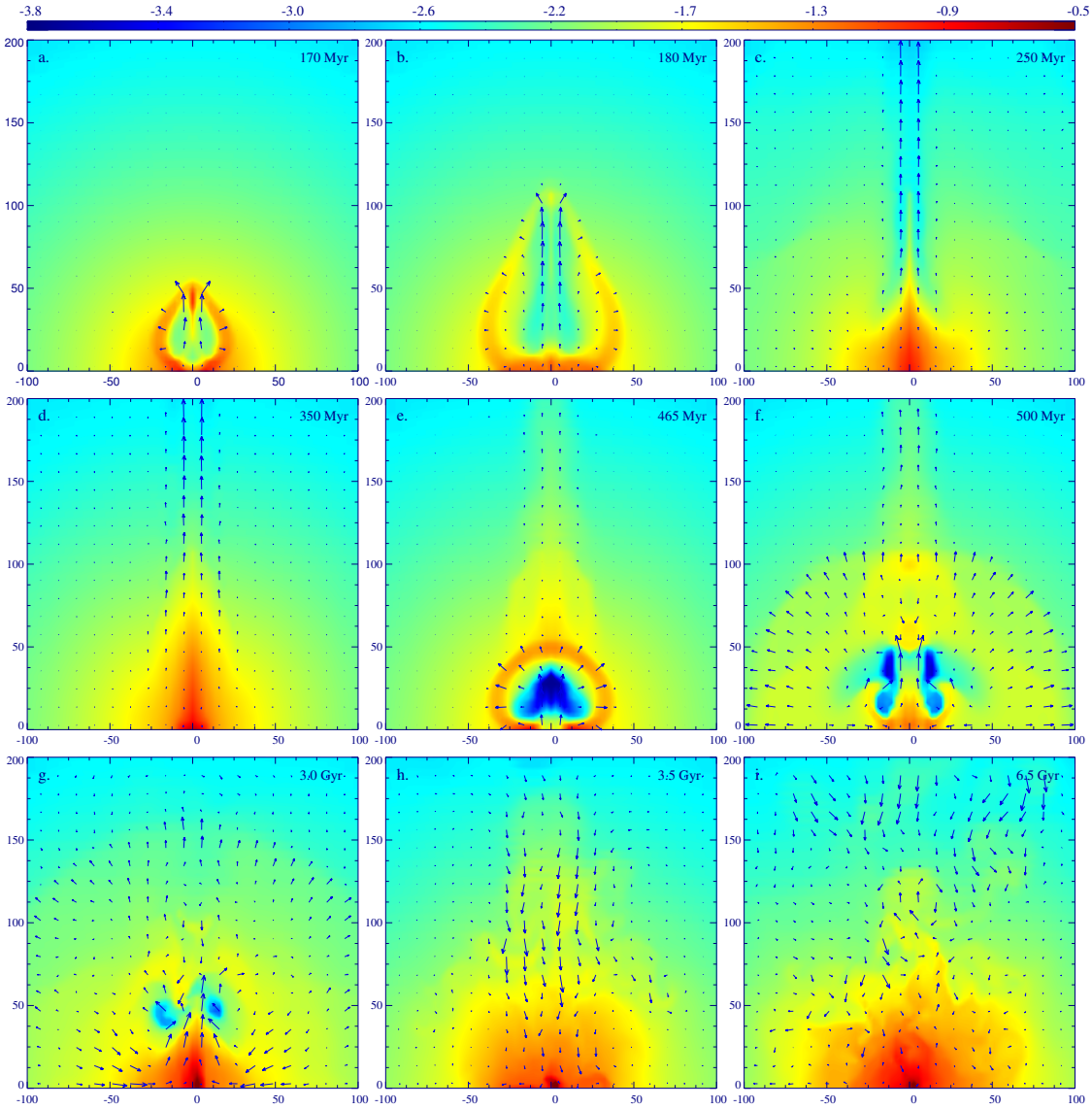

Figure 4.11. Best model cl-C5m3; logarithmic slices of electron number density (cm^{-3}) through the $x-z$ midplane (kpc unit), with the velocity field overlaid. The colour scale is given by the bar at the top, while arrows length normalisation varies. Times are indicated at every top right corner.

4.4 Dynamics of Best Model [cl-C5m3]

In this Section, I discuss the dynamical evolution of the outflows for one of the best models, cl-C5m3 ($\epsilon = 5 \times 10^{-3}$, cold feedback). Contrary to the almost steady, and not variegate, evolution of Bondi model, the density and temperature maps (through the $x-z$ midplane) show significant temporal variations. Note that in this Section we are analysing *physical* quantities, while the right comparison with observations should be done through *emission-weighted* ones. I expand on this in Section 4.5.

The first self-regulated outflow is triggered at $t \sim 160$ Myr (see Fig. 4.6), with a velocity $v_{\rm jet} \sim 2 \times 10^4$ km s^{-1}, mechanical power $P_{\rm jet} \sim 1.3 \times 10^{48}$ erg s^{-1} and total injected energy of $\sim 4.5 \times 10^{60}$ erg. The large jet power is due to our adopted feedback method, where outflows last only while gas is cooling to low temperatures. This implies

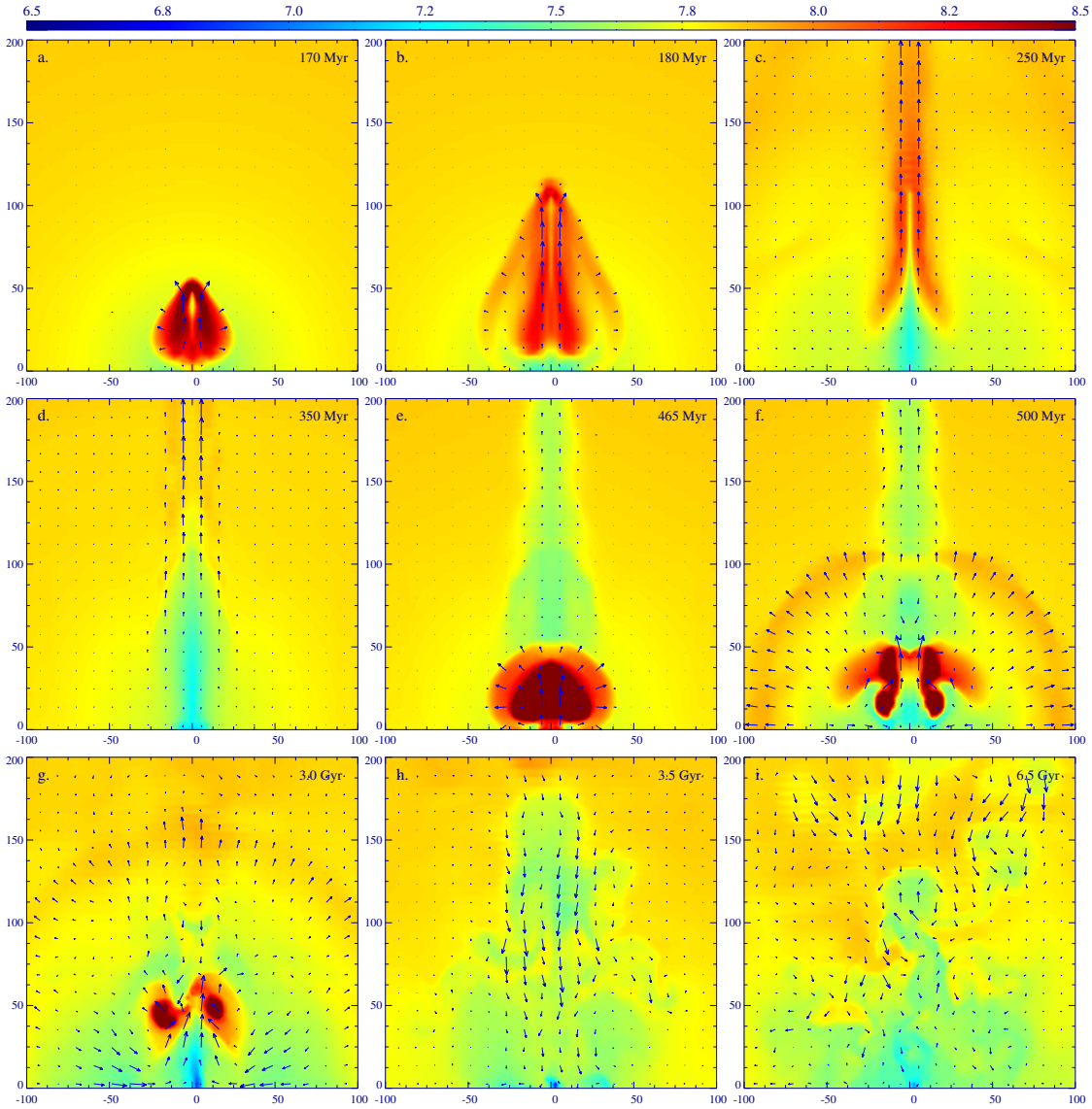

Figure 4.12. Best model cl-C5m3; logarithmic slices of the gas temperature (K) through the midplane. See Figure 4.11 for other details.

that the AGN is active only for few time steps (typically $\Delta t \approx 10^5 - 10^6$ yr), since the jet promptly stops the gas cooling in the central region. During a single time step large masses of gas can cool (also a result of the coarse resolution used), therefore the energy $\epsilon\, \Delta M_{\rm cool}\, c^2$, corresponding to the cooled gas mass $\Delta M_{\rm cool}$, results in a large, and perhaps exaggerated, instantaneous outflow power.

In Figures 4.11 and 4.12 are presented the density and temperature slices through the $x - z$ midplane for the first two AGN outbursts. At $t = 170$ Myr (panels a), after ~ 10 Myr since the jet started, an ellipsoidal cavity with major (minor) semiaxis of about 15 (10) kpc has been carved, surrounded by a shell of shocked gas, whose density is about twice the ambient density at nearby locations. The temperature of the shocked gas is $\sim 10^8$ K, about three times that of the unperturbed ICM. Therefore the young cavity, expanding approximately at the sound speed is surrounded by a weak, hot rim. The cavity

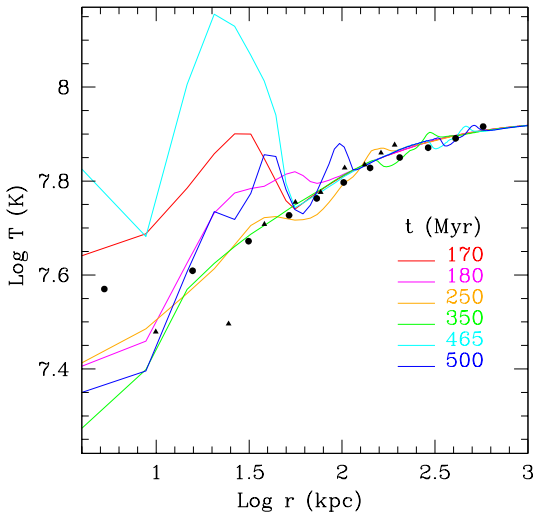

Figure 4.13. Best model cl-C5m3: mass-weighted temperature radial profiles for the six times shown in the upper two rows of Fig. 4.12.

has a relatively low[8] density contrast with the environment, $\sim 3-5$. Outside the cavity shock the ICM is still slowly flowing in, as a classical cooling flow. The mass-weighted temperature profile (Figure 4.13) shows a spike at $r \sim 30$ kpc, with a fractional increase $\sim 60\%$.

The cavity expands, increasing its ellipticity, and at $t \sim 180$ Myr (panels b) has approximately a cylindrical shape, extending up to $z \sim 100$ kpc, with a radius ~ 15 kpc. The bubble is filled with hot ($\gtrsim 2 \times 10^8$ K) gas raising along the z-axis at about its sound speed. The density contrast is again $3-4$. A very weak 'pear-shaped' shock surrounds the cavity. The density gradient along the post-shock region, with denser gas closer to the equatorial $x-y$ plane, makes the low$-z$ part of the shock detectable, while at large distance from the centre the low density contrast likely prevents the shock detection (see also the X-ray brightness map in Figure 4.14). The physical temperature jump across the shock for $z \lesssim 25$ kpc is only $\sim 25\%$ and increases slightly at large z. The structure qualitatively reminds the one observed in the elliptical galaxy NGC 4636 (Finoguenov & Jones 2001; Baldi et al. 2009). In the temperature radial profile (Fig. 4.13) the weak shock and heated gas are visible as a small bump $\sim 25\%$ in amplitude, located at $10 < r < 70$ kpc.

The cavity lengthens and narrows 20 Myr later, while the backflow generates a dense, relatively cold filament protruding in the cavity (e.g. Gardini 2007; Mathews & Brighenti 2008a). As for the previous times, in most of the cluster volume the ICM is inflowing as in a standard cooling flow, and the averaged profiles agree very well with those observed for A1795; after 40 Myr since the powerful AGN outburst, the cluster fully restored the 'cool-core' appearance it had at the beginning of the calculation. A very small amplitude ripple ($\Delta T/T \sim 10\%$) is visible in the temperature profile at ~ 100 kpc, as the integrated effect of the elongated weak shock.

At $t = 250$ Myr (panels c), the filament reaches $z = 100$ kpc, while the cylindrical

[8] We lack the effect of relativistic protons, whose pressure is likely to be relevant in expanding the cavity (Mathews & Brighenti 2008a,b; Ruszkowski et al. 2008; Guo & Mathews 2010).

(subsonic) outflows in the - now almost disappeared - cavity reaches $z \sim 250$ kpc. The temperature ripple moves forward at the sound speed and slowly weakens.

At $t \sim 350$ Myr (panels d), the cavity disappears while the dense, relatively cold filament formed by gas formerly at the centre and lifted at large z by the jet motion, is still clearly visible. The inner part of the filament, at $z \lesssim 40$ kpc, reverses its velocity and starts to fall back toward the centre. This is reminiscent of the kinematic of the emission-line filaments observed in the Perseus cluster (Hatch et al. 2006). The outer region around the $z-$axis is instead still slowly flowing out. This moment marks a new phase in the cluster lifecycle. The fallback of relatively dense gas preludes the next cooling/feedback event, which occurs at $t \sim 450$ Myr. The feedback cycle starts again in a qualitatively similar way.

At 465 Myr (panels e), a new cavity is formed, at first of approximately spherical shape centred at $z \sim 25$ kpc, radius ~ 20 kpc and high density contrast $(50 - 80)$. The almost spherical symmetry of the cavity is caused by the inflow along the jet axis, whose ram pressure slows down the expansion along that direction. The shock, already weak (Mach number ~ 1.5) is also nearly spherical, with radius ~ 35 kpc. Note that, at this time, the outflow has a mechanical energy of $\sim 8 \times 10^{60}$ erg, while the cavity has roughly $\sim 5 \times 10^{59}$ erg (with the usual $5/2\,PV$). Thus, most of the mechanical energy is not used to form the cavity.

Again the temperature profile shows the signature of the young AGN outburst with a strong peak for $r \lesssim 50$ kpc, approximately the location of the shock along the $z-$axis. A very weak ripple, vestige of the first jet event, is visible at $r \sim 400$ kpc.

At $t = 500$ Myr (panels f), the cavity shape is strongly affected by the backflow and the density contrast lowers. The weak shock ($M \sim 1$), slightly elongated in shape, is now located at a distance of ~ 100 kpc, much further away than the cavity. Within $r \sim 100$ kpc the cluster atmosphere is slowly moving outward (with velocity in the range $200 - 500$ km s^{-1}). Being the motion very subsonic the density profile changes very slowly. The outflow is decelerating and in ≈ 100 Myr reverses its direction approaching the dynamics of a classical cooling flow. Thus, the ICM in the cluster core undergoes cycles of slow contraction and expansion, following the rhythm of the AGN activity, in a global quasi thermal equilibrium.

The cylindrical outflow with average velocity $v_z \sim 300$ km s^{-1}, remnant of the previous AGN outburst, is still present, and extends beyond $z = 200$ kpc. At the same time the inflowing gas in the lower part of the filament is effectively preventing the cavity from expanding or raising buoyantly above $z \sim 50$ kpc.

Finally, in the bottom row of the map collection (panels g, h and i) are shown few snapshots at later times. As the cycle of feedback proceeds the flow develops a more turbulent character. In panels g are shown the maps at $t = 3$ Gyr. The cavity, generated at $t \sim 2.91$ Gyr, is distorted by the ascending backflow and by falling gas in the filament along the $z-$axis. As a result it acquires the shape of an asymmetrical torus. As in the previous aftermaths of the jet episodes, the ICM is flowing inward in most of the cluster volume, and is deviated outward along the $z-$direction when it reaches $r \sim 20$ kpc.

Panels h illustrates the cluster during a quiescent period ($t = 3.5$ Gyr), just before a

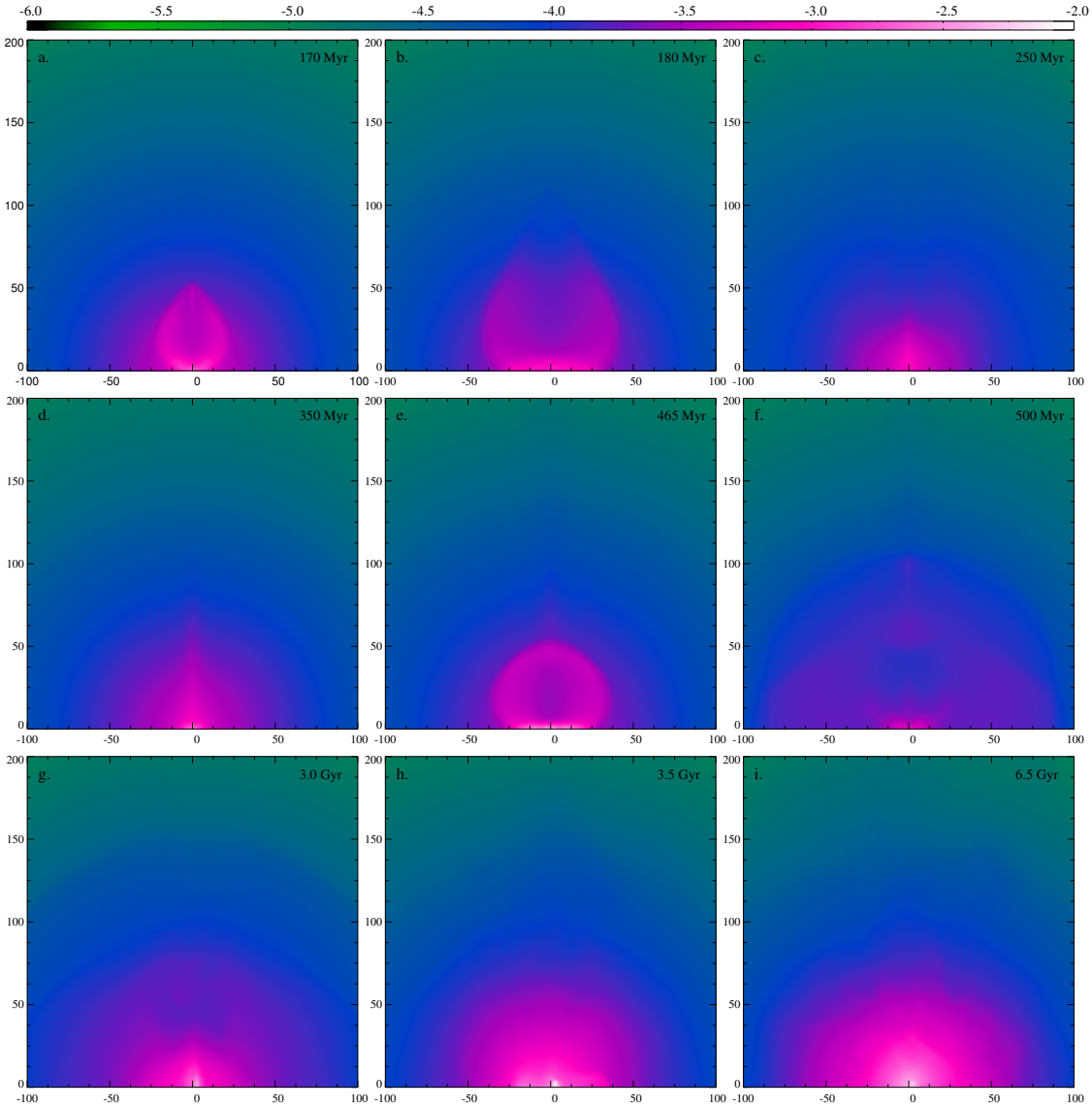

Figure 4.14. X-ray surface brightness maps for best model cl-C5m3 at various times. The x-axis is horizontal, while the z-axis is vertical (kpc units).

jet is triggered. The density distribution is very smooth and the cluster appearance is that of a standard cooling flow (see also the profiles in Fig. 4.6). A large, slightly overdense region around the $z-$axis is falling toward the centre with velocity varying between 50 and 500 km s^{-1}.

Finally, in panels i is shown the density distribution at t = 6.5 Gyr, again in an epoch long after an AGN outburst. The density is smooth in the core region, while showing some variation for $r \gtrsim 50$ kpc. On the contrary, the velocity field is chaotic and very subsonic; it promotes mixing of the metals produced by the SNIa exploding in the central galaxy (see Section 4.5.2). Few streams of moderately overdense gas are falling from large radii $r \gtrsim 100$ kpc with velocity ~ 300 km s^{-1}.

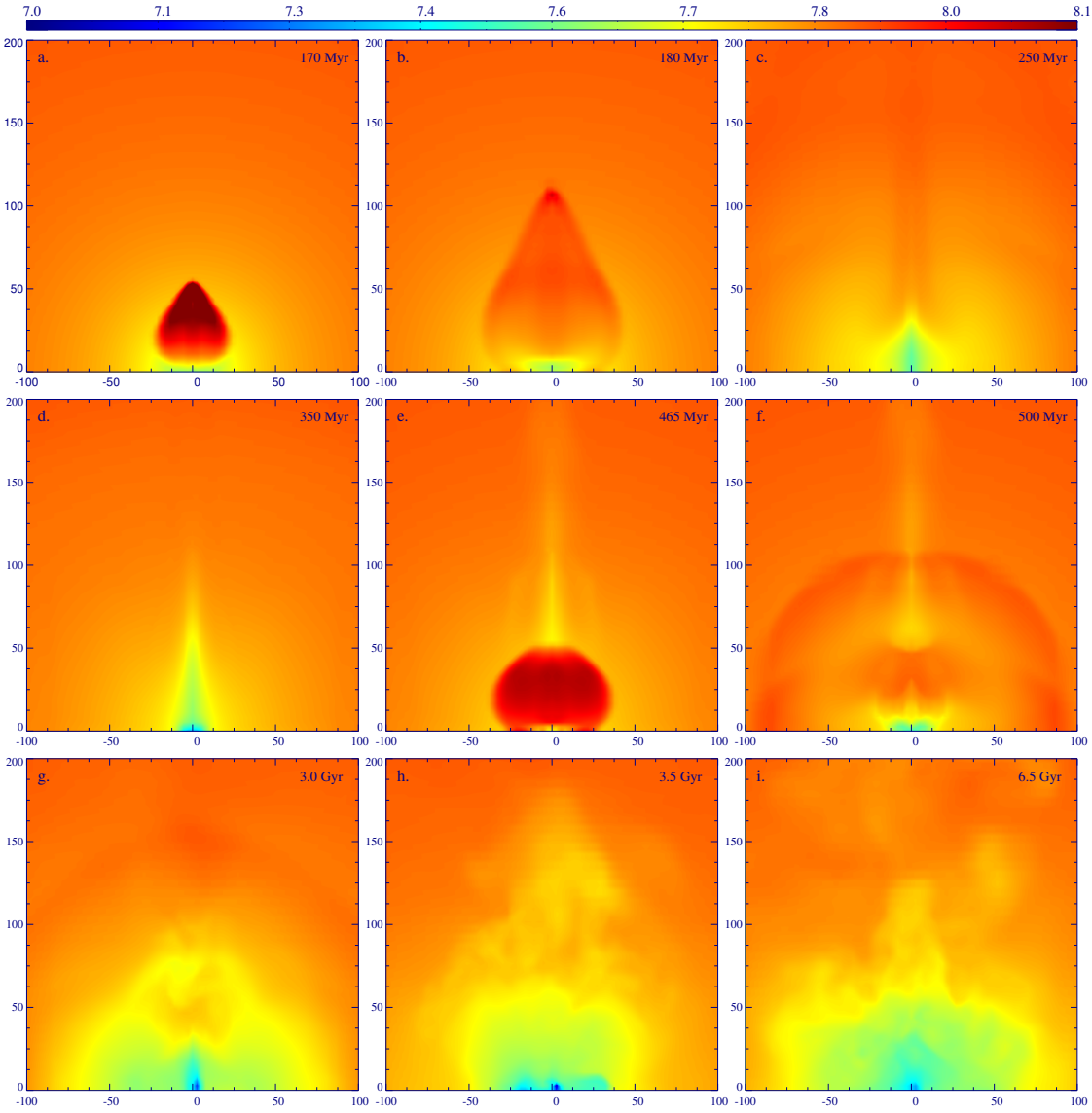

Figure 4.15. Emission-weighted temperature maps, projected along the y-direction, for model cl-C5m3 at various times (see also Figure 4.14).

4.5 X-ray Observables

The $x - z$ cuts through the centre of the cluster are very useful tools to investigate the intrinsic dynamical evolution of the flow variables, like density, temperature and velocity. However, in astrophysical studies we are commonly limited to observations based on the surface brightness (SB) in a certain spectral range (in our case mainly the X-ray band). In theory we should mock every aspect of the observation, from different atomic emissions to instrument response (e.g. Heinz et al. 2011). Due to our limited resolution, it is here sufficient to just integrate the emissivity or emission-weighted quantity along line of sight (y-direction) in an energy range of the X-ray band $\sim 0.5 - 10$ keV (similar to *Chandra*). I developed a parallel code that is able to interpolate every slice of the data cube (recall there are 9 different levels) and then perform the above-mentioned integration, in order to obtain more precise SB_x maps. With these maps we can test further the observability of our models and, in the lack of real ones, just make predictions that could be in the near

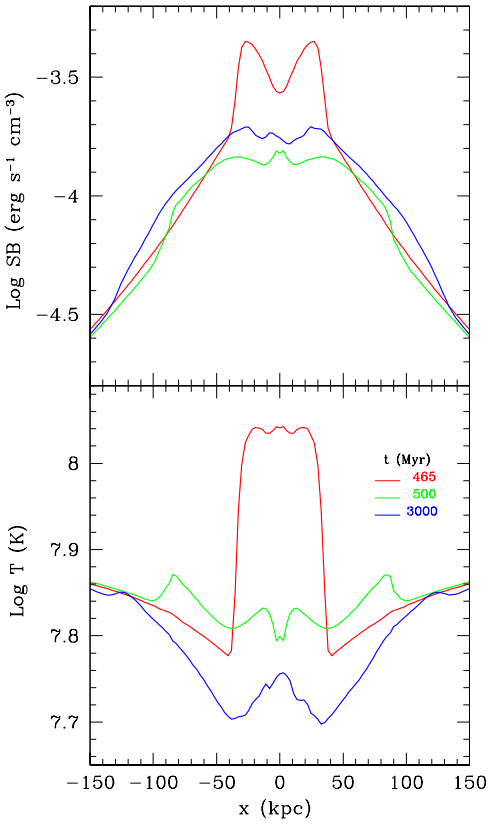

Figure 4.16. Best model cl-C5m3: X-ray surface brightness and emission-weighted temperature 1D cuts (of Figs. 4.14 and 4.15), through z = 25, 50, and 50 kpc, at 465, 500, and 3000 Myr, respectively.

future verified or falsified. We also test common assumptions regarding gas hydrostatic equilibrium, taken in many observational analysis, but that seem too restrictive.

4.5.1 Cavities and Shocks

We begin investigating the detectability of faint features, like X-ray cavities and shock waves, generated by the AGN outflows. In Figure 4.14, I show the X-ray surface brightness maps for run cl-C5m3, at the same times shown in Figures 4.11 and 4.12. The emission-weighted temperature map is displayed in Fig. 4.15. X-ray depressions are clearly seen at t = 180, 465, 500 and 3000 Myr. Evidently, subrelativistic, massive, collimated outflows can generate cavities with typical diameters of 15-40 kpc. The X-ray bubbles are often surrounded by bright rims of shocked gas. Relatively weak waves are present at large distance from old cavities, both features being generated by the same AGN outburst.

To better quantify the brightness perturbations produced by the outflows we show in Figure 4.16 the profiles along the $x-$direction at t = 465, 500 and 3000 Myr, taken at z = 25, 50, and 50 kpc, respectively. The sharp jumps at $x \sim \pm 30$ kpc (t = 465 Myr), where the cavity shock increases the brightness by a factor $\sim$ 2.5 would be manifestly visible in the X-ray image. The relative central depression (the cavity) is indeed brighter than the same region before the jet activity. The emission-weighted temperature map

reveals that the cavity region is markedly hotter (by $\sim 80\%$) than the nearby ICM, which is not commonly observed. This is a consequence of the most explosive outflow events.

The maps and profiles at $t = 500$ Myr show a weak cavity centred in $y \sim 30$ kpc, with radius ~ 20 kpc. This cavity is also slightly hotter than the surrounding gas. At this time the most interesting feature is the weak shock located at a radius ~ 100 kpc: the Mach number is ~ 1.1, in excellent agreement with observations of shocks driven by AGN (Blanton et al. 2009). The surface brightness profile shows a clear front at the shock position and the emission-weighted temperature jumps of $\sim 10\%$.

At $t = 3$ Gyr, another weak cavity, again ~ 20 kpc in radius, is present. The brightness depression is only ~ 10 % and the temperature is higher than that of the ambient by the same percentage.

To summarise, our best models presented in Section 4.3, with relatively powerful and infrequent outflows, are able to reproduce several features observed in AGN heated cores. In particular they usually inflate underdense buoyant bubbles, with the most powerful events tending to generate strong shocks that substantially heat the surrounding ICM (at least in the early stage of inflation).

4.5.2 Iron Enrichment and Mixing

It is expected that directional outflows would generate metal inhomogeneities through the ICM. Iron is the most relevant and easily measured element, being produced mostly by SNIa, which are still exploding in the giant elliptical at the centre of clusters. The same outflows, however, generate turbulence and bulk motions, which in turn tend to stir and mix the ICM, restoring homogeneity and erasing abundance gradients.

I present here a brief analysis of the emission-weighted iron abundance evolution for the best model cl-C5m3. We model only the Fe-enrichment produced by the SNIa (and stellar winds) occurring in the central galaxy, in the time interval $6.7-13.7$ Gyr (Sec. 3.8). Since we neglect the iron produced by the SNII and other cluster galaxies, we are not in the position to investigate the complete chemical evolution of the system. Instead, we are interested here in quantifying the abundance anisotropies caused by the AGN outbursts. The iron density is implemented in the code as a passive tracer of the flow (Equation 3.29).

In Figure 4.17 I present the $Z_{\rm Fe}$ maps at three different late times. Note that the background (black) is zero, but in reality should be around 0.3 $Z_\odot$; here we are just interested in the contrast. At 3 Gyr (first panel), the abundance is highly asymmetric. A powerful jet event has recently occurred (see Fig. 4.6), and therefore the metals created in the central elliptical galaxy (within few kpc) are transported out along the $z-$direction up to a distance of $150-200$ kpc. This is an unmistakable mark of the presence of a powerful AGN outflow. In fact, I suggest that iron abundance can be used as a reliable tracer for any AGN jet-outflow activity, instead of common entropy maps. At the centre, the abundance is about 0.4-0.6 $Z_\odot$, while further away along the jet axis the contrast is $\sim 0.1-0.2$. This kind of feature is supported by recent deep *Chandra* observations carried out by Kirkpatrick et al. (2009, 2011). They produced Fe-maps showing the enrichment

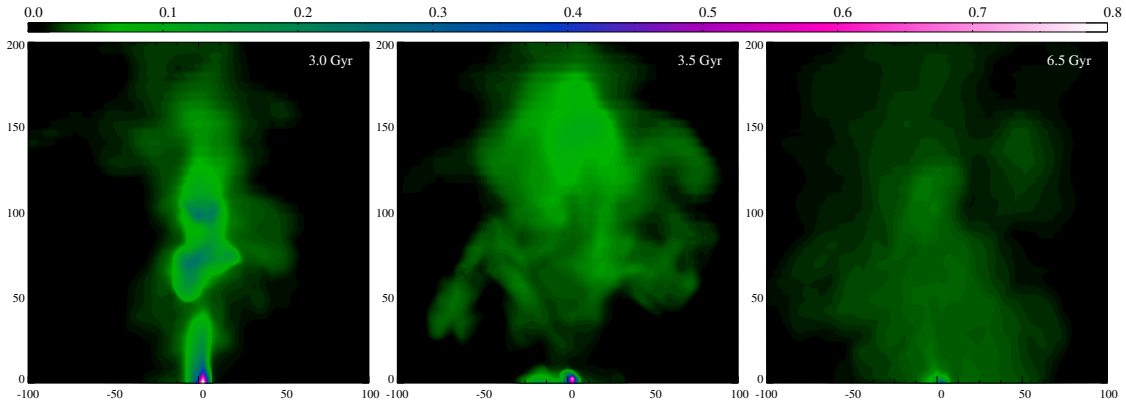

Figure 4.17. Emission-weighted iron abundance maps ($Z_\odot$ unit) for model cl-C5m3, at three different late times.

of gas along the jets of Hydra A, a quite massive galaxy cluster. It is striking that our simulated maps resemble those observations also in a quantitative way. Other authors (Rasmussen & Ponman 2009; O'Sullivan et al. 2011b) have found a similar behaviour in different systems dominated by AGN activity.

At 3.5 Gyr (second panel), we observe a period of relative quiescence and so the now dominating (AGN-induced) turbulence and vorticity promote the iron diffusion. At the centre, the new iron cloud associated with the cD galaxy is clearly detached from the older ejected material, the latter now covering a more uniform area. The iron diffusion is more evident at 6.5 Gyr (third panel), again in a moment of quiet, where the iron is very diffuse, with a low enhancement of $0.05 - 0.1\ Z_\odot$.

In the end, we can affirm that in a single cycle the iron abundance passes from a phase of high asymmetry along the jet axis, when the outflow has recently turned on, to a phase of turbulence and mixing, in which spherical symmetry is almost restored. The iron becomes spread within few 100 kpc, just as observed; without the influence of an AGN such material would be instead confined near the effective radius of the central galaxy.

4.5.3 Hydrostatic Equilibrium

In this Section, we investigate the effect of the perturbations generated by the AGN outflows on the mass determination using X-ray observations (through Equation 4.4). A standard method to estimate galaxy cluster mass profiles is to assume spherical symmetry and to calculate the gravitational mass using the hydrostatic equilibrium equation (e.g. Vikhlinin 2006; Buote et al. 2007 for two recent compilations). When the flow velocity is much lower than the sound speed, the hydrostatic assumption is fully justified.

It is well known that in real clusters turbulence or large scale motion can systematically bias the mass estimate by $\lesssim$ 20% (Rasia et al. 2006; Nagai et al. 2007; Mahdavi et al. 2008; Piffaretti & Valdarnini 2008). Therefore, it is interesting to investigate how much the flow perturbations generated by the AGN feedback affect the mass measure.

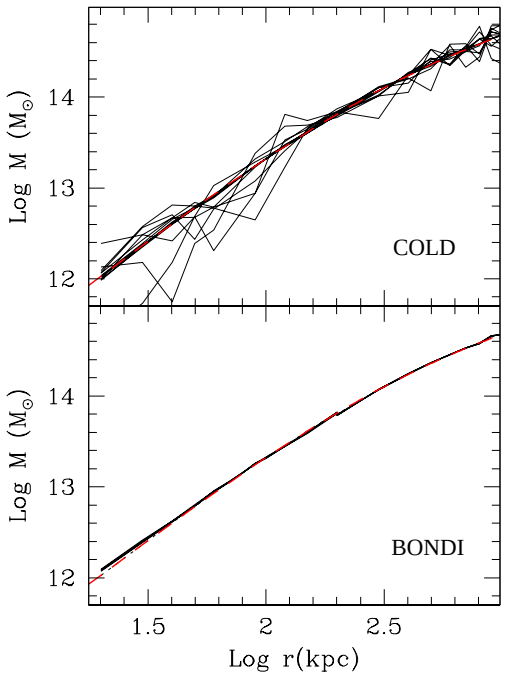

Figure 4.18. Mass profiles for model cl-C5m3 (top panel) and cl-B1m1S (bottom panel), calculated using the hydrostatic equilibrium equation at times separated by 0.5 Gyr (cl-C5m3) or 1 Gyr (cl-B1m1S), with the exact mass profile superposed (red-dashed line).

Here, I quantify the discrepancy between the estimated and real gravitational mass for a model adopting the cold feedback scheme and one assuming the more quiet Bondi-like feedback. I have calculated the averaged density and emission-weighted temperature profiles in shells of progressively increasing width, from 10 kpc in the centre up to 100 kpc at large radii. These profiles, inserted in the hydrostatic equilibrium equation give the estimated mass profile. This procedure is not perfectly accurate: we should have 'observed' our simulations with specific softwares like X-MAS (Gardini et al. 2004; Rasia et al. 2008) or XIM (Heinz et al. 2011) to properly compute the averaged profiles. However, it is not the purpose of this analysis to thoroughly investigate this topic and our approximation is sufficient to make our point.

The calculated mass profiles at various times, as well as the exact mass profile (red line), are shown in Figure 4.18 for model cl-C5m3 (top) and cl-B1m1S (bottom). In run cl-C5m3 the powerful outflows, although unable to significantly perturb the thermal state of the cluster (which always preserves the cool-core appearance), are effective in disturbing the quasi-hydrostatic equilibrium present in the pure cooling flow model. This results in a typical error in the mass determination of a factor 2-3. Most likely, the estimated mass is lower than the real mass, and the discrepancy is larger in the region $r \lesssim 100$ kpc, where the feedback affects the ICM the most.

In the Bondi model cl-B1m1S, instead, the outflows are 3-4 orders of magnitude less powerful and, despite the fact that they are continuously generated, they seem rather innocuous for the dynamical state of the ICM, and the hydrostatic equilibrium approximation is safe. The computed mass profile agrees very well with the real profile, with a slight discrepancy only visible for $r \lesssim 20$ kpc. Of course, the weak, continuous jets

present in this run are incapable to generate cavities, hence it is likely that real clusters undergo at least few stronger AGN outbursts, after which the dynamics of the ICM would be similar to that described for model cl-C5m3.

In summary, we expect that for clusters where X-ray cavities and/or shocks are present, the total mass estimated through the assumption of hydrostatic equilibrium might be in error by a factor of ~ 1.5, occasionally the error could be as large as a factor of 2-3. Conversely, with gentler continuous outflows generated by the accretion rate predicted by Bondi theory, the estimated and the real mass are in excellent agreement, with errors always below 8% (see also Guo & Mathews 2010).

4.6 Discussion

In the present Chapter, I have presented several moderate resolution simulations of the interaction between AGN outflows and the ICM in massive galaxy clusters. The purpose of these calculations was to investigate if a purely mechanical and anisotropic AGN feedback is able to solve the *cooling flow problem* (Chapter 1): the dearth of cooling gas in cool-core clusters with short central cooling times.

The necessity of covering a large range of spatial (kpc up to 5 Mpc) and temporal scales (fraction of Myr up to 7 Gyr), at the same time exploring the entire parameter space, limited the resolution of the very inner accretion region. Hence we are forced to link the feedback to some large-scale mean quantity, like $\Delta M_{\rm cool}$ or $\dot{M}_{\rm Bondi}$, which may lead sometimes to an overestimate of accretion and thus stronger instantaneous outbursts. Nevertheless, gas accretion onto the SMBH and the sub-pc origin of jets/outflows is still obscure, in particular the amount of entrained and shocked gas. In the end, our simplified scheme seems one of the few efficient ways to test AGN feedback on galaxy cluster scales.

4.6.1 Comparison with other Feedback Models

In the field of theoretical AGN feedback, most of the work done in the past (Brüggen & Kaiser 2002; Brighenti & Mathews 2003; Ruszkowski et al. 2004a; Dalla Vecchia et al. 2004; Brüggen et al. 2005; Sijacki et al. 2007; Brüggen & Scannapieco 2009; Mathews & Brighenti 2008a,b) has focused mainly on the creation of artificial off-centre bubbles. This scenario is valid only in the limit where the narrow and light relativistic (radio) jet does not entrain mass, thermalising the ICM only at the hotspot, with the subsequent inflation of a cavity (either due to thermal or cosmic ray pressure). However, as noted in Chapter 2, the ratio of the inferred (cavity) mechanical power to the jet radio power overcomes a value of 100-1000, suggesting that the process inducing the feedback *needs* to be massive, as assumed throughout this Thesis (see also Binney 2004; Soker & Pizzolato 2005 for related arguments).

Another difference with the present study is that we employ a momentum-driven heating, instead of a pressure-driven heating (pure thermal injection). As we have seen, purely kinetic feedback changes the whole dynamics. Loosely speaking, the healthy property of a jet feedback is that it can *gradually* thermalise the mechanical

energy along its path. Intermittent bubbles are naturally created, but this shocked and expanding gas is just one element of the heating process[9]: the bow shock, the cocoon with entrained gas, the mixing through turbulence and vorticity are all fundamental gears of the machine, everyone dominant at different phases of the evolution. Moreover, artificial (hydrodynamical) bubbles become rapidly unstable; on the contrary, a few studies (e.g. Sternberg et al. 2007) showed that jet-inflated bubbles should stay intact for over 40 Myr, thanks to the continuous vortex formed inside.

It is difficult to compare our work with other kinetic jet simulations (Reynolds et al. 2001, 2002; Ruszkowski et al. 2004a; Omma et al. 2004; Zanni et al. 2005; Brüggen et al. 2007; Sternberg et al. 2007), because most of them do not implement radiative cooling and an initial cool-core state. Additionally, these simulations last only for few 100 Myr and are not suited to study the cooling flow problem, without the long-term evolution.

Two interesting investigations, carried out in this direction, are those of Brighenti & Mathews 2006 and Cattaneo & Teyssier 2007. In the first one, as many previous studies, the jet velocity and power in the 2D computations were set by-hand following observational estimates. We have seen (Section 4.3.9), that in imposing such predetermined conditions, the mechanical feedback is not properly linked to the cooled mass or lower gas entropy (in quantity and time). The results are models with temperature and density profiles similar to a pure cooling flow or with high cooling rates.

In Cattaneo & Teyssier (2007), their hybrid thermal/kinetic injection is self-regulated by Bondi accretion (for 12 Gyr), but after a relatively weak outburst of $\sim 10^{45}$ erg s^{-1} the profiles do not present the cool-core appearance (flat temperature), although their considered cluster is ten times less massive. Also our successful Bondi model, with same ϵ, is able to prevent the cooling catastrophe, but we stress again that the mechanical efficiency required seems too high ($\gtrsim 0.1$). On the other hand, in Cattaneo's model the majority of injected energy is again thermal, and not kinetic (e.g. the jet velocity is quite low, $\sim 1.4 \times 10^3$ km s^{-1}), frequently leading to the the classic overheating problem.

Dubois et al. (2010) expanded the previous model in a cosmological resimulation. Even if they focused on the BH growth history, they found Bondi outflows can prevent very peaked density profiles, despite the presence of negative temperature gradients at various times[10]. Another main difference with our simulations (and thus some results) is probably the cosmological context. We calculate a fully relaxed cluster, while they analyse a 1:1 merging event. In any case, I underline the fact that all these results give one clear indication: AGN outflows are a key component of the feedback in galaxy clusters.

The last comparison is the one with Vernaleo & Reynolds (2006). They implemented a self-regulated jet mechanism similar to our boundary injection scheme. Their simulations present very different results from our analysis. After few hundreds Myr (with every AGN model) the cooling becomes catastrophic[11]: $> 2000\ M_\odot$ yr^{-1}. The problem of the creation of an unidirectional channel and subsequent deposition of energy is a difficulty

[9] Usually, most of the mechanical energy is not used to form the cavity (see previous Sections).

[10] The central negative/flat T gradient seems a poorly understood (numerical?) feature that afflicts most of the cosmological simulations, especially in pure cooling flow runs, and varying among different codes (SPH vs. Eulerian; see Borgani et al. 2004; Borgani & Kravtsov 2009 for further insights).

[11] Their fiducial pure cooling flow simulation is difficult to understand, showing an exponential catastrophe after 200 Myr, with $\dot{M}_{\rm cool} > 5000\ M_\odot$ yr^{-1}, instead of the typical asymptotic behaviour around $300 - 500\ M_\odot$ yr^{-1}.

found also in our outflow models, however it is solved by the AGN feedback itself on the long term, i.e via the driven turbulence and chaotic motions, which are able to fragment the jet symmetry and to increase the isotropisation of the feedback energy.

4.6.2 Cold Feedback

In the present Chapter, I covered a wide 'zoology' of triggering mechanisms, varying the mechanical efficiency and injection method.

In the first series of models, I linked the power of the AGN outflows to the cooling rate (the cold feedback; Sections 4.3.2-4.3-8), the latter being calculated as $\Delta M_{\rm cool}/\Delta t$, where $\Delta M_{\rm cool}$ is the mass of gas cooled within the region $r \lesssim 10$ kpc in a single time step Δt. It is clear that the energy of a single jet event depends also on the numerical resolution through the CFL stability condition (Eq. 3.8). Lower resolution calculations, with larger Δt and thus larger $\Delta M_{\rm cool}$, tend to generate more powerful outburst events.

Although the total kinetic energy injected at a given time rests on the integrated cooled mass (which is only weakly dependent on the resolution), and can in principle vary among different models (through ϵ), I find, somewhat surprisingly, that it is insensitive on the efficiency and always about $2-3\times10^{62}$ erg, a value comparable to the total energy radiated away. Evidently, the assumed self-regulation mechanism is very effective. However, the total injected energy is only a necessary requirement.

One astrophysically important result of these calculations is that the effect of the feedback crucially depends on how the mechanical energy couples to the ICM energy. When the efficiency is low and the outflows are frequent and relatively weak (models cl-C5m4 and cl-C1m3), the gas cooling proceeds at a rate much higher than the limit allowed by observations. Conversely, when $\epsilon \gtrsim 0.01$ (models cl-C5m2 and cl-C1m1) the cooling rate is reduced to a value fully consistent with the observational constraints. However, the ICM in the core is drastically overheated and the temperature and density profiles do not resemble those of a typical cool-core cluster.

Only cold feedback models with efficiency in the range $5 \times 10^{-3} \lesssim \epsilon \lesssim 10^{-2}$ are able to reduce the cooling rate to acceptable values preserving at the same time a central positive temperature gradient. Moreover, these models generate cavities and shocks, another important requirement that a plausible heating scenario must satisfy. Notice that also observational data (Merloni & Heinz 2008; La Franca et al. 2010) suggest an average AGN mechanical efficiency $\sim 5 \times 10^{-3}$.

As pointed out before, other more ad-hoc types of feedback (not directly linked to cooled gas), like intermittent or continuous schemes with fixed velocity (Sec. 3.4.9), present a pure cooling flow appearance, in the former case, or a too high total energy injection, in the latter. These models are not totally disastrous and show some good features, but in the long term they are not satisfactory.

It is worth now to analyse the riddles linked to these models. Adopting a severe critical point of view, successful cold feedback models may present two difficulties. First, gas often cools and accretes onto the black hole at a rate above the Eddington limit, a fact which make them unpalatable (King 2009), but not impossible (especially at higher

redshift, see for example Szuszkiewicz 2004; Ghosh et al. 2010). Several authors think that BHs grow mainly through the quasar-like phase, that is through radiative accretion at early times (e.g. Hopkins et al. 2006). Thus, our accretion rates could be overestimated, considering that the black hole mass should not increase much in the entire simulation time; on the other hand, note that SMBH masses can reach few 10^{10} $M_\odot$ at the centre of clusters (McConnell et al. 2011). The present resolution does not permit to track the exact amount of accreted material on sub-pc scale. Hence, it is probable that only a small part of $\Delta M_{\rm cool}$ falls onto black hole, and the other is just entrained or ejected by the outflow.

It might be possible that the real efficiency has higher values (instead of 5×10^{-3} adopted in the successful simulations). For example, let us follow this consideration and define the inflow rate as the sum of the real BH accretion rate and the gas outflow rate: $\dot{M}_{\rm in} \equiv \dot{M}_{\rm acc} + \dot{M}_{\rm out}$. If $\eta \equiv \dot{M}_{\rm out}/\dot{M}_{\rm acc}$, then the jet power $P_{\rm jet} \equiv \epsilon_{\rm real}\dot{M}_{\rm acc}c^2 = \epsilon_{\rm real}\dot{M}_{\rm in}c^2/(1+\eta)$. Thus, we can say that the mechanical efficiency adopted in the simulations could be $\epsilon = \epsilon_{\rm real}/(1+\eta)$. A mean η can be retrieved as $\Delta M_{\rm in}/\Delta M_{\rm acc} - 1$. Now, assuming a small BH mass variation in 7 Gyr of 0.1 $M_{\rm BH}$ (that is $\Delta M_{\rm acc} \simeq 3 \times 10^8$ $M_\odot$), and noting that for model cl-C5m3 $\Delta M_{\rm in} = \Delta M_{\rm cool} \simeq 3 \times 10^9$ $M_\odot$, then clearly $\eta \sim 9$. With this in mind, the real efficiency may be $\epsilon_{\rm real} = (1+\eta)\epsilon \sim 10\epsilon = 5 \times 10^{-2}$. In addition, we can estimate $\Delta M_{\rm out} \simeq 2.7 \times 10^9$ $M_\odot$ and, with a duty cycle of 10%[12], the mean outflow rate results in a few $M_\odot$ yr^{-1}. From here we can check the entrainment (or 'mass loading'): $\lambda_{\rm en} = \dot{M}_{\rm act}/\dot{M}_{\rm out}$, where $\dot{M}_{\rm act}$ is the outflow rate in the active region. Taking a mean value of 10^3 $M_\odot$ yr^{-1}, the entrainment results to be $\lambda_{\rm en} \sim 10^2 - 10^3$.

Regarding entrainment, in this first series of 3D simulations we just focused on the global consequences of massive outflows on the thermal and dynamical ICM evolution on large scales. We assume that the outflow is momentum-driven with negligible thermal energy. The detailed process of generating the entrainment is here not addressed. One possible explanation is given by Soker (2008), whose model forms slow massive wide jets.

Summarising, in order to induce a smaller BH growth, in one of our best models, we have to assume massive outflows with a rate ~ 9 times the accretion rate. The ratio η is not well constrained, but for example Moe et al. (2009) give values around 10. Nowadays nobody knows how much gas is really loaded by the original jet, but $\sim 10^2 - 10^3$ seems reasonable (Cattaneo & Teyssier 2007 adopted 100 for example). In future, this could be another observational constraint for our numerical models. I conclude that the high 'accretion' rates in the successful simulations can be easily reduced, introducing a higher (real) efficiency and considering that only a fraction of $\Delta M_{\rm cool}$ falls onto the BH, while the other part is ejected and entrained.

The second flaw in cold feedback models may be that the initial stage of cavity inflation heats the surrounding ICM perhaps too much: soon after jet ignition the temperature inside the bubble rises to high value ($\sim 10^8$ K), and the ICM is substantially shocked. On the other hand, observations (Fabian et al. 2000; McNamara et al. 2000; Blanton et al. 2001, 2003; Nulsen et al. 2002; Fabian et al. 2003, 2006) suggest that the bubble inflation should be gentler, in order to produce rims of gas cooler than the ambient medium. Again, the present resolution does not permit an accurate and detailed study of

[12]Therefore a single jet event has $\Delta M_{\rm out} \sim 10^7 - 10^8$ $M_\odot$.

this and other kind of features (like cold filaments; see instead Chapter 7). Certainly, a direct cause of the violent behaviour is that the injection energy in a single time step is substantial. As shown in Chapter 7, this will be avoided adopting higher spatial resolution and smaller Δt, and thus smaller $\Delta M_{\rm cool}$ and blowing instant power (still solving the cooling flow problem).

We can also argue that observations are usually seeing bubbles at a late time, well after their generation, and this could explain lower temperature and SB_x jumps (see also my argumentation in Section 2.2). In fact, of the three cavities analysed in Figure 4.16, just the newly born one shows sharp contrasts, while the others are older and hence feebler. Moreover, during the whole simulation we see also bubbles created in a gentler way by the weaker outbursts ($\lesssim 10^{46}$ erg s^{-1}).

4.6.3 Hot Bondi-like Feedback

To circumvent the above-mentioned explosive behaviour, I changed completely direction, calculating models where the accretion rate was linked to the Bondi rate. Contrary to cold feedback models, this prescription generates a continuous feedback of moderate power (typically few 10^{44} erg s^{-1}). In order to be efficient and to quench the cooling flow, such non-explosive jet power must be sufficiently steady. Our resolution is far above the Bondi radius ($\sim$ 50 pc), thus we have to rely again upon mean large-scale quantities. In this case we must stay as close as possible to the BH, avoiding the simplest case of a few cells, because of numerical fluctuations. With a fairly small ρ_0 and $c_{\rm s,0}$ averaging radius, $\sim$ 5 kpc, the power seems rather steady and the model successful: cooling rate are low, profiles follow observations, and energies are contained. However, also Bondi models present serious riddles (see next Chapter for a more detailed analysis).

A flaw of successful B1m1S model is that it does not naturally generate X-ray cavities. Instead, the continuous outflows carve a narrow and long tunnel along the z-axis. Again, the continuous jets, with ram pressure almost equal to gas thermal pressure, are highly disrupted by turbulence, especially in central regions. Hence, the fragmentation of a feeble jet may produce generations of gentle detached bubbles, which rise buoyantly, even in continuous feedback models. I propose that any kind of relatively strong (subsonic) turbulence can indeed disrupt a moderate-power jet. For example, Morsony et al. (2010) and Dubois et al. (2010) tried to start the simulation with a cluster atmosphere in non-hydrostatic equilibrium, i.e. following a real cosmological evolution (local density fluctuations, merging, etc.), and they found a fragmentation of the AGN jets, helping the deposition of energy in the inner core.

The main problem of Bondi feedback is that we are not theoretically justified to use it. In fact, Bondi (1952) theory requires several critical assumptions: the flow must be adiabatic and steady, without any initial angular momentum or subsequent perturbation. The fact that, to a certain degree, Bondi self-regulation works, can be mainly ascribed to $\dot{M}_{\rm B}$ being inversely proportional to the gas entropy, thus somewhat linked to the cooling gas, although not as strictly as in the cold feedback mechanism.

4.6.4 Best Models Comparison

It is interesting to find other important differences (or similarities) in successful models with cold or hot feedback. The latter displays low velocities on the order $6 - 7 \times 10^3$ km s^{-1}, a value consistent with line-absorption observations (Crenshaw et al. 2003 for a review). Explosive cold feedback models tend to show also higher velocities, in a few events reaching $\sim 10^5$ km s^{-1}, more similar to a fast jet than an outflow wind (but still consistent). Both models have reasonable final injected energies, below an idealised BH total energy with mass 10^9 $M_\odot$: $E_{\rm BH} \sim 2 \times 10^{62}$ erg.

Apart from cavities and shocks (previously discussed), our models produce other significant predictions, which are comparable to X-ray observations. Iron abundance maps play a relevant role in tracing the outflow activity. The metals, produced mainly by SNIa in the cD elliptical galaxy, are easily transported along the jet-axis up to 150-200 kpc, creating an unmistakable asymmetry, when the AGN is very active. The observations by Kirkpatrick et al. (2009, 2011) and O'Sullivan et al. (2011b) confirm this behaviour. In the period of quiescence, turbulence and bulk motions dominate the scene, smoothing and almost restoring the homogeneity. This phenomenon could be another constraint in choosing between continuous (Bondi-like) models or not: the steady AGN activity would be manifest via the marked metals asymmetries.

Finally, another striking diversity is the clear departure from hydrostatic equilibrium in cold feedback models, due to their more explosive nature. On the contrary, in Bondi runs, the mean fluctuations are very contained with errors below 8%. The consequence is, in the first case, a less precise mass determination using Equation 4.4, as found by other observational works (Rasia et al. 2006; Nagai et al. 2007).

I conclude pointing out that the gaps of cold feedback models, may be replenished by the features of Bondi feedback, and vice versa (especially for cavities). An intriguing solution may be a complementary scenario, in which few energetic AGN outbursts (like in model cl-C5m3), perhaps triggered by accretion rates close to the Eddington limit, are superposed or alternated to the weak activity induced by Bondi prescription. The first explosive mechanism may create large spheroidal bubbles, as those observed in real clusters, while the second quasi-steady outflow may be the sustaining pillar of the heating machine.

So far we have investigated the AGN feedback only in galaxy clusters. Despite the previous riddles, purely mechanical AGN outflows seem good candidates to uphold the wild and frenetic 'dance' between heating and cooling. We need now to test this successful scenario also in different environments, such as galaxy groups (Chapter 5) and ellipticals (Chapter 6). In Chapter 7, I tackle in depth the whole multiphase gas evolution (again in a galaxy cluster); for now, it is better to focus on the hot phase and the central cooling flow problem. I refer the reader to Chapter 8 for the final bullet conclusions of the whole investigation, including the main points discussed throughout this Chapter.

Chapter 5

AGN Feedback in Galaxy Groups

THE MECHANICAL self-regulated feedback mechanism must be valid in every cosmological system, solving the cooling flow problem in a similar efficient and consistent way. In the present Chapter, I extend the previously successful AGN heating model, based on massive mechanical outflows in galaxy clusters, to the environment of galaxy groups. At first sight, it might seem a trivial task. Galaxy groups appear just rescaled versions of galaxy clusters, having a mass one or two orders of magnitude lower; the self-regulated feedback should thus display the same behaviour, simply with rescaled outflow powers. However, this is not what happens. From an observational point of view, there are in fact various indications that groups deviate from the self-similar scaling relations. A less bound system will feel more severely the consequences of the AGN heating, even if rescaled. Galaxy groups are *not* scaled-down versions of clusters.

As in the previous Chapter, I first provide, in the following Section, a brief overview of the properties of galaxy groups in the universe, with emphasis on the differences with galaxy clusters. We will then tackle the main results of the three-dimensional hydrodynamic simulations, involving the competition of mechanical outflows versus radiative cooling in these lighter systems. Further details on groups can be found in the comprehensive review by Mulchaey (2000). The results of this Chapter are also presented in Gaspari et al. (2011b).

5.1 Galaxy Groups Overview

Remarkably, most of the galaxies in the universe reside in small groups, up to 70% in the nearby zone (Geller & Huchra 1983; Mulchaey 2000). Nevertheless, relatively little attention has been devoted to groups with respect to their 'big brothers', galaxy clusters. Based on the hierarchical cosmological ΛCDM model (Sec. 4.1), galaxy groups should play the role of main actors, as the common building blocks of the universe.

Groups, with typical total masses around few 10^{13} $M_{\odot}$, are thus a key class of objects, containing a significant fraction of the overall universal baryon budget and being a nursery

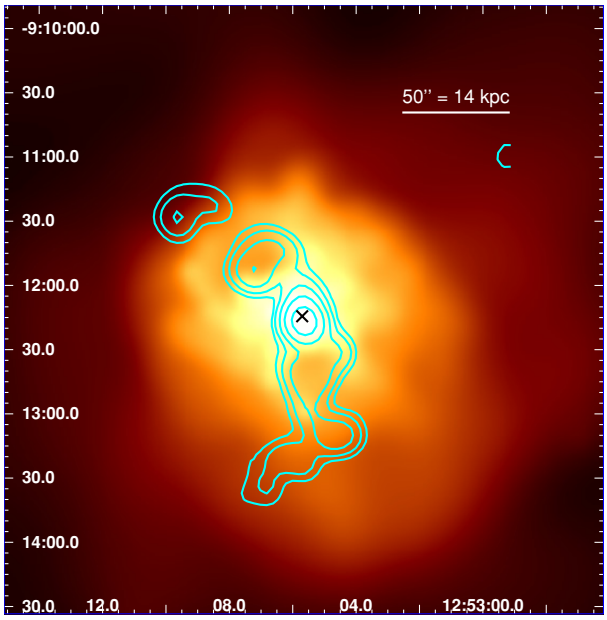

Figure 5.1. The X-ray bright galaxy group HCG 62 observed by *Chandra* (0.5-2.0 keV), with the *GMRT* 235 MHz radio emission overlaid (from Gitti et al. 2010).

for massive (early-type) galaxies. In fact, galaxy groups usually[1] possess 20-80 galaxies, in a virial radius $R_{\rm vir} \sim 1$ Mpc. The demarcation line between massive groups and poor clusters is not very clear and thus the classification may sometimes vary among authors[2]. Galaxy groups seem to contain relatively more spiral and young galaxies, compared to rich clusters, with this fraction decreasing in more compact systems (Hickson 1982).

Einstein observations confirmed the initial claims for X-ray detections of galaxy groups by telescopes of the 70s, such as *Uhuru*, *Ariel 5* and *HEAO 1* (see Mulchaey 2000 and references within). Galaxy groups are X-ray sources, with diffuse extended (50-500 kpc) emission similar to that of rich clusters, but with lower luminosities, ranging from 10^{41} erg s^{-1} up to several times 10^{43} erg s^{-1}, with temperatures $T_{\rm vir} \sim 3\times10^6 - 2\times10^7$ K. At the centre of luminous groups ($L_{\rm x} > 10^{42}$ erg s^{-1}) usually resides a massive elliptical or S0 galaxy, coincident with the X-ray peak of emission (e.g. NGC 2563, HCG 62 – Fig 5.1). The X-ray morphology becomes more irregular at lower luminosities, lacking a central dominant galaxy (e.g. HCG 16, HCG 90). In groups, the X-ray emission seems less extended, compared to clusters, usually covering $\sim 0.2-0.5\,R_{\rm vir}$ (Helsdon & Ponman 2000).

The X-ray emission mechanism is a combination of thermal bremsstrahlung and line emission from highly ionised trace elements (Fe, O, Si, etc.). This hot gas is called intragroup medium (IGM), in analogy with the intracluster gas (ICM; see Section 1.1 for the details on the X-ray emitting plasma). To first order, we can use the hydrostatic isothermal model to describe the X-ray surface brightness profile (Eqs. 4.4 and 4.5). The typical β parameter of groups is $\sim$ 0.5, somewhat lower than the cluster value $\sim$ 0.65

[1] A nice example is the Local Group, including our Galaxy and about other 40 galaxies, with both elliptical and spiral types.

[2] For example in optical band, Hickson (1982) defines a group based on the criteria of population, isolation and compactness (compared to the brightest group member).

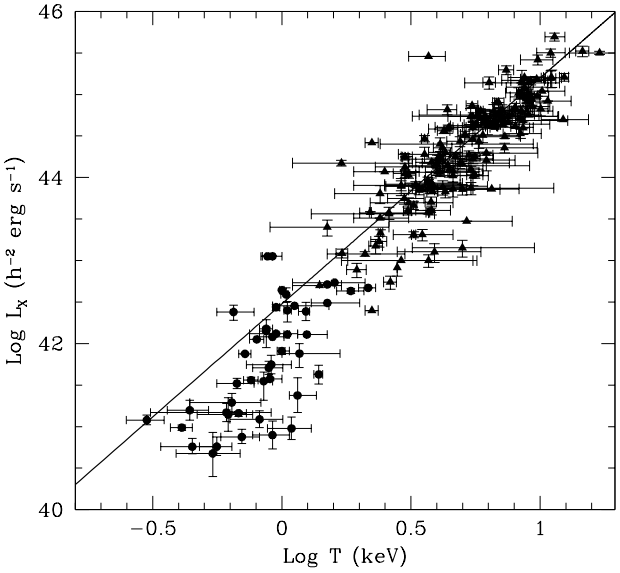

Figure 5.2. X-ray temperature versus X-ray luminosity for a sample of groups and clusters (from Mulchaey 2000). The scaling relation for groups is steeper than the cluster best-fit (solid line), possibly due to the effect of AGN feedback.

(Mulchaey 2000), one of the many indications that non-gravitational heating has played a more important role in low-mass systems.

Another important factor in groups is the gas metallicity, since the emission at lower temperatures ($T < 10^7$ K) is dominated by line cooling (mainly line excitation or radiative recombination; Figs. 1.1 and 1.2). The most important features in the X-ray spectra of groups include the K-shell transitions of carbon through sulphur and the L-shell transitions of silicon through iron. Particularly important is the Fe L-shell complex ($7 \times 10^6 - 2 \times 10^7$ K). Unfortunately, spectral observations of the IGM are very difficult to carry out and metallicities are still an open issue. Nevertheless, abundances vary significantly, from very low values ($Z \sim 0.1 - 0.2\ Z_\odot$; Mulchaey et al. 1993) up to solar values ($Z \sim 1\ Z_\odot$) at the centre of the group, where the massive elliptical resides (Ponman & Bertram 1993; Rasmussen & Ponman 2009). Since the fraction of the stellar mass to gas mass is larger with respect to clusters, it is not trivial to explain the low abundances. One solution may be based on the gas ejection due to galactic (and AGN?) winds, especially in smaller and lighter groups[3].

It is known that galaxy groups, and to a lesser extent clusters, do not exactly follow the global scaling relations predicted by self-similar models (e.g. Kaiser 1986; Evrard & Henry 1991; Osmond & Ponman 2004; Voit 2005; Vikhlinin 2006). Groups are indeed not perfect scaled-down versions of clusters. Helsdon & Ponman (2000) and Mulchaey et al. (2003) found a steeper[4] slope in the $L_X - T$ relation ($L_X \propto T^4$; see Figure 5.2). However, if groups are sampled at sufficiently large radii, excising the cool core, some X-ray scaling relations (e.g. $L_X - T$, $L_X \propto \sigma^4$, $T \propto \sigma^2$) become flatter and more similar to the relationships followed by clusters (Osmond & Ponman 2004; Sun et al. 2009),

[3]Since the escape velocities of groups are comparable to those of individual galaxies, material that is ejected from galaxies may also escape the group.

[4]Even galaxy clusters do not follow perfectly this scaling relation, showing $L_X \propto T^{2.5-3}$.

yet with a large scatter below $T \lesssim 10^7$ K. On the other hand, systematic differences between groups and clusters exist, with the former having clearly lower baryon fractions, $f_b \sim 0.1$, and flatter entropy profiles (Finoguenov et al. 2005; Voit 2005; Borgani et al. 2008; Sun et al. 2009). Moreover, groups have velocity dispersions of $\sim 200-500$ km s^{-1} (comparable to that of galaxies). For this reason, some processes are more (merging) or less (ram-pressure stripping, galaxy harassment) relevant than in clusters. For instance, the merging timescales for the brightest group members are typically a few tenths of a Hubble time (Zabludoff & Mulchaey 1998). Therefore, by the present day some groups ($\sim 20\%$) have likely merged into giant ellipticals, yet conserving the extended X-ray halo (fossil groups).

The discrepancies between the observed scaling relations and the predictions of self-similar models, and especially the systematic differences between groups and clusters quoted above, can be explained by the presence of non-gravitational heating, acting during or after the gravitational collapse. In lower mass systems the same amount of energy per unit mass has a stronger effect. This is a key point for the mechanical AGN feedback problem investigated here.

As in clusters and elliptical galaxies, many galaxy groups display the typical signatures of cooling flows (a most notable example being NGC 5044). Interestingly, the analogues of clear non-cool-core clusters on the group scale have been rarely detected (Johnson et al. 2011), implying that cooling has a key role in shaping the group appearance over its entire life. In fact, the central radiative cooling time is usually shorter than in massive clusters ($t_{cool} \lesssim 10$ Myr), with a sharply peaked X-ray surface brightness.

A recent large sample of X-ray groups is presented in Sun et al. (2009). Gathering 43 objects with *Chandra* data, they confirmed the existence of a general temperature profile (De Grandi & Molendi 2002; Voit 2005; Leccardi & Molendi 2008). The group profiles are slightly steeper than those of clusters for radii $\gtrsim 0.15\ R_{500}$. In the inner cool core, the scatter in the T profile is significant: the majority presents positive gradients (with the central T dropping even by 50%), while few are approaching a flat temperature profile – a possible signature of a heating cycle. The previous authors produced also the radial profiles of entropy, which should retain the thermal history of the gas. They confirmed previous works (Ponman et al. 1999, 2003; Finoguenov et al. 2002), suggesting deviations in the entropy from the self-similar relation ($K \propto r^{1.1}$; $K \propto T$), showing a clear flat core, and an excess relative to massive clusters.

I conclude this overview remarking that the observational features linked to the AGN feedback, such as buoyant bubbles inflated by the bipolar radio jets (Fig. 5.1), weak shocks, metals uplift and turbulence are widely present also in galaxy groups (Buote et al. 2003; Allen et al. 2006; Morita et al. 2006; Jetha et al. 2008; Gastaldello et al. 2009; Randall et al. 2011; Gitti et al. 2012). I refer to Chapter 2 for the observational details on AGN feedback. Here I stress only that the continuous relation between the AGN power, associated with the cavity formation, and the core X-ray luminosity (Nulsen et al. 2007) is even more evident in the group environment, strongly suggesting that some kind of directional energy input, like collimated outflows, is again required.

Table 5.1. Parameters and properties of the most relevant galaxy group simulations.

Model	Feedback	Efficiency ϵ	Jet width × height (kpc)	Injection	Notes
gr-CF	no AGN heating	-	-	-	-
gr-Bc1m2	Bondi	10^{-2}	1×2	entrainment	self-regulated
gr-Bc5m2	Bondi	5×10^{-2}	1×2	entrainment	self-regulated
gr-Bc1m1	Bondi	10^{-1}	1×2	entrainment	self-regulated
gr-Bi1m3	Bondi	10^{-3}	1×2	entrainment	cold timing
gr-Bi1m2	Bondi	10^{-2}	1×2	entrainment	cold timing
gr-Bi5m2	Bondi	5×10^{-2}	1×2	entrainment	cold timing
gr-Bi1m1	Bondi	10^{-1}	1×2	entrainment	cold timing
gr-C5m5	cold	5×10^{-5}	1×2	entrainment	self-regulated
gr-C1m4	cold	10^{-4}	1×2	entrainment	self-regulated
gr-C5m4	cold	5×10^{-4}	1×2	entrainment	self-regulated
gr-C1m3	cold	10^{-3}	1×2	entrainment	self-regulated
gr-I510l	intermittent	-	1×0	nozzle	cycle 5/10 Myr; $10^{-5}\,P_{\rm Edd}$
gr-I510m	intermittent	-	1×0	nozzle	cycle 5/10 Myr; $10^{-4}\,P_{\rm Edd}$
gr-I510h	intermittent	-	1×0	nozzle	cycle 5/10 Myr; $10^{-3}\,P_{\rm Edd}$
gr-BEth50	thermal (Bondi)	5×10^{-3}	1×0	nozzle	50% $E_{\rm th}$
gr-BIO10	InOut (Bondi)	10^{-3}	1×0	nozzle	$f_{\rm in} = 0.1$
gr-BIOen40	InOut (Bondi)	5×10^{-3}	1×0	nozzle	$f_{\rm in} = 0.3$, $\eta_{\rm load} = 40$
gr-BIOen80	InOut (Bondi)	5×10^{-3}	1×0	nozzle	$f_{\rm in} = 0.3$, $\eta_{\rm load} = 80$

Radiative cooling ($Z = 1.0\,Z_\odot$): Runge-Kutta (2nd), plus cold mass dropout ($T \lesssim 5 \times 10^5$ K; $r_0 \sim 3$ kpc).

Supernovae Ia & stellar winds: cD galaxy ($M_* \approx 3 \times 10^{11}\,M_\odot$; $r_{\rm e} \approx 10$ kpc).

5.2 Simulation Setup

The key objectives of the present simulations are the same as those required for galaxy clusters (Section 4.2). The main focus always involves trying to solve the cooling flow problem, drastically quenching the cooling flow and at the same time preserving the cool-core appearance (Sun et al. 2005, 2007). In the (isobaric) pure cooling flow scenario, for typical X-ray luminosities $\approx 10^{43}$ erg s^{-1}, the predictions of Fabian (1994) indicate very high cooling rates of several tens $M_{\odot}$ yr^{-1}.

Again, I think that AGN outflows are a very promising mechanism to simultaneously explain the quenching of cooling flows (and star formation), the deviation of scaling relations from self-similar laws and the presence of X-ray cavities and weak shocks, also in the intragroup medium. I recall that the motivation of massive outflows resides in the entrained-jet scenario (Giovannini 2004; Croston 2008) or in the widespread observational evidence of disc winds seen via blueshifted absorption lines (Crenshaw et al. 2003; Morganti et al. 2005, 2007; Nesvadba et al. 2008, 2011). In particular, we put here under the microscope the two previous best accretion models, the cold feedback versus the Bondi prescription and check if they are so dissimilar or not.

As anticipated, the impact of this type of heating is much more evident in less bound systems. We can thus speculate that gentler outflows are more appropriate to regulate the thermodynamic evolution of the IGM, while the strong explosive outbursts, effective in clusters, should easily overheat the group.

In Table 5.1 are summarised all the numerical details of the hydrodynamic simulations carried out with FLASH, including the type of feedback (Sec. 3.7), the efficiency, the jet width and height ($d_{\rm jet} \times z_{\rm jet}$), and other relevant properties (see Chapter 3 for the details of implementation). As usual, the hydrodynamic equations are solved via the split PPM solver (Sec. 3.2), although I tested also the unsplit HLLC and Roe solver. All the galaxy group computations use the RK2 solver for radiative cooling (with $Z = 1\ Z_{\odot}$; Rasmussen & Ponman 2009), and cold gas dropout enabled (Sec. 3.5). The outflows are always cylindrical, usually injected inside the domain, according to the entrainment scheme (Equation 3.18). When $z_{\rm jet} = 0$, the jet is instead injected through the internal boundaries, assuming $\rho_{\rm jet}$ about $1/10$ of the initial central gas density (Sec. 3.6).

5.2.1 Template: NGC 5044

I choose NGC 5044 as the template for a typical X-ray bright group of galaxies: all the presented results should be relevant for any object in this category. NGC 5044 was one of the first cool-core groups observed, due to its high X-ray brightness, with low redshift 0.009 (see Buote et al. 2003; Gastaldello et al. 2009; David et al. 2009, for recent *Chandra* and *XMM* data). The estimated X-ray bolometric ($0.1 - 100$ keV) luminosity is around 2×10^{43} erg s^{-1}, with a virial mass of $\sim 4 \times 10^{13}\ M_{\odot}$. The large scale morphology is very smooth and nearly spherical, despite a little disturbance in the form of a south-eastern cold front.

On the contrary, the core ($\sim$ 10 kpc) has been strongly perturbed by recent outbursts from the central AGN. The group presents many small radio-quiet cavities with a nearly

isotropic distribution and moderate mechanical power ($\sim 10^{42}$ erg s^{-1}; see Fig. 2.2). The two biggest cavities at larger radii (10 – 20 kpc) are instead filled with radio emission at 235 MHz (David et al. 2009); the associated mechanical power seems to be able to balance radiative losses. The NGC 5044 X-ray image also shows several cold filaments coincident with Hα and dust emission, indicating a physical connection between the various gas phases (Gastaldello et al. 2009). The *GMRT* observation (610 MHz) reveals the presence of extended radio emission with a torus-like morphology, threaded by the largest filament (probably cold material being uplifted from the centre).

The cooling time of the hot gas within the central 2 kpc is just $\sim 4 \times 10^7$ yr. In the absence of feedback, a pure cooling flow model predicts tens of $M_\odot$ yr^{-1}, while observations suggest the cooling rate is at least an order of magnitude lower, less than a few $M_\odot$ yr^{-1} (Tamura et al. 2003; David et al. 2009).

This galaxy group consists of a luminous giant elliptical galaxy (NGC 5044) surrounded by a cluster of $\sim$ 150 low luminosity dwarf galaxies, mostly of early type. We choose to model the elliptical galaxy with a de Vaucouleurs profile, with stellar mass $M_* \sim 3.4 \times 10^{11}\ M_\odot$ and effective radius $r_e \sim 10$ kpc (Buote et al. 2004).

As previously done, we start the calculations with the hot gas in spherical hydrostatic equilibrium in the potential well generated by the total system mass. At variance with the cluster runs, I use both the well-observed $T(r)$ and $n(r)$ (Buote et al. 2003, 2004, see the dotted lines of Figure 5.3) to calculate the total gravitational potential, under the assumption of hydrostatic equilibrium. At the virial radius the gas fraction is ~ 0.11, a reasonable value for X-ray bright groups (Mathews et al. 2005).

The computational rectangular 3D box in all the following models extends slightly beyond the group virial radius, $R_{104} \approx 870$ kpc. We simulate the $z \geq 0$ half-space with symmetric boundary condition at $z = 0$, while elsewhere is imposed outflow condition with inflow prohibited. The set of 10 grid levels (basic blocks of 8×8×4 points) guarantees a resolution in the finest inner grid of $\Delta x \approx 488$ pc.

5.3 Results

In the following Sections, I describe the results of the 3D hydrodynamic simulations based on self-regulated AGN outflows in an exemplary galaxy group, lasting at least 7 Gyr. The positive results of similar simulations for rich galaxy clusters (Chapter 4) are a strong motivation for a further in-depth analysis of this mechanical feedback mechanism in lower mass systems, exploring different types of self-regulation and parameters. Some of the main features of highly unsuccessful - but pedagogical - models are covered in the previous Chapter.

5.3.1 Pure Cooling Flow [gr-CF]

As a fiducial model for the galaxy group environment, I ran a simulation without AGN feedback, i.e. a pure cooling flow (the heating linked to stellar evolution shows again negligible effects). The results are shown in Figure 5.3.

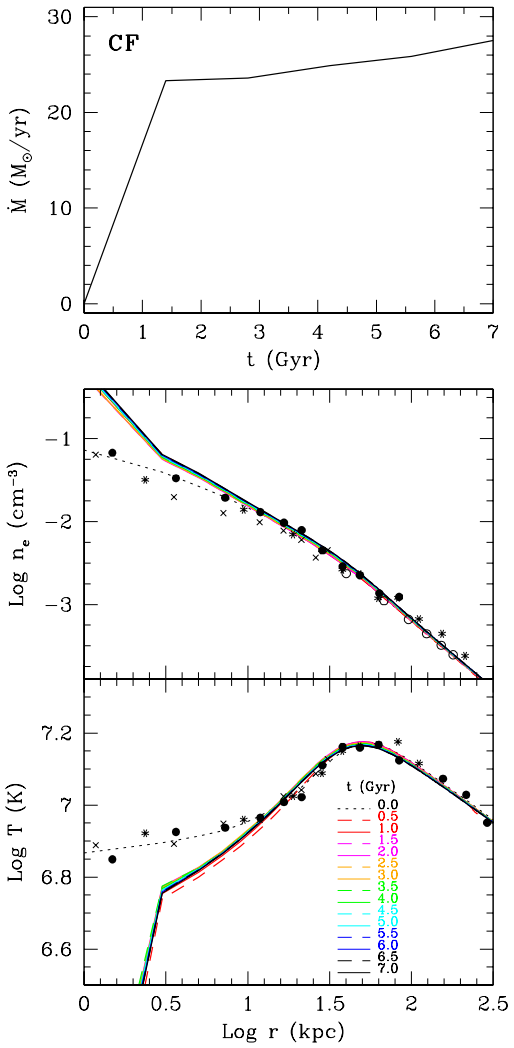

Figure 5.3. Evolution of the cooling flow model (gr-CF; no AGN feedback). Top panel: gas cooling rate versus time. Middle and bottom panels: temporal evolution of the gas (electron) number density and mass-weighted temperature radial profiles, respectively. *Chandra* and *XMM-Newton* observational data of NGC 5044 are represented by star and cross points (Buote et al. 2004), filled circles (Buote et al. 2003); open circles indicate *ROSAT* data (David et al. 1994).

The flaws of the classic cooling flow model are clearly depicted in this evolution (gr-CF). Both the density and (mass-weighted) temperature radial profiles steepen considerably in the central region: the radiative losses induce a subsonic inflow of gas, increasing the emissivity in a vicious circle. This trend is relatively more evident and faster in the galaxy group, rather than in the cluster. After just 1 Gyr the cooling rate has already approached a quasi-steady state, with an asymptotic value $\sim$ 25 $M_{\odot}$ yr^{-1}. This is the clearest discrepancy with observational data and one of the main failure of the standard cooling flow scenario.

The other two main observables, $T(r)$ and $n_{\rm e}(r)$, are also clearly inconsistent in the inner $\sim$ 15 kpc. Very cold gas, down to 10^5 K (which is soon dropped out), concentrates in the nucleus and generates unobserved gradients. A typical signature of such a strong cooling flow is also the temporal increase of the bolometric X-ray luminosity: from $\sim 1.9 \times 10^{43}$ erg s^{-1} up to $\sim 2.6 \times 10^{43}$ erg s^{-1} at 7 Gyr.

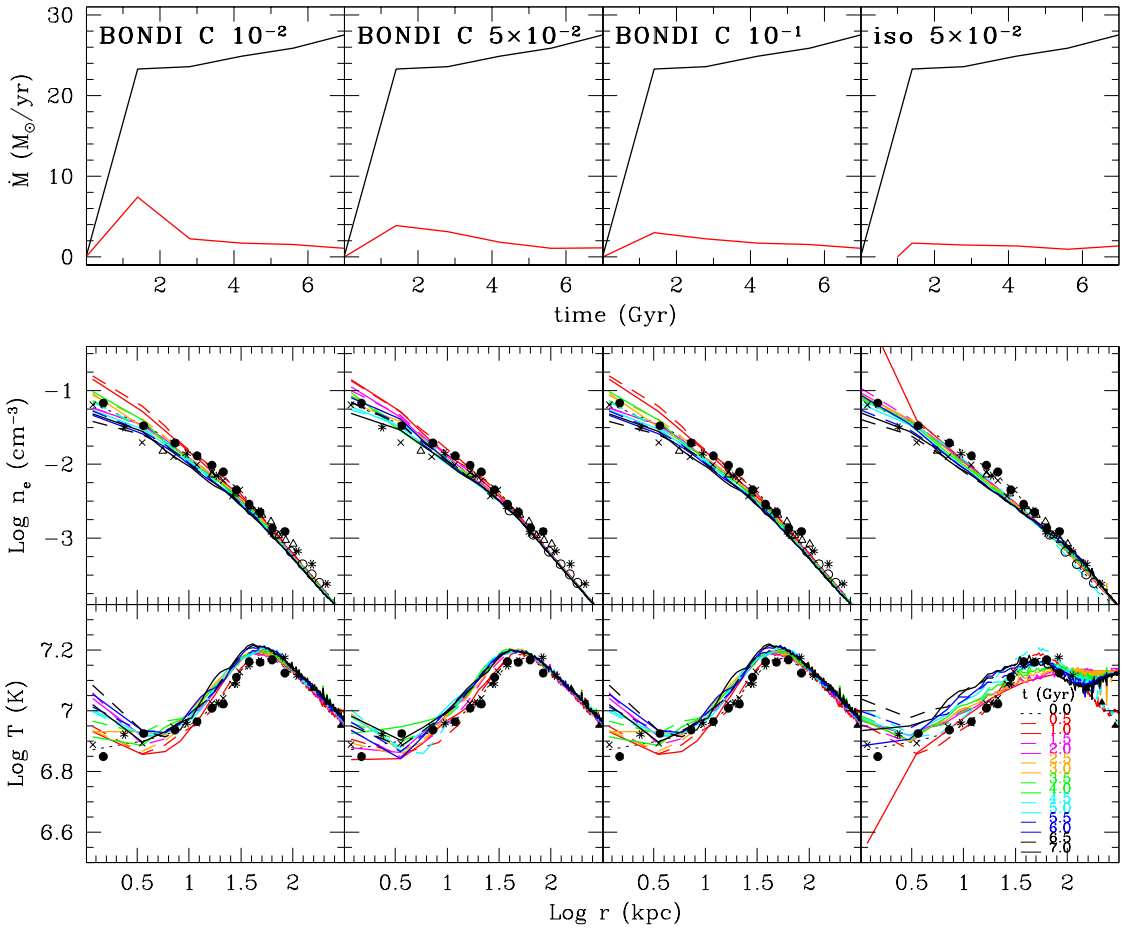

Figure 5.4. Evolution of Bondi (classic) feedback models with different efficiencies (the latter being the isothermal start). The panels show the same quantities as in Figure 5.3.

It is interesting to investigate the global energetic budget, because the common (misleading) sense would probably associate the irradiated energy with, mainly, the drop in internal energy. However, the internal energy within $R_{\rm vir}$ decreases by $\sim 7 \times 10^{58}$ erg (that is, by less of 1%), while the potential energy drops by $\sim 6{\times}10^{60}$ erg, considering both the hot gas remaining in the grid and the cooled gas at the centre of the group. The kinetic energy stays always around $\sim 10^{57}$ erg, thus negligible. The conclusion is that energy is radiated away ($E_{\rm rad} \sim 6 \times 10^{60}$ erg in 7 Gyr) mainly at the expense of the potential energy of the IGM. This behaviour was less evident in the cluster, but still present.

In order to test the effect of numerical resolution on the cooling flow results, I calculated a cooling flow simulation with a resolution three times higher: the results are almost identical to the lower resolution run described above. Therefore, with the adopted resolution our models are in the convergence limit.

5.3.2 Bondi Feedback: $\epsilon = 5 \times 10^{-2}$ [gr-Bc5m2]

I begin to analyse the results of the simulations with AGN feedback turned on, starting from the two best Bondi models. Then I discuss, from higher to lower efficiencies, computations displaying worser results, alternating the continuous and hybrid (Sec. 5.3.3)

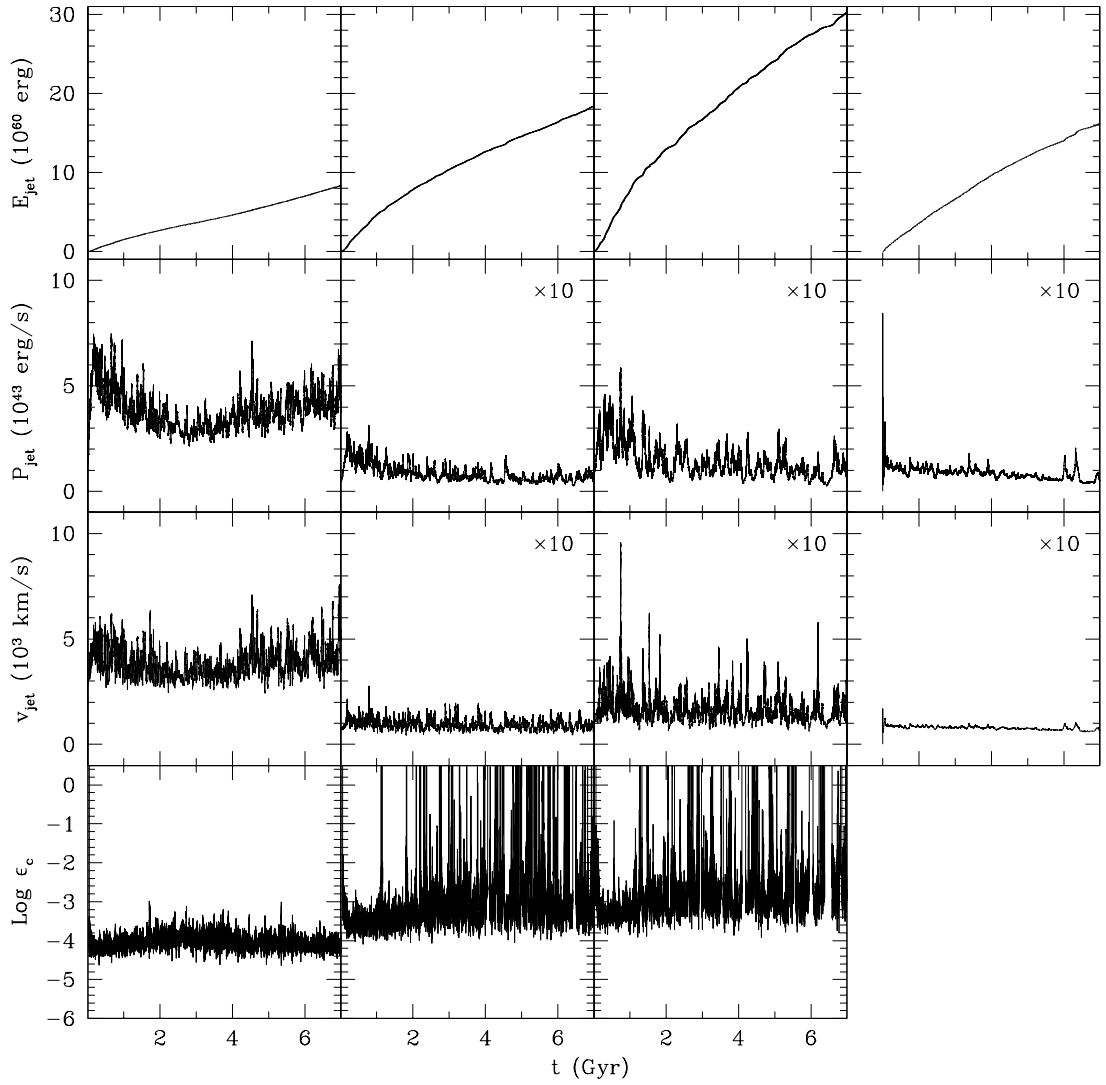

Figure 5.4. *Continued.* Outflow properties for the (classic) Bondi feedback models. From top to bottom row: total injected kinetic energy (in the half-space), outflow power, outflow velocity, and associated cold efficiency (see text). The label ×10 means that the units in the ordinate axis have been multiplied by a factor of 10.

types feedback. The order is dictated by the flow of the discussion and comparison, rather than being strictly sequential (the same applies to the description of figures).

Despite our resolution is far[5] from capturing the Bondi radius (tens of pc) and despite the fact that the radiative cooling is important in the central region, Bondi accretion can display the properties of a 'thermostat'. The Bondi rate is indeed proportional to $K^{-3/2}$ (where $K \propto T/n^{2/3}$ is the entropy parameter), thus feeling the cooling of the hot gas, although not as strictly as in the cold feedback mechanism.

The first retrieved good model has efficiency $\epsilon = 5\times10^{-2}$ (gr-Bc5m2[6]; second column in Figure 5.4), using the injection in the active region. The overall Bondi feedback

[5]The averaging zone for the Bondi boundary conditions is ∼ 2.5 kpc.

[6]As previously done, I name a simulation according to the system-feedback-parameter (usually the efficiency; in this case Bc means the classic continuous Bondi prescription).

is gentle and moderate, with rates that are always sub-Eddington ($\sim 10^{-3} - 10^{-2}$ the Eddington rate) and supported by observations (Allen et al. 2006). The mean cooling rate (first panel) is well below 10% of the pure cooling flow, with only a transient peak ($\dot{M} \sim 3.5\ M_\odot\ \mathrm{yr}^{-1}$) at 1.5 Gyr. An important feature for a successful continuous feedback is the stability in time. The moderate power stays around $P_{\rm jet} \sim 10^{44}$ erg s^{-1} (fifth panel, in the continued Figure 5.4), without strong variations, which allows to balance the instantaneous cooling rate in an efficient way.

The mass-weighted temperature profiles ($T(r)$; third panel) are in agreement with the observations in the nucleus of the group, with a smooth and almost flat curve. In the outer regions tiny acoustic oscillations are present, while between 10-30 kpc the continuous injection of energy tends to slightly overheat this region, especially at late times. The electron number density profiles ($n_{\rm e}(r)$; second panel) also show little variation from the initial observed ones, an indication that the gas is not drastically accumulating in the core.

The final injected energy is relatively low, $\sim 1.8 \times 10^{61}$ erg (3.6×10^{61} erg for the bipolar outflow; fourth panel), compared to the total 'available' BH energy 1.8×10^{62} erg – roughly estimated as $E_{\rm BH} \sim 0.1\, M_{\rm BH}\, c^2$, with $M_{\rm BH} = 10^9$. This is a typical feature of galaxy groups, in contrast to the high input energies of massive clusters, whose models can exceed the above quantity.

It is worth noting that I tested several initial conditions and concluded that the dynamics and results of our feedback models are, overall, not distorted by relatively different initial temperature and gravity profiles. For example, in Figure 5.4 (fourth column), I started the computation with an isothermal profile ($\sim 1.35 \times 10^7$ K), retrieving the density structure from a theoretical NFW[7] plus the galaxy deVaucouleurs potential. After the first Gyr of pure cooling flow, the Bondi feedback ($\epsilon = 5 \times 10^{-2}$) is again very effective in quenching the cooling flow and at the same time preserving the cool core appearance.

A possible riddle for continuous models remains the absence of frequent jet-inflated cavities. The continuous AGN activity (mean $v_{\rm jet} \sim 10^4$ km s^{-1}; sixth panel) carves a narrow tunnel of ~ 30 kpc in length, although its density contrast with the environment is large only for $z \lesssim 10$ kpc (and not particularly evident in the $\mathrm{SB_x}$ maps; Sec. 5.4).

5.3.3 Hybrid Feedback: $\epsilon = 5 \times 10^{-2}$ [gr-Bi5m2]

In a self-regulated (subgrid) mechanism we have to face substantially two problems. The first one is how much power to link to the feedback, while the second one is the right timing, i.e. when to turn on and off the heating machine.

In the following simulation (Figure 5.5, third column), I link the activation of the AGN heating to the gas cooling, but use the standard Bondi rate for the gas accretion onto the black hole. In other words, an outflow is generated when $\Delta M_{\rm cool} \neq 0$, with the mechanical energy linked to $\dot{M}_{\rm B}$ in the usual way. This feedback scheme tries to reproduce a self-regulated intermittency of the outflows (classic Bondi models can only be continuous), with cycles of inactivity corresponding to moments of high hot gas entropy. In fact, when

[7] The NFW parameters are $c_{102} \simeq 6.6$ and $M_{\rm vir} = 4 \times 10^{13}\ M_\odot$.

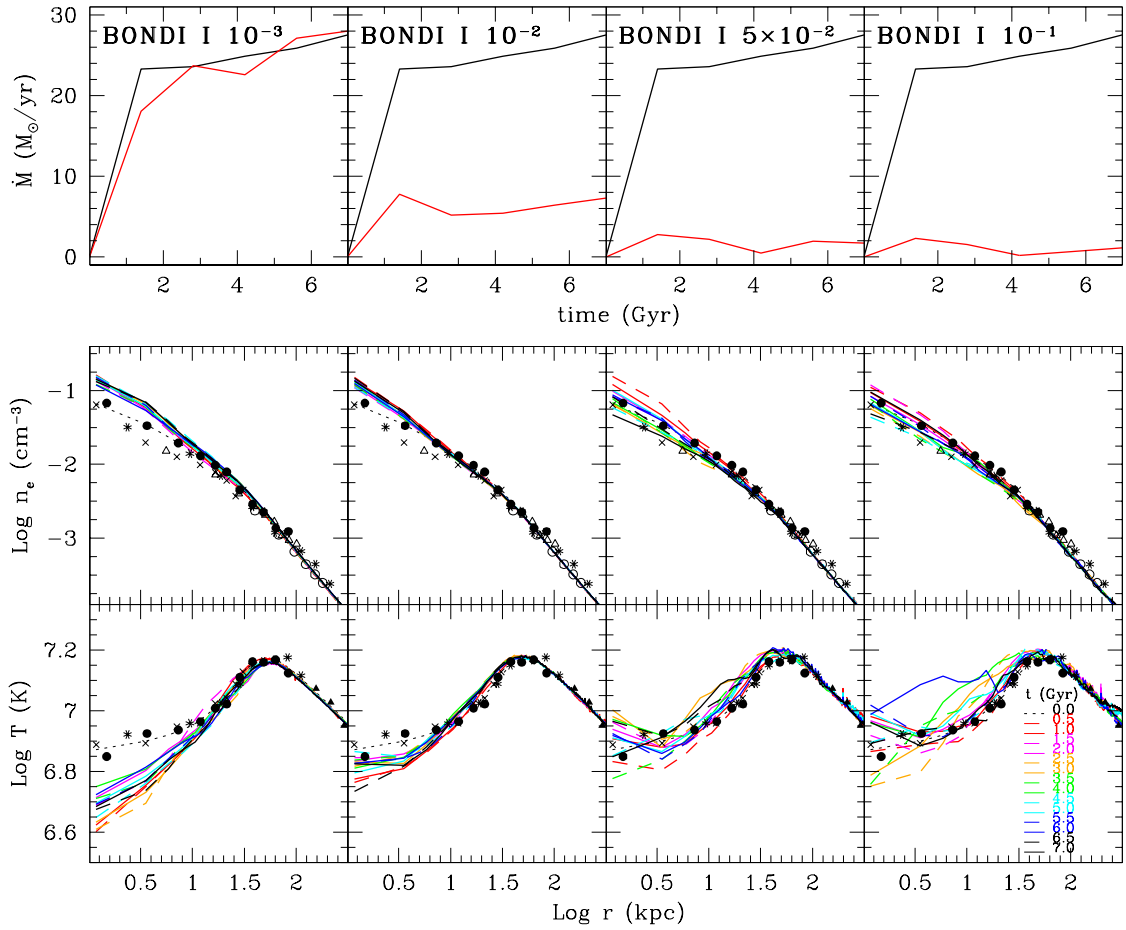

Figure 5.5. Evolution of Bondi hybrid models (cold timing) with increasing efficiencies, from left to right. The description of the plots is the same as for Figure 5.4.

the gas begins to cool, it will usually start to flow towards the central black hole.

Following this prescription, the temperature profiles are a bit more consistent with the observational data, especially at intermediate radii. Although the jets are intermittent, their frequency is high, a condition that grants the quenching of cooling rates ($\dot{M} \sim 0.5-2$ $M_\odot$ yr^{-1}). The density profiles do not depart from the cool-core status, without a strong steepening (central values ~ 0.1 cm^{-3}).

Bondi accretion rates are almost identical to gr-Bc5m2, with the total energy injected in 7 Gyr slightly reduced: $E_{\rm jet} \sim 1.5 \times 10^{61}$ erg. The average jet power is also a factor ~ 1.3 less, $P_{\rm jet} \sim 5.5 \times 10^{43}$ erg s^{-1}.

This model clearly solves the problem of jet-inflated cavities in the IGM. The outflows duty cycle[8] is roughly 80-85 per cent (in the whole computation). The pattern is not very regular, in fact the cycle is more frenetic between 2 and 5 Gyr, when the central gas has been heated efficiently. Every time the jet (with velocities usually $v_{\rm jet} \sim 8 - 10 \times 10^3$ km s^{-1}) turns on again, a bubble of small size (10 – 15 kpc) is generated and observed in the density map. Note that after a period of quiescence the subsequent injection produces a

[8]The common duty cycle retrieved by observations can be quite different from our numerical estimates, because the definition of an 'active' AGN highly depends on some luminosity threshold (in the X-ray, radio, etc.) and on the properties of the sample.

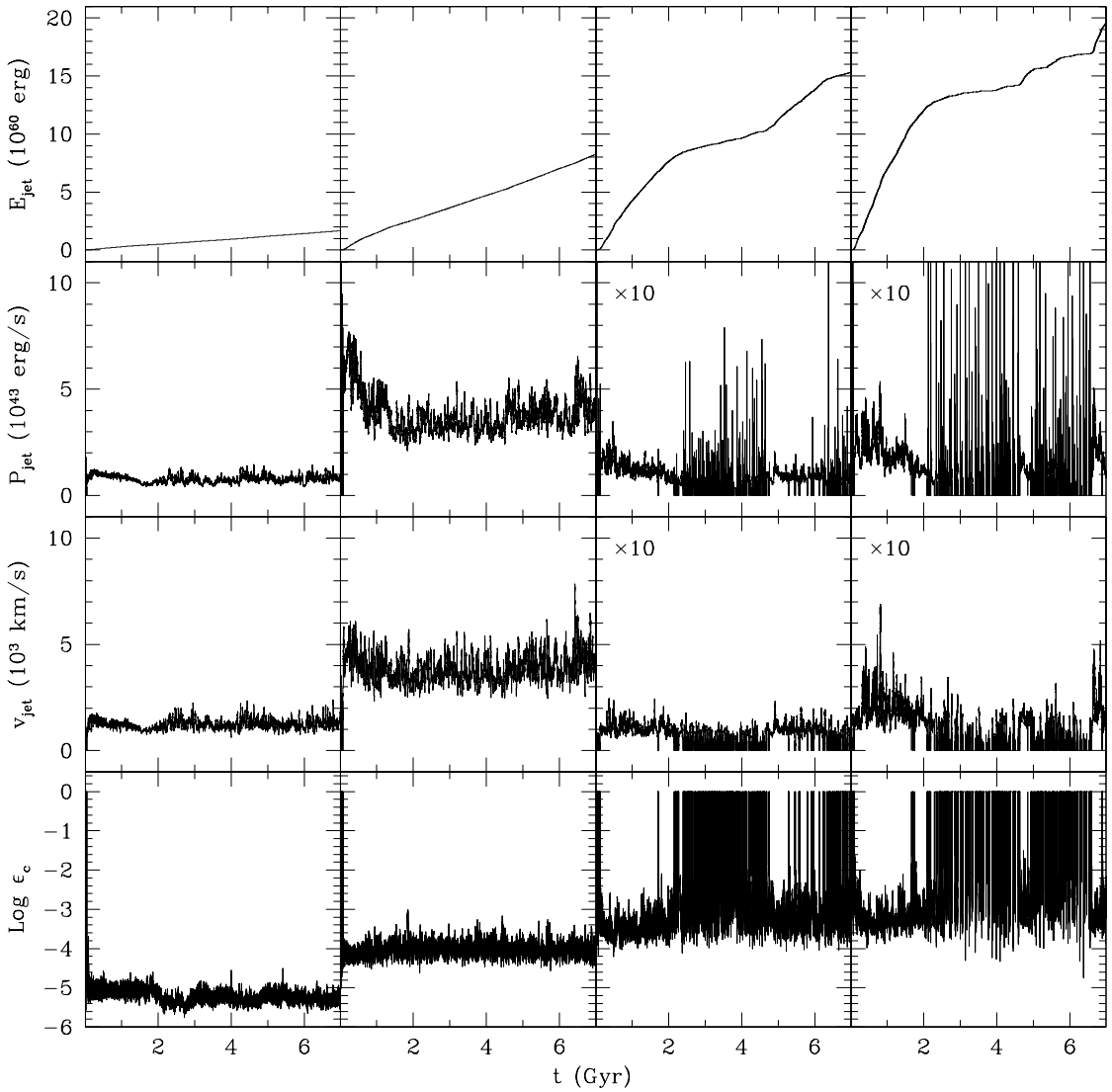

Figure 5.5. *Continued.* Outflow properties for the Bondi hybrid models (cold timing). The description of the plots is the same as for Figure 5.4.

peak in the power, promoting the above mentioned cavity inflation through shock heating. The side effect consists in more evident perturbations in some T profiles (e.g. 3 and 7 Gyr), however still compatible with typical galaxy group observations.

Finally, during runtime I calculated, at every time step, the efficiency (ϵ_c) that the cold feedback mechanism would have (last panel in Fig. 5.5). The result is striking: on average, the two schemes are almost coincident with ϵ_c around 10^{-3}, except for few short time steps, in which the cold feedback requires a 100 per cent efficiency (because the cooled mass is almost zero).

5.3.4 Bondi Feedback: $\epsilon = 10^{-1}$ [gr-Bc1m1]

I begin now to describe models from higher to lower efficiencies, alternating again continuous and intermittent Bondi methods (Figures 5.4 and 5.5, respectively).

The following simulation is very computationally expensive, because the (continuous) outflow velocity rises often over 2×10^4 km s^{-1}. It is shown in Figure 5.4, third column. The cooling rate is quenched to a fraction of $M_\odot$ yr^{-1} after just a few Gyr. The total injected energy is 3×10^{61} erg (about 1.5 times greater than that of the intermittent counterpart, next model gr-Bi1m1). The consequence of this high energy deposition is a progressive steepening in the temperature gradient, with a moderate spike in the inner 4 kpc, where the jet is always active. During some time steps the outflow reaches 5×10^{44} erg s^{-1}, a quite strong power for Bondi accretion.

The compared efficiency analysis (last panel) shows that a cold feedback triggering could not even be possible in 20-30 per cent of the evolution, because it would break the unity threshold. In the other periods, it would be associated with a value around 2.5×10^{-3}.

5.3.5 Hybrid Feedback: $\epsilon = 10^{-1}$ [gr-Bi1m1]

The following run (Fig. 5.5, fourth column) is another computationally expensive model, which touches the limit of acceptability in the parameter space, for Bondi models. The timing is again associated with the cold gas. The cooling rate is very similar to the precedent continuous model (gr-Bc1m1), within the reasonable range $\dot{M} \sim 0.5 - 1.5$ $M_\odot$ yr^{-1}, declining at late times. The density profiles are optimal, not altered from the initial data. Temperatures start to feel the strong outbursts, which have sometimes power in excess of 10^{45} erg s^{-1} (with velocity larger than 2×10^4 km s^{-1}). In fact, at later times the central gas is heated up to 10^7 K, during some event.

The associated cold efficiency has a common trend around 2.5×10^{-3}, but with many oscillations after 3 Gyr, reaching easily unity. Notice that these moments last very few time steps, after which ϵ_c resets to lower values (in contrast to a first impression of the tight plot).

5.3.6 Bondi and Hybrid Feedback: $\epsilon = 10^{-2}$ [gr-Bc1m2, gr-Bi1m2]

When the efficiency is lowered to $\epsilon = 10^{-2}$ (gr-Bc1m2), the heating provided by the feedback is considerable ($\sim 8 \times 10^{60}$ erg). This decreases the cooling rate down to at least 30-40 per cent of that of the pure gr-CF (Figure 5.4, first column). The profiles are close to the observed data, thanks to an always continuous outflow with velocity $4 - 5 \times 10^3$ km s^{-1} and power $4 - 5 \times 10^{43}$ erg s^{-1}.

The intermittent simulation, gr-Bi1m2, is very similar to the continuous evolution (see Fig. 5.5, second column), except that, initially, the system is permitted to cool. Without this early opposition, the outflows - with same power - can not halt the cooling so efficiently like in the previous case. The feedback finds an equilibrium only at 4 Gyr, while at later times it will slowly increase, on the contrary of a reasonable self-regulated model.

The associated efficiency of a cold feedback model would be near 10^{-4}. In fact, we will see that the correlated cold feedback model will produce an almost identical outcome, i.e. weak heating (Fig. 5.6, second column).

5.3.7 Bondi and Hybrid Feedback: $\epsilon = 10^{-3}$ [gr-Bc1m3, gr-Bi1m3]

As a template for a typical weak model, a simulation with Bondi efficiency of 10^{-3} (gr-Bi1m3) produce a cooling rate, which is identical to a pure cooling flow run: $\dot{M} \sim 25-26$ $M_\odot$ yr^{-1} (Fig. 5.4, first column).

The only clue for the presence of AGN heating is that the profiles do not suffer a heavy decline with time, even if they posses a remarkable steep gradient (T down to 4×10^6 K). The outflow is always continuous (the model is identical to gr-Bc1m3), with a very low velocity around 1000 km s^{-1} and a power often under 10^{43} erg s^{-1}. There is no possibility that this model will become intermittent at any time, due to the constant central cooling.

5.3.8 Cold Feedback: $\epsilon = 5 \times 10^{-5}$ [gr-C5m5]

The results presented in the previous Sections for the Bondi accretion models suggest that, compared to galaxy clusters, groups require lower efficiencies, at least a factor of 10. Therefore, I start illustrating the cold feedback mechanism for the lowest adopted ϵ and then moving to more efficient outflows. Here we still use the entrainment injection method. In Chapter 4, we concluded that the size of the jet and the type of injection do not change drastically the evolution of the feedback.

As shown in the first top-left panel of Figure 5.6, the cooling rate for model gr-C5m5 settles on a steady value around $\dot{M} \sim 10$ $M_\odot$ yr^{-1}. This rate is obviously unacceptable, although reduced to the $\sim 50\%$ of the pure CF model value. With such a low efficiency, the shell-averaged, mass-weighted temperature and density profiles become only slightly modified by heating, and present the excessive accumulation of gas near the centre, typical of the cooling flow model. In the centre, the temperature is $T \sim 5.6 \times 10^6$ K, with electron number densities $n_e \sim 0.18$ cm^{-3}.

The outflows, have a typical power of $P_{jet} \sim 4 - 5 \times 10^{43}$ erg s^{-1} and velocity of $v_{jet} \sim 3 - 4 \times 10^3$ km s^{-1}. The total injected mechanical energy is in fact quite low, $E_{jet} \approx 6 \times 10^{60}$ erg, and the outflows are almost continuous, incapable to stop the cooling flow. Given the rare period of inactivity, the 'duty cycle' is ~ 95 per cent.

At the end of the simulation 6×10^{10} $M_\odot$ have cooled and dropped out of the hot phase. The vast majority of gas cools at the very centre. If all the cooled gas were accreted onto the central black hole, as I have simplistically assumed in this scheme, the final black hole mass would result about an order of magnitude greater than the expected one. In principle, we could avoid the problem of the excessive black hole mass by assuming that only a fraction of the cooled gas actually accretes on it, with a higher mechanical efficiency (see Section 5.3.14).

5.3.9 Cold Feedback: $\epsilon = 10^{-4}$ [gr-C1m4]

As anticipated, the next step is to increase the efficiency, in order to find a more suitable heating power. In the following model (gr-C1m4), where the efficiency is increased by a factor of 5, $\epsilon = 10^{-4}$, we obtain in fact a jet power of $\approx 10^{44}$ erg s^{-1} and velocity oscillating around 5×10^3 km s^{-1} (Fig. 5.6, second column). However, the cooling rate is

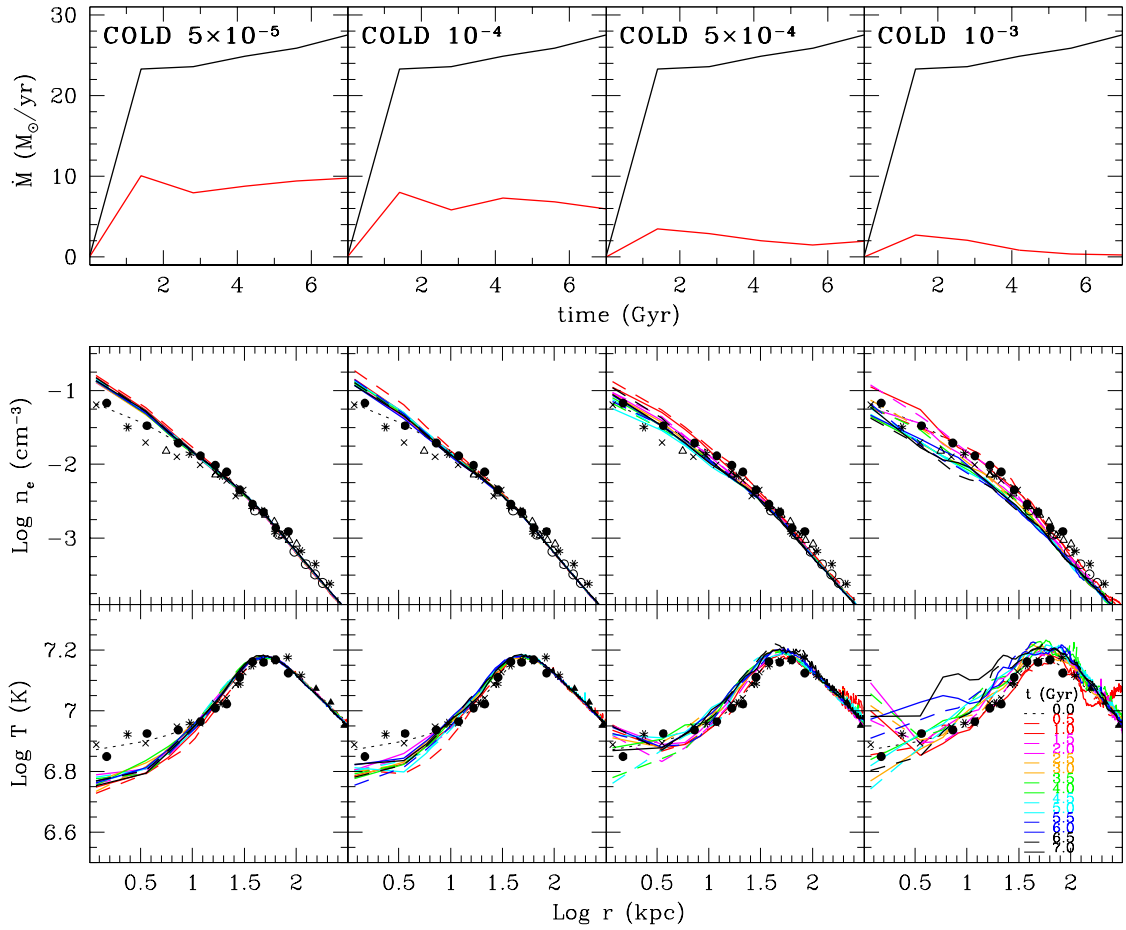

Figure 5.6. Evolution of the cold feedback models with increasing efficiencies, from left to right. The description of the plots is the same as for Fig. 5.4.

only slightly reduced to $6-7\ M_\odot\ \mathrm{yr}^{-1}$ and radial profiles tend to be similar to the ones of previous model. The difference is that now the curves decline at 6 kpc, instead of 10 kpc. Evidently, the outflows deposit their energy in more inner zones.

We conclude that, even if the total injected energy reaches almost 10^{61} erg, at this stage the cooling flow is not quenched in a successful manner. This is also underlined again by the almost continuous presence of the outflows.

5.3.10 Cold Feedback: $\epsilon = 5 \times 10^{-4}$ [gr-C5m4]

At 5×10^{-4} (gr-C5m4), we finally recover a successful heating evolution. As in previous computations, at early time (first Gyr) the radiative cooling prevails over the outflow mechanical heating and the cooling rate reaches a peak of $4\ M_\odot\ \mathrm{yr}^{-1}$. However the long-term evolution presents different intriguing results. After 2 Gyr the system becomes much more turbulent and chaotic, inducing a reasonable amount of mixing, that permits the gas circulation and reheating in a very efficient way, also in the 5 kpc nucleus.

As shown in the third column of Figure 5.6, the temperature in that region is almost constant, with values close to those observed for NGC 5044 ($T \approx 8 \times 10^6$ K; Buote et al. 2003; David et al. 2009). This very important quality is shown also by the density

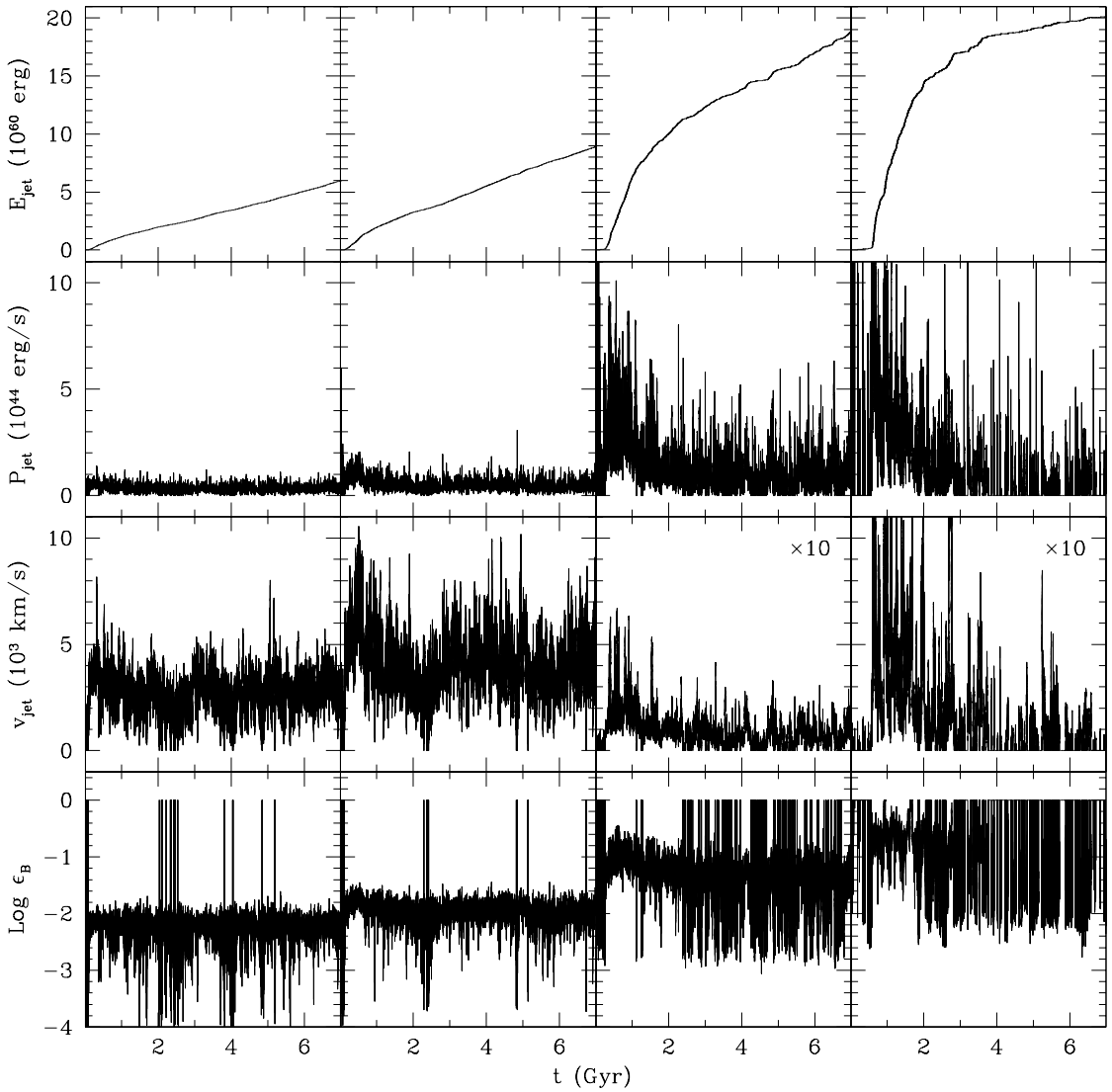

Figure 5.6. *Continued.* Outflow properties for the cold feedback models. Same description as for Fig. 5.4 (in the last row is now shown the associated Bondi efficiency).

curves: a gradual flattening of the central profile is seen throughout the entire evolution. It is striking that the 7 Gyr (black) profile is practically superposed to the initial fit. At that time (redshift zero) the cooling rate is $\sim 2\ M_{\odot}\ \mathrm{yr}^{-1}$, about 7% of the pure CF run, a significant suppression which brings the value of $\dot{M}$ in reasonable agreement with the observations (Buote et al. 2003; Tamura et al. 2003; David et al. 2009).

The shock waves generated by the outflows, with power usually between $\sim 2-5\times10^{44}$ erg s^{-1}, are not strong enough to significantly alter the global positive temperature gradient, although small amplitude ripples are present. These waves correspond to weak shocks associated with the jet propagation and are visible up to a distance of ~ 300 kpc. They are not so evident as in galaxy clusters because the power involved here are two or three orders of magnitude lower. In fact, the total jet energy is 1.8×10^{61} erg. The gas is typically ejected with $v_{\mathrm{jet}} \sim 10^4$ km s^{-1}.

Furthermore, an important difference between clusters and groups is the duration of

each event. In cluster models, a duty cycle of 0.1 was quite usual, because the very short super-Eddington bursts could stop instantly the cooling flow, with the consequence of perturbed profiles, near the ignition time. Here, our estimated duty cycle is roughly 0.85. Therefore the situation is reversed: successful cold feedback models in groups require an almost continuous heating, with short pauses of tens Myr.

Notice that the Eddington luminosity, $L_{\rm Edd} \approx 1.5 \times 10^{38}\,(M_{\rm BH}/M_\odot) \sim 10^{47}$ erg s^{-1} (for a 10^9 $M_\odot$ black hole), is far above the regime of the current model. In fact, the accretion rate oscillates between 10^{-3} – 10^{-2} the Eddington rate. As shown in Section 5.3.12, an Eddington jet can easily erase the cool-core structure of the group.

In summary, the analysed behaviour of gr-C5m4 seems to be similar to the quiet Bondi feedback. In the bottom panel I have calculated, at each time step, the associated Bondi accretion rate and the required $\epsilon_{\rm B}$ to ideally reproduce the same instantaneous mechanical energy. As a remarkable result, a Bondi efficiency of $\sim 5 \times 10^{-2}$, especially after 2 Gyr, is retrieved from this analysis. Only in a few events, the cold mechanism detaches from the regular regime of Bondi, because of its intrinsic impulsivity. Nevertheless the similitude is quite evident and indeed, if we compare the outcomes of both models (cf. gr-Bi5m2; Fig. 5.5, third column), they appear deeply connected also in a quantitative manner.

5.3.11 Cold Feedback: $\epsilon = 10^{-3}$ [gr-C1m3]

Increasing the efficiency by a factor of 2 generates another positive model, with some features approaching the borderline of a violent disruptive heating. In fact, with a jet power up to 10^{45} erg s^{-1}, the cooling flow is perfectly stifled, asymptotically decreasing to a fraction of $M_\odot$ yr^{-1} after a few Gyr (Fig. 5.6, fourth column). The beginning of the violent regime is quite evident in the radial profiles, which now tend to oscillate in a large $\sim$ 50 kpc region. Overall, the cool core is preserved, but the temperature indicates some overheating in the nucleus at later times.

With our adopted active region, during a few outbursts, the jet velocity becomes greater than 10^5 km s^{-1}, while the outflow mass rate is several tens $M_\odot$ yr^{-1}, as in all previous cold feedback models. This is a clear indication that at higher efficiencies we will approach a relativistic regime and a catastrophic heating[9]. The equivalent Bondi efficiency for model gr-C1m3 is sometimes 0.5 or more, difficult to justify.

The total injected energy of gr-C1m3 is similar to the previous successful model, an indication of a good self-regulation during the global feedback process. This energy can be compared with the total energy radiated away, $\approx 1.38 \times 10^{60}$ erg (in the simulated half-space $z > 0$). Interestingly, the present heating provides more energy than that lost by radiation ($E_{\rm rad} \sim 1.4 \times 10^{60}$ erg). Notice that, in every described model, the total outflow energy (for the full-space system) is about an order of magnitude lower than the available BH energy ($\sim 1.8 \times 10^{62}$ erg). The evolution of the energetics is very similar to the description presented in the previous Chapter. The core kinetic energy increases after every intense AGN outburst, but it is soon dissipated and transformed into potential energy through the expansion of the IGM.

[9] I will not show here results for $\epsilon > 10^{-3}$; see the previous Chapter for the analogous cluster model.

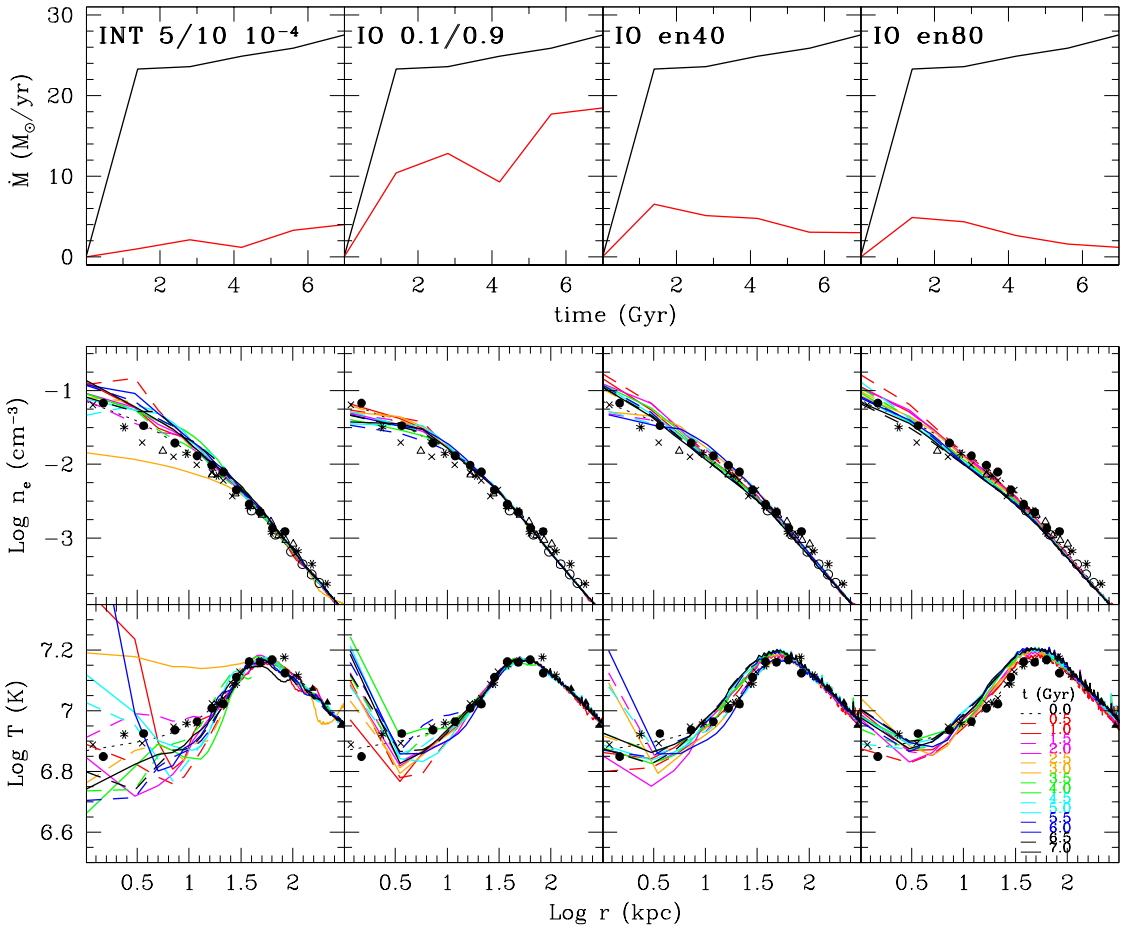

Figure 5.7. Evolution of intermittent and inflow-outflow models (with or without mass loading). The description of the plots is the same as for Fig. 5.4.

5.3.12 Intermittent Feedback

In this series of models we want to decouple the simulation from the self-regulation engine, in order to control some important AGN outburst parameters. For example, it is interesting to fix the frequency of the outflows. In Section 4.3.9, I found that intermittent outflows, with jets activated every 10 Myr, are marginally acceptable, and can reasonably inhibit gas cooling. I thus test a fixed AGN cycle of 10 Myr, with every event lasting 5 Myr. This AGN activity agrees with the observations of acoustic ripples in Perseus cluster (e.g. Fabian et al. 2006).

In the models described in this Section I do not insert an ad-hoc velocity, but retrieve its value from setting a constant power, here taken equal to $10^{-4}\ P_{\rm Edd}$, thus $P_{\rm jet} \sim 4 \times 10^{43}$ erg s^{-1} (model gr-I510m). Unlike the previous runs, I use now the nozzle injection method, with resulting constant velocity ≈ 7000 km s^{-1} (the efficiency is irrelevant).

With the previous fixed power and intermittency (Figure 5.7, first column), the cooling rate is less than a few $M_\odot$ yr^{-1}, for several Gyr, and shows a slow increase after 4.5 Gyr, up to 4 $M_\odot$ yr^{-1}. The density radial profiles are almost superposed to the observations, becoming slightly flatter at later time. Thus, like in Bondi models, the radiative cooling is significantly reduced by the simulated heating process. It is visible a spike in the inner

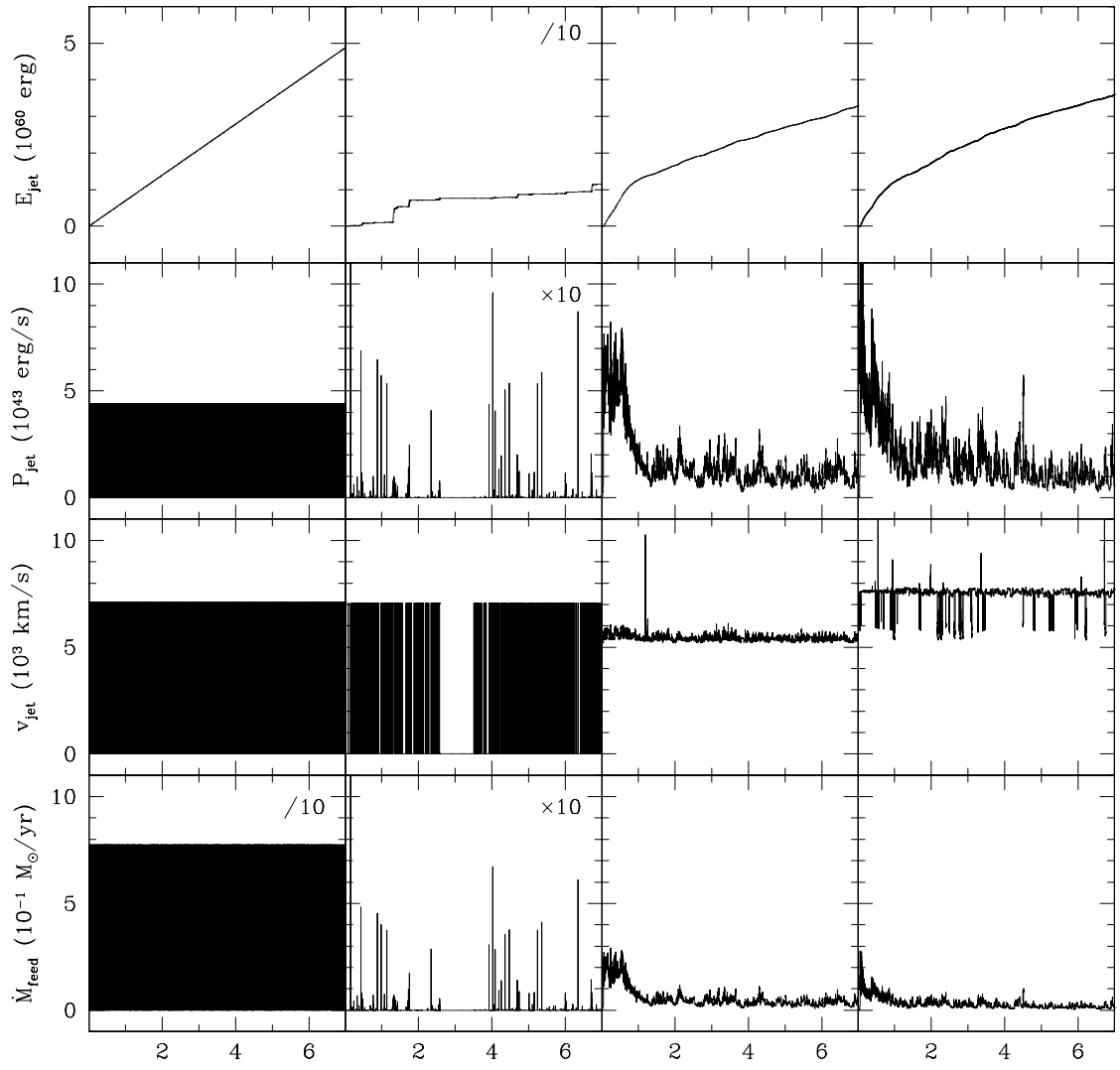

Figure 5.7. *Continued.* Outflow properties for the intermittent and inflow-outflow models. Same description as for Fig. 5.4, except that the bottom row shows now the accretion rate.

few kpc, while at radii greater than 10 kpc the fluctuations from initial $T(r)$ are almost zero. As expected, shock heating seems slightly more vigorous in the nucleus when the outflow is injected through the boundary, while more effective at intermediate radii, when the entrainment method is adopted.

In this type of intermittent models it is not granted that the feedback produces evident cavities. In fact, with a cycle of 5-10 Myr the head of the jet cocoon almost touches the backflow tail of the last bubble. Thus, we expect that with a duty cycle greater than 50 per cent the jet becomes practically continuous.

Keeping the same cycle scheme (5-10 Myr), but increasing the power by a factor of 10 produces a typical explosive simulation (gr-I510h; not shown). The temperature profile becomes very steep, with a negative gradient, as soon as the outflow ignites, destroying the entire cool core and generating a plateau in $n(r)$. The cooling rates are obviously zero, a typical sign of heating catastrophe (overheating).

On the other hand, a model with a much reduced power (4×10^{42} erg s^{-1}; gr-I510l) shows $\dot{M} \sim 12\ M_{\odot}\ \mathrm{yr}^{-1}$, after just 1 Gyr. Generated bubbles are quite stable and, being slowly inflated, show cold rims in the early phases. Nevertheless, the density and temperature profiles resemble those of a classic cooling flow, with less peaked gradients.

We can conclude that, even with fixed intermittency, an acceptable AGN feedback model should not approach the Eddington regime (as proposed in some analytical works, e.g King 2009), at least in galaxy groups, where a strong burst can easily wreck the delicate thermodynamic structure of the core.

I also tested several types of intermittency, keeping the same jet power of acceptable model gr-I510m. However, these models must be rejected. In fact, when each outflow event has a duration of 1.0, 2.5 or 3.3 Myr (not shown), the intermittent feedback becomes quite ineffective in halting the inflowing cold gas: the central gas density slowly grows with time until radiative cooling prevails over heating, causing the cooling rate to surpass the threshold of acceptability. For example after just 1 Gyr, with 3.3 Myr duration, the cooling rate overcomes 7 $M_{\odot}\ \mathrm{yr}^{-1}$ and the temperature curves turn very similar to those of model gr-CF. On the contrary, when the jet duration exceeds 5 Myr, the inflated cavities disappear, because the different outbursts melt rapidly in the inner ten kpc zone, producing an almost continuous injection. The consequence is a steep T gradient at the centre, which can halt the cooling flow, but without self-regulation it easily overheats the system.

5.3.13 Thermal Feedback

It is worth noting that one difficulty of a purely kinetic outflow (often called 'momentum-driven') is that it can often carve a tunnel in the surrounding IGM, if the ram pressure of the jet ($\rho_{\mathrm{jer}} v_{\mathrm{jet}}^2$) is much larger than the gas thermal pressure ($\rho c_{\mathrm{s}}^2/\gamma$). Thus, a feedback with high kinetic energy will advance undisturbed in the group core, depositing its energy at intermediate radii (15 – 30 kpc). At the base, the cold gas accumulates in a torus-like manner. This is especially evident at early stages of a momentum-driven outflow, starting from idealised symmetric conditions without any kind of perturbation. The successful models are able to quench cooling flow, because at some point the generated turbulence induces strong mixing in the gas, also in the very centre. Therefore the circulation inside the jet path makes shock heating very effective. In our models the turbulence is sustained only by the AGN feedback. It is likely that this process dominates in the very central region of the system, although turbulent and bulk motions caused by cosmological accretion, usually very subsonic, may also contribute (e.g. Heinz et al. 2006).

Nevertheless, the high density gas in the torus cools efficiently and triggers the AGN feedback in an almost continuous way. It is physically reasonable that a fraction of the jet power is converted in thermal energy, especially during the entrainment process. Based on these considerations, we simulate some models with a fraction of the total injected energy in the form of thermal energy, through the nozzle. We use the Bondi prescription for these runs.

With pedagogical purpose, I first set the fraction of E_{th} to 99% the total jet energy. This setup is similar to the model of Cattaneo & Teyssier (2007) with loading factor of 100 and Bondi efficiency 0.1. As expected, the first powerful outflow (over 10^{44} erg s^{-1})

destroys the entire thermodynamic structure of the cool core: the produced shock (with temperatures above 10^{10} K) is almost spherical. This is another indication that the group necessitates a much more delicate heating compared to a cluster. Lowering the efficiency to 10^{-3} still generates a similar catastrophic heating.

On the other hand, keeping the above efficiency, but reducing the fraction of $E_{\rm th}$ to 20% or 33% results in models overall similar to purely kinetic ones. One major difference resides in tiny puffs at the base of the jet, that enable more turbulence. The problem is that, in the inner $8 - 10$ kpc, temperature profiles show a spike, due to injected $E_{\rm th}$. Another interesting effect is the enlargement of the tunnel carved by the outflow, due to the increased internal pressure, compared to the pure momentum-driven feedback.

The best model seems to be gr-BEth50 (figure not shown), with 50% thermal energy and efficiency 5×10^{-3}. The feeble jet is almost always continuous, with velocity 3000 km s^{-1}, but the thermal energy injection generates a strong break-up in the jet structure, fragmenting in small buoyant bubbles of size $5 - 8$ kpc; a very interesting feature that is observed also in NGC 5044 (David et al. 2009, 2011).

I conclude that a good fraction of thermal energy associated with the AGN feedback can help the deposition of heating at very small radii, reducing the cold torus at the base of the jet and fragmenting the outflow in small-size bubbles. At the same time, however, it is difficult to obtain a flat or positive T profile, requiring some sort of fine tuning.

5.3.14 Inflow-Outflow Feedback

One problem of self-regulated feedback models is how much of the gas contributes to the growth of the black hole mass. Needless to say, with a resolution of ~ 500 pc we can not consistently estimate the accretion rate onto the BH. As noted in some works (Cattaneo & Teyssier 2007; Ostriker et al. 2010), part of the inflowing gas could be thrown back by the induced outflow, probably via entrainment. Therefore, only a fraction of the accreting mass, $\Delta M_{\rm acc}$, might actually be captured by the black hole. From another perspective, we can see this as a reduced total efficiency.

That being stated, I compute some models in which we attempt to track the part ($f_{\rm in}$) of infalling gas that really increases the BH mass. The residual fraction ($f_{\rm out} = 1 - f_{\rm in}$) is considered the active mass of the outflow:

$$\frac{1}{2} f_{\rm out} \dot{M}_{\rm acc} v_{\rm jet}^2 = f_{\rm in} \epsilon \dot{M}_{\rm acc} c^2. \tag{5.1}$$

Note that in these models it is better to use the nozzle injection mode, in order to totally control the outflowing mass, without altering the internal domain cells.

An interesting feature of this method is that the outflow velocity is almost constant, dependent on $f_{\rm in}/f_{\rm out}$ (and ϵ). An observational constraint of the outflow velocity may thus provide hints about this ratio between infalling and outflowing matter.

Setting $f_{\rm in} = 0.1$ ($f_{\rm out} = 0.9$) and efficiency $\epsilon = 10^{-3}$, the outflow coming out of the nozzle has a velocity ~ 7000 km s^{-1}. With cold accretion, the power of the jet presents strong oscillations between 10^{43} and 10^{45} erg s^{-1} while the cooling rate approaches in a few Gyr the gr-CF simulation. Even with Bondi accretion (same efficiency; Figure 5.7,

second column), which in theory is more regular, the high outflow power can not find a stable balance in time, resulting in $\dot{M} \sim 18\ M_\odot\ \mathrm{yr}^{-1}$ at 7 Gyr. While some accretion events reach 4-5 $M_\odot\ \mathrm{yr}^{-1}$, the produced strong feedback does not last long enough. In fact, the total injected energy is very low: $E_{\rm jet} \sim 10^{59}$ erg. It is interesting that the radial profiles of this model (gr-BIO10) show a cool core, with the exception of a central negative temperature gradient. Therefore, overall acceptable mean T and n profiles do not necessary imply that the system is not cooling.

Trying to increase the efficiency is a serious problem for the inflow-outflow feedback models, because the velocity would constantly overtake $> 5\times10^4$ km s^{-1}. We could lower $f_{\rm in}$ in order to increase the jet mass, but with just 1 per cent of accreting mass (probably unrealistic) the velocity would still have very large values.

The only solution, I have found, is to return back to the 'entrainment hypothesis' and multiply $f_{\rm out}$ by a factor $\eta_{\rm load}$ (like a mass loading factor). Following this assumption, with $\eta_{\rm load} = 40$ and $f_{\rm out} = 0.3$ (gr-BIOen40), we can thus enhance the Bondi efficiency ($\epsilon = 5 \times 10^{-3}$) to obtain an acceptable cooling rate, below 5 $M_\odot\ \mathrm{yr}^{-1}$ (Fig. 5.7, third column), after the small bump at 1.5 Gyr. Now the velocity has a value of $\sim$ 6000 km s^{-1}. With $\eta_{\rm load} = 80$ (gr-BIOen80), the average cooling rate is further reduced, asymptotically decreasing to 1 $M_\odot\ \mathrm{yr}^{-1}$ (fourth column). Both simulations generate some of the best radial profiles, which keep the cool-core appearance for the entire evolution, almost glued to the initial (observed) condition. This is an indication that the feedback has returned stable (around $P_{\rm jet} \sim 1 - 3 \times 10^{43}$ erg s^{-1}), gentle and continuous, very similar to successful Bondi models (Sec. 5.3.2-5.3.3). Notice that the accretion rate becomes again sub-Eddington.

Overall, a pure inflow-outflow model exhibits a spasmodic behaviour, because of the intrinsic linking between accreting and outflowing matter, which can be smoothed out only by introducing a mass loading factor. However, this parameter is nowadays unknown and therefore its value is chosen ad hoc, in order to retrieve reasonable jet velocities. Since the results are analogous, it is therefore simpler and cleaner to adopt the usual entrainment feedback of the previous main models.

5.4 Dynamics and Observables of Best Models

In this Section I analyse in depth the typical features produced by the AGN feedback in the best models, at some relevant times, via the density slices and other astronomical observables, like the integrated emission-weighted maps.

In Figure 5.8, the first column shows the 2D density cuts trough the x-z midplane (panels a-d) with the velocity field superposed. The first row is associated with Bc5m2 model (at 5 Gyr), one of the successful models in the set of simulations (see Table 5.1). This snapshot depicts one of the three typical stages of the AGN-regulated simulation in a galaxy group. The gentle and continuous heating of the outflow ($\sim 10^{44}$ erg s^{-1}) carves a narrow tunnel in the intragroup medium with electron density around 2×10^{-4} cm^{-3}. The diameter of the channel is usually 4-5 kpc, collimated in the inner region by the thermal pressure of the surrounding gas. At 14 kpc, where the jet ram pressure becomes

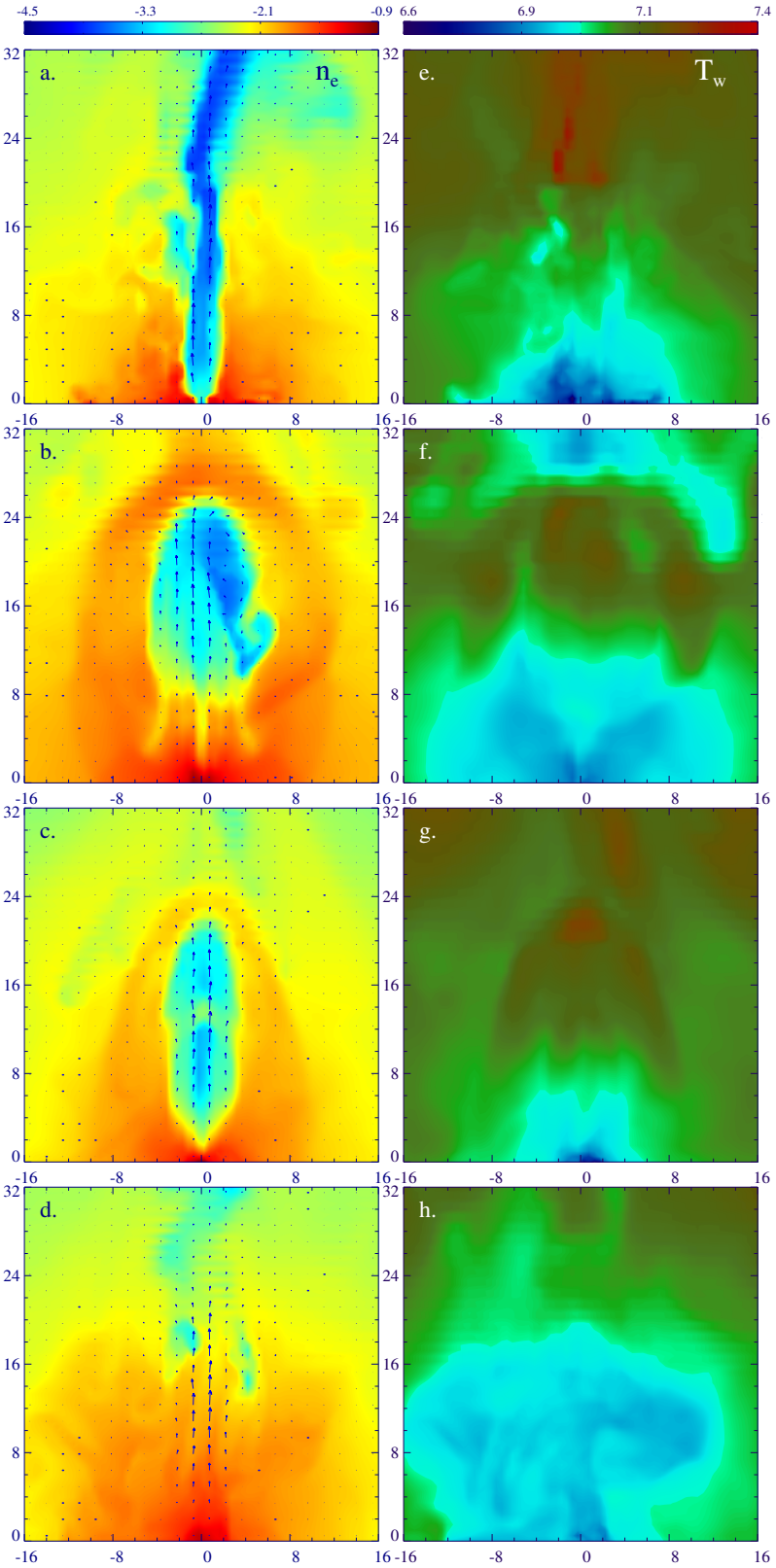

Figure 5.8. Logarithmic maps of the four best models (kpc unit). The two columns show the cut through the x-z midplane of n_e (cm^{-3}), with the velocity field superposed, and the emission-weighted projected temperature (K). From top to bottom row: model gr-Bc5m2 (5 Gyr), gr-C1m3 (0.5 Gyr), gr-Bi5m2 (7 Gyr), and gr-Bi1m1 (6.5 Gyr).

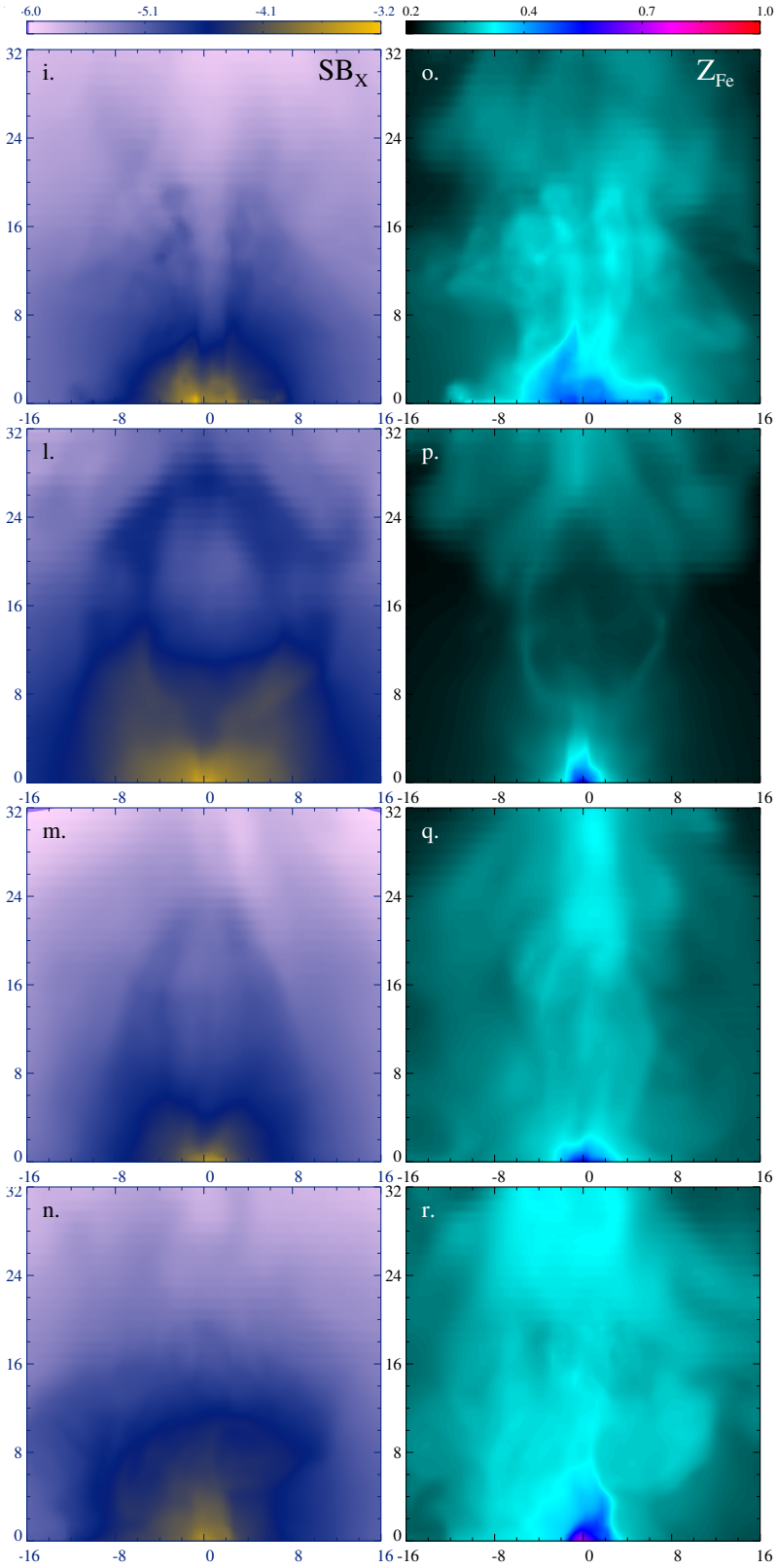

Figure 5.8. *Continued.* The two columns show the X-ray surface brightness (erg s^{-1} cm^{-2}; logarithmic) and the projected emission-weighted iron abundance ($Z_\odot$ unit).

comparable to the thermal pressure of the ambient gas ($P \sim 2.5 \times 10^{-11}$ erg cm^{-3}), the outflow structure becomes perturbed and more turbulent[10]. In fact, near the tunnel, instabilities are visible, a signature of further IGM entrainment and turbulent mixing. The latter has a relevant role in the feedback process, especially at later times, when the AGN has been active for several Gyr (Fig. 5.4; the cooling rate decreases with time). In fact, even if the turbulent mixing does not directly heat the gas, it greatly favours the deposition of energy at the base of the jet, where the cooling tends to dominate.

The fact that the global cool-core appearance is not greatly modified, is another key result. Although the continuous outflow generates a tunnel, the overall initial structure is conserved. On the other hand, increasing the efficiency of Bondi models leads to a wider conical channel, which begins to dominate the core of the group. This is not observed and in fact those models are rejected also for the central negative T gradient. As seen in the second column (panel e), the emission-weighted temperature of Bc5m2 has instead a positive gradient, almost flat in the 5 kpc nucleus.

The continuous presence of the channel (interrupted sometimes by the fragmentation) is a feature not commonly seen in real groups, at least in the local universe[11]. However, the X-ray surface brightness map (panel i) does not show an evident channel, with only two very faint features (at 12 – 16 kpc), similar to a pair of arms. To be more quantitative, I performed 1D cuts through z of SB_X at different levels (from 4 up to 20 kpc; Figure 5.9, non-black lines). It is clear that the central depression is not deep (15 – 20%, usually with a difference of 5×10^{-6} erg s^{-1} cm^{-3}), plus the width is particularly slim (few kpc), making the detection of the channel extremely difficult[12]. Over 20 kpc, the slim tunnel is lost in the integration trough line of sight.

In panel o (always Fig. 5.8) is shown the tracer of the iron abundance (again emission-weighted), injected by SNIa and stellar winds of the cD galaxy. This type of advected quantity is deeply linked to the history of the AGN heating. It is indeed possible to recognise in the map the anisotropic outflow pattern, which can drag the metals, produced inside the central elliptical galaxy, up to 15-20 kpc. The abundance values are $\sim 0.3 - 0.4$ $Z_\odot$. This characteristic is commonly observed in the core of AGN heated systems (e.g. Kirkpatrick et al. 2009, 2011; Rasmussen & Ponman 2009; David et al. 2011).

The second row of maps (Fig. 5.8) is associated with another good model, this time based on the cold feedback. Model gr-C1m3 (at 0.5 Gyr) shows the other face of the AGN-regulated evolution: an AGN outburst with power $\sim 1.2 \times 10^{45}$ erg s^{-1} generates a big cavity in the IGM density, with major/minor axis of 16/10 kpc. The injected energy is almost 10^{60} erg, with an outflow velocity over 10^4 km s^{-1}. The buoyant bubble has a high density contrast with the environment, ~ 100.

In contrast to the violent cavities generated in the previous galaxy cluster simulations, the cold feedback in groups is able to inflate low density cavities without heavy shocks. The outflow power, in the group environment, is several orders of magnitude lower,

[10] At 24 kpc, the outflow is almost stopped by the IGM, generating a rise in temperature, $\sim 1.55 \times 10^7$ K (see also Figure 5.9).

[11] The evolution of groups is still far to be certain, lacking a complete sample at intermediate and high redshift.

[12] In addition, Poisson noise, background, resolution, and response of the X-ray detector (not present in our synthetic maps) could easily alter or obscure this very faint and narrow feature.

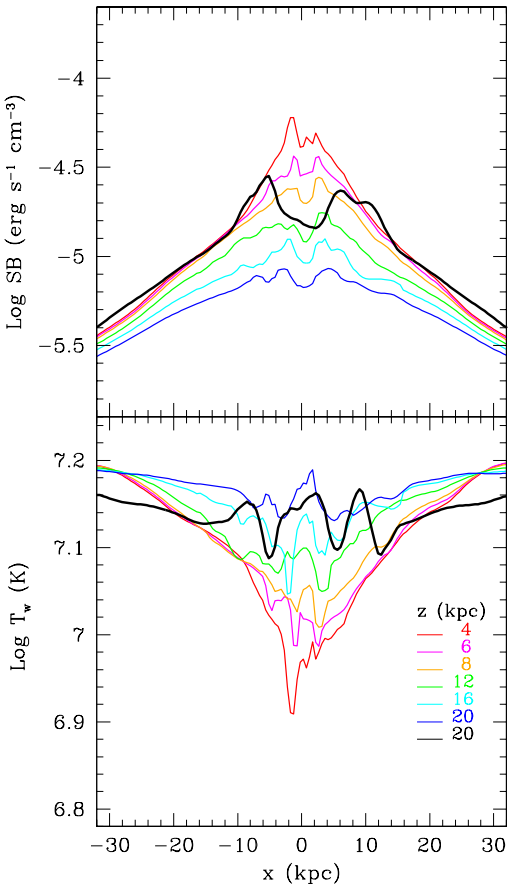

Figure 5.9. X-ray surface brightness and emission-weighted temperature 1D cuts through z (see label). Black thick lines correspond to model gr-Bi1m1 (panels n and h of Fig. 5.8), while the other lines belong to model gr-Bc5m2 (panels i and e).

usually with a smoother injection per time step. In fact, $T_{\rm w} \sim 1.45 \times 10^7$ K inside the shell, which is only slightly larger than the surrounding gas value (see panel f and the black line in Fig. 5.9). This is also suggested by the homogeneity of the map above 12 kpc (reddish colours).

A striking feature, while hard to detect, is the bright rim, that surrounds the cavity (panel l). The rim, especially the low-z region, is formed by low-entropy gas originally at the centre. This feature is seen in deep X-ray observations (e.g. Salomé et al. 2006 and references therein), suggesting that the rims are colder than the average ambient medium. The 1D cut through $z = 20$ kpc (Fig. 5.9) clearly confirms the presence of the rim, with a drop of temperature ($\sim 40\%$) coincident with the high X-ray emission (at $x = \pm 6$ kpc).

In panel p, I show the (emission-weighted) iron abundance map in the $x-z$ plane. The iron-rich core, few kpc in size, is clearly visible. At $z \sim 28$ kpc there is a region of Fe-rich gas, lifted by the outburst. The dense cavity rims have a slightly larger abundance than the ambient gas, also revealing that the origin of a part of the rim material is connected to the nucleus of the group.

The $\rm SB_X$ inside the cavity (panel l) exhibits a depression of ~ 50 per cent with respect to the rims. Notice how this feature (Fig. 5.9, black line) would be easily detectable in the X-ray, compared to the vanishing faint channel, due to its deep depression and large

width. Moreover, the nucleus (5-8 kpc) dominates the emission, while the upper part of the bubble vanishes rapidly in the background (> 30 kpc). The future of this bubble is to buoy outwards and being destroyed, after few tens Myr, by the backflow and instabilities.

The third row presents the snapshots of model gr-Bi5m2 at 7 Gyr. At that stage of evolution the IGM has accumulated more turbulence, after several AGN events, promoting the diffusion of iron in a radius of 20 kpc from the centre (panel q). However, this particular moment is again dominated by another AGN outburst (2×10^{43} erg s^{-1}). The young bubble (panel c) still buoys undisturbed in the IGM, generating a slight asymmetry in the iron distribution along the jet axis, over the more uniform background.

At this time, we caught indeed the early injection phase of the outflow. A quasi-cylindrical cocoon envelops the core of the jet, which has now a velocity around 3000 km s^{-1}. The injected initial velocity was over 10^4 km s^{-1}, meaning that the jet commonly decelerates in a rapid way after few kpc. At $z = 22$ kpc the emission-weighted temperature reaches the maximum value of 1.62×10^7 K (panel g), clearly indicating the effect of shock heating. Around the contact discontinuity the gas is weakly shocked, with temperatures above 1.25×10^7 K. The average Mach number is around 1.2, a typical value found by observations (Blanton et al. 2009; Gitti et al. 2010). The arc is also visible in the SB_X map (panel m), while the decrement associated with the cavity is $\sim 35 - 40$ per cent.

Notice that the maps of this model are very similar to those of gr-C5m4, another successful model, which has analogous bubbles production. This behaviour confirms further the strict relationship between (intermittent) Bondi and cold models, as previously noted by the compared efficiency analysis.

The last row of maps (Fig. 5.8) displays another moment, typical for intermittent feedback models, like gr-Bi1m1. The big outburst and the generated bubble have vanished, leaving the system in the aforementioned turbulent phase, in which mixing distributes the low residual heating to the central IGM. Soon after this period, the gas will cool and start the inflow. The velocity field is relatively chaotic (panel d), with maximum velocity of 640 km s^{-1}, a bit lower than local speed of sound, evidently decreasing in the turbulent zones. The mixing of gas at this epoch restores the spherical symmetry of the cool core, with average temperature of $\sim 9 \times 10^6$ K (panel h). This is underlined also by the symmetric SB_x map (panel n) and by the substantial diffusion of iron at $r \sim 10 - 30$ kpc (panel r). Note that the abundance radial profile at the very centre is more peaked during this quiescent cooling flow phase ($\sim$ 0.8 $Z_\odot$), compared to the AGN outburst period. Thus, our AGN models might also explain the dichotomy of the cool-core and non-cool-core groups, having the former higher central abundances (Johnson et al. 2011).

An interesting feature, captured at this stage (often present after an AGN outburst), is the sequence of very small bubbles at $r > 15$ kpc, with typical diameter of a few kpc. The origin of this tiny bubbles is the fragmentation of the jet due to turbulent and chaotic motions, previously discussed. In this map they are in a very late phase, almost disappearing in the ambient medium. In this case they would be probably not detected in the X-ray (just a 10 per cent jump in surface brightness). To capture their signature, an observation should be done at an earlier evolutionary moment, after a big event, when the jet is rapidly fragmenting. Nevertheless, it is striking that David et al. (2009, 2011) find exactly this type of configuration in NGC 5044: few big cavities and many small

'weather-driven' bubbles (see Figure 2.2), which appear to be radio quiet (not directly inflated by the jet).

Overall, we conclude that the AGN outflows dynamics is particularly complex, as expected from the previous study in galaxy clusters (Chapter 4). The main stages of evolution for the best models are: (i) a gentle continuous outflow, which sustains the cooling flow for the majority of time (or always in the classic Bondi models) and which is barely observable in SB_X maps; (ii) a phase of large cavity inflation, with cold rims and high density/SB_X contrast (only for non-continuous models); (iii) small periods of quiescence in which the turbulence and vorticity promotes mixing and tiny weather-driven bubbles.

The presence of the above-described features (big and small cavities, asymmetry of Fe abundance, low-Mach shocks, etc.), is consistent with several recent X-ray observations of heated systems, and demonstrates the fundamental role of AGN-driven outflows in the evolution of groups.

5.5 Discussion

In this Chapter, I have carried out 3D numerical simulations of self-regulated AGN outflows in the galaxy group environment. We have followed the long-term evolution of the interaction between two main characters: radiative cooling and feedback heating. The aim of this investigation is to understand the large-scale features of the feedback process, in order to solve the cooling flow problem, i.e. quenching the cooling rates, but at same time preserving the cool-core structure.

Two relevant models, previously successful in clusters (Chapter 4), were tested: cold and hot Bondi-like feedback. Galaxy groups, with masses approximately two orders of magnitude less than big clusters are more fragile systems and the feedback must be consequently more delicate. In the following, I discuss and summarise the main results obtained, along with the merits and flaws of the computed models.

5.5.1 Hot Bondi-like Feedback

In the first set of simulations the commonly adopted Bondi prescription is applied to evaluate the accretion rate onto the black hole. Although the Bondi scenario is quite naive, it can be treated as the template model for a typical self-regulated feedback linked to entropy ($\dot{M}_{\rm B} \propto K^{-3/2}$). The efficiency, as a free parameter, might just incorporate the discrepancies between the ideal Bondi model and the real dynamics.

Overall, I found (similarly to clusters) that the Bondi accretion models are able to satisfy our main requirements for a plausible evolution, with a mechanical efficiency in the range $5 \times 10^{-2} - 10^{-1}$. As expected, the accretion rates are always two to three orders of magnitude lower than the Eddington limit. This implies that the outflow 'touch' is always delicate and non-explosive, with powers on the order of 10^{44} erg s^{-1} and velocity 10^4 km s^{-1}. These values are consistent with numerous observations of AGN outflows via absorption lines (see Chapter 2).

In the best models, cooling rates are reduced below a few or fraction of $M_\odot$ yr^{-1}, with a monotonic decrease in time. The density radial profiles of these models do not deviate too much from the observed ones. The same can be said for the temperature gradient, with a small overheating in the inner 4 kpc nucleus. The last feature is probably associated with the continuous nature of the feedback: the Bondi formula is in fact based on the accretion of hot gas, whose reservoir never drains.

A problem for this model may be the continuous injection of energy, which carves a tunnel in the IGM. However, as shown in Section 5.4, this channel is usually very narrow and almost disappears in the surface brightness image (on the contrary of buoyant bubbles). The important result is that a feeble continuous heating could operate, without being in contradiction with observations.

The lack of direct cavity inflation is another issue. However, during the increasing generation of turbulence (due to the AGN), the jet becomes gradually more disturbed: eventually it fragments, producing a series of small buoyant bubbles. This phenomenon is certainly enhanced by a cosmological evolution through merging and other large scale motions (e.g. Morsony et al. 2010). Big cavities seem nevertheless difficult to generate.

I have also checked that slightly different initial conditions, like an initial isothermal temperature profile and a NFW dark matter profile, do not alter the behaviour of the feedback, producing similar results.

5.5.2 Cold Feedback

In galaxy clusters, the triggering mechanism linked to the instantaneous cooling rate induced a very powerful outburst, often super-Eddington. In much less massive galaxy groups, such a powerful feedback would easily destroy the thermal structure observed, producing negative temperature gradients up to 100 kpc. Therefore, successful models show efficiencies about an order of magnitude lower compared to those for clusters. With ϵ between 5×10^{-4} and 10^{-3} cooling rates are still well below 10 per cent of the pure cooling flow model, but now with consistent central densities and temperatures.

The model is naturally impulsive, but this time the duty cycle is high compared to the cluster evolution. In fact, for the majority of time, the outflow is continuous with moderate power, similar to the previous Bondi models. The AGN stays in a quiescent phase only 15-20 per cent of the time, after which it will ignites with outbursts up to 10^{45} erg s^{-1}. These powerful jets are essential for creating big bubbles of 10-20 kpc diameter.

One of such event has been analysed in Section 5.4 (Fig. 5.8). The bubble does not show high temperature within (e.g. 10^8 K or more), like in clusters: it is very underdense with respect to the ambient medium, with a relatively large contrast in the SB_X map ($> 50\%$). It is striking that the metal abundance is often highly asymmetric, enhanced along the outflow direction. All the previous features are commonly present in deep X-ray observations (McNamara & Nulsen 2007; Baldi et al. 2009; Gastaldello et al. 2009; Kirkpatrick et al. 2009, 2011; Rasmussen & Ponman 2009; David et al. 2009, 2011).

Overall, it is surprising that, in galaxy groups, models with cold feedback resemble, most of the time, simulations with Bondi accretion, with the merit of adding important

features like X-ray cavities and ripples at larger radii (essentially weak shocks with Mach number around $1.1 - 1.3$). This fact clearly indicates the required property of the feedback process: if AGN outflows are the main driving mechanism, they need to be gentle and extremely frequent.

5.5.3 Hybrid feedback

Simulations using a third class of self-regulation have been carried out to test the combined effect of Bondi accretion and cold triggering mode, in order to avoid Bondi continuous injection (intrinsic in the classic formulation). In some preliminary tests (here not shown), I found that a very simple superposition of the two feedback schemes leads to unacceptable models, because the outcome is just a more powerful jet, which carves a larger and deeper continuous channel. Therefore, I tried another way to combine both methods. Keeping Bondi accretion prototype (entropy-regulated) for the value of power, I assumed that when the gas begins to cool at the centre (i.e. the inflow initiates), the feedback is activated. This prevents too peaked instantaneous outflow powers and, at the same time, the feedback acquires a duty cycle.

The results are very encouraging. The required Bondi efficiency for best models stays again in the range $5 \times 10^{-2} - 10^{-1}$. Assuming $\epsilon < 10^{-2}$, the evolution manifests the typical flaws of a pure gr-CF run. On the contrary, if $\epsilon > 10^{-1}$ the feedback becomes very explosive and easily 'burns' the cool core. The best hybrid models show instead radial profiles with gradients not far detached from the initial observed state, along with very low cooling rates (usually one or less solar masses per year).

The look of the hybrid simulations has been analysed in depth in Section 5.4. The general features are almost identical to the previous discussed models. Extensive periods of a continuous Bondi-like injection ($P_{\rm jet} \sim 10^{44}$ erg s^{-1}, $v_{\rm jet} \sim 10^4$ km s^{-1}) produce a narrow heating channel, alternated with dormant AGN phases ($\sim 15\%$). As in the cold feedback runs, the short inactivity promotes the subsequent generation of outbursts with greater power (3-4 times more than the continuous phase), producing important observed features, such as tens of kpc cavities and oscillations in the flow quantities.

It is relevant to note that, as in previous good cold models, only a fraction of the injected mechanical energy is used to inflate the cavities (usually under 50 per cent[13]). One of the main results, also pointed out in Chapter 4, is that the success of a feedback crucially depends on how the energy is transferred to the surrounding medium, not only on the total amount of available energy. Furthermore, the heated flow has a very complex dynamics, with numerous facets. After the mechanical energy is injected in the system, a part of energy inflates the bubble, but the rest generates the cocoon and weak shocks. When the jet is more continuous, the moderate energy released at intermediate radii induces a turbulence growing in time. These chaotic motions permit a more efficient circulation of the hot gas, promoting the deposition of energy through mixing at the base of the jet, where the cooling tends to dominate. Furthermore, while the system

[13]For instance, the inflation energy of the bubble in Fig. 5.8, panel b, is $4\,PV \sim 4\,(2 \times 10^{-11}$ erg cm$^{-3})\,(1.1 \times 10^{68}$ cm$^3) \approx 9 \times 10^{57}$ erg, while injected mechanical energy is 2.45×10^{58} erg. Thus, the inflation energy is just 37% of the total injected energy in that single event.

becomes more turbulent, the feeble jet can be fragmented and can cyclically produce tiny bubbles, few kpc in size (albeit very faint in the SB_X map). Their buoyant motion may promote additional mixing and heating, helping the global feedback process. Quite simple feedback models still generate an amazing variety of heating processes.

As a concluding remark for these models, the efficiency comparison (last row in Fig. 5.5) underlines again the strict relationship with the cold best models, exactly around $\epsilon_{\rm cold} \sim 5 \times 10^{-4} - 10^{-3}$. We can therefore affirm that the feedback in galaxy groups, able to quench the cooling flow but at the same time preserve the cool-core structure, is globally only of one type: moderate, gentle, often continuous and turbulent, with very short periods of inactivity and following outbursts.

5.5.4 Rejected Models

It is also interesting to highlight the main features of unsuccessful models, in order to understand why some kinds of feedback do not work.

First of all, while a small part of the total injected energy could be in thermal form (Sec. 5.3.13), above a threshold fraction of ~ 50 % the centre of the group becomes too hot with respect to the observations (see also Brighenti & Mathews 2002, 2003). Injection of a modest amount of thermal energy can have the beneficial effect of disrupting the otherwise ordered structure of the outflows. This model intermittently eliminates the long tunnel, usually not observed in real systems. Moreover, the deposition of heat in the nucleus helps preventing the formation of a cold torus. Injection of thermal energy can be justified assuming that shocks heat the hot IGM in the unresolved core.

Another rejected model considers the active outflowing mass directly linked to the real accreted mass onto the BH (inflow-outflow feedback; Sec. 5.3.14). The main problem is that, even with very low $f_{\rm in}$ (thus $f_{\rm out} > 0.9$), the jet velocity often exceeds 10^5 km s^{-1}. This unappealing result can in principle be fixed adding a mass loading factor ($\eta_{\rm load} f_{\rm out}$; see also Cattaneo & Teyssier 2007; Ostriker et al. 2010). However, this assumption would mimic entrainment, just as our standard outflow generation method. It is thus not surprising that we recover acceptable results, similar to those discussed previously.

Intermittent models (Section 5.3.12), with fixed jet power, are only partially acceptable, as also found for galaxy clusters. The most successful run has relatively weak outflows ($P_{\rm jet} \sim 10^{-4} P_{\rm Edd}$), activated every 10 Myr, with a duration of 5 Myr each. I have also tested jets with Eddington power ($\sim 10^{47}$ erg s^{-1}). As expected they will destroy the cool core generating systems very different from the real ones.

The major flaw of the intermittent models is their artificial nature. Cooling rates can be suppressed, compared to a pure cooling flow, but the central temperature profiles oscillate strongly. This further supports the common notion that heating *must* be self-regulated.

5.5.5 Comparison with other Works

Regarding clusters, we can account for several variegated computations (e.g. Omma et al. 2004; Ruszkowski et al. 2004a; Brüggen et al. 2005; Brighenti & Mathews 2006;

Sternberg et al. 2007), but very little work has been done to explore the role of AGN heating in the intragroup medium evolution, especially from a theoretical and numerical point of view.

Brighenti & Mathews (2003) studied thermal heating (plus conduction) in 2D simulations, showing that this type of feedback, while very efficient in stopping the cooling process, often generates negative temperature gradients, with the total erasure of galactic cooling flows commonly observed in gE (Sun et al. 2005, 2007).

Zanni et al. (2005) studied the purely hydrodynamical evolution of a single jet outburst for a short time (few 100 Myr). Their 2D cylindrical simulations do not implement radiative cooling, nevertheless, they found a consistent $L - T$ relation, suggesting again the high importance of AGN jets.

Unfortunately, carrying out large cosmological simulations (Puchwein et al. 2008; McCarthy et al. 2010) does not permit, nowadays, a detailed analysis of the feedback physics in the inner cool core, mainly because of the lack of resolution, and they are thus more suited to study global sample-averaged properties. Furthermore, none of the above-mentioned works has investigated a purely mechanical feedback, but only hybrid solutions, usually ending up with a strong thermal injection (similar to Cattaneo & Teyssier 2007). Finally, almost all cosmological simulations use Bondi accretion, with an ad-hoc boosting factor ($\sim 100\times$), in order to inject a significant feedback energy.

For all these reasons it is practically impossible to make a comparison with cosmological simulations. There is also one numerical argument to highlight. Today there is still much controversy between SPH (lagrangian) and grid (eulerian) cosmological simulations (e.g. Borgani et al. 2002; Younger & Bryan 2007), finding often different results. A serious problem concerns the temperature profiles which emerge from the pure cooling flow calculations (possibly due to numerical effects): these runs often present negative or flat gradients at several times, in contradiction with the typical substantial T decrement that should normally occur (Figs. 4.4 and 5.3; Brighenti & Mathews 2002a). Such different behaviour could profoundly alter the computations with the AGN feedback activated. In future, I intend to test the feedback studied in this Thesis in a fully cosmological simulation, adopting a very high resolution thanks to the AMR capabilities.

5.5.6 Comparison with Galaxy Clusters

The simulations presented in this Chapter show that AGN heating has a deeper impact in galaxy groups than in clusters, because the same mechanical power per particle has a greater effect for a lighter, less bound systems. As seen in the previous Sections, a jet with Eddington power can easily erase the entire thermodynamic structure of the cool core. The same applies for all the self-regulated simulations with very high efficiencies ($> 5 \times 10^{-3}$ for cold models; $> 10^{-1}$ for Bondi feedback). In Chapter 4, I showed that consistent cold models tend to produce super-Eddington outbursts ($> 10^{47}$ erg s^{-1}), with a low frequency (~ 10 per cent). Despite the huge power injected, the shock-heating phase can not destroy the observed density and temperature gradients, and the cluster quickly restores the usual cool core. The only marked consequences are more ripples at larger radii and cavities, which in the early phase present high internal energy and shocked rims.

On the contrary, galaxy groups, with much less binding energy (per particle), can not recover from the same strong impulsive feedback. In order to prevent such 'heating catastrophe', cold feedback models in galaxy groups require an efficiency at least $5 - 10$ times lower. The outcome is striking, because the evolution resembles that of Bondi models, with low power jets ($10^{44} - 10^{45}$ erg s^{-1}) activated in a quasi-continuous gentle way. These outbursts, occurring after short quiescence periods (tens Myr), generate $\sim$ 10 kpc cavities surrounded by relatively cold rims in the region close to the centre of the group, similar to some observations (e.g. Gastaldello et al. 2009). Unlike in galaxy clusters, cavities in groups present the usual low density contrast with temperatures similar to the surrounding medium, even if young.

The best models assuming classic Bondi accretion, on the other hand, are equivalent in both clusters and groups (except for the efficiency, lower in groups). Accretion rates always follow a sub-Eddington regime. The moderate outflows carve a narrow tunnel in the IGM, which is very faint in the SB_X map and thus hard to resolve. The absence of inflated bubbles is still a riddle for this type of feedback. In galaxy clusters the low-power outflows ($\epsilon = 0.1$) have more difficulty in halting the massive cooling flow (tens $M_\odot$ yr^{-1}), showing more peaked density profiles. Therefore, in the cluster, cold accretion was favoured as an acceptable model.

Another common feature in both clusters and groups is the asymmetrical distribution of metals (mostly iron) produced by the SNIa in the central galaxy. They tend to accumulate along the jet axis, in agreement with recent observations (Rasmussen & Ponman 2009; Kirkpatrick et al. 2009, 2011; David et al. 2011).

In the successful group models the sub-Eddington outflow powers imply that the total injected energy (a few 10^{61} erg) is always an order below the total 'available' BH energy. In fact, during the simulated evolution, the BH mass increases at most 10 per cent in Bondi models. In the cold feedback models the lower ϵ imply a much higher $\Delta M_{\rm BH}$, similarly to clusters. However, the real efficiency (free parameter) could be just higher, with a lower mass actually falling onto the BH. Our simple approximation of the real sub-pc accretion does not allow to answer why the efficiency in groups should be a factor 5-10 smaller than in clusters, besides the strong observational requirement of the cool core survival. A future dedicated investigation on the detailed accretion process may provide this answer.

As a concluding remark, I argue that the discrepancies in the scaling relations, like the entropy floor and the steepening in the $L - T$ relation (Sec. 5.1), should be deeply linked to the AGN feedback, which - as we have shown - can easily modify the main physical properties of the group, compared to the idealised self-similar evolution. A fully cosmological simulation, with a larger sample, is required in order to further support the present study, limited to a single relaxed object.

I refer the reader to the final Chapter for the bullet conclusions, which briefly summarise also the points discussed in this Chapter. In the next pages, I continue to tackle the cooling flow problem in even lower mass systems, i.e. elliptical galaxies. In order to be successful, the proposed feedback mechanism must in fact work in every type of hot halo system.

Chapter 6

AGN Feedback in Elliptical Galaxies

THE THIRD type of virialised structures in the universe, possessing a (substantial) hot gas halo, are elliptical galaxies (Es), also known as early-type galaxies. Since any relatively dense plasma should have a cooling time lesser than the Hubble time, we expect to observe cooling flows also in elliptical galaxies, in analogy with galaxy clusters (Chapter 4) and groups (Chapter 5). Single isolated galaxies are even less bound objects, compared to groups and clusters, and thus the same successful AGN feedback mechanism should work in a lower regime, in order to avoid drastic overheating or totally emptying the galaxy for several Gyr.

In the present Chapter, I study how the AGN feedback self-regulates in a galactic environment and test the models against several observational constraints. Massive elliptical galaxies are in fact important laboratories to study the AGN feedback process in the local universe. Their ISM shines in X-ray and many giant ellipticals are relatively nearby, within a distance of $\sim 15 - 30$ Mpc, a valuable virtue compared to X-ray bright, but distant, massive clusters. The relative proximity allows thus the investigation of a region closer to the AGN, where the feedback engine might manifest itself in a clearer way.

As in the previous two Chapters, I first provide a brief overview of elliptical galaxies, with emphasis on the hot gas halo, before diving into the results of the AGN feedback simulations. For further details on early-type galaxies I refer the reader to the comprehensive review of Mathews & Brighenti (2003). The results of this Chapter are also presented in Gaspari et al. (2012b).

6.1 Elliptical Galaxies Overview

Following Hubble (1936), we still classify galaxies as ellipticals, spirals and irregulars. This classification is based only on the apparent morphology of the galaxy. In the Hubble sequence E0, E1, E2, ..., E7, the number[1] is related to how flattened the ellipse

[1]The ellipticity is defined as $\varepsilon = 10\,(1 - b/a)$, where b and a are the projected angular extent of the minor and major axis, respectively.

appears (through the isophotes), with E7 corresponding to a very elongated ellipse. The morphology correlates also with the stellar population content, with typical ellipticals being redder than other galaxies. E galaxies exhibit indeed far less evidence for young stars and dust than spiral galaxies. As a consequence, astronomers often refer to them as early-type galaxies (ETG).

The total masses of elliptical galaxies cover a large range: from 10^7 up to 10^{13} $M_\odot$. The corresponding range of diameters is about 0.1 kpc up to $\sim$ 100 kpc, with absolute blue magnitudes in the range from -8 to -23. Thus, the smallest of the E galaxies, dwarf ellipticals, are only slightly larger than globular clusters, while the giant elliptical galaxies, like M87 and NGC 5813 (Fig. 6.1), are among the largest galaxies in the universe.

Assuming the ΛCDM hierarchical cosmology, elliptical galaxies form through a sequence of galactic mergers (in contrast to the older scenario of monolithic collapse). although the build-up should still be considerably fast ($z \sim 2$; Cimatti et al. 2004). Observations indicate that the most massive ETGs reach the completion of star formation and assembly first (the downsizing scenario; see Cimatti 2009 for a review). Overall, ETGs are the building blocks of galaxy groups, and later, of clusters. Several properties tackled in the previous Chapter can therefore be applied also to ellipticals, although with some distinction (for instance, since Es are the oldest collapsed structure, they may be less disturbed by ongoing mergers).

The two main sources of the hot gas (known as interstellar medium – ISM) in elliptical galaxies are internal and external. Evolving stars inside the galaxy continuously eject gas at a rate of $\sim$ 1 $M_\odot$ yr^{-1}, which becomes shock-heated to the virial temperature. The large X-ray luminosities of massive ellipticals, $L_x \sim 10^{41} - 10^{43}$ erg s^{-1}, indicate that the hot gas is trapped in the galactic potential (the halo extension increases with L_x). The external reservoir of gas is instead provided by the cosmological inflow linked to the group or cluster environment. Most of the massive Es appear to reside at the centre of dense environments and deep potential wells; purely isolated galaxies are rather rare, yet possessing some kind of moderate hot gas halo.

The electron density of the hot plasma in giant elliptical galaxies is typically $n_e \sim 0.1$ cm^{-3} at the centre and declines with radius as $n_e \propto r^{-1}$. The total mass of hot gas in massive E galaxies can even reach up to $\sim 10^{11}$ $M_\odot$. All the plasma processes studied in Section 1.1 are therefore relevant also in elliptical galaxies. The (iron) abundance in the plasma usually increases from $Z_{Fe} \sim 0.2 - 0.4$ $Z_\odot$, beyond the optical image, to few $Z_\odot$ in the centre. At early times, the ambient was enriched in metals by SNII that accompanied the formation of the dominant old stellar population. At later times, further enrichment has been provided by SNIa and material expelled from red giant stars (e.g. Loewenstein & Mathews 1991; Finoguenov & Jones 2000). It is worth noting that the heating linked to SNIa and stellar winds can only drive a galactic outflow in low luminosity ellipticals (e.g. Ciotti et al. 1991), with a very shallow gravitational potential, but not in X-ray bright ellipticals.

To a good approximation, the global hot gas in ellipticals is in hydrostatic equilibrium, because systematic and turbulent velocities are subsonic; the typical sound speed is $c_s \sim 500$ km s^{-1}, with a sound crossing time $t_{sc} \sim 10^7$ yr. Thus, Equation 4.4 can be used to retrieve the total mass (see Humphrey et al. 2006). The observed values for the β

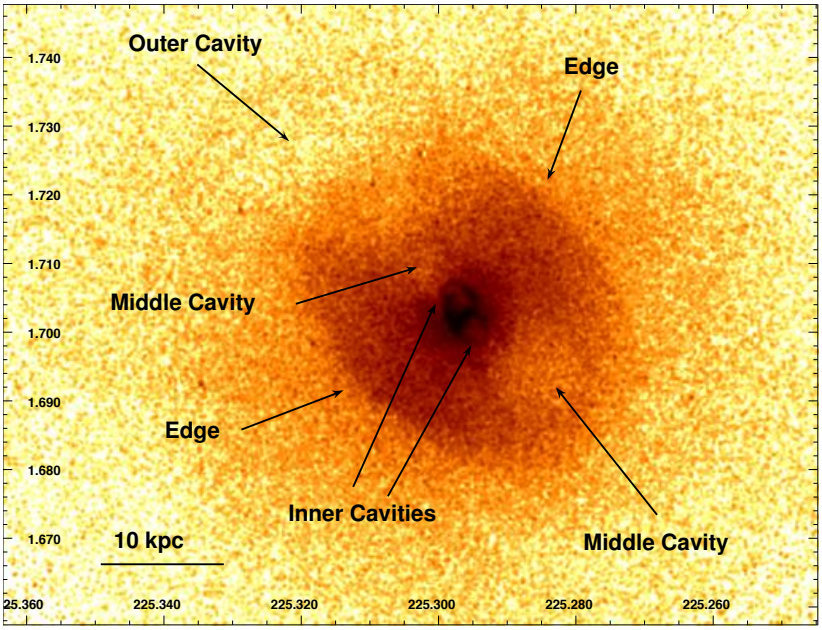

Figure 6.1. *Chandra* image (0.3-2.0 keV) of NGC 5813, a typical bright E1 galaxy (from Randall et al. 2011). The image shows two pairs of cavities (with bright rims), plus an older outer cavity, and two sharp edges being consistent with shocks.

parameter (Sec. 4.1) are ~ 0.6, clearly requiring a dark matter component.

If elliptical galaxies were perfectly homologous stellar systems with identical stellar populations, then the central velocity dispersion σ_0, stellar mass M_* and half-light (effective) radius R_e would be related via the virial theorem, $\sigma_0^2 \propto M_*/R_\mathrm{e} \propto (L/R_\mathrm{e})(M_*/L)$. Instead, stellar population variations[2] place real Es on a nearby fundamental plane (Kormendy & Djorgovski 1989):

$$R_\mathrm{e} \propto \sigma^{1.4}\, I_\mathrm{e}^{-0.9}\,, \tag{6.1}$$

where $I_\mathrm{e} \propto L/R_\mathrm{e}^2$ is the surface brightness inside the effective radius (usually in the V band). The width of the fundamental plane is remarkably small (Renzini & Ciotti 1993; the power indexes have a typical deviation ± 0.1). In projection, the fundamental plane provides several famous scaling relations for ellipticals, like the well-known Faber-Jackson relation $L \propto \sigma_0^4$.

Elliptical galaxies usually present a stellar SB profile following the de Vaucouleurs' prescription, $\ln I \propto R^{1/4}$ (Equation 3.24), determined only by R_e and M_*. The profile seems a natural consequence of hierarchical mergers (Bender 1996). The dark halo mass starts to dominate only for $r > R_\mathrm{e}$, typically with a NFW halo. In spite of these regularities Es show two types of morphology: low luminosity ellipticals have power-law central stellar density profiles, disky isophotes, and oblate symmetry consistent with their moderate rotation; on the other hand, high luminosity galaxies ($M_\mathrm{V} \lesssim -20$) have flatter stellar cores within $\sim$ 100 pc, boxy isophotes, and aspherical structures caused by anisotropic stellar velocities, without significant rotation (Kormendy & Bender 1996). Finally, several ellipticals present a kinematically decoupled core, usually revealing a

[2]For instance, the stellar mass-to-light ratio slowly varies as function of the galaxy mass.

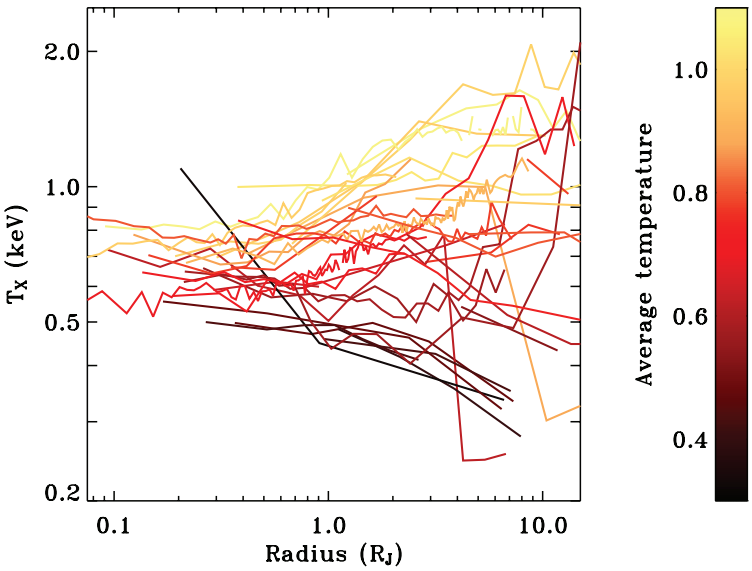

Figure 6.2. Projected temperature profiles of 36 elliptical galaxies observed by *Chandra*, as a function of radius (scaled by the J-band effective radius R_J). The profiles are coloured according to the luminosity-weighted average temperature (from Diehl & Statler 2008b).

dense and cold rotationally-supported disk (possibly a byproduct of the quenched cooling flow; see Chapter 7).

The X-ray luminosities correlate well with the B-band luminosity, L_B, with a steepening observed for larger ellipticals ($L_X \propto L_B^2$), although with large scatter (O'Sullivan et al. 2001). It is quite interesting that the optical and X-ray surface brightness profiles are almost identical for typical bright ellipticals, like NGC 4472 (Trinchieri et al. 1986), id est $\rho_* \propto n_e^2$.

The gas temperature profile in the group-dominant E galaxies ($T_{vir} \sim 10^7$ K) rises from a minimum value near the galactic centre to a maximum at several R_e (Figure 6.2; lighter curves). The (fewer) isolated ellipticals are typically associated with a lower mean temperature ($\lesssim 7\times10^6$ K) and an interesting T gradient with a negative slope (Figure 6.2; darker curves), due to the increasing importance of compressional heating. It is striking that the central temperature is always maintained around $\sim 6-8\times10^6$ K (Diehl & Statler 2008b), an indication that the required AGN heating should be frequent and gentle.

As in groups, massive Es has somehow acquired an additional entropy $K \sim 100$ keV cm^2 in excess of that received in the cosmic accretion (known as the entropy floor; Ponman et al. 1999). Early preheating by ~ 1 keV per particle could explain the aberrant behaviour of low mass systems in both the $L_X - T$ and $K - T$ relations (Borgani et al. 2001, 2002). However, given the strong energy input of AGNs, the gas could be simply heated after collapsing in the dark halos.

About 80% of elliptical galaxies have dusty[3] clouds, lanes, or disks within the central few kpc (Martel et al. 2000; Tran et al. 2001; Colbert et al. 2001; Verdoes Kleijn et al. 2002), with associated gas masses $10^4 - 10^7$ $M_\odot$. Some of the Hα-emitting gas is undoubtedly related to the photoionised boundaries of these dusty clouds (Goudfrooij

[3]Dust emission is observed in the infrared band (tens μm).

et al. 1994; Ferrari et al. 1999). A few investigations suggest that dusty filamentary cores are related to recent AGN outbursts (e.g. Temi et al. 2007), albeit it is not trivial to explain the survival of the grains in such hot environments.

As in clusters (Chap. 4) and groups (Chap. 5), several elliptical galaxies exhibit the same amazing AGN features (e.g. Biller et al. 2004; Machacek et al. 2006, 2011; Diehl & Statler 2008a,b; Baldi et al. 2009; O'Sullivan et al. 2011c; Giacintucci et al. 2011; Randall et al. 2011; Gitti et al. 2012). For further insights about X-ray cavities (typically filled by the jet radio emission), weak cocoon shocks, metal enhancements, and turbulence, I refer to the previous introductions and in particular to Chapter 2. Figure 6.1 depicts an exemplary case of AGN feedback in ellipticals. It is worth noting that a strong support for AGN heating has been provided by Allen et al. (2006), who measured the mechanical energy associated with X-ray cavities in nine bright elliptical galaxies. Besides a tight correlation between the 'Bondi' accretion rate[4] and the mechanical energy injected into the ISM, they found that the *mechanical* input is sufficient to prevent the gas from cooling. However, fundamental questions still remain unanswered: can the AGN mechanical energy properly couple to the surrounding medium, even in the low-density environment of elliptical galaxies?

On the galactic scale, the lower X-ray luminosities imply a typical pure cooling flow rate of few $M_{\odot}$ yr^{-1}, which exceeds by 10-20 times the observed cooling rate in typical massive ellipticals ($\sim 0.1\ M_{\odot}$ yr^{-1}; Peterson et al. 2001, 2003; Oegerle & Hill 2001; Xu et al. 2002; Tamura et al. 2003; Bregman et al. 2001, 2005, 2006). Another piece of evidence for the reduced cooling rates comes from the lack of significant star formation in most Es (e.g. Ferreras & Silk 2000; Trager et al. 2000; Graves et al. 2009; Jeong et al. 2009), which are typically located in the quiescent part of the infrared colour-colour diagram (Temi et al. 2009).

The problem of ISM heating and the related absence of cold gas/star formation in E galaxies is long-lasting. This was investigated forty years ago by Mathews & Baker (1971) seminal work, proposing that SNIa heat and eject the ISM, which is continuously supplied by stellar winds from evolving stars. Subsequent investigations (MacDonald & Bailey 1981; Mathews & Loewenstein 1986; Loewenstein & Mathews 1987; Ciotti et al. 1991; David et al. 1991) have analysed in depth the secular evolution of the ISM in isolated ellipticals. Furthermore, galaxy formation theory requires a mechanism to halt star formation in order to agree with the observed sharp cut-off of the luminosity function at the high-mass end (Benson et al. 2003; Balogh et al. 2006; Croton et al. 2006; Cattaneo et al. 2009). It is now clear that supernova heating alone is insufficient to prevent the gas from cooling and forming stars (e.g. Tornatore et al. 2003; Piontek & Steinmetz 2011). The supermassive black hole at centre of the system becomes therefore the natural suspect for providing the required heating.

[4]The Bondi radius is basically never resolved and only inferred from the extrapolated profiles.

Table 6.1. Parameters and properties of the most relevant elliptical galaxy simulations.

Model	Feedback	Efficiency ϵ	Jet width × height (kpc)	Injection	Notes
iso-CF	no AGN heating	-	-	-	isolated E
cgg-CF	no AGN heating	-	-	-	gE + CGG
iso-C1m4	cold	10^{-4}	0.30×0.15	entrainment	self-regulated
iso-C3m4	cold	3.3×10^{-4}	0.30×0.15	entrainment	self-regulated
iso-C1m3	cold	10^{-3}	0.30×0.15	entrainment	self-regulated
cgg-C8m4	cold	8×10^{-4}	1.00×1.00	entrainment	self-regulated

Radiative cooling (Z self-consistently from stellar evolution): Runge-Kutta (2nd), plus cold mass dropout ($T \lesssim 2 \times 10^4$ K; free-fall time delay).

Supernovae Ia & stellar winds: isolated galaxy (Sec. 6.2.1) or NGC 5044 (Sec. 6.2.2).

6.2 Simulation Setup

In the previous two Chapters, I have shown that massive, subrelativistic outflows are a viable mechanism to solve the cooling flow problem either in clusters or groups. In lighter systems the AGN feedback must be however more gentle and continuous; in fact, only the massive galaxy clusters can easily recover from sporadic, very powerful outbursts, even if a low-power activity may still be present. With the following investigation on elliptical galaxies, either isolated or group-dominated, I close the circle, extending the theoretical modelling of self-regulated massive outflows to every cosmological structure with a substantial hot gas halo.

In Table 6.1 are summarised all the numerical details of the hydrodynamic simulations carried out with FLASH, including the type of feedback (Sec. 3.7), the efficiency, the jet width and height ($d_{\rm jet} \times z_{\rm jet}$), and other relevant properties (see Chapter 3 for the details of implementation). As usual, the hydrodynamic equations will be solved via the split PPM solver (Sec. 3.2). All the galaxy group computations use the RK2 solver for radiative cooling (Z is self-consistently calculated from the stellar evolution), with cold gas dropout enabled (Sec. 3.5). The outflows are cylindrical, always injected inside the domain, according to the entrainment scheme (Equation 3.18).

On the group scales, the self-regulation imposed by cold gas accretion tends to generate on average a very frequent gentle feedback, qualitatively similar to what expected for a boosted (by a factor ~ 100) Bondi accretion. However, during the evolution more powerful events occur, producing visible cavities and shocks. Cold feedback seems thus a more consistent self-regulation mechanism. Since the E galaxy simulations are extremely expensive, I only compute models with this preferred method, linking the feedback to the cooled (dropped) gas, which is now assumed to accrete in about a free-fall time onto the black hole (see Sec. 3.7 for the details of this slightly improved implementation).

6.2.1 Isolated Elliptical

I choose to model the elliptical galaxy with a de Vaucouleurs' stellar density profile (Sec. 3.8), with effective radius $R_{\rm e} = 8.5$ kpc and total stellar mass $M_* = 7 \times 10^{11}\ M_\odot$. Assuming a stellar mass-to-light ratio of 8 in the B band, appropriate for an old stellar population, the resulting luminosity is $L_B = 8.75 \times 10^{10}\ L_\odot$. Thus, our model represents a typical elliptical galaxy similar to NGC 4649, NGC 4472 and many others in the local universe, although without their circumgalactic gas. The dark matter is modelled as a NFW halo with virial mass $M_{\rm vir} = 4 \times 10^{13}\ M_\odot$ and a concentration $c = 8.8$ (Humphrey et al. 2006). Note that inside $R_{\rm e}$ the dynamics is governed by the galaxy potential. Stellar winds and SNIa are modelled according to the usual semianalytic prescription (see Sec. 3.8).

In the 'isolated galaxy', the ISM is produced by internal processes alone (stellar mass loss and SNIa ejecta). Although the hot ISM of massive, X-ray bright ellipticals can not be realistically explained without a circumgalactic gas component (Brighenti & Mathews 1998, 1999), we use this approach for its simplicity and to allow a direct comparison

with previous calculations of hot gas flows in ellipticals (e.g. Loewenstein & Mathews 1987; Ciotti et al. 1991; Ciotti & Ostriker 1997). Within $\sim R_e$ most of the ISM is indeed likely to come from stellar mass loss (Brighenti & Mathews 1999). Thus, the terminology 'isolated' galaxy does not refer to the presence of other (large) galaxies nearby, but that the ISM is not largely contaminated by the group or cluster gas.

The simulations of the isolated galaxy start at cosmic time $t = 1$ Gyr, with the galaxy essentially devoid of gas, conforming to the usual assumption that the gas has been cleared by a SNII-driven wind. The ISM is then gradually supplied by the stars. After few 10^8 yr, the system loses memory of the initial conditions and, if not heated, approaches a quasi-steady state with secular changes controlled by the slow variation of stellar mass loss (Loewenstein & Mathews 1987; Ciotti et al. 1991). The simulations are evolved to the final time, 13 Gyr.

The computational rectangular 3D box extends up to 150 kpc, with the same boundary conditions adopted in the previous Chapters. I employed a set of 7 grid levels (basic blocks of $16 \times 16 \times 8$ points), with the finest, inner grid reaching a resolution of $\Delta x \approx 146$ pc.

6.2.2 Elliptical with Circumgalactic Gas

In the second class of models, more realistic and appropriated for a detailed comparison with well-observed galaxies, we take into account the presence of the circumgalactic gas (CGG). Many of the famous well-observed ellipticals belong to this breed. A distinctive characteristic of classic cooling flow models with CGG is the presence, often observed in real systems, of a relatively broad cool core, in perfect analogy with galaxy clusters (Brighenti & Mathews 1998, 1999; Humphrey et al. 2006; Diehl & Statler 2008b). The separation between galaxies with CGG and galaxy groups is largely semantic, so these models are tightly linked to those calculated in Chapter 5. However, here we focus mainly on the region close to the galaxy ($r \lesssim R_e$), with higher resolution and a slightly improved cold feedback method (free-fall time delay).

The galaxy parameters are chosen to agree with NGC 5044, the X-ray bright galaxy in the centre of the homonymous group, with $R_e \approx 10$ kpc, $M_* \approx 3.4 \times 10^{11}\ M_\odot$ and $M_*/L_B \approx 7.5$ (Buote et al. 2004). In these simulations I use the observed $T(r)$ and $n(r)$ profiles (David et al. 1994; Buote et al. 2003; dotted lines in Figure 6.6), in order to retrieve the total potential under the assumption of hydrostatic equilibrium. The CGG model is integrated for 7 Gyr. Due to the high computational cost of these runs, the resolution is lowered, $\Delta x \approx 293$ pc, compared to the isolated galaxy simulations. The box is instead 4 times larger (with 8 levels), $L \approx 600$ kpc.

6.3 Results: Isolated Elliptical

In this Section, I report the results for models in which the ISM is produced only by the mass loss of the galactic stellar population. I explore the effect of the mechanical feedback varying the key parameter, the efficiency ϵ (Table 6.1). I recall that in order to solve the cooling flow problem, AGN outflows must quench the cooling flow, without

overheating the ISM in a drastic way. The former request is easy to satisfy, if the feedback is energetic enough. The simultaneous fulfilment of the two conditions above is instead complicated. A successful feedback needs also to reproduce other observational features, such as cavities, shocks, turbulence, multiphase gas and metals dredge-up.

6.3.1 Pure Cooling Flow

In Figure 6.3, I show the relevant global quantities which characterise a pure cooling flow model in an isolated elliptical galaxies, with AGN heating switched off and the heating provided mainly by the SNIa. The densest gas loses thermal pressure support due to radiative losses, inducing a slow subsonic inflow ($v_{\rm r} \lesssim 50$ km s^{-1}) that further increases the plasma emissivity. I emphasise that when no AGN heating is considered, the gas cooling rate (top panel), occurring at the very centre of the galaxy, roughly decreases in pace with the stellar mass loss ($\dot{M}_* \propto t^{-1.3}$), reaching $\dot{M}_{\rm cool} \sim 1\ M_\odot$ yr^{-1} at $t = 12.7$ Gyr, when the simulation ends. Needless to say, this is a much larger cooling rate than allowed by the spectroscopic observations (Sec. 6.1).

The X-ray luminosity also secularly drops, from $L_{\rm x} \sim 5 \times 10^{42}$ erg s^{-1} at $t = 2$ Gyr to $\sim 9 \times 10^{41}$ erg s^{-1} at final time. I refer here to the bolometric X-ray luminosity, calculated within $r \lesssim 200$ kpc. The reason for the luminosity drop is the decline of the ISM density illustrated in the middle panel of Figure 6.3. The slope of the density radial profile does not vary significantly with time and, as expected, is too steep at the centre, a well known problem of classic cooling flow models (Sarazin & White 1988; Sarazin & Ashe 1989).

I also note that classic cooling flows in isolated galaxies lack the large cool core typical of cooling flow clusters or groups (see the spectroscopic-like[5] temperature profile in the third panel). Instead, the temperature monotonically increases toward the centre (except for the very inner region). This can be understood because the steep gravitational potential associated with the peaked de Vaucouleurs' density profile (the dark halo is sub-dominant within $\sim R_{\rm e}$) provides enough gravitational heating to the inflowing (and thus compressing) gas to balance the radiative losses (needless to say, this process terminates when the gas reaches the centre, where it cools catastrophically).

Ideally, we would compare the profiles with a well-observed elliptical which is at the same time massive *and* isolated. However, most of the known giant ellipticals reside at the centre of groups or clusters and their hot ISM is contaminated by the CGG. NGC 6482 is one of the few massive and X-ray bright ellipticals with a negative temperature gradient (Khosroshahi et al. 2004) and I show the data of this system in Figure 6.3 for comparison. On the other hand, NGC 6482 presents some differences compared to our model. The dark halo is less massive (Khosroshahi et al. 2004; Humphrey et al. 2006) and it owns a relatively extended X-ray halo with $L_{\rm x} \sim 10^{42}$ erg s^{-1}, likely contaminated by CGG. Nevertheless for $r \lesssim R_{\rm e}$, i.e. the region more relevant to our investigation, the hot gas should be dominated by the internal component only.

[5]To be more adherent to X-ray observations, throughout this Chapter I compute projected temperatures via the more realistic spectroscopic-like method suggested by Vikhlinin (2006). $T_{\rm sp}$ seems nevertheless similar to the emission-weighted temperature in the majority of cases.

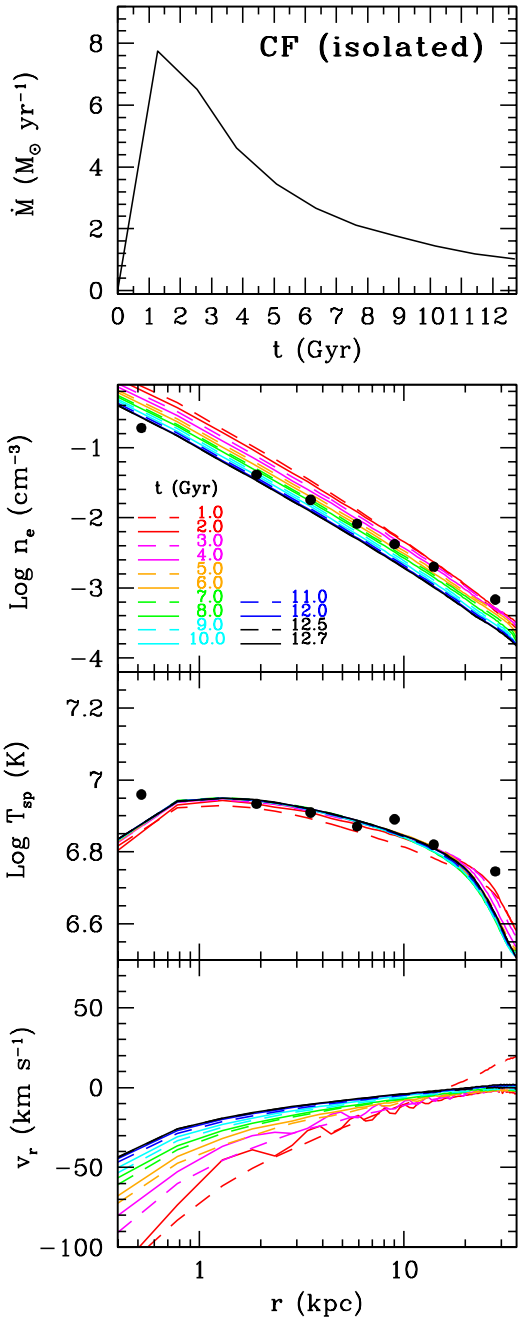

Figure 6.3. Evolution of the cooling flow model (no AGN feedback), for the isolated galaxy (iso-CF). From top to bottom panel: gas cooling rate ($\dot{M}$) as a function of time, radial profiles of electron number density (n_e), projected spectroscopic-like temperature (T_{sp}), and radial velocity (v_r). Times and colours are indicated in the second panel. Filled circles represent observational data points for the elliptical galaxy NGC 6482 (Khosroshahi et al. 2004; Diehl & Statler 2008b).

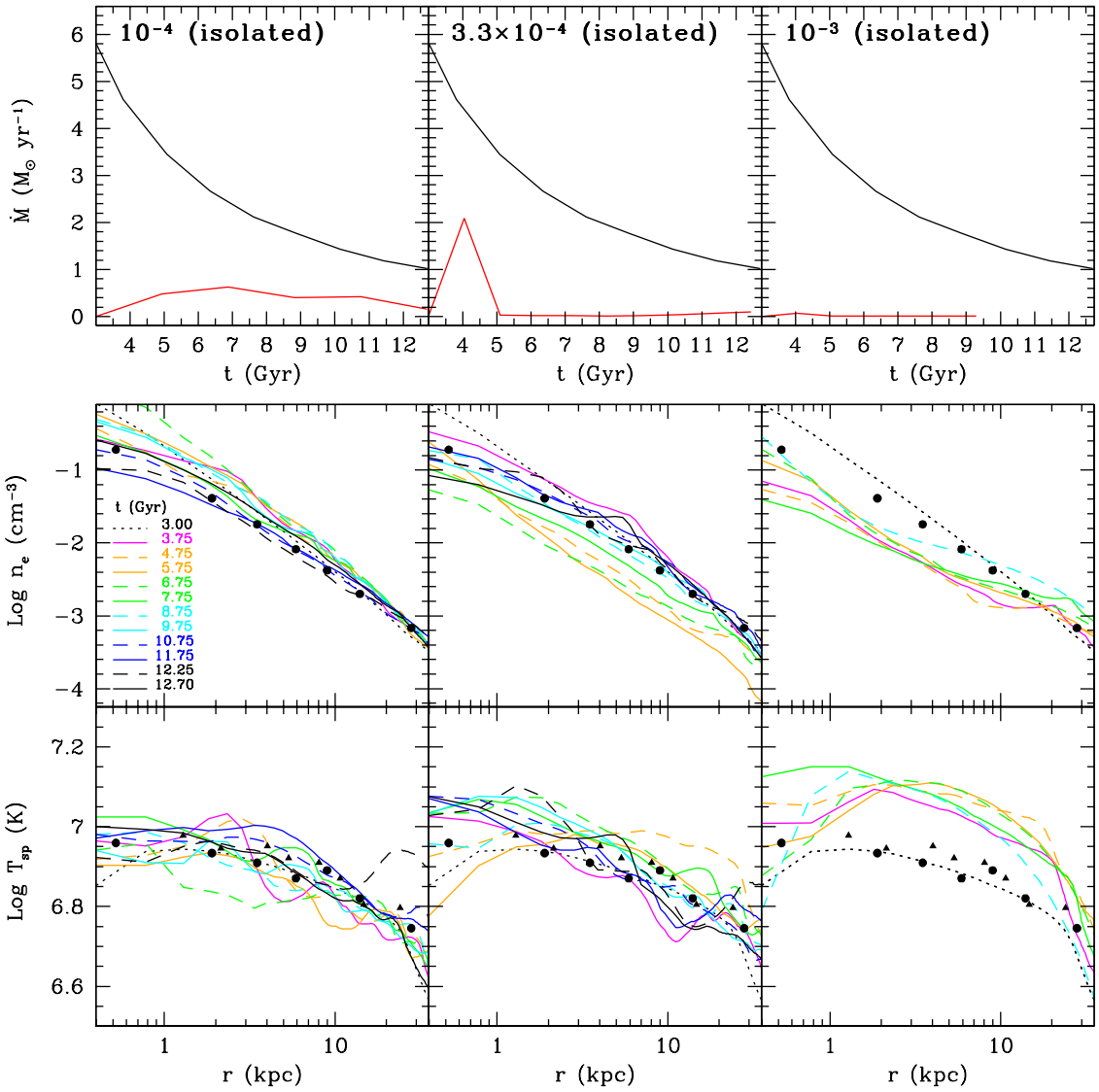

Figure 6.4. Isolated galaxy models with AGN feedback and increasing mechanical efficiency (from left to right): $\epsilon = 10^{-4}$, 3.3×10^{-4}, and 10^{-3}. From top to bottom: cooling rate versus time, radial profiles of electron number density and spectroscopic-like temperature (at twelve times).

6.3.2 Cold Feedback: $\epsilon = 10^{-4}$ [iso-C1m4]

I now describe some results for the simulations with AGN feedback, progressively increasing the efficiency and focusing on their global properties. I compare them with the cooling flow model discussed above and perform a critical analysis of the observable quantities. Figure 6.4 shows the gas cooling rate, plus the radial profiles of electron number density and (projected) spectroscopic-like temperature, for three representative (cold) feedback models.

In the first column, top panel, the model with $\epsilon = 10^{-4}$ (iso-C1m4) exhibits a cooling rate significantly reduced compared to the iso-CF simulation (red vs. black line), with an average value of $\sim 0.4\ M_\odot\ \mathrm{yr}^{-1}$ and $\dot{M}(12.7\,\mathrm{Gyr}) \sim 0.2\ M_\odot\ \mathrm{yr}^{-1}$. These values are probably still a bit too high compared to available X-ray and UV observations (Bregman et al. 2001, 2005; Xu et al. 2002; Tamura et al. 2003) or star formation estimates in

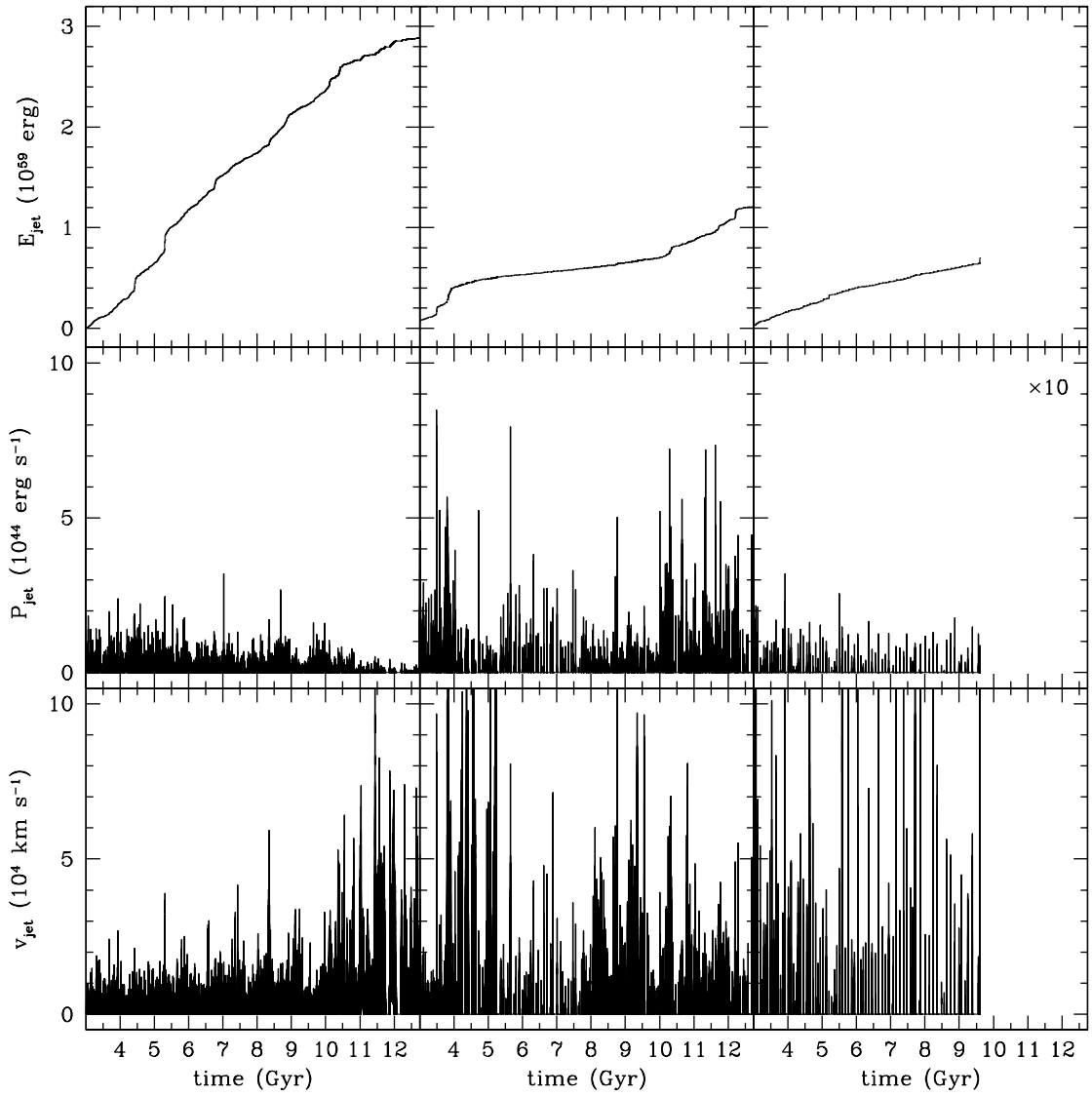

Figure 6.4. *Continued.* Isolated galaxy models with AGN feedback and increasing mechanical efficiency: $\epsilon = 10^{-4}$, 3.3×10^{-4}, and 10^{-3}. From top to bottom: evolution of injected mechanical energy, instantaneous power and velocity of the AGN feedback (half-space jet).

massive ellipticals (Temi et al. 2009).

The density profile (middle panel) oscillates in time, especially in the inner region, but retains reasonable values, as noticed through a comparison with typical observations of ellipticals (Humphrey et al. 2006).

The density cycles correspond to the accumulation of gas during periods of less intense AGN activity, e.g. between 6 and 7 Gyr there is no powerful outburst. This leads to an increase of the gas density in the central region, a higher cooling rate and finally a powerful ($\sim 3 \times 10^{44}$ erg s^{-1}) event which quickly expands the hot gas atmosphere. The density cycles also reflect in the variation of the X-ray luminosity which, in turn, fluctuates between $10^{41} \lesssim L_{\rm x} \lesssim 2 \times 10^{42}$ erg s^{-1} (with a mean value of $\sim 10^{42}$ erg s^{-1}). This variation can in part explain the long-standing problem of the scatter in the L_B (or L_K) - $L_{\rm x}$ diagram (Eskridge et al. 1995; Beuing et al. 1999; Ellis & O'Sullivan 2006),

along with the occurrence of SNIa winds (Ciotti et al. 1991; David et al. 2006) and the variation of the dark halo masses at a given optical luminosity (Mathews et al. 2006).

The temperature profile is a sensitive probe of AGN heating scenarios, yet often neglected in the comparison with observations. As expected, heating processes originating close to the galactic core often overheat the central ISM, an effect rarely or never observed in real galaxies (Brighenti & Mathews 2002b, 2003). The best observed systems (which, unsurprisingly, are the X-ray brightest) commonly show positive temperature gradient, with the centre hosting the coolest X-ray gas of the system (Humphrey & Buote 2006; Diehl & Statler 2008b). On the other hand, observed galaxies which are isolated or in a less dense environment usually show a moderate negative or flat T gradient (see Figure 6.2).

In the third row (left column in Fig. 6.4) are shown the radial profiles of the spectroscopic-like temperature at twelve different times. In this feedback model, the ISM is never overheated in the central region and always maintains an acceptable thermal structure (Kim & Fabbiano 2003; Fukazawa et al. 2006; Humphrey et al. 2006; Sansom et al. 2006; Diehl & Statler 2008b; Nagino & Matsushita 2009), i.e. the central negative T gradient is rather shallow and the central temperature remains at or below $\sim 10^7$ K. The lack of a substantial cool core must be ascribed to the absence of the CGG, not to the presence of the AGN feedback. Ripples in the temperature profile are caused by weak shock waves generated by the AGN outbursts. However, these waves would be largely diluted if the azimuthal average is made in relatively larger radial bins, as in real observations.

The last three rows of (continued) Figure 6.4 show the detailed evolution of the mechanical feedback (for the half-space jet). The total injected energy for this model is $E_{\rm jet} \approx 3 \times 10^{59}$ erg, the typical power is on the order of $P_{\rm jet} \sim 3 \times 10^{42} - 10^{43}$ erg s^{-1}, with velocities around $v_{\rm jet} \sim 10^4$ km s^{-1}.

6.3.3 Cold Feedback: $\epsilon = 10^{-3}$ [iso-C1m3]

The previous model, with efficiency $\epsilon = 10^{-4}$, was found in satisfactory agreement with several observational constraints. However, the cooling rate, although significantly reduced with respect to the classic iso-CF model, was slightly too large compared with observational limits. It is thus natural to increase the heating efficiency, essentially a free parameter of any current feedback scheme, to test if the cooling rate can be reduced further without scrambling the variable profiles.

When $\epsilon = 10^{-3}$ (third column of Figure 6.4), the effect of the feedback is excessive: the ISM becomes rarefied in the inner region ($r \lesssim R_{\rm e}$) and simultaneously overheated. Because the $\epsilon = 10^{-3}$ model was unsatisfactory, I stopped this simulation at $t \sim 9.5$ Gyr. It is interesting that the energy released by the AGN feedback is lower when the efficiency ϵ is larger (cf. the fourth row of Figure 6.4, $E_{\rm jet} \gtrsim 10^{59}$ erg). Evidently the more powerful and faster outflows (several 10^{44} erg s^{-1} and over 5×10^4 km s^{-1}) of iso-C1m3 model are able to stop the cooling flow for a relatively long time. The interval between AGN outbursts is in fact $\sim 6 \times 10^7 - 10^8$ yr, while for $\epsilon = 10^{-4}$ the AGN activates at least one order of magnitude more frequently, with the net result of injecting less energy over

the galaxy lifetime. This confirms the same trend found for galaxy clusters and illustrate that the complexity of the problem makes reasonings based on the energetic budget alone rather inaccurate.

The lower gas density implies a generally lower X-ray luminosity, with mean $\sim 5 \times 10^{41}$ erg s^{-1}. With efficiencies $\epsilon > 10^{-3}$ (models not shown), the simulated profiles strongly depart from those of real ellipticals (like NGC 6482) and the X-ray luminosity drops to undetectable values. It is worth noting that low-$L_{\rm x}$ early-type galaxies usually show the presence of some ISM in the central region, which has a relatively low temperature (see for example NGC 4697, Sarazin et al. 2001; NGC 1291, Irwin et al. 2002; NGC 3379, Trinchieri et al. 2008). Thus, their low X-ray luminosity may not be associated with strong AGN feedback generating a galactic wind.

6.3.4 Cold Feedback: $\epsilon = 3.3 \times 10^{-4}$ [iso-C3m4]

Finally, I have calculated a model with intermediate efficiency, $\epsilon = 3.3 \times 10^{-4}$ (iso-C3m4), which serves as best model in the following discussion. As displayed in the middle column of Figure 6.4, the cooling rate is now below the limits placed by current observations ($\lesssim 0.1\ M_\odot$ yr^{-1}), besides a narrow, transient peak at $t \sim 4$ Gyr. The density and temperature profiles vary in time slightly more than in model with $\epsilon = 10^{-4}$, but remain consistent with observations (cf. NGC 6482 data points). The spatial oscillations in the (projected) temperature profiles, with maximum amplitude $\sim 20\%$, are compatible with those shown in deep *Chandra* observations (see for example figure 10 in Randall et al. 2011).

The final injected energy is 10^{59} erg (fourth panel). Typical outburst powers are in the range several 10^{42} – few 10^{44} erg s^{-1} (fifth panel), while the velocity of the outflows (sixth panel) vary in the range[6] $10^3 - 10^5$ km s^{-1}, in good agreement with nuclear outflow and feedback observations (Chapter 2). The power values correspond to instantaneous accretion rates $\dot{M}_{\rm acc} = P_{\rm jet}/(\epsilon c^2) \sim 0.1 - 10\ M_\odot$ yr^{-1}.

I consider iso-C3m4 the best model because the cooling rate is in good agreement with known constraints for many Gyr, and the variable profiles always resemble those of real galaxies. Thus, the model with $\epsilon = 3.3 \times 10^{-3}$ (and to a lesser extent iso-C1m4) passes the first checkpoint, a necessary condition for a viable heating mechanism. In order to further test the robustness of the model, in the next Section, I analyse the detailed galaxy appearance in the X-ray band. I emphasise that the value of the ϵ parameter should not be taken as the exact physical value, given the uncertainties on the simulated accretion rate.

6.3.5 X-ray Observables

In this Section, I investigate the most significant X-ray features, naturally generated by the AGN heating process, like shocks and buoyant cavities. A direct comparison with a specific real system is not possible because the models are intended to be general and not tailored on an individual object. Moreover, cavities, shocks and perturbations are intermittently created, continually changing the ISM appearance. The

[6]The relativistic factor $\gamma \sim 1.06$ is still low enough to safely using classic hydrodynamics.

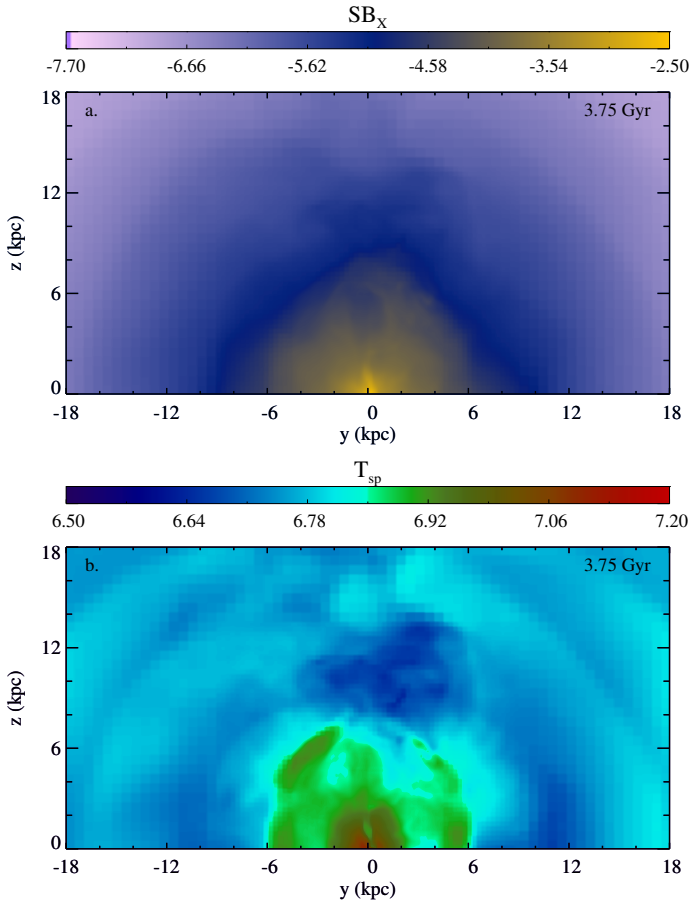

Figure 6.5. Maps, in logarithmic scale, of X-ray surface brightness, SB_X (erg s^{-1} cm^{-2}), followed by the projected spectroscopic-like temperature, T_{sp} (K), for best model iso-C3m4, at five different times: 3.75, 4.25, 5.75, 6.25 and 11.75 Gyr (figure continued in the next two pages).

main aim of the analysis is to show that the proposed feedback mechanism leads to ISM perturbations similar to those observed in galaxies. A feedback scenario not satisfying basic requirements, such as the formation of cavities or weak shocks, should be rejected.

I discuss below several X-ray snapshots, taken at different times, of the best model iso-C3m4. In Figure 6.5 (panel a) is shown the X-ray surface brightness map of the central region after 0.75 Gyr of feedback evolution. An outburst with energy 2.85×10^{56} occurred 8×10^6 yr before the time of the snapshot. The outflow, ejected with velocity $v_{jet} \sim 5400$ km s^{-1}, generated a weak shock, now at a distance ~ 6 kpc from the centre, with a Mach number $M \approx 1.2$ (calculated from T_{sp}, jumping from ~ 0.5 keV in the pre-shock region to ~ 0.6 keV in the post-shock ISM). The outflow generated a small X-ray cavity centred at $z = 4.5$ kpc and ellipsoidal (prolate) shape with semiaxes 1.5 and 1 kpc. The X-ray surface brightness depression within the cavity is about 20%, a typical value for observed cavities. Relatively colder rims surround the cavity, although the T_{sp} difference between the rims and the nearby gas is only $\sim 10\%$ (panel b). The ISM adjacent to the rims has been slightly heated by the weak shock. In the spectroscopic-like temperature map are also visible (but probably not detectable with current X-ray telescopes) very weak waves, separated by $\Delta r_{waves} \sim 6$ kpc, corresponding to a period of $t_{waves} = \Delta r_{waves}/c_s \sim 1.6 \times 10^7$ yr, roughly the typical time between significant AGN

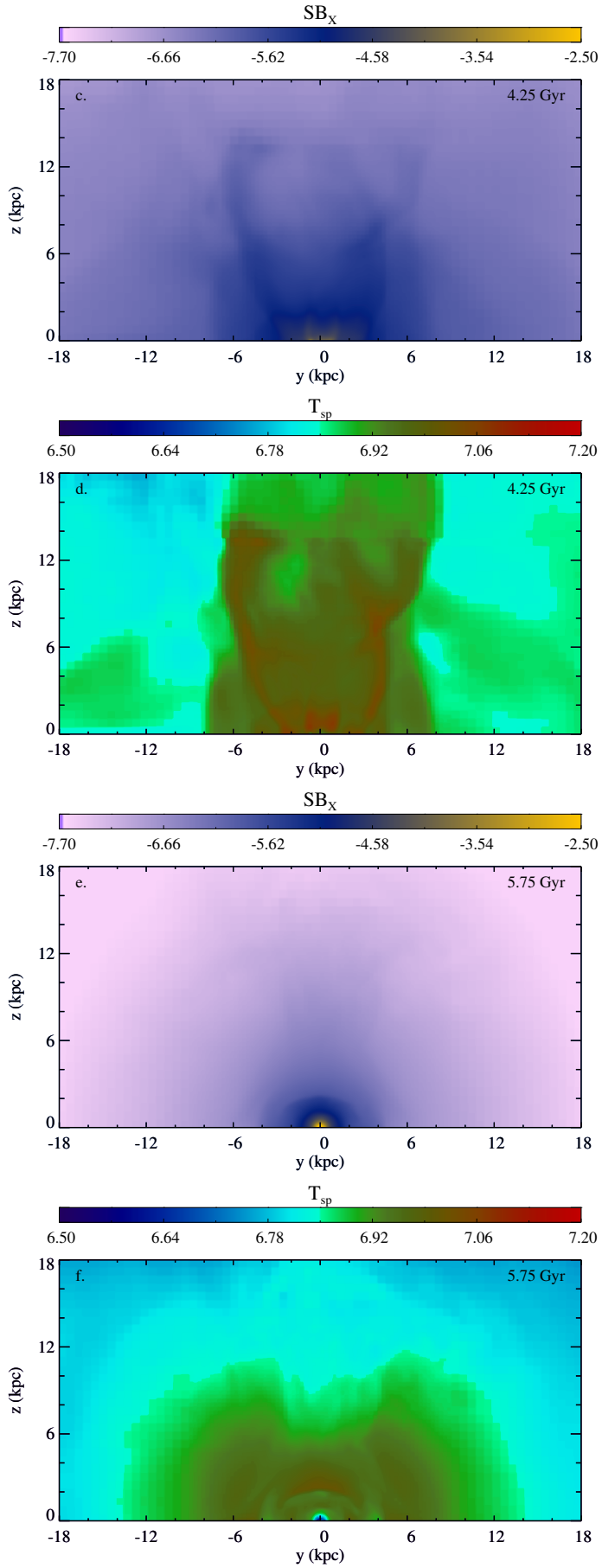

Figure 6.5. *Continued.*

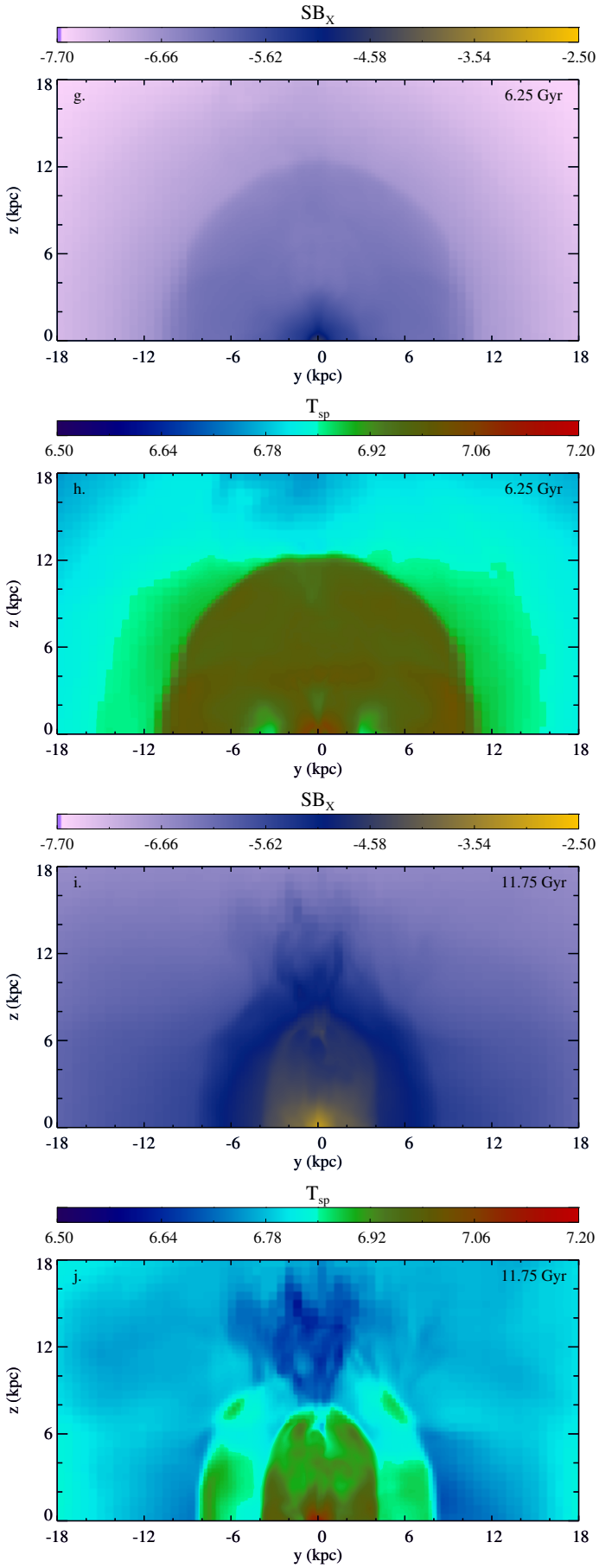

Figure 6.5. *Continued.*

outbursts at this epoch (t = 3.75 Gyr). I emphasise that these X-ray features are faint and the ISM looks quite relaxed at this time.

The situation after 0.5 Gyr is different (panels c and d – continued Figure 6.5). At this epoch the AGN is more active and perturbs the ISM in a remarkable way. The X-ray arms and cavity have been generated by four series of AGN outbursts of moderate power (few 10^{42} erg s^{-1}), occurred in the previous 10 Myr. The energy injected during this time interval is $\sim 1.4 \times 10^{57}$ erg. Panel c shows that the X-ray surface brightness map is rich of features, with two symmetric bright arms, $\sim$ 15 kpc long. This structure is similar to that observed in NGC 4636, a massive elliptical galaxy in the outskirt of the Virgo cluster (Jones et al. 2002; Baldi et al. 2009). Thus, it might be possible that the ISM of NGC 4636 has been shaped by multiple, moderate AGN outflows.

In the spectroscopic-like temperature map showed in panel d, the X-ray bright arms are slightly hotter than the local ISM. The temperature jump is about 30% (from 0.67 keV to 0.89 KeV) corresponding to a shock Mach number of $\sim$ 1.3.

The galaxy alternates periods of quiescence, typically lasting 50-100 Myr, with moments during which the AGN is more active and, consequently, the ISM more disturbed. Other interesting features appear with the evolution. At t = 5.75 Gyr a cold front is visible in both the brightness and temperature maps, at $\sim$ 2 kpc from the centre (panels e and f). The front has not been caused by galaxy sloshing in our simulations, but by the encounter between gas which is falling back toward the centre, after an outflow, and the gas currently located in the central region.

At t = 6.25 Gyr (panel g) the brightness map shows a weak cavity about 3 kpc in radius, surrounded by a $\sim$ 10 kpc shock with Mach number $\sim$ 1.3 (panel h). This situation is similar to that at t=3.75 Gyr, described in panel a. This demonstrates that the ISM cyclically evolves, with recurrent cavities generated by the outflows and weak shocks, just as indicated by observations.

Although not a common circumstance, a series of shocks are visible at the same time. This occurrence is shown in panel i (t = 11.75 Gyr), where two ellipsoidal shocks are depicted (Mach $\sim$ 1.4 – 1.5). The shocks intersect the $y-$axis at $\sim$ 4 and $\sim$ 8 kpc and are clearly visible both in the surface brightness and temperature maps (panels i and j).

This brief description of the ISM appearance in X-ray is intended to illustrate the richness of structures generated by the AGN outflows. It is important to realise the strong similarity of simulated features, like X-ray cavities, filaments and shocks, with the structures seen in deep X-ray observations of ellipticals and groups (e.g. Biller et al. 2004; Machacek et al. 2006, 2011; Baldi et al. 2009; Gastaldello et al. 2009; Giacintucci et al. 2011; O'Sullivan et al. 2011c; Randall et al. 2011). This fact, together with the analysis in the previous Section, strongly indicates that AGN outflows are indeed a very robust feedback mechanism, capable to highly inhibit gas cooling, keeping reasonable density and temperature profiles, and giving rise to the wealth of asymmetric structures in the ISM, seen in high-resolution deep X-ray observations.

6.4 Results: Elliptical with Circumgalactic Gas

As previously mentioned, most massive, X-ray bright ellipticals host a very extended hot ISM that can not be explained via internal processes alone (e.g. Brighenti & Mathews 1998, 1999). These galaxies are at the centre of large dark matter halos (Mathews et al. 2006) and the ISM is likely composed of gas shed by the stellar population, plus circumgalactic gas linked to the cosmological evolution. It is thus important to test if mechanical AGN outflows are successful for this class of objects, which include many famous X-ray targets, such as NGC 4636, NGC 4472, NGC 5044, and NGC 4649.

Interestingly, in these cool-core objects the evidence for AGN heating seems stronger, as revealed by the presence of X-ray cavities and other ISM perturbations (e.g. Biller et al. 2004; Diehl & Statler 2008a; Baldi et al. 2009; Gastaldello et al. 2009; Dong et al. 2010; Dunn et al. 2010; Randall et al. 2011; O'Sullivan et al. 2011c). It might be a selection effect, but it is ironic (and instructive) to note that just where we know that the AGN is injecting energy, the ISM close to the feedback engine is cooler than everywhere else.

6.4.1 Cold Feedback: $\epsilon = 8 \times 10^{-4}$ [cgg-C8m4]

In this Section, I present only the best feedback model for the CGG elliptical (efficiency $\epsilon = 8 \times 10^{-4}$), able to properly solve the cooling flow problem. It is interesting that the same feedback method requires now a larger efficiency to be acceptable, in line with the results of the previous Chapter, indicating that in more massive systems the feedback should act more efficiently.

As in the case of the isolated galaxy, I have run a classic cooling flow model (no AGN heating) which serves as a reference calculation to gauge the effects of the feedback. I do not show the evolution of the pure CF profiles here (cgg-CF). The results are almost identical to those presented in Section 5.3.1, although the numerical resolution there was about two times coarser ($\Delta x \approx 500$ pc), compared to the present model. The gas cooling rate, also very similar to gr-CF, is shown in Figure 6.6 (black line in the top left panel). As suggested by the resulting bolometric $L_{\rm x} \sim 3 \times 10^{43}$ erg s^{-1}, the cooling rate stays around $\sim 25\ M_\odot$ yr^{-1}, revealing again the cooling flow problem at the galactic/group scale.

The AGN feedback model, with $\epsilon = 8 \times 10^{-4}$, is fully presented in Figure 6.6. The cooling rate (red line, first panel) is quenched to $\sim 1\ M_\odot$ yr^{-1} at the current epoch, implying a satisfactory 20-fold cooling suppression, broadly consistent with XMM-RGS observations (Tamura et al. 2003).

The spectroscopic-like temperature and density radial profiles are in excellent agreement with those observed for NGC 5044 (left column: middle and bottom panel). Remarkably, the cooling reduction did not come at the expense of the cool core: the temperature still decreases toward the galactic centre – a fundamental quality of anisotropic mechanical feedback (gradual thermalisation).

The total mechanical energy released by the AGN is $E_{\rm jet} \sim 9 \times 10^{60}$ erg (first panel in second column), which in principle would correspond to a total mass accreted on the black hole of $\sim 6 \times 10^9\ M_\odot$, given the assumed efficiency. This accreted mass may

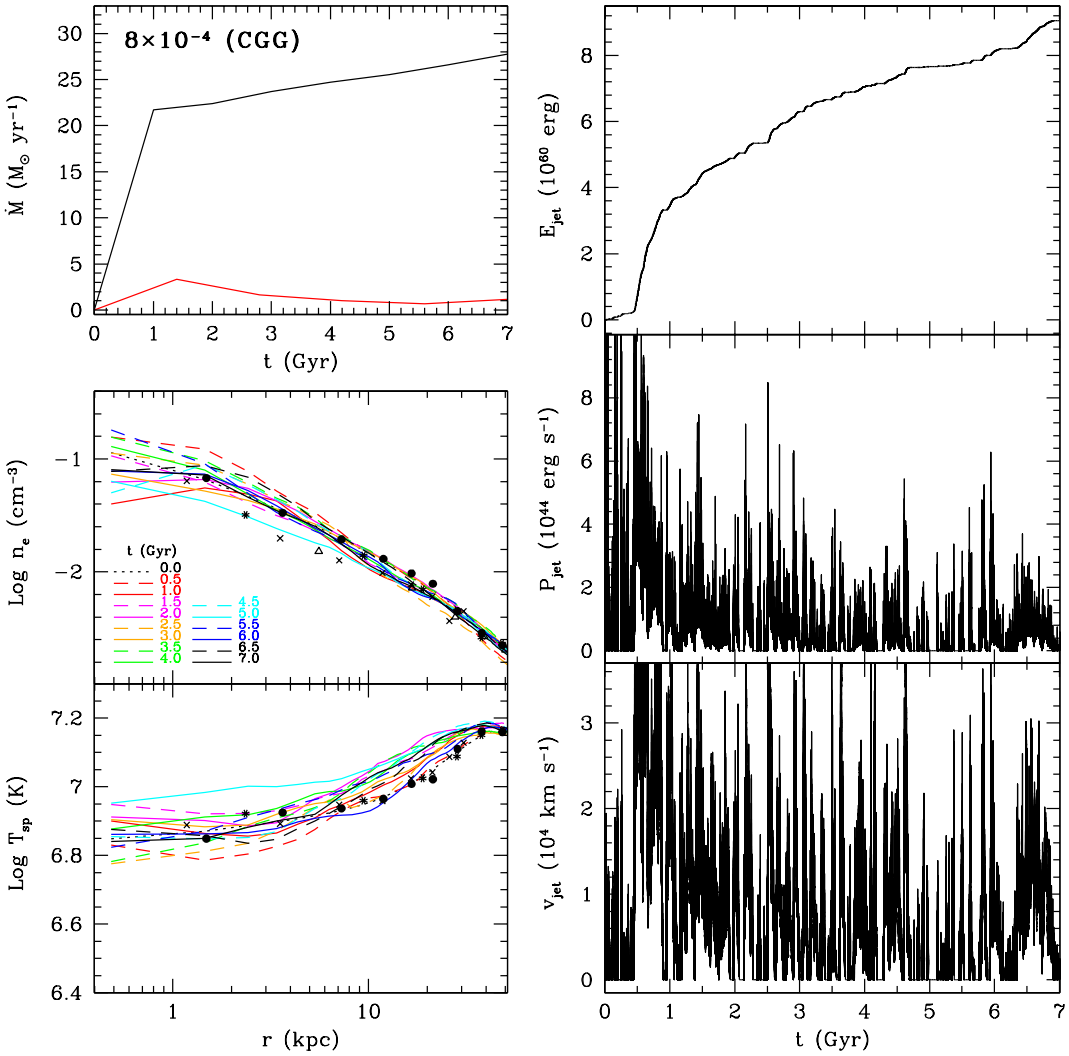

Figure 6.6. Elliptical galaxy with circumgalactic gas and AGN feedback efficiency $\epsilon = 8 \times 10^{-4}$. Left column, from top to bottom panel: cooling rate as a function of time (red line; cf. cgg-CF model – black line); electron number density and spectroscopic-like temperature at several times. The points represent observational data of NGC 5044 (David et al. 1994; Buote et al. 2003). Right column: evolution of the injected mechanical energy, (half-space) outflow power and velocity.

appear substantial, but I stress that the simulated accretion rate is quite uncertain (see the arguments in Sec. 4.6.2).

The most relevant astrophysical result, here, is that self-regulated massive outflows are indeed capable to solve the cooling flow problem on kpc or larger scales, although the fully consistent picture – explaining the details of the BH accretion process and the formation of the outflows – needs to be clarified in future via high-resolution investigations.

The time record of the outflow power and velocity is shown in the right column in Figure 6.6. Powers on the order of few 10^{44} erg s^{-1} and velocity of several 10^4 km s^{-1} are again typical for the stronger events.

I conclude that massive outflows, activated when gas cooling occurs, are able to regulate the thermal evolution of the ISM, suppressing the cooling rate by a factor 20

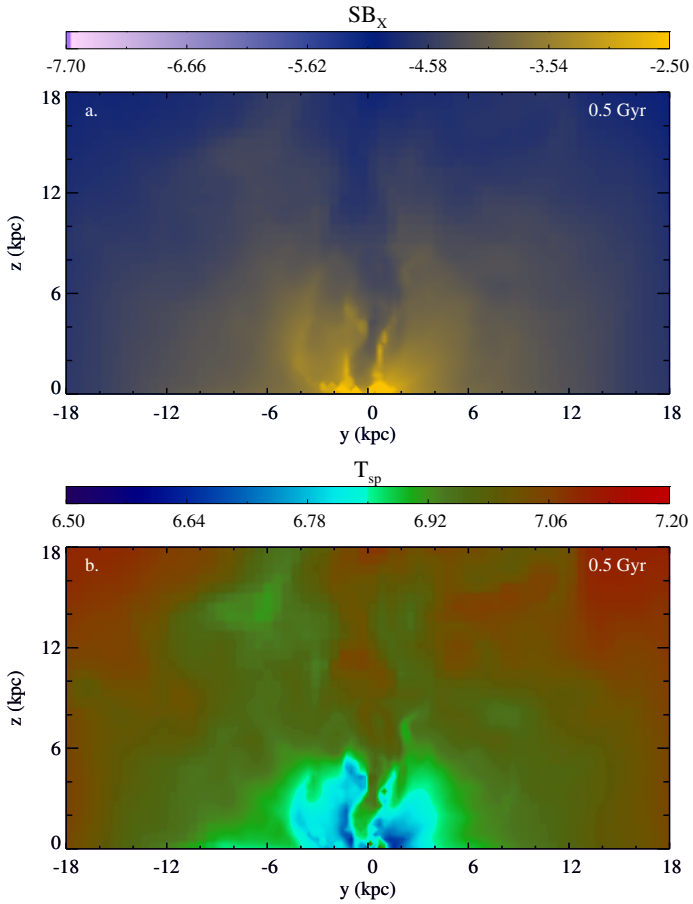

Figure 6.7. Maps, in logarithmic scale, of X-ray surface brightness, followed by the projected spectroscopic-like temperature, for the best model with circumgalactic gas (cgg-C8m4), at six different times: 0.5, 1.0, 2.0, 4.0, 6.5, and 2.5 Gyr (figure continued in the next pages).

or more and keeping the cool-core aspect of massive, X-ray bright ellipticals. It is now time to test the model via other key observational constraints.

6.4.2 X-ray Observables

The variety of X-ray features induced by the AGN outflows in the isolated galaxy (Section 6.3.5), such as buoyant bubbles and shocks, is widely present also in the CGG simulation. For the cgg-C8m4 model the AGN activity is more frequent and powerful compared to the isolated galaxy (cf. Figures 6.4 and 6.6). Nevertheless, the X-ray appearance of the two models is remarkably similar.

In Figure 6.7, I present an extensive collection of X-ray surface brightness and spectroscopic-like temperature maps, starting from $t = 0.5$ Gyr (panels a and b). We focus our attention on the inner 20×10 kpc of the maps, where the observations could return better details. The outflow carved a long cavity (or channel) $\sim$ 10 kpc long and $\sim$ 2 kpc wide. The brightness depression is about a factor of 2, which should make this feature detectable in deep, high resolution images. For $z \lesssim 4$ kpc the cavity is surrounded by sharp bright rims (or filaments), which remind the southern open cavity in NGC 5044 (Buote et al. 2003; David et al. 2009; Gastaldello et al. 2009). The cavity is slightly hotter

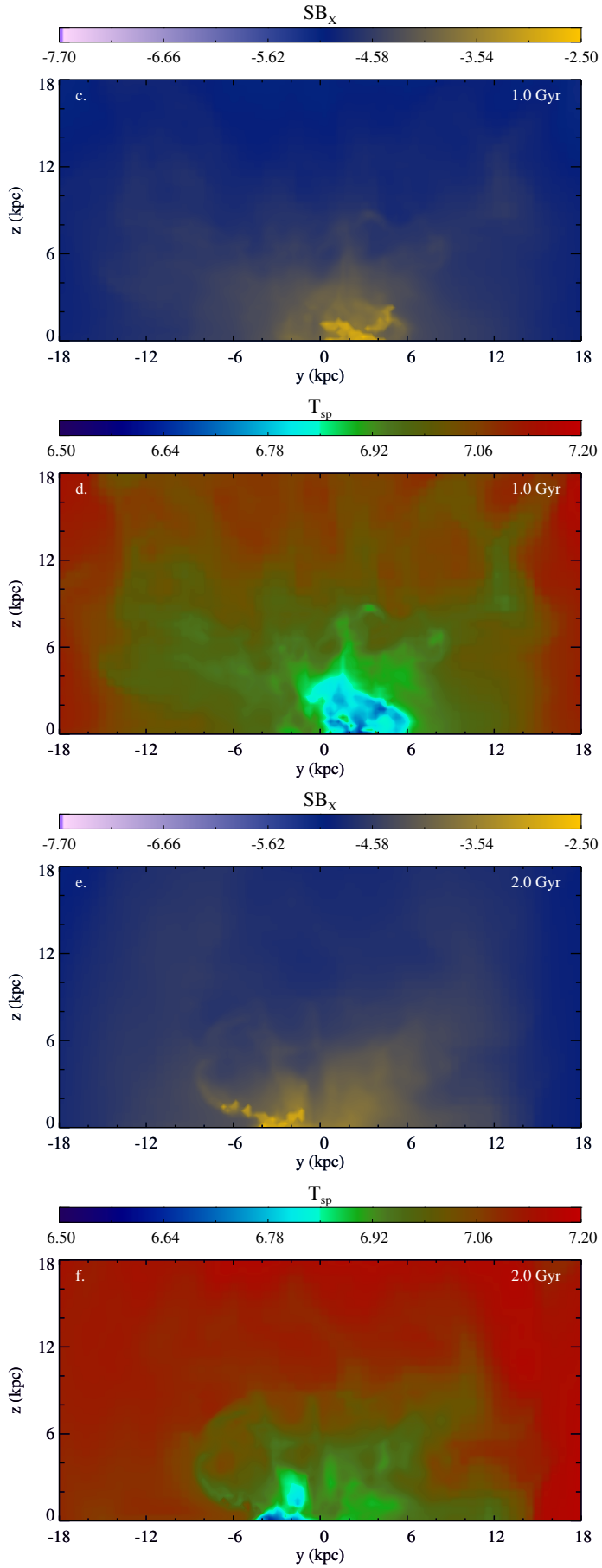

Figure 6.7. *Continued.*

(by $\sim$ 10%, see T_{sp}) than the nearby gas. At $z \gtrsim 6$ kpc broad regions ($\Delta y \sim 3$ kpc) of enhanced surface brightness, confining the X-ray feature, are present. This channel is typically fragmented by AGN turbulence or strong recurrent outbursts. On the $z = 0$ plane, close to the centre, the inflowing gas forms a dense torus which is punched, but not cleared away, by the outflows. This feature could, however, be numerically amplified by the forced planar symmetry ($z = 0$ plane), where reflection boundary conditions are implemented.

At $t = 1$ Gyr (panel c, continued Figure 6.7), the SB_x map shows a region of enhanced emission, several kpc in size, close to the centre of the galaxy ($0 \lesssim y \lesssim 5$ kpc). They are caused by relatively dense and cold gas, some of which is actually cooling to low temperatures ($T \lesssim 10^5$ K) and dropped out from the flow (see Figure 6.8, panel o). This is a very interesting phenomenon, because the off-centre cooling might explain the widespread presence of cold ($T \sim 10^4$ K) gas in large ellipticals with conspicuous hot gas (Sec. 6.1). Despite being linearly stable against thermal instability (Balbus 1988; Balbus & Soker 1989; Loewenstein 1989; Malagoli et al. 1990), the non-conducting hot gas may well cool if the amplitude of the perturbations is sufficiently large (Reale et al. 1991; Yoshida et al. 1991; McCourt et al. 2012; Sharma et al. 2012). High resolution X-ray maps show indeed a wealth of irregularities in the hot gas, which certainly imply large perturbations in the gas density. Localised gas density enhancements are naturally generated in regions of converging flows, resulting in local cooling times much lower than the free-fall times, and inducing hot gas condensation ($T \lesssim 5 \times 10^4$ K). This process of multiphase gas formation will be investigated extensively in the next Chapter.

Cooling gas at large distance from the galactic centre is seen also at $t = 2$ Gyr (panel e), in an enhanced SB_x region defined by $z \lesssim 1$ kpc and $R \lesssim 7$ kpc. Several cavities surrounded by relatively cold, bright rims buoyantly rise on various scales (panel f), while very weak shocks rapidly vanish as sound waves at large radii. The cold rims are metal rich, as expected, being formed by gas originally at the centre of the galaxy. In the present model, in fact, we followed the chemical enrichment of the hot gas halo, with emphasis on the evolution of the iron expelled by SNIa. The map of the (emission-weighted) iron abundance is shown in Figure 6.9 (panel q). The AGN outflows generate asymmetries in the Fe distribution: the relatively metal-rich gas originally in the centre is uplifted along the direction of the outflow and cavities. This results in regions of enhanced iron abundance (by $20 - 30\%$) which trace the dynamics of the recent outflows. Beside this global behaviour, kpc-sized inhomogeneities are also evident in the abundance map.

At $t = 4$ Gyr (panels g and h) a complex structure is visible in the X-ray surface brightness image, mainly due to the generation of multiple cavities and bright filaments. As usual, brightness contrasts are accompanied by temperature and metallicity variations, here on the order of 10%. These images show that the recurrent AGN outflows naturally generate and drive turbulence in the core, with typical velocities of few hundreds km s^{-1} (Section 6.5.2). The chaotic turbulent environment naturally produces the complex irregular features, at the same time increasing the level of thermalisation in the central region via jet fragmentation.

At $t = 6.5$ Gyr (panels i and j), almost at the end of the simulation, we observe irregular regions of high surface brightness in the central few kpc, where the gas cools

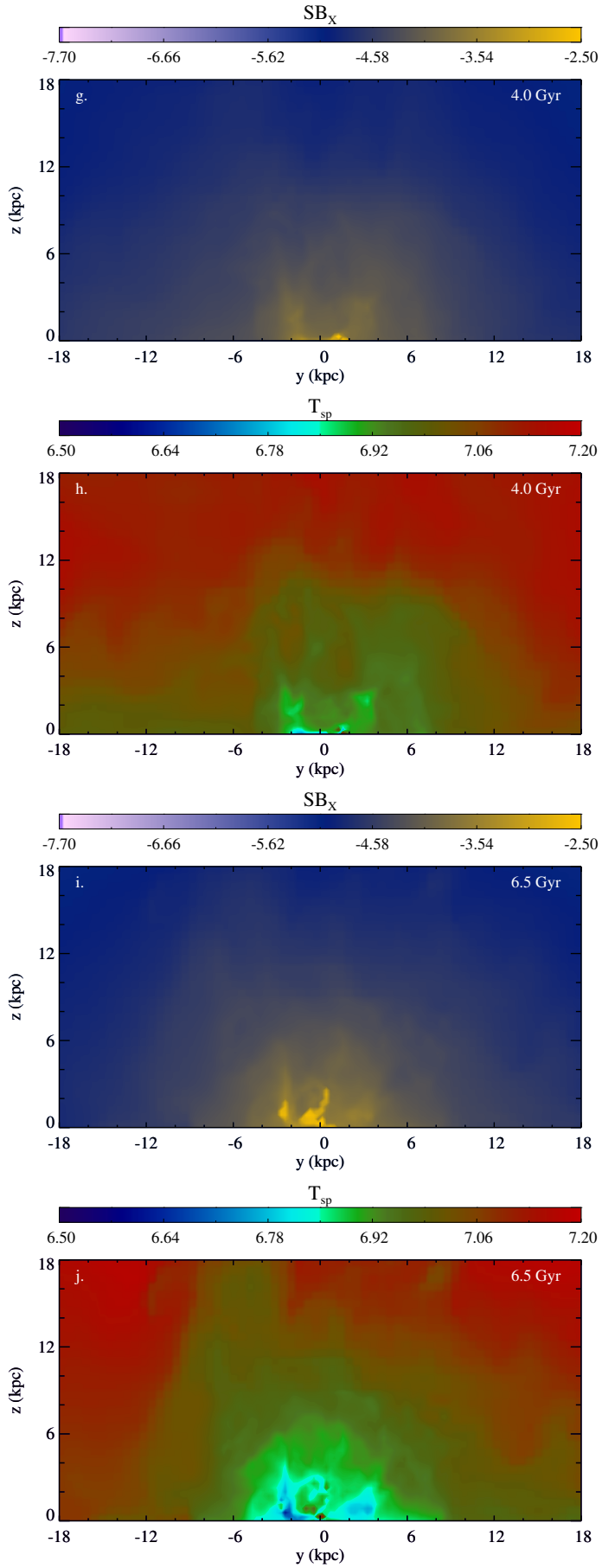

Figure 6.7. *Continued.*

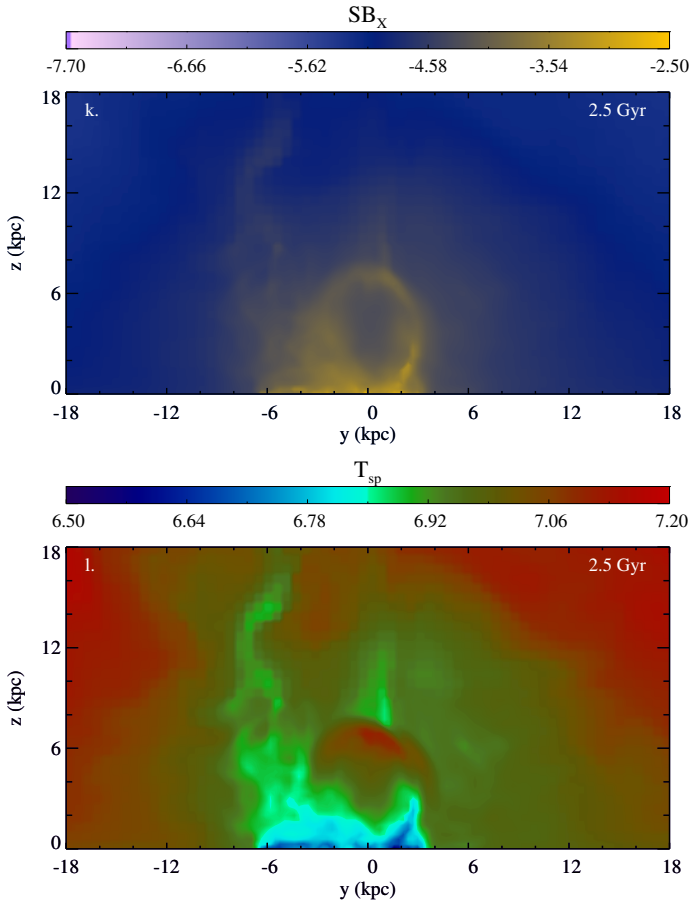

Figure 6.7. *Continued.*

to very low temperatures producing diffuse Hα emission. Figure 6.8 (panel p) provides the total dropped cold mass (integrated in time), indicating again that the cold phase condenses out of the hot flow not only at the very centre, but in an extended region of radius 7 – 15 kpc. Although we do not follow here the dynamics of the cold clouds, the result seems qualitatively robust: off-centre cooling exists, as indicated by observations, and it can be triggered by the AGN feedback process.

I conclude the snapshot analysis for the CGG model showing a textbook example of X-ray cavity confined by bright rims (panels k and l). The largest brightness contrast between the X-ray hole and the rims is about a factor of two. From the spectroscopic-like temperature map we see that the lower part of the rims ($z \lesssim 3$ kpc) are colder, in projection, than the nearby ISM, while the upper part is slightly hotter, because of shock heating. Again, the rims, being originated from central gas, are slightly more metal-rich than the ISM at the same radius, by 15-25% in the iron abundance (Fig. 6.9, panel r). For this time, I also show the projection along the z-direction (Fig. 6.7, panels m and n). Several structures and cavities are visible, together with X-ray bright filaments. In this projection the $T_{\rm sp}$ is characterised by an arc-shaped region about $\sim$ 20% colder than the neighbouring gas. This comparison between two different projections warns how complicated is the interpretation of real data, especially when the inclination of the outflow, in respect to the plane of the sky, is uncertain.

The generation of buoyant bubbles, together with all the previous consistent

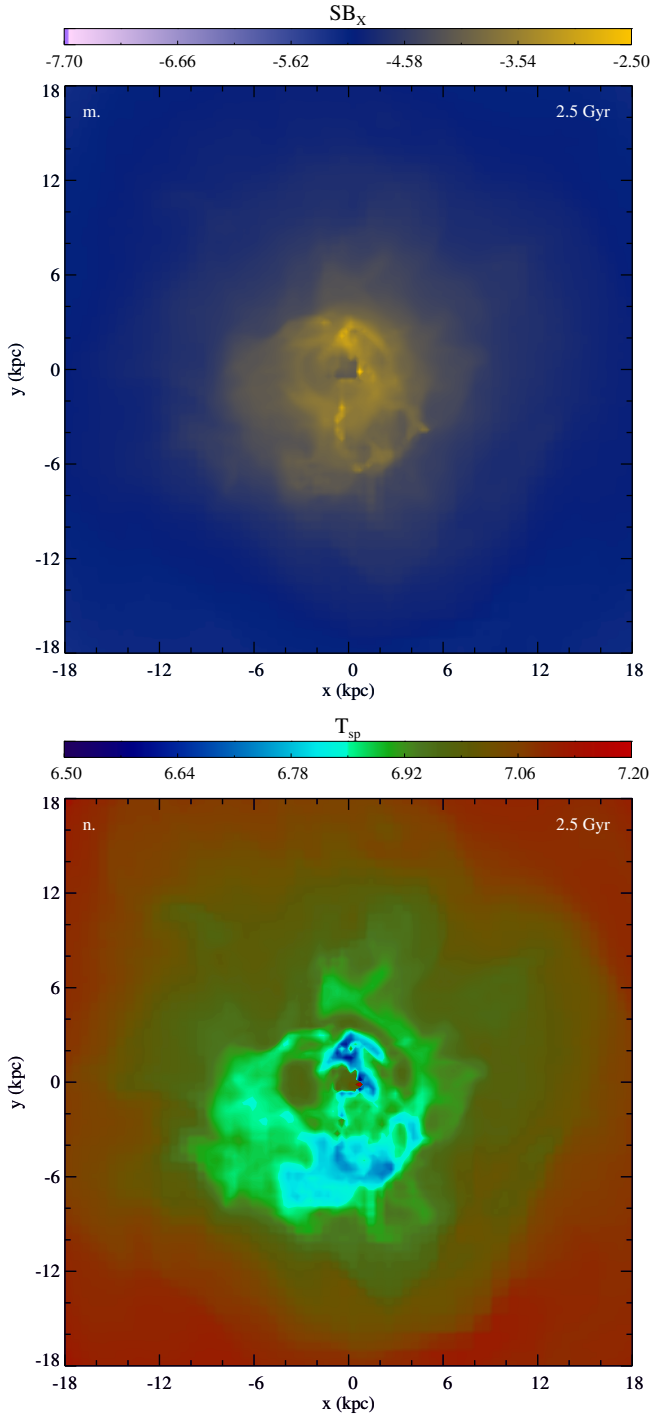

Figure 6.7. *Continued.* For time 2.5 Gyr are presented also the z-axis projection of the X-ray surface brightness and spectroscopic-like temperature.

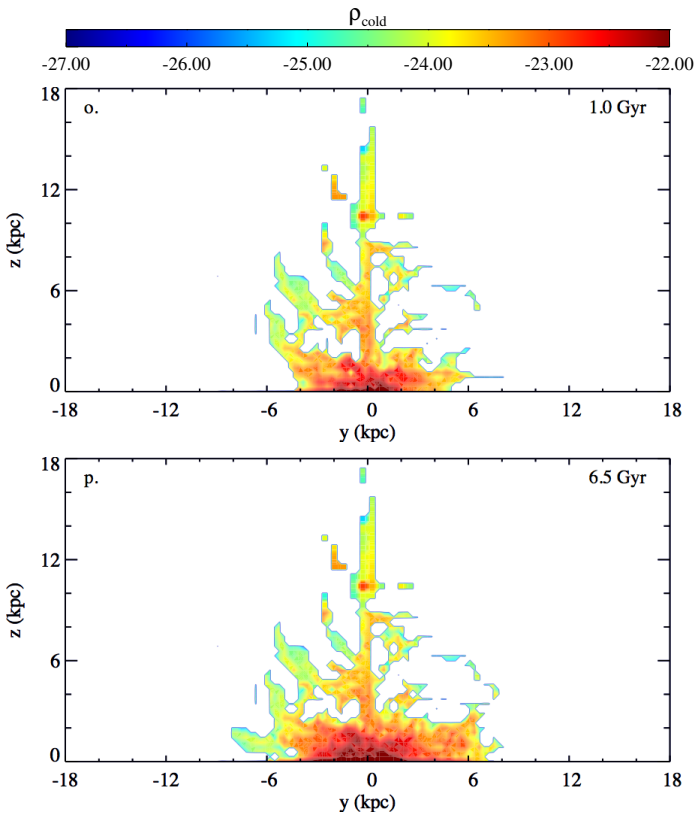

Figure 6.8. Maps, in logarithmic scale, of accumulated dropped cold gas ($T \lesssim 2 \times 10^4$ K), simply summed along the x-axis, for best model cgg-C8m4 at two different times.

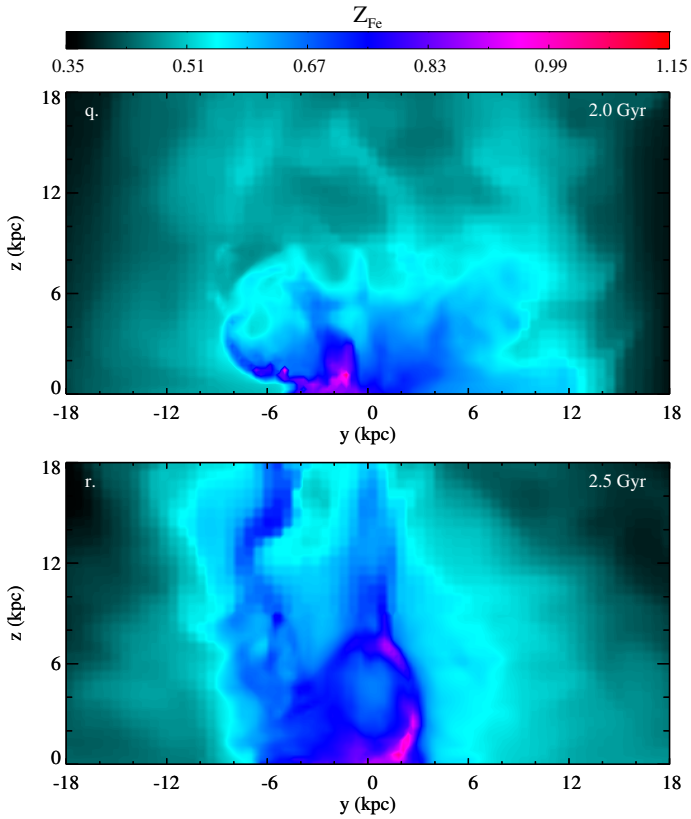

Figure 6.9. Maps of emission-weighted iron abundance (in solar units), projected along the x-axis, for best model cgg-C8m4 at two different times.

observational features (extended multiphase gas, metals asymmetries, turbulence, weak shocks), strengthens the key role of mechanical AGN outflows in regulating the thermal and dynamical evolution of elliptical galaxies, with or without circumgalactic gas.

6.5 Discussion

Before discussing the main results and a new observational test (AGN turbulence), it is interesting to compare our purely mechanical feedback with other types of AGN heating processes.

6.5.1 Comparison with other Feedback Models

To our knowledge, only very few investigations focused on AGN feedback in ellipticals. For example, Ciotti, Ostriker and collaborators (1997, 2010) have investigated a type of feedback triggered by AGN radiation (mainly Compton heating, radiation pressure, plus an approximation of a broad-line-region wind), through 1D hydrodynamic simulations. The best models have been analysed in detail by Pellegrini et al. (2012) and compared to observations. The key feature of these models is the formation of a cold shell at $r \sim 1$ kpc, whose evolution governs the whole quasar-like feedback heating (in order to be efficient, radiative feedback requires a very dense - optically thick - absorbing medium). Note that in 1D simulations a cold shell can numerically form under several circumstances, with or without AGN heating (see for instance the 'galactic drip' phenomenon described in Brighenti & Mathews 2002b). It is not clear how 1D calculations are able to realistically follow the formation and evolution of the shell. Subsonic, non-radial gas velocity appearing in multidimensional models tend to suppress this feature (Brighenti & Mathews 1997). The cold shell is also Rayleigh-Taylor unstable and should fragment in about a dynamical time, $\sim$ few $\times 10^6$ yr. Another complication is the difficulty for hydrodynamic simulations to reproduce the real complexity of the observed multiphase ISM in the inner $<$ kpc.

Given these uncertainties, it seems more appropriate to compare our results with those presented in Novak et al. (2011), where the 2D version of the previous feedback scenario for an isolated elliptical galaxy is investigated. In these simulations, conical outflows representing BAL winds are generated near the centre of the grid, making the computed scenario qualitatively similar to our models. Novak et al. (2011) found that the accretion process significantly changes in 2D, reducing the effectiveness of the feedback mechanism with respect to isotropic 1D models. They explored the effect of varying the mechanical efficiency, finding that an acceptable BH growth is attained when $\epsilon \gtrsim 10^{-4}$, consistent with the preferred values found in our work. About 10^{10} $M_\odot$ of stars form in Novak's ellipticals, almost independently on the wind efficiency, implying a substantial mean star formation rate of ~ 0.8 $M_\odot$ yr^{-1}. It would be interesting to estimate the central Balmer indexes (dependent on the star formation history) and compare them with the available observations (e.g. Kuntschner et al. 2010).

Unfortunately, Novak et al. (2011) do not show azimuthally averaged temperature and density profiles, thus it is not possible to assess the effect of the AGN feedback on

these key observable constraints. Nevertheless, together with our calculations, the results presented in Novak et al. (2011) corroborate the potential importance of bipolar outflows as a primary source of AGN feedback.

Debuhr et al. (2011) carried out 3D SPH simulations of AGN outflows driven by quasar radiation during a major merger. They noted that radiation pressure alone does not produce any substantial feedback, requiring an additional momentum kick with velocity $\sim 10^4$ km s^{-1} (like BAL winds), similar to our best models. Large values of the optical depth are usually required to boost such fast outflows ($\tau \sim 5 - 10$). The strong isotropic outburst produces a clear galactic outflow, drastically reducing the mass inside 3 kpc (two orders of magnitude). This is a typically feature associated with strong isotropic heating (either mechanical or thermal), which unbinds and shocks the central gas to unobserved levels in normal ellipticals. Bipolar mechanical outflows are instead gentler, capable to reproduce the observed anisotropic X-ray features like cavities.

As a concluding remark, I note that the radiative feedback displays a strong impact on the ISM only in the presence of quasar-like objects, which are certainly rare in the local universe, with a rapid decline below redshift ~ 1.8 (Schneider et al. 2005).

6.5.2 AGN Turbulence

Another interesting test every feedback model should pass, although not stringent as those previously discussed, is the generation of turbulence (or bulk motion) in the ISM, especially in the central region. Deep X-ray observations start to provide reliable estimates on the turbulent pressure (Werner et al. 2009; Sanders et al. 2011; de Plaa et al. 2012). The latter authors, in particular, give estimates of the ISM velocity dispersion in the central ~ 10 kpc for two exemplary groups: $320 < v_{\rm turb} < 720$ km s^{-1} (NGC 5044) and $140 < v_{\rm turb} < 540$ km s^{-1} (NGC 5813). In order to compare the prediction of our CGG model with this observation, I calculate the gas velocity dispersion along the line of sight l, weighted by the emission-measure, as

$$\sigma^2_{\rm turb} = \frac{\int \rho^2 (v_l - \bar{v}_l)^2 \, dl}{\int \rho^2 \, dl} , \tag{6.2}$$

where the (global) mean velocity $\bar{v}_l$ is typically very close to zero.

In the (projected) circular region $0 < R < 5$ kpc, the time average velocity dispersion is ~ 200 km s^{-1}, when the system is viewed along the outflow z-axis. In the phases where the AGN is more active $\sigma_{\rm turb}$ can reach values as high as 400 km s^{-1}. Note that the outflow, with velocity often exceeding 10^4 km s^{-1}, poorly contributes to $\sigma_{\rm turb}$, because of the very low density. The gas turbulence becomes weaker at larger distances from the centre. In the ring $5 < R < 20$ kpc, $\sigma_{\rm turb}$ decreases to $\sim 60 - 100$ km s^{-1}, while in the region $20 < R < 40$ kpc, $\sigma_{\rm turb} \sim 40 - 70$ km s^{-1}. One missing element of our models is the effect of cosmological merging and inflow, which may trigger additional turbulence, although more efficiently at large radii (> 0.1 the virial radius; e.g. Vazza et al. 2011).

When the galaxy is observed along a line of sight perpendicular to the outflow direction (like the $x-$axis) the mean central $\sigma_{\rm turb}$ has lower values, ~ 100 km s^{-1}, with peaks about a factor of two larger. For the standard cooling flow model I find instead

$\sigma_{\rm turb} \lesssim 45$ km s^{-1}; this quantity is certainly not associated with turbulent motions, while it represents the steady radial inflow velocity due to the massive cooling flow.

I conclude that subrelativistic outflows are able to generate the observed turbulent pressure and hot gas velocity dispersions. This non-thermal pressure is generally a fraction of the thermal energy, in the range $5-15\%$: $E_{\rm turb}/E_{\rm th} \approx 0.1\,(v^2_{\rm turb,200}/T_7)$, where the turbulent velocity is expressed in units of 200 km s^{-1}, and the temperature in 10^7 K.

6.5.3 Concluding Remarks

In this Chapter, I have investigated the effect of AGN feedback on the evolution of the ISM in massive elliptical galaxies. In designing the 3D hydrodynamic simulations I have been guided by several ideas.

1. The AGN feedback in low-redshift ellipticals acts mainly through a (radiatively inefficient) mechanical and directional process, in the form of massive outflows
2. These outflows interact with the ISM and heat the medium on scales of several kpc, as indicated by X-ray observations of cavities and shocks.
3. The AGN reacts to gas cooling: cold gas condenses out of the hot phase in the central region, and it is assumed accreted onto the black hole in a few dynamical times, triggering the AGN feedback. The uncertainties on the the real accretion rates force to adopt a parametrisation as simple as possible (the governing parameter being the mechanical efficiency ϵ).
4. The feedback mechanism must work for objects of any scale, from isolated galaxies to massive galaxy clusters.
5. The calculated evolution of the hot gas must be checked against many available observational constraints, for a long time span (several Gyr).

In Chapter 4 and 5, I have shown that AGN outflows are able to solve the cooling flow problem for both massive clusters and groups, for more than 7 Gyr. We are left now to demonstrate that these mechanical massive outflows, self-regulated by cold accretion, represent also the dominant feedback mechanism on the galactic scales, either in an isolated or in a group-dominant system.

The two key tests that the models must pass are the agreement with the low cooling rates allowed by observations, and the moderate gas temperature in the central region of galaxies (no overheating). The former sets a lower limit for the feedback mechanical efficiency, the latter provides an upper bound.

In Figures 6.4 and 6.6 I showed that assuming an efficiency $\epsilon \gtrsim 3\times10^{-4}$ ($\epsilon \gtrsim 8\times10^{-4}$) for the isolated (CGG) model, the cooling rate drops to values close the observational limits. The previous values for the mechanical efficiency are lower than those working for clusters (Chap. 4) and similar to those quoted in Ciotti & Ostriker (2007), although for a different feedback scheme. Because the estimated accretion rate onto the BH is likely an upper limit, a firm result of our calculations is that the mechanical efficiency must be

$\epsilon \gtrsim$ few $\times 10^{-4}$ in order to prevent significant gas cooling in massive elliptical galaxies. It is more difficult to place an upper bound for the efficiency. When $\epsilon \gtrsim 10^{-3}$, the AGN feedback is too intense and the ISM in the central region is overheated. However, larger mechanical efficiencies would be allowed if the accretion rate is grossly overestimated.

While the exact details of feedback engine (such as the duty cycle) are uncertain and must be investigated by high-resolution, specialised simulations, the astrophysically most relevant and solid result is that AGN outflows can solve the cooling flow problem, not only in clusters and groups, but also in galaxies, drastically quenching the cooling rates and properly maintaing a quasi thermal equilibrium in the core. This is a remarkable result, given the difficulties encountered with purely thermal feedback (regardless of its origin, i.e. artificially inflated bubbles or radiative heating).

They also agree with a number of other key and independent observational constraints. A crucial requirement for an AGN feedback scenario is the ability to produce (weak) shocks, X-ray cavities and abundance inhomogeneities, common features shown in deep X-ray observations (e.g. Figure 6.1). These properties point toward a feedback mechanism able to distribute energy and momentum in a directional way, on scales of several kpc. Observationally, these ISM perturbations are best studied in X-ray bright objects, often giant ellipticals with CGG or groups. About 25-50% of galaxies/groups observed at high resolution show evidence of cavities (McNamara & Nulsen 2007; Dong et al. 2010), a number likely underestimated. In galaxy clusters the detection fraction rises to $\gtrsim 2/3$ (Dunn & Fabian 2006). Moreover, cavities are more likely present in cool-core systems (Dong et al. 2010), implying that the feedback action must preserve the positive temperature gradients. Elliptical weak shocks are also commonly found (Gitti et al. 2012), surrounding stable buoyant cavities, a natural by-product of jets and outflows.

Through an extensive collection of snapshots (Sections 6.3.5 and 6.4.2), I have illustrated the wealth of observable features created by the (anisotropic) mechanical feedback scenario. Deep X-ray observations of galaxies (NGC 4472, Biller et al. 2004; NGC 4374, Finoguenov et al. 2008; NGC 4636, Baldi et al. 2009) and groups (NGC 5044, David et al. 2009; HCG 62, Gitti et al. 2010; NGC 5813, Randall et al. 2011; NGC 5836, Machacek et al. 2011) reveal a wealth of features certainly linked to the AGN feedback outbursts. In particular, the two typical fingerprints naturally left by collimated AGN outflows, i.e. X-ray cavities surrounded by a weak shock, are seen in many snapshots of Figures 6.5 and 6.7, often resembling observations also from a quantitative point of view (e.g. elliptical cocoons, Mach number, bubble size and temperature; see Figure 6.1). It is impossible to make a 1:1 comparison with real objects, catching the exact evolutionary moment, with the same instantaneous feedback values. Unfortunately, we are not in the position to calculate the time fraction in which the simulated cavities or shocks are visible; this would require an analysis of the flow very finely spaced in time, subject of a future investigation.

Typically, the cavities inflated by the outflows have size of few kpc and are surrounded by bright rims (see Figure 6.5: t = 3.75, 4.25 and 11.75 Gyr; Figure 6.7: t = 0.5, 2.0, 2.5 and 4.0 Gyr). The rims are often slightly cooler and metal-richer compared to the nearby gas, although there are few exceptions. Dedicated simulations tailored for NGC 4636, indicate that it is possible to explain most of the properties of the cavities detected in

NGC 4636, assuming the feedback proposed in this work (Ballone & Brighenti, in prep.).

In the case of the galaxy with CGG (similar to a group environment), the frequent activity of the AGN causes the common presence of a low-density channel along the $z-$direction carved by the outflows, $\lesssim 1$ kpc wide and several kpc long. This feature is very difficult to detect in the surface brightness map. In Figure 6.7 we see that only at the beginning of the calculation, at $t = 0.5$ kpc, the tunnel is visible, with a brightness contrast of $\sim 2-3$ (rapidly decreasing beyond $z = 5$ kpc). Most of the time, the thin channel is wiped out in the brightness image by projection effects. Occasionally, the tunnel may resemble a X-ray cavity (Fig. 6.7, $t = 2$ Gyr). A dedicated analysis through a very deep X-ray observation in the core of the galaxy may detect this feature or, at least, set constraints on its presence (few hints are already available: see Figure 6.1). The channel is nevertheless a transient feature, fragmented and destroyed by the AGN turbulence, a key element for a proper deposition and thermalisation of mechanical energy in the core.

The proposed AGN feedback mechanism has another impact on the gas cooling process, besides significantly lowering the total rate. It promotes spatially distributed cooling (via thermal instabilities), on an extended region of size ~ 10 kpc centred on the BH. Figure 6.8 show the density map of total cold gas which has cooled and dropped out of the flow, highlighting both the extended and concentrated toroidal distribution of cooler gas (see next Chapter). The current numerical setup does not follow the dynamics of the cooling gas, but it is plausible that some of the cooled gas accretes on the BH, and some is instead used to form new stars and the emission-line nebulae commonly observed in elliptical galaxies (see references in Sec. 6.1). At the moment of cooling, the gas has a chaotic motion, with typical velocities of $100-200$ km s^{-1}, concordant with Hα spectroscopic studies (Caon et al. 2000).

Finally, the mechanical feedback is able to reproduce the anisotropic distribution of metals, commonly observed in AGN-heated cores (e.g. Rasmussen & Ponman 2009; David et al. 2011; Kirkpatrick et al. 2011; O'Sullivan et al. 2011b). The powerful mechanical jets can indeed uplift up to ~ 10 kpc the metals processed by SNIa and stellar winds in the nuclear region (with a peak metallicity of $Z_{\rm Fe} \lesssim 1\ Z_\odot$; Mathews & Brighenti 2003). In the more quiescent phases (Figure 6.9), AGN turbulence tends instead to stir and diffuse the metals, restoring the homogeneous distribution.

With the present and previous two Chapters we close the circle of the investigation, studying and testing the mechanical AGN feedback in every virialised structure possessing a substantial hot gas halo. I have proven that massive subrelativistic outflows are the key to solving the cooling flow problem, avoiding overcooling and overheating, and reproducing the wealth of features observed in deep X-ray data. We are now left to understand in depth the AGN cycle and thermal equilibrium, i.e. dissecting the cold feedback mechanism and focusing on the - previously dropped out - cold phase.

Chapter 7

Multiphase Gas

THE GLOBAL picture emerging from the previous three Chapters is encouraging. Mechanical massive AGN outflows can indeed solve the cooling flow problem, simultaneously avoiding overcooling and overheating for the whole evolution. On relatively large temporal and spatial scales the system attains a quasi thermal equilibrium. The fact that the equilibrium is not perfectly maintained might appear at first a bad sign. However, the *quasi* equilibrium is a necessary property of a healthy self-regulated feedback in every virialised system. Previously, we focused mainly on the hot phase of the ISM/ICM, dropping out the cooling gas as soon as it approaches very low temperatures ($T \lesssim 10^5$ K). Since the cold gas is the engine of the AGN feedback, it is now time to carry out more advanced simulations, including the hydrodynamics of the entire multiphase gas ($T \geq 10^4$ K).

The following more realistic feedback simulations will investigate when and where extended multiphase gas forms. In the scenario of quenched cooling flows, we can speculate that the cold/warm phase may be deeply linked to the development of nonlinear thermal instabilities via the AGN feedback. Another relevant process may be the dredge-up and entrainment of the cold gas due to the jet ram pressure.

Before analysing the simulation results on thermal instabilities in the exemplary cluster A1795, I first present an overview of the cold gas properties (molecular and ionised) in virialised structures, with emphasis on cool-core systems and their BCG (the brightest central elliptical; see also Sections 1.4.4 and 1.4.5). Unfortunately, there is not yet a comprehensive view on this fundamental topic, although several investigations provide key insights into the observational features of the cold phase; the highest resolution survey in cooling flow systems is probably provided by the excellent works of McDonald et al. (2009, 2010, 2011a,b, 2012). The results of this Chapter are also presented in Gaspari et al. (2012a).

7.1 Cold Gas Overview

Cooling flows should not be entirely suppressed. As anticipated in Section 1.4.4, there is widespread observational evidence of optical line-emitting 'nebulae', found primarily

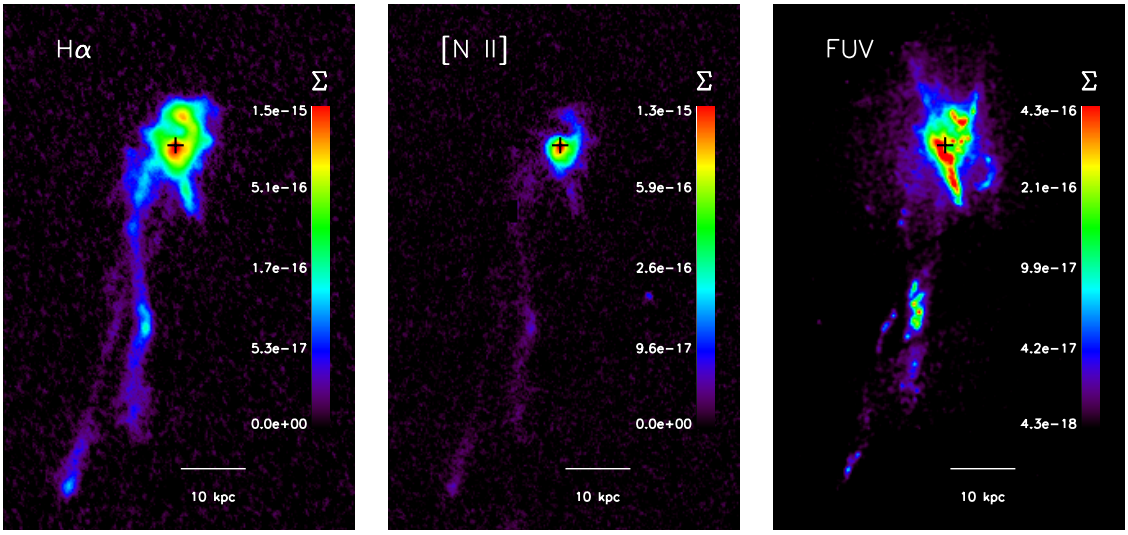

Figure 7.1. Surface brightness maps of Hα (*MMTF*), [NII] (*MMTF*) and FUV (*HST*) for the galaxy cluster Abell 1795 (from McDonald & Veilleux 2009). The images show the spectacular filamentary and nuclear structures of the cold/warm phase in the cluster core.

in cooling flow systems, a sign that cooler gas ($\sim 10^4$ K) coexists with the hot phase (e.g. Hu et al. 1985; Heckman et al. 1989; Crawford et al. 1999; Hatch et al. 2007). The Hα emission (6563 Å), resulting from the recombination of the hydrogen ion, is in fact an optimal tracer for the cooler - molecular and neutral - gas (e.g. Jaffe et al. 2005; Oonk et al. 2010), which is instead more difficult to directly detect and quantify.

Molecular gas, mainly H_2, is usually revealed through CO emission, typically through the lines (1-0) and (2-1). Via interferometric mm mapping of the CO emission (*IRAM* 30m telescope), Salomé and collaborators (2003, 2004, 2006, 2008) find masses of molecular gas in the range $10^9 - 3 \times 10^{11}$ $M_\odot$, confirming earlier preliminary results in cool-core clusters (Edge 2001). The spatial extension of the molecular gas never exceeds ~ 50 kpc, with associated velocities $\sim 100-200$ km s^{-1}. The identified CO features are very similar to the structures observed in Hα and the star forming regions linked to the UV-continuum excess. Another relevant component of the cold phase can be neutral hydrogen, observed via 21-cm emission and reaching masses of $\sim 10^{10}$ $M_\odot$ (NGC 1275; Jaffe 1990).

Since Hα emission is more trivial to detect, it is worth to focus on this well-studied tracer of the cold gas. The deep, wide-field, narrow-band survey conducted by McDonald et al. (2010, 2011a,b, 2012), thanks to the *Magellan* tunable filter *MMTF*, shows the ubiquity of this 'warm' ionised phase. Well-studied nearby examples, including NGC 1275 (Perseus – Conselice et al. 2001; Hatch et al. 2006), NGC 4696 (Centaurus – Crawford et al. 2005) and A1795 (McDonald & Veilleux 2009), exhibit extended filamentary nebulae (up to several tens kpc from the centre), usually cospatial with soft X-ray filaments and associated with AGN outbursts or galactic winds[1]. Approximately a third of BCGs have complex, filamentary morphologies at Hα, another $\sim$ 30% have marginally extended or nuclear Hα emission. Thus, in the majority of cool-core systems the cold gas is a fundamental element of the evolution, that any AGN feedback model

[1]The bright, soft X-ray and Hα filaments in these winds have strikingly similar patterns on both small and large scales, $\sim 0.01 - 10$ kpc, further supporting the entrainment scenario (see Veilleux et al. 2005 for a review).

must also reproduce. There is no difference in the morphology or detection frequency of Hα filaments in groups versus clusters over the mass range $10^{13} < M_{500} < 10^{15}\ M_{\odot}$ (McDonald et al. 2011a). This also implies that the AGN feedback must scale with the total mass (to avoid drastic heating and the erasure of the filamentary cold gas), in agreement with our previous theoretical findings (Chapters 5 and 6).

Tracing the evolution of optically emitting BCGs may indirectly probe the evolution of cool cores in galaxy clusters, which proves exceedingly difficult using X-ray techniques at high redshift. There is indeed increasing evidence for a decline in the fraction of BCGs with optical emission-line nebulae from $z = 0$ to $z = 0.3$ (McDonald 2011), suggesting that feedback processes may be more effective at earlier times.

A textbook example of cold phase, both in the form of extended filaments and a nuclear structure, is the massive galaxy cluster, Abell 1795. Figure 7.1 clearly shows the impressive Hα double filaments, $\sim$ 50 kpc long, emanating from the central AGN and a very disturbed, star-forming central region. The width is remarkably small, less than few kpc, possibly shaped by the magnetic field, which is in theory able to suppress conduction (Fabian et al. 2003; Hatch et al. 2007) and thus to help the growth of thermal instabilities. The narrowness of the strands also supports the highly nonlinear runaway cooling of the plasma.

Along the filaments, UV-bright knots indicate substantial star formation ($\sim 1\ M_{\odot}\ \mathrm{yr}^{-1}$; right panel in Fig. 7.1). The identification of star-forming regions in cool cores has a rich history in the literature (see Sec. 1.4.5). Several studies found significant amounts of star formation in cool-core BCGs (the blue-light excess; Rafferty et al. 2008), still two orders of magnitude lower than the classic cooling rates (see Figure 1.9; O'Dea et al. 2008). Typical SFRs are $1 - 10\ M_{\odot}\ \mathrm{yr}^{-1}$, with an efficiency of $\sim 10 - 15\%$. Filaments are therefore the ideal nursery for stellar formation. Another sign of strong stellar evolution is dust, emitting in the IR band, confirmed by the small amount of reddening found in the extended, filamentary cold phase (with typical $\mathrm{E(B-V)} \lesssim 0.2$).

[NII] emission at 6583 Å is another tracer of the warm ionised gas (although less bright). The ratio [NII]/Hα provides a measure of the relative importance of ionisation, which seems high and fairly uniform throughout the filaments. The ionisation source remains a matter of debate. Based on the ratio of the FUV and Hα luminosity, it seems likely that the massive young stars formed inside the cold phase can indeed photoionise the filaments (McDonald et al. 2012). Other scenarios involve heat conduction, the central AGN or cosmic rays heating (Crawford et al. 2005).

Most of the filamentary cold structures correlate well[2] with the X-ray emission (see Figure 1.8), suggesting that the warm ionised gas traces indeed the (X-ray) cooling flow, as speculated more than 30 years ago (e.g. Cowie et al. 1980; Fabian et al. 1984; Heckman et al. 1989). The idea of thermally unstable, rapidly cooling ICM was gradually discarded, lacking a source able to drive nonlinear thermal instabilities (that here I argue to be the active nucleus). Nevertheless, the observational evidences are now substantial. Along the filaments the cooling rates are usually enhanced by an order of magnitude; there is a strict correlation between the presence of Hα filaments and the properties of the cool core,

[2]Sometimes the X-ray emission shows a small spatial offset.

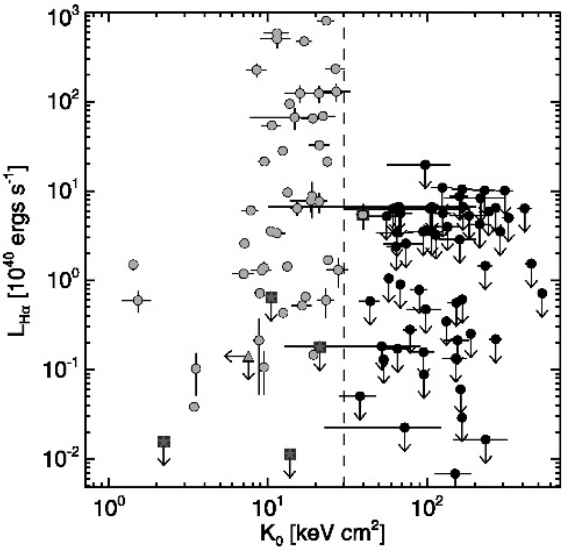

Figure 7.2. Hα luminosity vs. central entropy for a sample of 222 clusters (from Cavagnolo et al. 2008). Note that cool-core systems ($K_0 < 30$ keV cm^2) often harbour extended multiphase gas.

namely the (lower) entropy and the average temperature of the medium (McDonald et al. 2010, 2011a). In particular, Cavagnolo et al. (2008) and Voit et al. (2008) have found a key threshold (important also for our models[3]): only systems with central entropies below 30 keV cm^2 show evidence for extended multiphase gas (see Figure 7.2). Moreover, the extent of the Hα filaments never exceeds the cooling radius, further supporting the (quenched) cooling flow origin.

In the central regions ($r < 10$ kpc), the cold/warm gas usually shows kinematic signatures of rotation, while the extended filaments are broadly consistent with both infall and outflow, with velocities around few 100 km s^{-1}, interestingly similar to our previously computed AGN-driven turbulence (Section 6.5.2). The filaments and clouds with radial outflowing velocities seem often coincident with the boundaries of the AGN cavities. Thus, some authors (e.g. Churazov et al. 2001; Hatch et al. 2007; Revaz et al. 2008) argue that the buoyant bubbles can uplift the central cold gas and form the filaments. This mechanism is not in contradiction with the thermal instability origin, as highlighted by the simulations of this Chapter.

So far, we have focused mainly on the massive ellipticals at the centre of groups and clusters. However, it is worth noting that cold - ionised and molecular - gas is really ubiquitous among galaxies. The cold phase is widely present in spiral galaxies. Furthermore, in recent years, the myth of the 'red and dead' ellipticals has been gradually dismantled. The GALEX, ATLAS^{3D} and SAURON surveys have provided a unique view on the ISM properties of ETGs: at least[4] $\sim 25-30\%$ possess substantial gas reservoir of molecular gas (up to 10^9 $M_\odot$; Combes et al. 2007; Young et al. 2011; Crocker et al. 2012); $\sim 44-66\%$ have detectable neutral hydrogen (Oosterloo et al. 2010); $\sim 75\%$ show dust features (Colbert et al. 2001); more than 30% have an excess of UV emission, attributable

[3]This criterion can be expressed in terms of the ratio of the cooling and free-fall timescales, governing the whole condensation process (Section 7.4).

[4]The fraction of S0 galaxies harbouring molecular gas can reach sometimes even 80% (Welch & Sage 2003).

to ongoing residual star formation (Kaviraj et al. 2007). Galaxies can regenerate a cold ISM through both internal and external processes, e.g. by stellar mass loss, accretion from the circumgalactic medium (IGM/ICM), and/or mergers (Davis et al. 2011). Overall, it seems that cold gas reservoirs and residual star formation are never erased. Even strong AGN outbursts, capable of drastically quenching cooling flows, show a positive feedback, inducing subsequent turbulence and compression, which lead to sudden nonlinear thermal instabilities and to the condensation of the hot phase.

7.2 Simulation Setup

For most microscopic heating mechanisms the ICM is expected to be locally thermally unstable. In other words, even if the ICM maintains global thermal balance without a cooling flow, some of the gas can experience runaway cooling. Analytical estimates and idealised simulations by McCourt et al. (2012 – M12) and Sharma et al. (2012 – S12) point out that a spatially extended and inhomogeneous cold phase can form whenever the cooling time[5], $t_{\rm cool}$ (Equation 1.2), drops below the free-fall time, here roughly estimated as

$$t_{\rm ff} = \left(\frac{2r}{g(r)} \right)^{1/2}, \tag{7.1}$$

where $g(r)$ is the total gravitational acceleration at a certain radius r (mainly governed by the dark matter halo – Section 3.9).

Previous studies (e.g. Balbus & Soker 1989) did not predict the presence of multiphase gas because they neglected a spatially distributed heating, which provides global thermal stability. Here I perform high-resolution three-dimensional simulations which incorporate our realistic type of heating, i.e. self-regulated massive AGN outflows, in a realistic astrophysical scenario, i.e. the massive galaxy cluster A1795. The focus of the investigation is to understand the (possible) condensation of the hot gas into an extended or nuclear cold phase, as widely suggested by the observations mentioned in the previous Section.

In Table 7.1 are summarised all the numerical details of the hydrodynamic simulations carried out with FLASH, including the type of feedback (Sec. 3.7), the efficiency, the jet width and height ($d_{\rm jet} \times z_{\rm jet}$), and other relevant properties (see Chapter 3 for the details of implementation). As usual, the hydrodynamic equations are solved via the split PPM solver (Sec. 3.2). All the multiphase gas computations use the new exact cooling solver (described at end of Section 3.5), without any mass dropout, in order to follow the dynamics of thermal instabilities. The assumed metallicity for the cooling function is 0.3 $Z_\odot$ (the temperature floor is the usual 10^4 K). The outflows are in almost every run cylindrical (standard setup), injected through the internal boundaries (with $v_{\rm jet} = 5 \times 10^4$ km s^{-1}; Section 3.6). At variance with the previous simulations, the self-regulation is not linked to either cold or hot accretion, but given by the inflow through a 'spherical' surface very near the centre, $r \sim 500$ pc (see end of Section 3.7).

[5]The cooling time and the thermal instability timescale are similar for a microscopic heating mechanism which is independent of density, so I use $t_{\rm TI}$ and $t_{\rm cool}$ interchangeably (see also M12).

Table 7.1. Parameters and properties of the most relevant multiphase gas simulations.

Model	Feedback	Efficiency ϵ	Jet width × height (kpc)	Injection	$\min(t_{\rm cool}/t_{\rm ff})$	Notes
r7-CF	no AGN heating	-	-	-	7	-
r21-CF	no AGN heating	-	-	-	21	-
r7-i6m3	inflow	6×10^{-3}	0.60×0.0	nozzle	7	standard
r7-i6m3w	inflow	6×10^{-3}	0.60×0.0	nozzle	7	random wobbling
r7-i6m3c	inflow	6×10^{-3}	0.60×0.0	nozzle	7	convergence ($2\Delta x$)
r7-i1m2	inflow	10^{-2}	0.60×0.0	nozzle	7	standard
r21-i6m3	inflow	6×10^{-3}	0.60×0.0	nozzle	21	standard
r21-i1m2	inflow	10^{-2}	0.60×0.0	nozzle	21	standard

Radiative cooling ($Z = 0.3\ Z_\odot$): new exact method, without cold mass dropout (Sec. 3.5).

Perturbed initial conditions (A1795): Gaussian random field, with a white noise power spectrum ($\xi = 0.3$).

7.2.1 Initial Conditions

The massive galaxy cluster A1795 ($M_{\rm vir} \approx 10^{15}$ M$_\odot$) is modelled in the same way as explained in Section 4.2.1, although here the resolution is drastically increased, reaching a maximum $\Delta x \approx 300$ pc (in the core), and we simulate the entire cluster (with the AGN at the centre of the box).

In order to model a more realistic atmosphere, we choose to perturb these initial density and temperature profiles (avoiding the idealised perfect spherical symmetry). Depending on the amplitude (here $\xi = 0.3$), thermal instabilities can thus develop even in the early stages of evolution, before the AGN has become very powerful. The fluctuations leading to the initial thermal instability could be produced by the turbulence associated with cosmological mergers. Using dispersion relation and direct simulation, M12 and S12 demonstrated that thermal instability does not dramatically depend on the range of the driving modes in Fourier space. For now, it is thus sufficient to adopt a simple Gaussian random field with a white noise power spectrum (see Section 3.9.1 for the implementation). More importantly, after several cooling times the growth of instabilities is mainly driven by the AGN turbulence – as also seen in the previous simulations (e.g. Figure 6.8).

The obtained initial conditions correspond to the initial minimum ratio of $t_{\rm cool}/t_{\rm ff} \sim 7$, an important parameter for the early development of nonlinear instabilities. In a few models (Sec. 7.3.5), the central density profile is modified (shallower) in order to test a higher ratio, $t_{\rm cool}/t_{\rm ff} \sim 21$.

I decided to neglect magnetic fields and anisotropic thermal conduction. M12 showed that anisotropic conduction changes the morphology of the cold gas (becoming more filamentary), but does not affect the criterion for the generation of the multiphase gas due to thermal instabilities. I defer the study of these effects to future specialised works.

7.3 Results

I present simulation results for different AGN efficiencies ϵ, jet inclinations (steady and wobbling jets), and different initial values of the minimum $t_{\rm cool}/t_{\rm ff}$ in the ICM (TI-ratio; minimum value over all radii). The previous results (Chapter 4) demonstrated that a suitable choice of the mechanical AGN efficiency, in the cluster regime, should be in the range $5\times10^{-3}-10^{-2}$. This seems also supported by observational constraints (e.g. Merloni & Heinz 2008; La Franca et al. 2010). Common observed values for the minimum initial TI-ratio are in the range from 5 to 25 (M12). Motivated by these results, we perform computations with initial TI-ratio 7 or 21, and $\epsilon = 6 \times 10^{-3}$ or 10^{-2} (Table 7.1[6]). All models are evolved for 5 Gyr.

In the following analysis, I focus mainly on the multiphase gas and the growth of thermal instabilities, showing the related key plots. At the same time, the models need to solve the cooling flow problem. Since we have extensively investigated this topic in

[6]The elevated computational cost of the simulations (more than 500 000 CPU-hours) restricted the number of tested values in the parameter space.

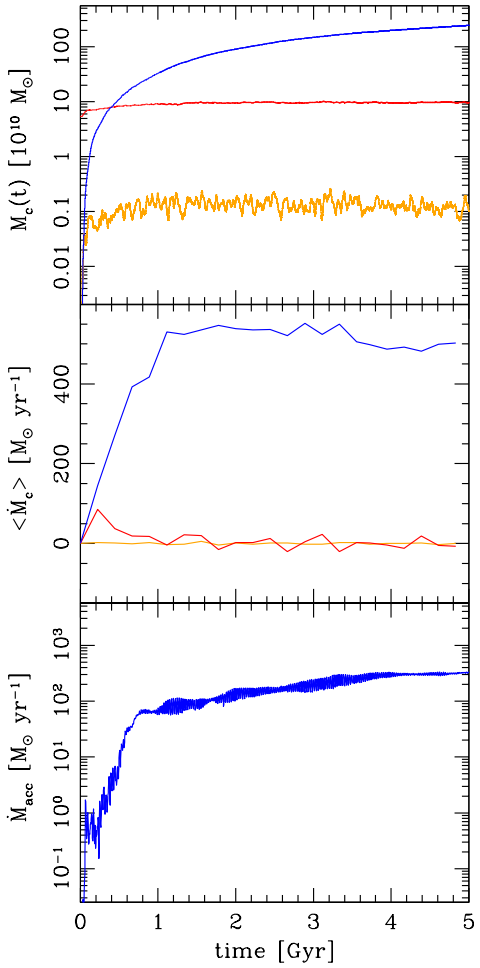

Figure 7.3. Diagnostics for the pure cooling flow simulation with initial minimum $t_{\rm cool}/t_{\rm ff} = 7$ (r7-CF). From top to bottom panel: total mass and average mass cooling rate as a function of time in the central 20 kpc; accretion rate (in the sink region) as a function of time. Colours correspond to the three gas phases: blue - cold ($T < 5 \times 10^5$ K), yellow - warm ($5 \times 10^5 \leq T < 10^7$ K), red - hot ($T \geq 10^7$ K). Notice the strong cooling rate of $\sim 500\ M_\odot\ {\rm yr}^{-1}$, after just 1 Gyr.

Chapter 4, the related diagnostics, like radial profiles and detailed jet properties, will be only briefly described. I refer to the previous three Chapters for more details on avoiding the cooling flow catastrophe and drastic overheating.

7.3.1 Pure Cooling Flow [r7-CF]

I first analyse the reference model, i.e. the simulation without AGN heating. In this simulation we keep the central gas sink term but neglect feedback. This case leads to the classic cooling flow catastrophe. The plasma in the central region of the cluster (~100-200 kpc) looses energy due to radiative cooling. Consequently, the gas pressure drops, leading to a subsonic spherical inflow. The increase in the central gas density results in higher cooling rates, which, in turn, accelerates the mass accretion rate, leading to runaway cooling and accretion. The results from a cooling flow run for the initial TI-ratio of 7 are presented in Figures 7.3 and 7.4.

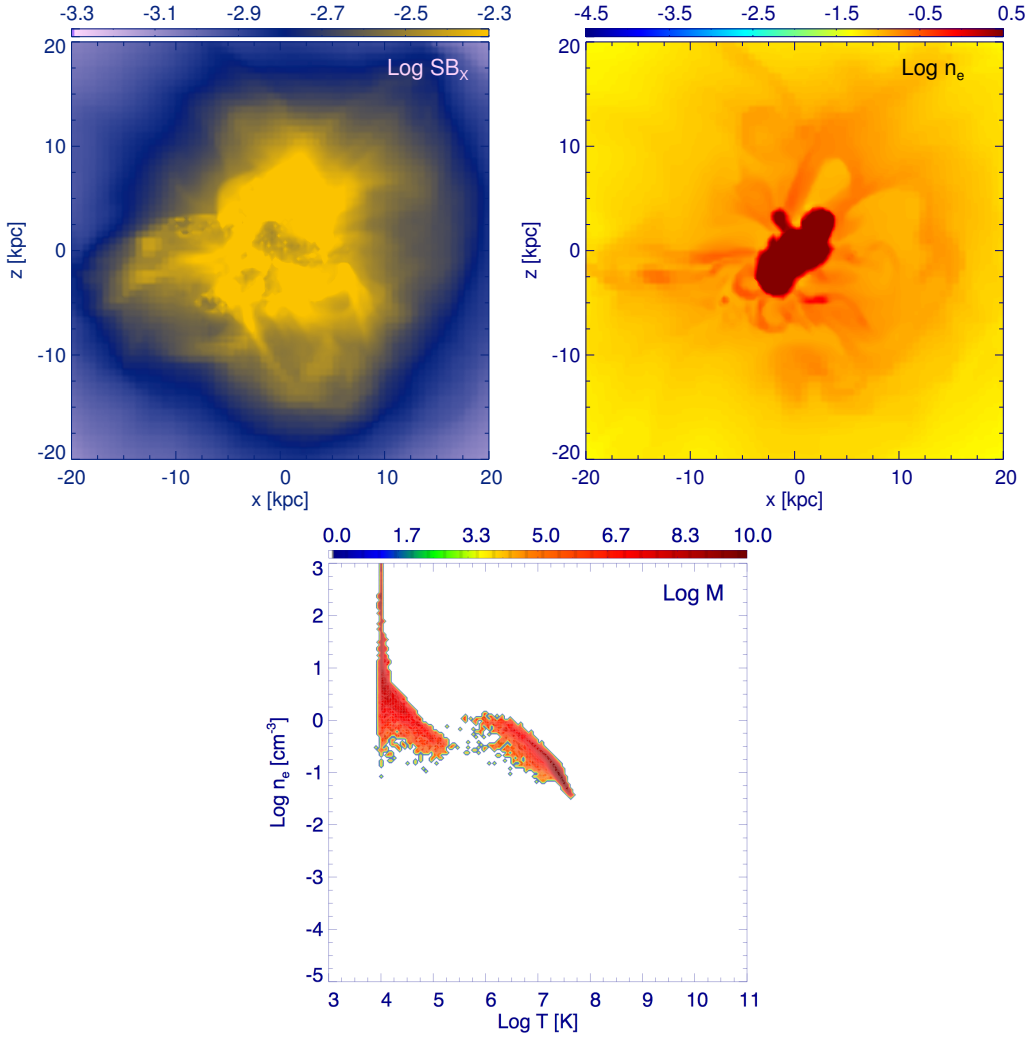

Figure 7.4. Pure cooling flow simulation (r7-CF) at 1.51 Gyr. Left: X-ray surface brightness (erg s^{-1}cm^{-2}; in the *Chandra* energy band 0.3 – 10 keV). Right: n_e midplane cut (cm^{-3}). Middle: joint distribution of $\log T$ versus $\log n_e$, coloured by gas mass in each bin ($M_\odot$); the size of the logarithmic bins is 0.05. Each map has logarithmic scale, describing only the central 20 kpc (cluster core). Thermal instabilities and extended cold gas are possible only in the early stage; later the collapse becomes monolithic, with a huge central accumulation of cold gas.

In Figure 7.3, I show the total mass, the average mass rate and the accretion rate as a function of time. The quantities in the first two panels correspond to the gas within the central 20 kpc. Different gas phases are coded according to: 'cold' ($T < 5 \times 10^5$ K, blue), 'warm' ($5 \times 10^5 \leq T < 10^7$ K, yellow), 'hot' ($T \geq 10^7$ K, red). The choice is not arbitrary because the limits of these temperature ranges correspond approximately to different critical slopes in the cooling function $\Lambda(T)$. Top panel reveals that the total mass of cold gas exceeds 10^{12} $M_\odot$ after a few Gyr. Middle panel shows that after 1 Gyr the cold phase continues to accumulate in the core (20 kpc) at a steady average rate of $\sim$ 500 $M_\odot$ yr^{-1} (peaks can reach $\sim$ 800 $M_\odot$ yr^{-1}), a blatant discrepancy with observations (Peterson et al. 2001, 2003; Peterson & Fabian 2006). The cold gas never decreases with time, usually overwhelming the hot and warm phase by one and three orders of magnitudes, respectively. The accretion rate in the sink region is closely linked to the cooling rate (last

panel). However, not all of the cooling gas gets accreted because the inflowing cold gas forms a rotationally-supported structure.

The pure cooling flow manifests itself as a sudden decrease in temperature, lesser than $T_{\rm vir}/3$. The projected emission-weighted ($T_{\rm ew}$) temperatures falls below the observational data of A1795 (e.g. Tamura et al. 2001 and Ettori et al. 2002). The electron number density $n_{\rm e}$, linked to the surface brightness, increases rapidly within 70 kpc from the centre, with the simulated profiles lying above the observational data points. The entropy ($k_{\rm b}T/n_{\rm e}^{2/3}$) near 1 kpc is $\sim$ 1 keV cm^2, without showing any sign of the typical observed floor (Cavagnolo et al. 2008).

In Figure 7.4 are presented the maps of X-ray surface brightness, the midplane cut of electron number density ($n_{\rm e}$), and the gas phase diagrams with temperature versus $n_{\rm e}$ (values are coloured by gas mass in each bin). Each map has logarithmic scale and contains the data only for the central core (20 kpc). The density maps (1.51 Gyr) reveal significant cold gas accumulation in the core, accompanied by a strong increase in the central surface brightness. Since in the 'warm' temperature range the gas has a short cooling time, the ICM tends to accumulate in the 'cold' and 'hot' phases. This effect is clearly visible in the phase diagram.

In the cooling flow run distinct cold gas clouds and filaments can be seen predominantly in the early stages of the evolution. At late times (like t = 1.51 Gyr) the collapse proceeds in a monolithic way, and the atmosphere is globally unstable. Note that the $t_{\rm cool}/t_{\rm ff}$ criterion does not apply to a cooling flow, because the theoretical analysis assumes thermal balance (see M12). In order to generate multiphase gas in a cooling flow, a substantial amplitude of perturbations is required, e.g. $\xi \gtrsim 0.1$ (see also Pizzolato & Soker 2005 and S12). Both initial TI-ratio of 7 and 21 (r21-CF; not shown) produce similar results. The latter case has longer saturation time and slightly smaller mass in the cold phase (the initial total mass in the box is also 8% smaller).

All the features of the pure CF model, discussed above, are in contrast with observations of cool-core systems (Peterson et al. 2001, 2003; Ettori et al. 2002; Tamura et al. 2003; Peterson & Fabian 2006). This simulation merely serves as a reference case for the runs presented in the subsequent Sections. As usual, a successful model will instead be characterised by a quasi equilibrium between heating and cooling, with low cooling rates ($\lesssim$ 10% of the pure cooing flow), profiles consistent with observations. At the same time, the model needs now to account for the spatially extended (up to $\sim 15-20$ kpc) distribution of cold blobs and filaments while not violating the constraints on the total mass in these features. Below I discuss models that meet these requirements.

7.3.2 AGN Feedback: $t_{\rm cool}/t_{\rm ff} = 7$ and $\epsilon = 6 \times 10^{-3}$ [r7-i6m3]

Before including AGN jet feedback, I verified that using the idealised prescription of M12 and S12, i.e. local heating rate given by the cooling rate averaged in spherical shells, produces thermal instabilities and spatially extended multiphase gas. The results were consistent. However, unless cooling and heating are turned off in the central zones, this very rough prescription led to the massive accumulation of cold gas in the central few kpc, especially when the gas dropout or outflow through a central boundary was neglected.

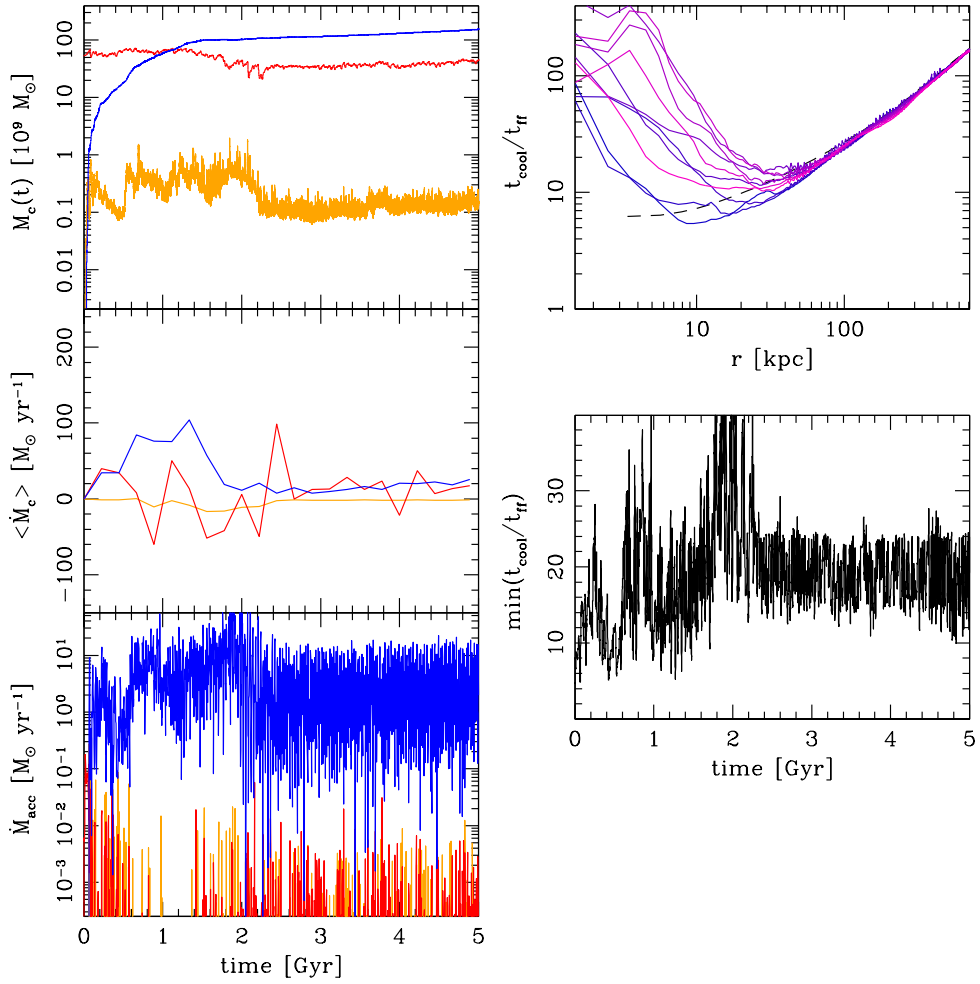

Figure 7.5. Diagnostics for the AGN feedback simulation with initial minimum $t_{\rm cool}/t_{\rm ff} = 7$ and $\epsilon = 6 \times 10^{-3}$ (r7-i6m3). First column: cooling and accretion diagnostics; see the description of Figure 7.3 for details. Second column: radial profile of $t_{\rm cool}/t_{\rm ff}$ and the temporal evolution of its minimum (gas with $T > 0.3$ keV). Note that the cooling rate is reduced to $\sim 4\%$ of the pure CF value and that a steady average equilibrium is maintained for several Gyr.

These findings provide additional motivation to include a realistic feedback mechanism, like self-regulated massive AGN outflows.

Mechanical feedback due to AGN jets dramatically changes the entire evolution of the galaxy cluster, compared to the pure cooling case. In Figures 7.5 and 7.6 are presented the diagnostic plots and maps for the runs that include AGN jets with mechanical efficiency $\epsilon = 6 \times 10^{-3}$.

The first column in Fig. 7.5 show the same quantities as those in Fig. 7.3. The gas mass in the cold phase $M_{\rm c}(t)$ (top panel) reaches $\sim 10^{11}\ M_\odot$ at the end of the evolution. This is consistent with molecular cold gas observations (Edge 2001; Salomé & Combes 2003), and is reduced by over a factor of 10 compared to the pure cooling flow value. Middle panel indicates that the average cooling rate $\langle \dot{M}_{\rm c} \rangle$ is also significantly quenched: after an initial transient phase, in which cooling is slightly elevated, the system starts to self-regulate through more powerful outbursts, and eventually reaches a steady rate of ~ 20 $M_\odot\ {\rm yr}^{-1}$. This value is about 4% of the value recorded in the r7-CF simulation, entirely

consistent with observations (e.g. Peterson & Fabian 2006). The instantaneous cooling rate (not shown) is quite variable, changing rapidly from positive to negative values due to the action of AGN heating.

As the cold gas mass M_c in the central 20 kpc exceeds the mass in the hot (3 times) and warm phases (10^3 times), the accretion rate is determined by the cold gas (last panel of first column); most of the time the black hole accretes cold gas at a rate between $1 - 5$ $M_\odot$ yr^{-1}. Cold accretion rate (blue) exceeds hot accretion rate (red) by at least two orders of magnitude. The latter is commonly associated with a Bondi-like mode; since the hot accretion rate is so weak, feedback simulations based on Bondi prescription would require an artificial boost factor or high mechanical efficiencies $\gtrsim 0.1$ (see for instance Chapter 5).

The mass accretion rate determines the AGN power and mass outflow rate. At 5 Gyr the total injected energy is $\sim 10^{62}$ erg. Even if the entire mass of the gas that falls into the sink region is added to the SMBH, its total mass will still be within reasonable limits (several 10^9 $M_\odot$). As suspected in Chapter 4 (see the Discussion), increasing the resolution leads to a less explosive feedback, due to the less massive accretion rates per single time step. The outflows are thus more continuous and frequent (albeit the total injected energy is similar on the long term), still showing peaks over 10^{46} erg s^{-1}; mass outflow rates can reach few $M_\odot$ yr^{-1}.

I emphasise that even with a different duty cycle, the cooling flow problem is anyway solved: the density inside 70 kpc is similar to the initial conditions, while the temperature and entropy profiles do not fall below $T_{vir}/3$ and 10 keV cm^2, maintaining a positive gradient – a sign that the cool core has not been destroyed during the quenching of the cooling flow. This is a remarkable fact, implying that the success of the mechanical feedback is not dependant on the exact details of the accretion, typically linked to the (numerical) resolution in the core.

In Fig. 7.5 (second column) are shown the radial profiles of t_{cool}/t_{ff} and the minimum value as a function of time. Although I discuss the relationship between t_{cool}/t_{ff} and the presence of the multiphase gas in more detail in Section 7.4, here I point out that whenever this timescale ratio falls below ≈ 10, thermal instabilities grow and cold gas clumps condense out of the hot phase. Initially, the cold phase has a filamentary structure; then it turns into small clumps which fall toward the centre in about a free-fall time.

The SB_X map and the the two-dimensional snapshot of n_e at 1.5 Gyr, shown in Figure 7.6, corresponds to a moment when the TI-ratio falls below 10. The jet outburst creates two cavities along the $z-$direction, which on larger scales become larger and move buoyantly outward (see the last three Chapters for a more detailed dynamics of the generated AGN features). At the same time, the perturbations due to the jets seem to lead to the formation of dense cold blobs up to $\sim$ 10 kpc away from the centre. The presence of multiphase gas is also apparent in the $n_e - T$ phase diagram (Fig. 7.6, middle panel), which displays two distinct diagonal islands occupied by the gas in the cluster core, with small variations away from pressure equilibrium.

Because the AGN heating is anisotropic close to the base of the jet and the cooling gas possesses small amount of angular momentum, the cold gas tends to accrete and

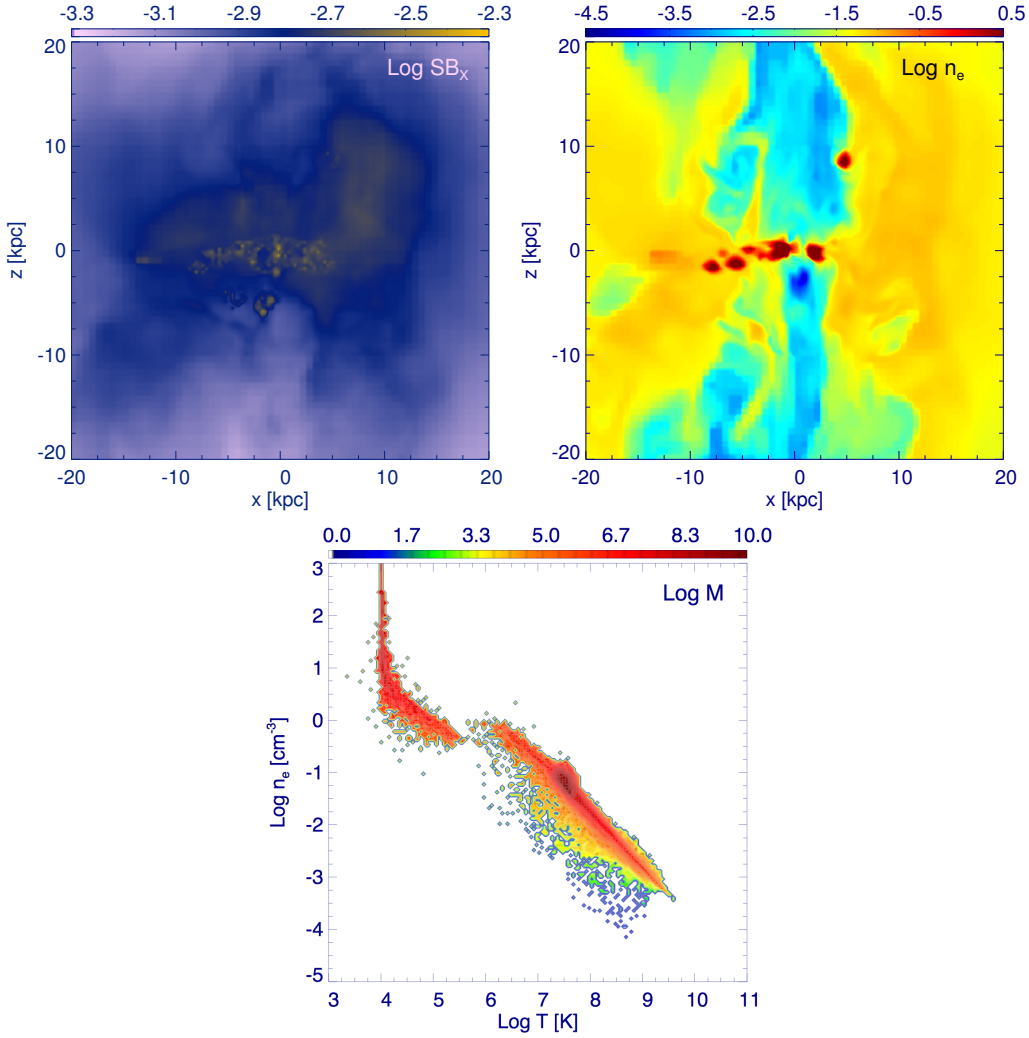

Figure 7.6. X-ray surface brightness map, density cut and phase diagram for AGN feedback model r7-i6m3 (initial minimum $t_{\rm cool}/t_{\rm ff} = 7$; AGN feedback $\epsilon = 6\times10^{-3}$). See the description of Figure 7.4 for details. The maps correspond to the time of 1.51 Gyr since the beginning of the simulation. The salient feature is the amplification of thermal instabilities, due to the AGN perturbations, with cold blobs condensing out of the hot phase ($t_{\rm cool}/t_{\rm ff} \lesssim 10$), up to 10 kpc away from the centre.

condense more along the equatorial region. In a realistic situation this gas can not be entirely removed in a brief time; consequently, a cold rotationally-supported torus is formed, which provides most of the fuel for the AGN. The fuel supply from the torus, or the torus itself, can be temporarily disturbed by AGN outbursts, shocks, and the ICM turbulence. The central accumulation of cold gas could be further reduced by including star formation.

Overall, the heating due to realistic AGN outflows, with mechanical efficiency $\epsilon \approx 6\times10^{-3}$, appears to reproduce the main properties of the observed clusters: quenching the cooling flows while preserving the cool cores for several Gyr. At the same time, the model predicts the formation of the multiphase medium in the form of cold blobs and filaments while satisfying the observational constraints on the amount of cold gas (e.g. Edge 2001; Salomé & Combes 2003, 2004; McDonald et al. 2010, 2011a,b).

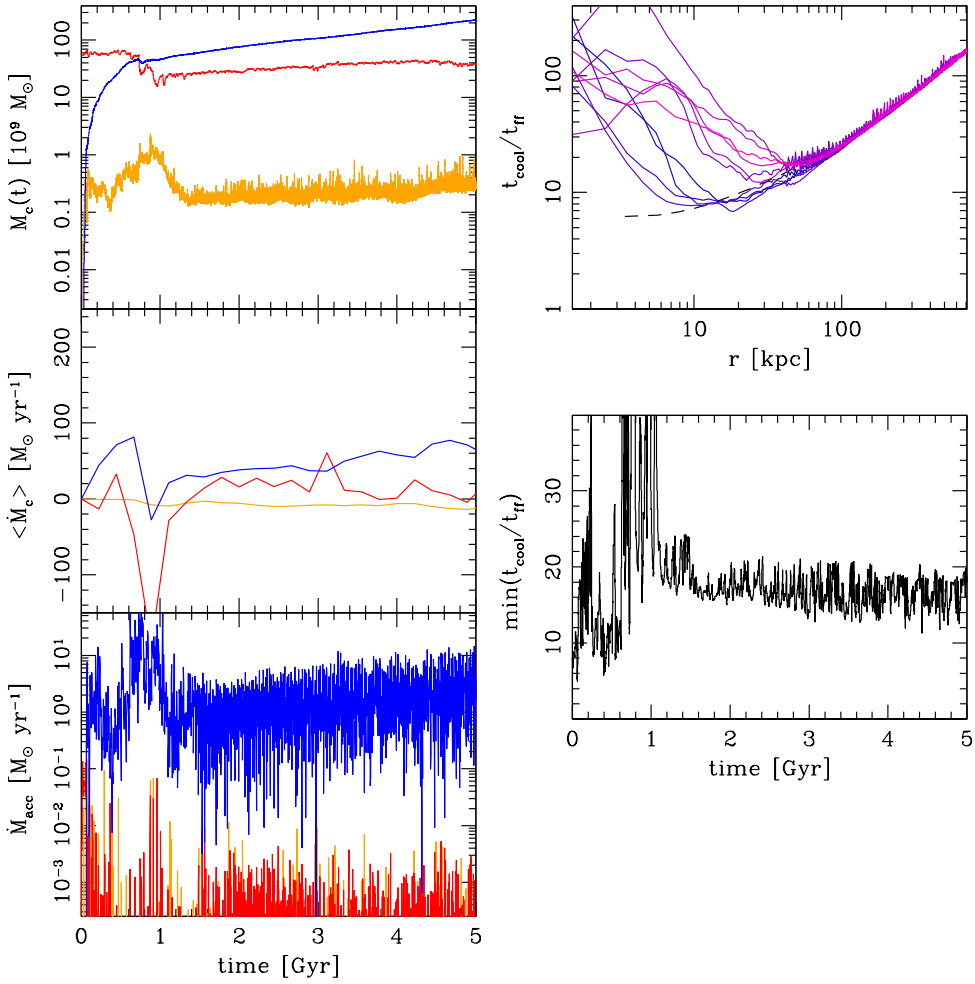

Figure 7.7. Same as Figure 7.5 but for AGN feedback efficiency $\epsilon = 10^{-2}$ (r7-i1m2). Raising the efficiency produces stronger and more massive outflows, which have more difficulty in stopping the cooling flow, because they tend to release their energy at larger radii. Values are still consistent with observations.

7.3.3 AGN Feedback: $t_{cool}/t_{ff} = 7$ and $\epsilon = 10^{-2}$ [r7-i1m2]

I now discuss a run for higher mechanical efficiency ($\epsilon = 10^{-2}$) compared to the one considered in the previous Section. I use the same set of diagnostic plots as before, discussing only the differences between these models. The results for $\epsilon = 10^{-2}$ are shown in Figures 7.7 and 7.8, which are direct counterparts to Figures 7.5 and 7.6.

The increase in the mechanical efficiency of the jets leads to stronger outflows characterised by a slightly more peaked jet power distribution (exceeding sometimes few 10^{46} erg s^{-1}). Since the outflows are more massive (due to the higher P_{jet}), they carry larger amount of linear momentum and, thus, have more piercing power. Consequently, the jets release more of their energy at relatively larger distances from the cluster centre, allowing a bit more cold gas accumulation along the equatorial region. The projected surface brightness map (Fig. 7.8) clearly shows the formation of a torus-like structure that was less pronounced in the lower efficiency run.

The initial increase in the average cooling (and accretion) rate is strongly quenched at

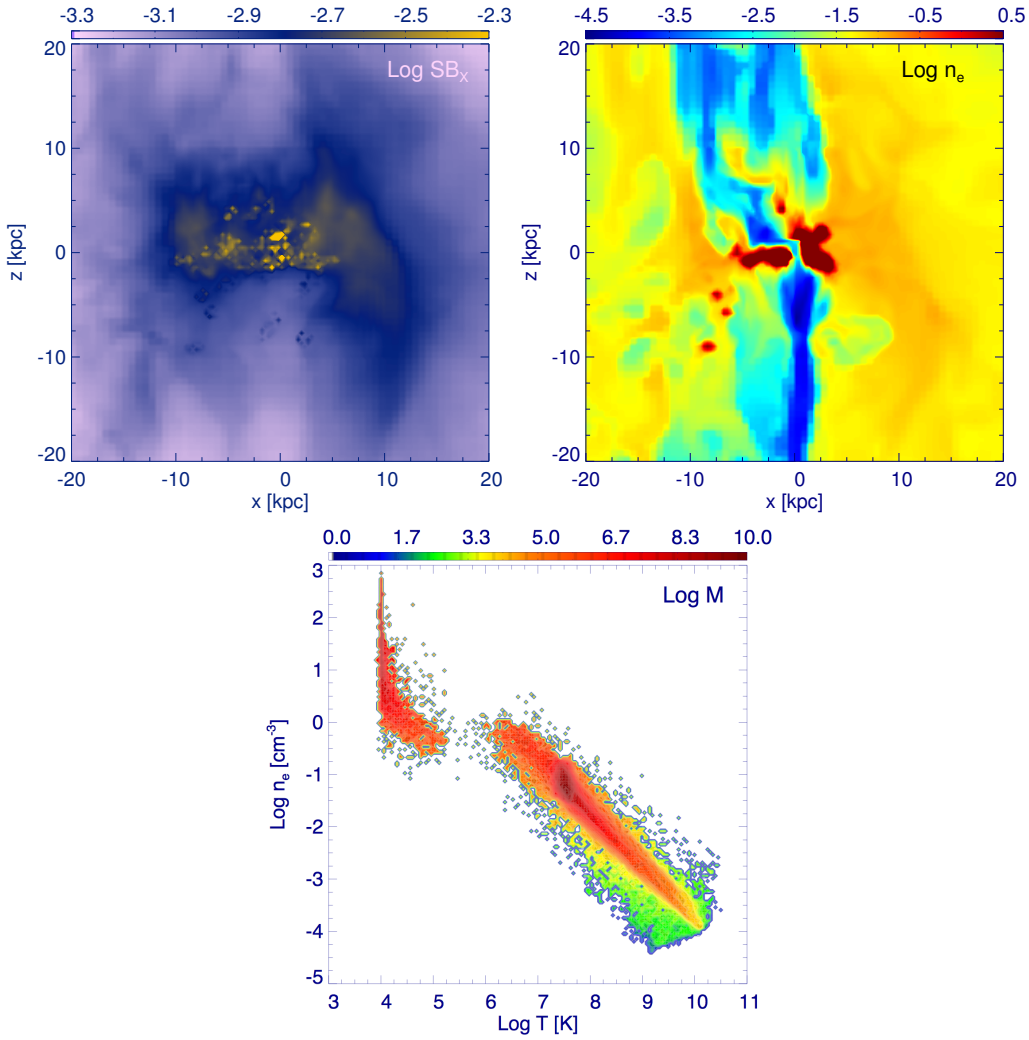

Figure 7.8. X-ray surface brightness map, density cut and phase diagram for model r7-i1m2 (initial minimum $t_{\rm cool}/t_{\rm ff} = 7$; AGN feedback $\epsilon = 10^{-2}$). The time of the maps is 0.61 Gyr. Notice that concentrated cooling, in the form of a rotating cold torus, is favoured over extended cold gas ($t_{\rm cool}/t_{\rm ff}$ is usually > 10).

around 1 Gyr since the beginning of the simulation (Fig. 7.7), which is earlier than in the previous run. After this short phase, the system gradually settles to a quasi equilibrium state, with cooling rates around 40−50 $M_\odot$ yr^{-1}, twice the level seen in the lower efficiency case. Paradoxically, more powerful jets are less efficient in stopping the cooling flow, due to tunnel carving. The total injected energy is comparable in both runs ($\sim 10^{62}$ erg), a sign that the self-regulation process is overall very similar. The total cold gas mass (2×10^{11} $M_\odot$) is slightly larger than in the preceding case, but still only 10% of the pure cooling flow value, which is consistent with the observational constraints (Sec. 7.1).

During the entire evolution, the outflows tend to produce bigger bubbles or a deeper channel (see also the n_e cut). The effect of more powerful jets is also to increase the scatter in the phase diagram (Fig. 7.8): the gas in hot phase occupies a wider range of values in the $n_e - T$ plane about the (imaginary) diagonal line representing average pressure.

The minimum TI-ratio falls below 10 only early in the evolution (Fig. 7.7). Extended

cold gas, in the form of blobs and filaments, is mainly formed at that epoch (see the n_e cut). At later times, more powerful events raise $t_{\rm cool}/t_{\rm ff}$ well over 10, and the ICM becomes hotter. Even if the system settles later around a minimum TI-ratio of 13, extended cold filaments may be occasionally seen at moderate radii due to dredge-up of the cold torus by the outflows. The uplift of the cold gas and the expansion of bubbles may further increase density, possibly triggering new thermal instabilities. This picture is also consistent with the observational analysis presented in M12 (see Figure 7.11), suggesting that value 10 marks an approximate transition to the regime where the multiphase gas may appear.

7.3.4 AGN Feedback: Wobbling Outflows [r7-i6m3w]

To test the robustness of our results, I included jet wobbling in the run with mechanical efficiency $\epsilon = 6 \times 10^{-3}$. Observational data is consistent with the possibility that the jets may precess or their orientation may change. Since the data is very limited, we keep the model very simple and change jet orientation whenever the accreted mass reaches a threshold of $10^7\ M_\odot$. For typical mass accretion rate of order $\sim\ 1\ M_\odot\ {\rm yr}^{-1}$, this corresponds to a reorientation timescale of ~ 10 Myr (e.g. Dunn & Fabian 2006).

In the first simulation with jet wobbling, the probability of jet pointing in a given direction is given by a random uniform distribution over 4π steradians (the bipolar jets are always collinear). Initially, the jet orientation changes at a slower rate, ~ 100 Myr, because the accretion rate is relatively low. Thus, in this early stage, the evolution is very similar to that for the non-wobbling case with efficiency of $\epsilon = 6 \times 10^{-3}$ (r7-i6m3). However, the energy is better spatially distributed, and thus the cooling rate is more quenched, reaching values $\lesssim 10\ M_\odot\ {\rm yr}^{-1}$. As the accretion rate accelerates, and the jet orientation starts to change on timescales of 10 Myr or less, the deposition of energy becomes nearly isotropic. A more uniform distribution of energy makes it more difficult to feed the black hole via the cold torus, which is now strongly disturbed. Rather than being used to drill a channel through the ICM, the AGN jet is no longer able to efficiently deliver the energy to the ICM beyond $r > 15$ kpc. This enables the gas to cool rapidly at these radii, which leads to the cooling catastrophe in about 1 Gyr. Larger efficiencies could possibly stop the cooling, but the nearly isotropic centrally-concentrated energy distribution would destroy the cool core.

In order to remedy this situation, I considered models where the jet orientation is confined to two conical regions of half opening angle 75°, 45°, and 25°. As before, the probability distribution of the jet orientations is randomly uniform within these regions. In the first two cases, the final result is similar to the case considered above, but the cooling flow is quenched for an additional time of $\lesssim 1$ Gyr.

For half opening angle of 25°, the jet energy distribution becomes narrower and more anisotropic. Apart from larger bubbles and a more frequent jet channel fragmentation, this computation resembles the previous best model r7-i6m3: the cooling rate is steady for several Gyr ($\sim 10-30\ M_\odot\ {\rm yr}^{-1}$), with total cold gas mass around $10^{11}\ M_\odot$. Cold blobs are produced mainly in the first 1.5 Gyr when TI-ratio oscillates around 10. At later times, the system settles to a hotter state characterised by the TI-ratio of ~15-16. Jet events are also more variable than in the r7-i6m3 model because more inclined outbursts are able to

partially dismantle the central torus, temporarily inhibiting accretion.

In summary, randomly wobbling jets with small and moderate opening angles produce similar results to unidirectional narrow outflows, especially for stopping the cooling flow catastrophe and generating extended multiphase gas. On the contrary, almost spherically-symmetric injections prevent proper fuelling of the black hole and, in the long term, the feedback can not quench the cooling flow. Therefore, I warn against implementing subgrid models based on isotropic injection, as is customarily done in SPH simulations (e.g. Power et al. 2011). The other relevant feature is that the central accumulated cold torus can be frequently destroyed, depending on the wobbling parameters.

7.3.5 AGN Feedback: $t_{\rm cool}/t_{\rm ff} = 21$ and $\epsilon = 6 \times 10^{-3}$ [r21-i6m3]

In order to study the effect of feedback in slower cooling systems, new initial hydrostatic conditions are generated as follows. I decreased the central density preserving the initial profile slope at $r \gtrsim 80$ kpc; simultaneously, the central temperature is raised to ensure that the ICM remains in hydrostatic equilibrium. The new initial conditions correspond to the minimum TI-ratio of ~ 21. The entropy is elevated to 30 keV cm^2 at 10 kpc – still within observational bounds (Cavagnolo et al. 2009) – while the total gas mass is decreased only by 8%. The results from the runs corresponding to these new initial conditions and AGN mechanical efficiency of $\epsilon = 6 \times 10^{-3}$ are shown in Figures 7.9 and 7.10. These figures are analogous to those previously discussed.

Overall, the behaviour of the system is quite similar to what we observed before. The model is successful in predicting a globally stable ICM core, low cooling rates (~ 50 $M_\odot$ yr^{-1}, 10% of pure cooling flow), preservation of the cool core (e.g. entropy, $\mathrm{SB_X}$), typical features of AGN jets (bubbles, shocks, turbulence), and the amount of multiphase medium consistent with observations. The main result is that the local thermal instability is triggered despite the fact that the *initial* minimum TI-ratio exceeds ~ 10. It is only when the instantaneous value of this ratio falls below the critical threshold of ~ 10 that the multiphase medium suddenly appears in the simulation (e.g. after 1 Gyr). As before, this leads to increased feedback that brings the system back to the high TI-ratio regime, which in this case is well above ~ 20, and higher than in the previously considered systems.

The total injected energy is about half the value of model r7-i6m3, due to the shallower initial density profile and thus reduced accretion rates. On the other hand, the AGN outflows have a relatively stronger impact on the lighter ICM, secularly increasing the TI-ratio back above 20. As a consequence, spatially concentrated cooling, in the form of a rotating torus, is present during the entire evolution. In Section 7.4, I provide an in-depth comparison between the models with different initial $t_{\rm cool}/t_{\rm ff}$ ratio.

7.3.6 AGN Feedback: $t_{\rm cool}/t_{\rm ff} = 21$ and $\epsilon = 10^{-2}$ [r21-i1m2]

The total cold gas mass in the model discussed above reaches 2×10^{11} $M_\odot$, which is higher than r7-i6m3. Although this is observationally acceptable, some systems show smaller amounts of cold gas mass. Therefore, I experimented with increasing the mechanical efficiency in order to decrease the amount of cold gas (figures not shown).

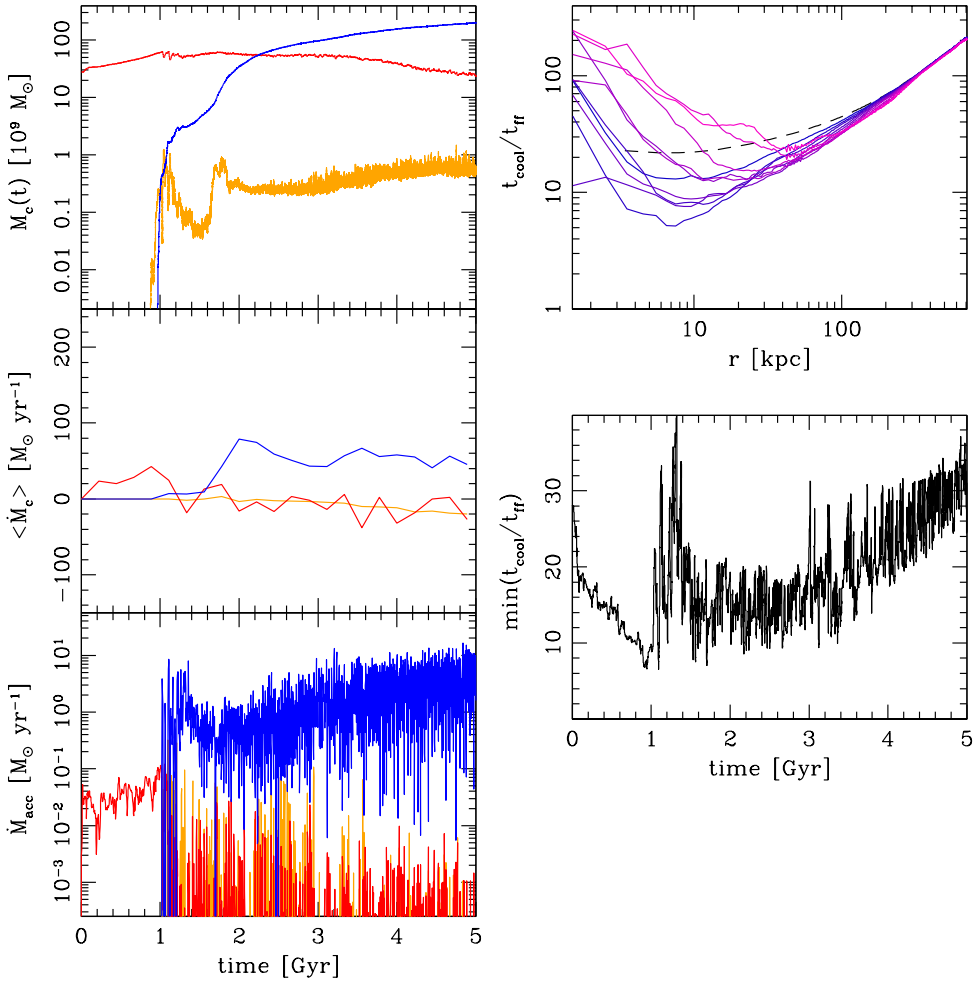

Figure 7.9. Same as Figure 7.5 but for initial minimum $t_{\rm cool}/t_{\rm ff} = 21$ and AGN feedback $\epsilon = 6 \times 10^{-3}$ (r21-i6m3). Starting with a higher TI-ratio produces an initial phase of slow cooling, followed again by strong heating when $t_{\rm cool}/t_{\rm ff}$ approaches 10 (the multiphase gas threshold). AGN outflows have a relatively stronger impact on the lighter ICM, secularly increasing the TI-ratio back above 20. This computation shows that the average thermal equilibrium is actually quasi stable, with phases of slight cooling or heating dominating throughout the entire evolution.

However, higher efficiencies lead to stronger and more mass-loaded jets that deposit their mechanical energy farther away from the centre. If in the initial outbursts the system appears to be more heated due to shocks, the situation reverses later, when the jet carves a deeper channel in the ICM. Thus, more accretion occurs along the equator and a strong cooling flow develops. As seen before, this feature could be alleviated by a randomly wobbling outflow, with a less anisotropic energy deposition.

Overall, the simulations with higher minimum initial TI-ratio 21, can again produce extended multiphase gas whenever the instantaneous $t_{\rm cool}/t_{\rm ff}$ falls $\lesssim 10$. In fact, in the early phase of the evolution, when cooling slightly prevails over heating, the TI-ratio slowly decreases, crossing the threshold in about a Gyr. Later, stronger outbursts set the system back to a hotter state and higher TI-ratio, until the cycle restarts again (it may require several Gyr). The main trend for the entire 5 Gyr is therefore concentrated cooling occurring in the core.

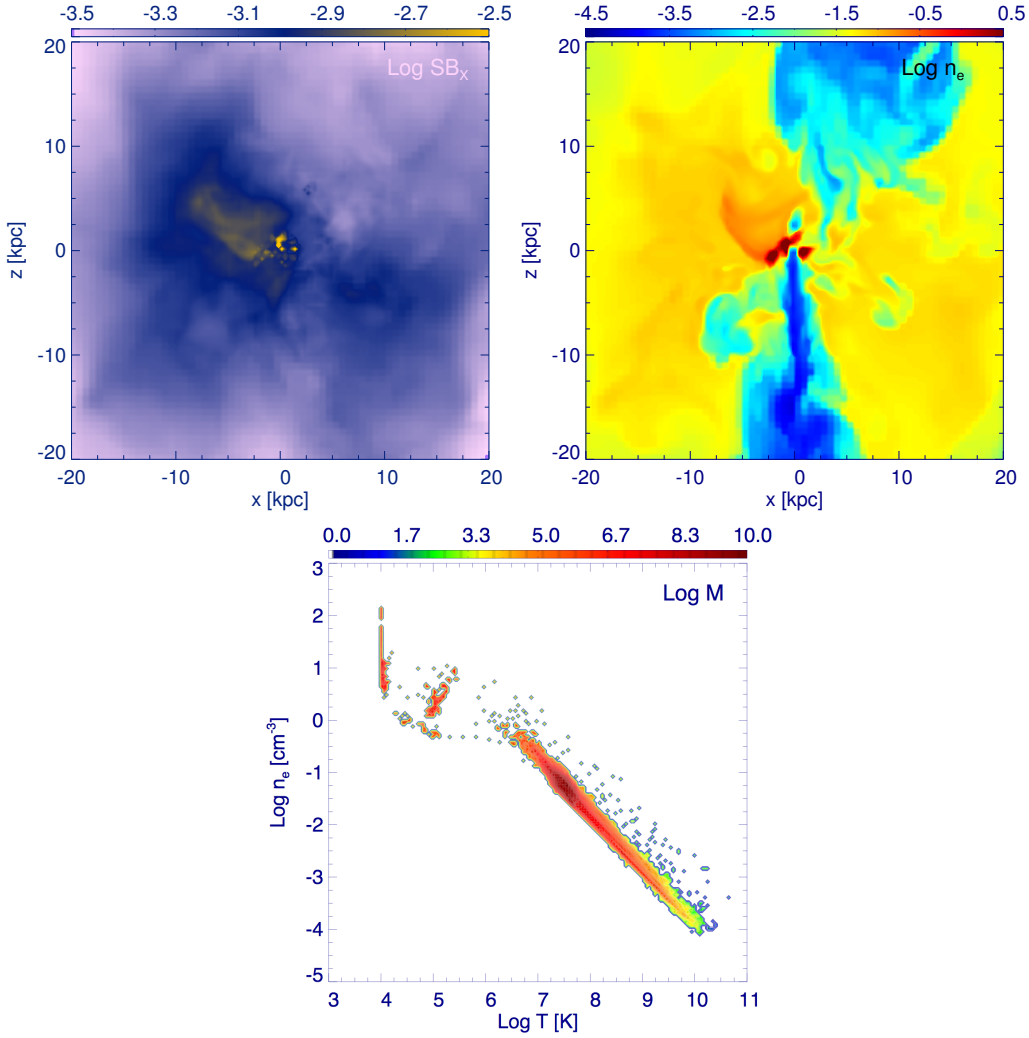

Figure 7.10. X-ray surface brightness map, density cut and phase diagram for model r21-i6m3 (initial minimum $t_{\rm cool}/t_{\rm ff} = 21$; AGN feedback $\epsilon = 6 \times 10^{-3}$). The time of the maps is 1.27 Gyr. Notice that concentrated cooling is favoured through the whole evolution, while cold extended blobs condense out of the hot phase only in short windows (again whenever $t_{\rm cool}/t_{\rm ff} \lesssim 10$).

Contrary to the more massive models (TI-ratio 7), the right efficiencies in order to quench the cooling flow and preserve the cool core should not be more than 6×10^{-3}. A less massive system is in fact more susceptible to mechanical outbursts, and requires a more delicate feedback, in analogy to the environment of galaxy groups or ellipticals, as demonstrated in the previous two Chapters.

7.4 Discussion: the Detailed Thermal State

The fundamental result of the previous computed models is that extended cold filaments and clouds condense out of the hot phase whenever $t_{\rm cool}/t_{\rm ff} \lesssim 10$. This is remarkably consistent with the analysis of McCourt et al. (2012): the observed profiles of clusters reveal exactly this threshold (see Figure 7.11). Since the cooling time is tightly related to

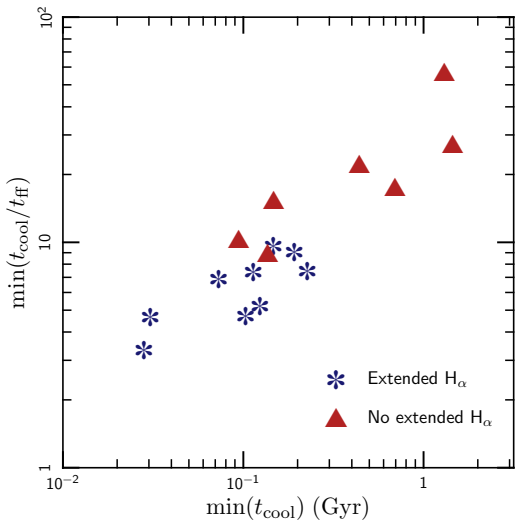

Figure 7.11. A sample of well-observed clusters in the $t_{\rm cool}$ vs. TI-ratio plane (from McCourt et al. 2012). The points represent the minimum value emerging from the radial profiles. The TI-ratio is an optimal predictor for the multiphase structures, appearing whenever $t_{\rm cool}/t_{\rm ff} \lesssim 10$, consistent with our feedback simulations.

the entropy[7] ($\propto K^{3/2}$), then

$$\frac{t_{\rm cool}}{t_{\rm ff}} \sim 10 \frac{K_{30}^{3/2}}{T_{7.5}^{1/2}\,\Lambda_{-22.7}\,t_{\rm ff,30}}, \tag{7.2}$$

where the entropy K is expressed in units of 30 keV cm^2, the temperature T in 3×10^7 K, the cooling function Λ in 2×10^{-23} erg cm^3 s^{-1}, and the free-fall time in units of 30 Myr. Therefore, for these typical values of cluster cores, the condensation ratio can be converted in the familiar observational entropy limit for the presence of *extended* multiphase gas (Cavagnolo et al. 2008; Rafferty et al. 2008; Voit et al. 2008; see Figure 7.2), that is $K \lesssim 30$ keV cm^2. Note that the criterion is somewhat dependent on $t_{\rm ff}$ and Λ, albeit in the core they do not drastically vary; this is because the entropy is not the fundamental parameter governing the thermal instability saturation (see M12 for a related discussion).

After condensation, the cold clumps fall toward the centre in about a free-fall time, forming a central cold rotating torus and in part boosting the black hole accretion rate. The formation of cold filaments is a result of interplay between thermal instability and gravity. The recent idealised analyses by M12 and S12 enforce strict thermal equilibrium (via an ad-hoc heating), finding that multiphase gas is generated according to the same threshold[8]. However, a realistic feedback displays a variegated self-regulated evolution, producing complex observed phenomena, which are not captured by simple idealised prescriptions.

In the present Chapter, I tested bipolar AGN outflows tied to the inflow/accretion rate at very small radii[9]. The asymmetrical input of energy produces strong elliptical shocks

[7] As previously done, I associate here the entropy with the adiabatic 'constant': $K = k_{\rm b} T n_{\rm e}^{-2/3}$.

[8] The criterion in spherical coordinates ($\lesssim 10$) is less stringent compared to the Cartesian case ($\lesssim 1$; see M12), because instabilities are amplified by the geometrical compression, as the clouds sink toward the centre.

[9] The simulations do not resolve the sphere of influence of the SMBH, so the actual mass accretion rate might

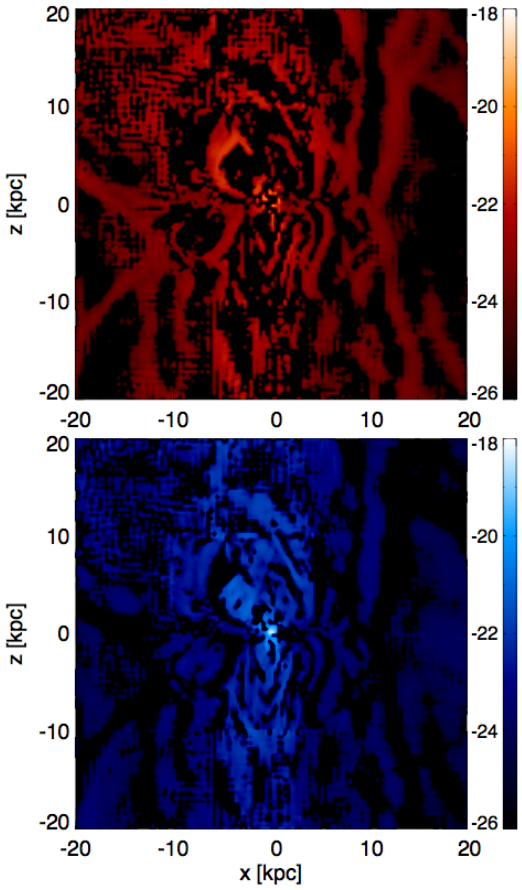

Figure 7.12. Thermal equilibrium diagnostics (best model r7-i6m3). 2D midplane cut of the cluster core (20 kpc) showing the net internal energy increase (top) or decrement (bottom), averaged between 1 and 2 Gyr (erg s^{-1} cm^{-3}; in logarithmic scale).

and regularly inflates hot bubbles, which rise outwards. At the same time the inflow is not entirely stopped: along the equatorial direction the gas, mainly cold, continues to fuel the black hole. Turbulence, entrainment and mixing dissipate the directional kinetic energy of the jets, further inhibiting the cooling flow near the centre. When the jet ram pressure is substantial, the cold gas is also uplifted, as observed in a few cases such as Perseus and Hydra (Hatch et al. 2006; Gitti et al. 2012). The cycle repeats, when cooling starts to dominate again and the cold gas condensation ignites more powerful outbursts, setting the system to a slightly hotter state.

Overall, thermal equilibrium is roughly maintained, on large spatial and temporal scales. For example, the two maps in Figure 7.12, for best model r7-i6m3, display the net thermal energy increase (red) or decrement (blue) per volume and time; the evolution of the internal energy density (erg cm^{-3}) is given by

$$\frac{\partial E_{\rm th}}{\partial t} = -\nabla \cdot (E_{\rm th}\mathbf{v}) - P\,(\nabla \cdot \mathbf{v}) - \; n_{\rm e} n_{\rm i} \Lambda(T). \tag{7.3}$$

The maps point out that 'heating' ($\partial E_{\rm th}/\partial t > 0$) and 'cooling' ($\partial E_{\rm th}/\partial t < 0$) alternate on scales of a few kpc. Averages of $\partial E_{\rm th}/\partial t$ in radial shells of width $\gtrsim 4-5$ kpc suggest that

be smaller. As previously pointed out, the feedback efficiency could be however larger. More work is needed to satisfactorily study the fate of the accreting cold gas.

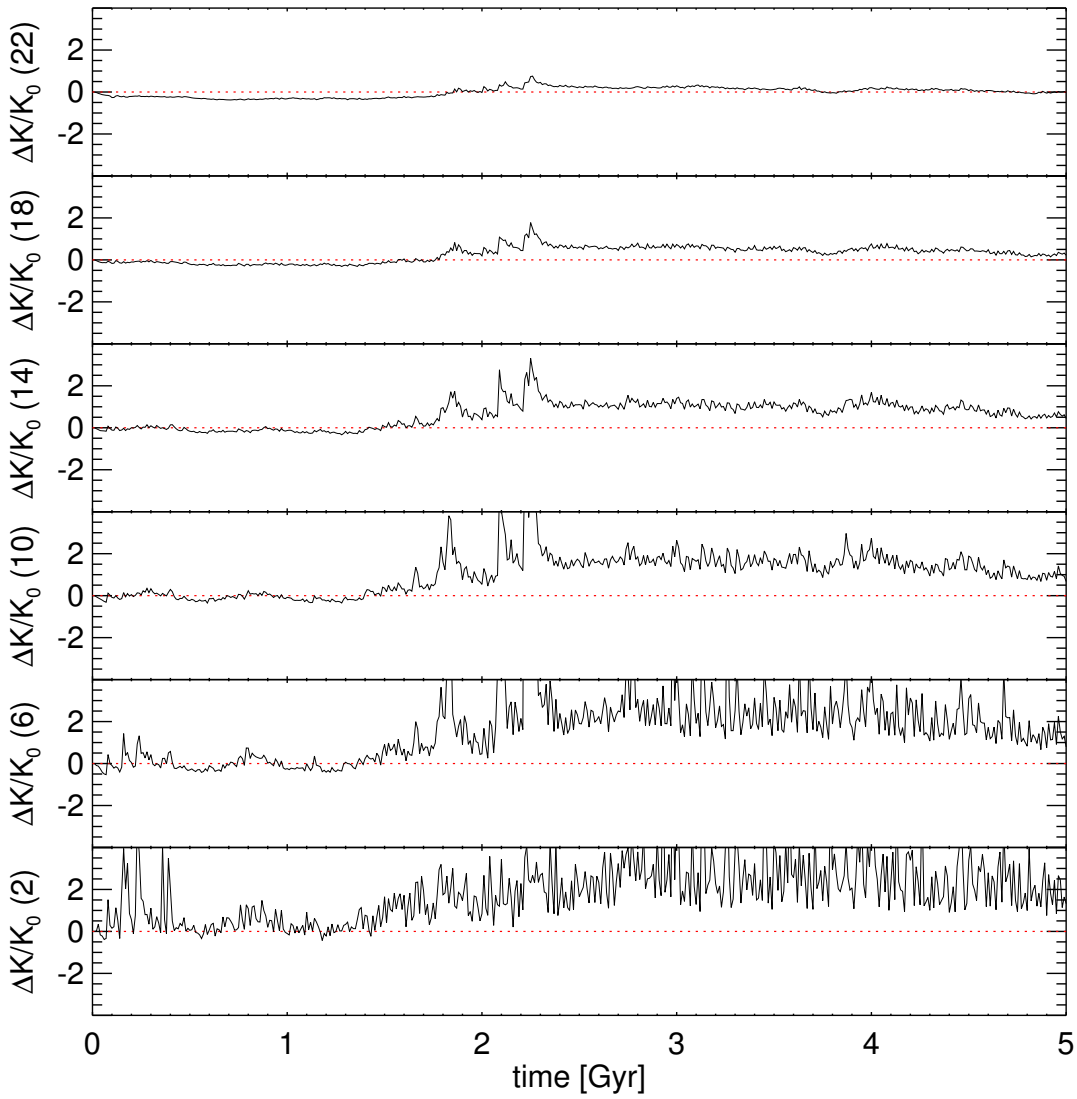

Figure 7.13. Thermal equilibrium diagnostics (best model r7-i6m3). Temporal variation of entropy in the whole ICM with respect to the initial value K_0. The six panels show $(K - K_0)/K_0$ as a function of time, every 10 Myr, in different spherical shells of width 4 kpc centred at r = 22, 18, 14, 10, 6 and 2 kpc (from top to bottom row).

a rough thermal equilibrium is maintained, although cooling appears slightly dominant in the central 10 kpc, while the jets tend to deposit their energy at larger radii. Equation 7.3 does not, however, fully capture the irreversible heating associated with turbulent mixing, shocks and wave damping due to numerical effects. A better direct indicator of the balance between cooling ($\mathcal{L}$) and heating ($\mathcal{H}$) is the variation of the entropy S ($\propto \ln K$), which is insensitive to adiabatic compressions or expansions:

$$\rho T \frac{dS}{dt} = \mathcal{H} - \mathcal{L}, \tag{7.4}$$

where d/dt is the Lagrangian derivative. The panels in Figure 7.13 show the time variations in radial shells of K for the whole ICM, with respect to the initial value K_0. As expected the entropy increases on a secular timescale due the continuous action of the AGN feedback. On smaller temporal scales, e.g. a few typical cooling times

(100 – 200 Myr), the amplitude of the fluctuations in the six thick spherical shells (centred at r = 22, 18, 14, 10, 6 and 2 kpc; from the top to bottom row) can reach 2 or 3 times the mean value, especially in the nuclear region. Although the fluctuations in K can be substantial, its mean saturates at a stable level. This suggests that the cluster core does not *dramatically* deviate from the state of (quasi) equilibrium between cooling and heating, at least on scales of tens kpc and hundreds of Myr. This was also suggested by the low cooling/accretion rates compared to the pure cooling flow. The assumption of strict global thermal equilibrium made in the work of M12 and S12 is therefore very idealised. It is thus particularly remarkable that our criterion for the formation of the multiphase gas is in good agreement with their result.

Unlike in S12, the central kpc region is not excised, allowing the cold gas (either nuclear cooling or fallen blobs) to form an angular momentum-supported torus as observed in the core of M87 (e.g. Ford et al. 1994). Such a disk can be partially dismantled when the jet direction is perturbed by turbulence or by random jet precession (Sec. 7.3.4). Nevertheless, the central dense disk is a common feature among elliptical galaxies (e.g. Macchetto et al. 1997; Jaffe et al. 1999; Mathews & Brighenti 2003; Verdoes Kleijn et al. 2006). Centrally concentrated atomic gas is also seen in the survey of McDonald et al. (2010, 2011a). The central disk is certainly a nursery for new stars. Since the star formation efficiency is quite uncertain (few per cent, up to 50%, with an average value of 15%; Sec. 7.1), I decided to not model star formation via a sink term. Thus, the central accumulation of cold gas could be further reduced.

The presence of multiphase gas is clearly seen in the $n_e - T$ joint distributions (e.g. Figure 7.6). The cold dense phase ($10^4 - 10^5$ K), in the upper left corner, is present in large quantities and detached from the hot rarefied gas (> few 10^7 K), with a lack of gas at intermediate temperatures. The Hα survey of McDonald et al. (see Sec. 7.1) has shown that extended cold filaments are found in $\gtrsim 35\%$ of cool-core systems. It is striking that most of their maps (Figures 1.8 and 7.1) resemble our computed morphologies, with extended clouds and filaments up to $\sim$ 20 kpc: e.g. Abell 0496, Hydra A, Abell 1644, Sersic 159-03, and Abell 1795. Another case with substantial extended Hα emission is the Perseus cluster (Salomé et al. 2006; Fabian et al. 2008). Moreover, the total cold gas mass we obtain, $\sim 10^{11}\ M_\odot$, is consistent with the constraints quoted in Section 7.1 (e.g. Edge 2001; Salomé & Combes 2003), whose observations indicate cool-core systems harbouring up to $3 \times 10^{11}\ M_\odot$ of molecular gas.

The white noise perturbations in the initial conditions are wiped out over some cooling times. In fact, in the pure cooling flow computation (r7-CF), multiphase gas is only possible in such restricted interval, while the secular evolution is dominated by monolithic cooling. On the contrary, AGN feedback drives and sustains the fluctuations in the long-term evolution, although the original seeds initially help to distribute better the jet energy due to the interaction of jet with the inhomogeneous ICM. The thermal state of the cluster core depends mainly on the feedback efficiency: with smaller ϵ the frequency of cold filaments condensing out of the hot phase is larger. Nevertheless, higher initial $t_{\rm cool}/t_{\rm ff}$ (and lower density) generates extended multiphase gas according to the TI criterion, but thermal equilibrium is reached at later epochs. In agreement with the previous two Chapters, the AGN feedback is more effective in lighter systems, requiring therefore lower

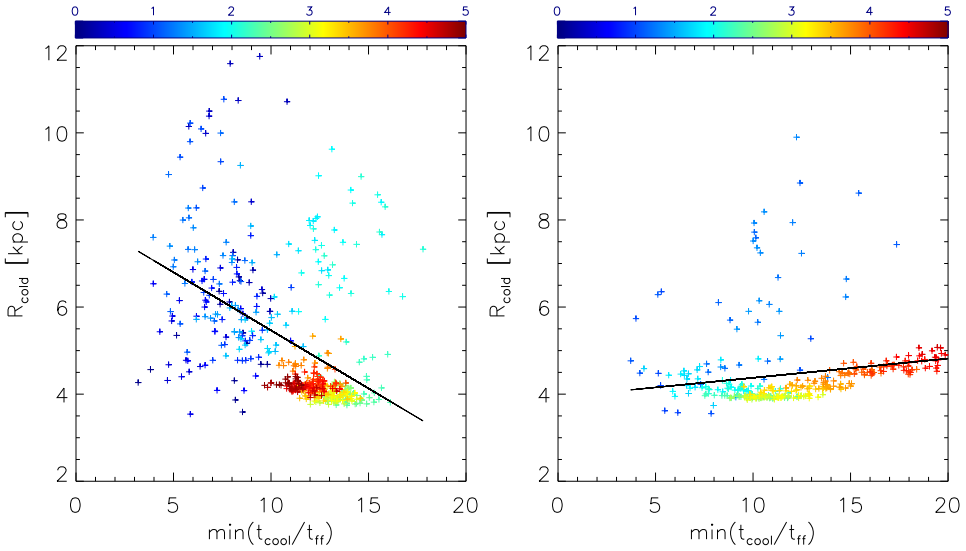

Figure 7.14. Extended cold radius as a function of minimum shell-averaged TI-ratio. This radius is defined as the average distance from the centre of cold cells that do no belong to the bulk of concentrated cooling ($r < 3.5$ kpc). The points are coloured according to time (Gyr; see colour bar). Left: r7-i6m3 simulation. Right: r21-i6m3 simulation. Black line represents the linear regression fit to the scatter plot (points are drawn every 10 Myr). Notice that these plots only show where the cold gas instantaneously resides (on average), not where it originally formed.

efficiencies ($\lesssim 6 \times 10^{-3}$).

To better quantify the presence of extended multiphase gas, Figure 7.14 shows a scatter plot of the average distance of cold gas ($R_{\rm cold}$; excluding $r < 3.5$ kpc) as a function of $t_{\rm cool}/t_{\rm ff}$. The points are coloured according to time: from blue (early) to red (late). For the run with the initial $t_{\rm cool}/t_{\rm ff} = 7$ (left panel), the cold gas is much more spatially extended, especially in the first 2 Gyr. The run with less dense initial conditions (TI-ratio 21) shows a lower frequency of cold blobs at large distances because $t_{\rm cool}/t_{\rm ff} \gtrsim 10$ most of the time. In both cases, the points clustered around ~ 4 kpc correspond to the rotating cold torus. Since this plot shows the current average distance rather than the radius where the cold gas originates, extended filaments appear even when TI-ratio is elevated to $\sim 12 - 15$ due to AGN heating. This tendency is further enhanced when cold blobs are uplifted by powerful outflowing jets. Moreover, as the TI-ratio is averaged in spherical shells, a few cold zones may contribute to $R_{\rm cold}$, without changing much the average $t_{\rm cool}/t_{\rm ff}$. That is, some extended Hα emission is consistent with $t_{\rm cool}/t_{\rm ff}$ slightly greater than 10.

Figure 7.15 displays $R_{\rm cold}$ gas as a function of time. With denser initial conditions (r7-i6m3), $t_{\rm cool}/t_{\rm ff}$ is less than 10 for several short intervals within 2 Gyr and we expect extended cold gas[10]. Indeed, the average distance of the cold gas is significantly larger than that of the cold torus (≈ 4 kpc) during this period. Similarly, for the lower initial density run we see extended cold filaments at $1 - 1.5$ Gyr, again when $t_{\rm cool}/t_{\rm ff} \lesssim 10$; later times are however dominated by the nuclear cold gas. We conclude that the instantaneous value of $t_{\rm cool}/t_{\rm ff}$ is a robust indicator of extended cold gas formation, while nuclear cold gas can be present irrespective of the TI-ratio (e.g. right panel of Figure 7.14).

[10] $\dot{M}_{\rm acc}$ is boosted exactly during this period (see Fig. 7.5).

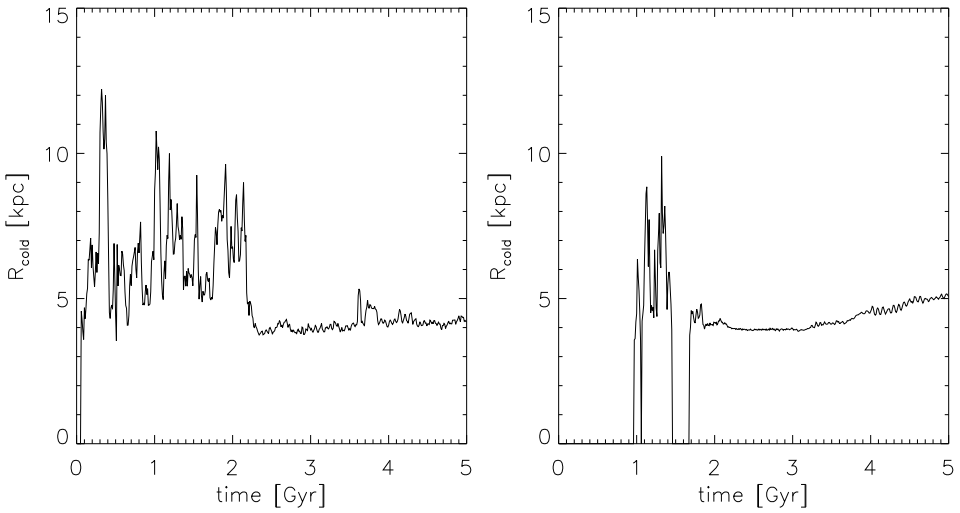

Figure 7.15. Extended cold radius as a function of time. Left: r7-i6m3. Right: r21-i6m3. Starting with lower TI-ratio leads to an evolution characterised by both extended ($t_{\rm cool}/t_{\rm ff} \lesssim 10$) and concentrated cold gas. On the contrary, extended multiphase gas is rarer in the opposite starting regime, although not absent.

It is likely that other physical processes play an important role in shaping the morphology of condensing multiphase gas. Sharma et al. (2010) and M12 showed that anisotropic thermal conduction leads to cold gas stretched along the local magnetic field direction. In order to be able to fully understand the exact topology of cold filaments, this physics should be included in the simulations (with an adequately higher resolution). However, the generation of cold filaments, whenever $t_{\rm cool}/t_{\rm ff} \lesssim 10$, is not likely to be affected by the presence of anisotropic thermal conduction.

The other physics that is missing in the present simulations involves cosmological accretion and mergers, which drive additional turbulence, inducing more instabilities. Like AGN feedback, major mergers are associated with entropy generation and strong heating of cluster cores, raising the cooling time over the cluster age. Thus, mergers may be responsible for extreme non-cool-core clusters. However, they are also rare with timescales much longer than the cluster-core cooling times (e.g. Fakhouri et al. 2010). Therefore, AGN feedback, rather than mergers, is expected to be responsible for balancing cooling in most systems.

The simulated models are again able to solve the cooling flow problem for several Gyr, as in the previous Chapters, even if the details of the feedback appear different (like the higher duty cycle – due to the 10 times higher resolution). The key factor resides in adopting realistic mechanical AGN jets, mainly self-regulated by cold gas accretion. The bulk of AGN heating is a combination of shock dissipation and gradual thermalisation of the mechanical energy (see also Brüggen et al. 2007). Random motions, either due to AGN, multiphase gas, and cosmological turbulence, strongly help the deposition of the feedback energy in the cool core, in contrast to idealised symmetric atmospheres (e.g. Vernaleo & Reynolds 2006).

An important issue is whether our results depend sensitively on resolution. The morphology of the cold phase depends on the resolution. I note that finite resolution

may prevent the disruption and mixing of the formed infalling clouds with the ambient ICM. Thus, limited resolution could in fact mimic some of the effects of the physics that are not included (e.g. magnetic draping). I performed a test (r7-i6m3c) with two times lower resolution outside the central $\sim$ 2 kpc (thus keeping the same resolution around the jet injection region and sinking radius). In the end, I obtained very similar results. In particular, a steady global thermal equilibrium is reached in a few Gyr, with only a slightly larger final cold mass (2×10^{11} $M_{\odot}$). The evolution of the TI-ratio and condensed cold clouds appears also similar to the higher resolution model (r7-i6m3), although the increased numerical dissipation tend to slow down the growth of thermal instabilities at larger radii.

Overall, the main thermal properties of cluster cores are determined by global quasi-thermal equilibrium, with an amazingly detailed complexity of cold filaments/torus, jets, bubbles and shocks. The present study demonstrates that multiphase gas due to thermal instabilities is an essential element of the feedback cycle: end product of cooling and fuel for the central black hole.

This Chapter concludes the complete analysis and discussion of the results, obtained during the Thesis research. In the next final Chapter, I summarise all the essential conclusions of the whole investigation, including the cardinal remarks, the main limitations and the future developments.

Chapter 8

Conclusions

A FUNDAMENTAL gap in the current understanding of collapsed structures in the universe is the thermodynamical evolution of the baryonic component. Most of the cosmic virialised structures possess an extended halo of hot plasma, typically dominating the amount of ordinary matter. Such hot ionised gas, with temperatures above ten million degrees, rapidly looses energy through (X-ray) radiation, leading to a massive subsonic cooling flow, initiating from the denser central regions and inducing the peripheral gas to flow toward the nucleus of the galaxy, group or cluster. The predicted (classic) cooling flow rates are blatantly unrealistic, reaching a thousand of solar masses per year for the most massive systems. In the core, huge amount of cooler gas accumulates in just a few hundred Myr, monolithically condensing out of the hot phase and creating a tremendous peak in surface brightness (Chapter 1).

This is the *cooling flow problem*.

The main objective of the systematic investigation conducted throughout the present Thesis is to solve this problem. Assessing the fate of the cooling plasma is an essential step, in order to understand the wealth of condensed structures forming in galaxies, groups and clusters. The condensed hot gas is in fact the nursery of the giant molecular clouds, stars, dust and planets.

The amazing details provided by the last-generation X-ray telescopes, *Chandra* and *XMM-Newton*, have revealed that the central active galactic nucleus (AGN), where a supermassive black hole resides, strongly interacts with the surrounding medium in the form of buoyant bubbles, radio jets, elliptical shocks, sonic ripples, turbulence and gas entrainment. The measured energies released by the AGN (over 10^{62} erg) are indeed capable to balance (or even overwhelm) the radiative losses. However, we absolutely need to find a common denominator, the actual origin of the above features and, ultimately, how the AGN energy couples to the surrounding plasma (ISM, IGM or ICM).

The leitmotiv of the present work is that massive subrelativistic AGN outflows are the key to solving the cooling flow problem. Their origin near the Schwarzschild radius is still unclear, either resulting form an entrained and decelerated (magnetic) jet, or directly from a nuclear (radiative) disc wind. Nevertheless, on kpc scales the observations point toward a massive feedback process, governed by a directional mechanical input of energy

(Chapter 2).

The adopted method of analysis consisted in carrying out 3D hydrodynamic simulations, via the state-of-the-art Eulerian parallel code FLASH, substantially modified and upgraded in order to study (high-energy) astrophysical phenomena, such as AGN outflows, strong shocks, radiative cooling, thermal instabilities, and multiphase gas (Chapter 3).

I systematically studied the effect of mechanical AGN feedback, self-regulated for 7-10 Gyr, in every virialised system with a hot halo, i.e. from the scales of galaxy clusters (Chapter 4) and groups (Chapter 5), down to isolated elliptical galaxies (Chapter 6). Remarkably, massive AGN outflows are able, in every system, to *properly* solve the cooling flow problem, implying the following fundamental (best models) results.

8.1 Consistency with Observations

- **NO OVERCOOLING**

The cooling flow rates are suppressed below $5 - 10\%$ of the classic cooling flow predictions (Fabian 1994), consistent with the spectroscopic constraints (Peterson et al. 2001, 2003, 2006; Bregman et al. 2001, 2005, 2006; Ettori et al. 2002; Tamura et al. 2003): in the galaxy cluster $\dot{M}_{\rm cool} \lesssim 10 - 20\ M_\odot\ {\rm yr}^{-1}$, in the group $\dot{M}_{\rm cool} \lesssim 1\ M_\odot\ {\rm yr}^{-1}$, and in the isolated elliptical $\dot{M}_{\rm cool} \lesssim 0.1\ M_\odot\ {\rm yr}^{-1}$. The cooling rates are suppressed for several Gyr, in a quasi steady state with respect to the cooling timescale ($\sim 10 - 50$ Myr). The central temperature does not fall below one third of the virial temperature (cluster: $T \gtrsim 3 \times 10^7$; group/elliptical: $T \gtrsim 8 \times 10^6$ K), avoiding the drastic steepening of the density, and thus SB_x, profile (slope $\gtrsim -1$).

- **NO OVERHEATING**

At the same time, the assumed AGN feedback does not erase the cool-core structure, an often unwelcome - and ignored - product of exaggerated concentrated heating (like thermal and radiative feedback). This means that the temperature[1] profile maintains the typical positive gradient (cluster and group), and does not drastically depart from the observed trend for a long time (elliptical). Moreover, the system core or galaxy is not totally emptied for Gyr (the density slope does not become positive). No overheating means also that the cooling flow is not completely suppressed, except for a transient evolution (e.g. tens Myr).

- **BUOYANT BUBBLES**

The anisotropic injection of mechanical energy is able to naturally inflate a pair of underdense cavities in the surrounding hot atmosphere (cf. Boehringer et al. 1993;

[1]The emission-weighted/spectroscopic-like T profiles, more adherent to observations, tend to relax the overheating problem; since the denser, high-emitting regions contribute more to the line-of-sight integration, they mask in part the stronger fluctuations, linked instead to the very hot and diffuse component.

Blanton et al. 2001; Finoguenov & Jones 2001; Jones et al. 2002; Bîrzan et al. 2004; Dunn et al. 2005; Dunn & Fabian 2006; Allen et al. 2006; Fabian et al. 2006; Rafferty et al. 2006; Forman et al. 2007; McNamara & Nulsen 2007; Finoguenov et al. 2008; Rafferty et al. 2008; Baldi et al. 2009; Giacintucci et al. 2011). In the cluster regime (Sec. 4.4), the X-ray cavities have usually a radius of tens kpc, with emission-weighted temperatures slightly hotter than the ambient medium (at least in the early stage of inflation). The reduced power in groups and ellipticals produces more gentle cavities (with radius several and few kpc, respectively), showing relatively cold metal-rich rims and mild internal temperatures (Secs. 5.4, 6.3.5, 6.4.2). The jump in SBx is typically $20-40\%$. The jet-inflated bubbles are also stable for tens Myr (due to the internal vortexes), contrary to artificially ad-hoc inflated cavities, more prone to Rayleigh-Taylor instability.

- **SHOCKS**

Not the entire mechanical energy is transformed into the bubble enthalpy, as often assumed. At the beginning of the outburst, massive outflows spend most of their energy to generate the elliptical cocoon shock (with jumps in SB_x and T), enveloping the subsequent bubbles. The primordial strong shock (Mach ~ 10) is practically impossible to catch in a snapshot, due to the rapid deceleration (Eq. 2.4). In fact, the usual retrieved Mach numbers are slightly supersonic, $\sim 1.1-1.7$, as also[2] found by several deep observations (e.g. McNamara et al. 2005; Nulsen et al. 2005a,b; Blanton et al. 2009; Randall et al. 2011). The recurrent shocks become very weak at larger radii ($> 30-50$ kpc) transforming into sonic ripples, as observed for instance in Perseus (Fabian et al. 2006).

- **METALS DREDGE-UP**

The anisotropic outflow ram pressure is fundamental for uplifting the metals (mainly Fe), from the central reservoir, replenished by the BCG stellar evolution, up to $50-200$ kpc along the jet axis (Secs. 4.5.2, 5.4, 6.4). The typical contrast with the background is $\sim 10-20\%$. This dredge-up is consistent with recent dedicated observations (Rasmussen & Ponman 2009; Kirkpatrick et al. 2009, 2011; David et al. 2011; O'Sullivan et al. 2011b). In the more quiescent phases, the turbulence and stirring motions tend to restore the more homogeneous metal distribution. Together with metals, stronger outbursts can also uplift the central condensed cold gas (as observed by Gitti et al. 2011), creating extended filamentary structures (Chap. 7).

- **TURBULENCE**

Repeated AGN outbursts generate a considerable level of subsonic turbulence inside the core. The estimated velocity dispersions are $200-400$ km s^{-1} for the group/elliptical (Sec. 6.5.2), and hundreds more in the galaxy cluster, in line with recent constraints (Werner et al. 2009; Sanders et al. 2011; de Plaa et al. 2012). The moment of strong turbulence (especially in the cluster regime) can substantially alter the hydrostatic equilibrium (Sec. 4.5.3), leading to an error in the total mass estimate even by a factor

[2]Few exceptions are the shocks of Centaurus A, with Mach 8, and NGC 3801, with Mach 4.

$\sim 1.5 - 2$; on the other hand, during more gentle outbursts the equilibrium is maintained below 10%. The AGN turbulence (clearly manifest after a Gyr) is a key ingredient for the deposition of the mechanical energy in the core, via the fragmentation of the jet channel. AGN turbulence is also the ultimate cause of the thermal instability nonlinear growth, leading to extended hot gas condensation.

- **MULTIPHASE GAS**

Mechanical AGN feedback prevents the runaway monolithic cooling, avoiding the huge central accumulation of cold gas over several 10^{12} $M_\odot$. The total mass of residual cool gas never exceeds $\sim$ 10^{11} $M_\odot$ (cluster), consistent with the molecular gas constraints ($\lesssim 3 \times 10^{11}$ $M_\odot$; Edge 2001; Salomé & Combes 2003, 2004). Multiphase gas, with cold ($T \sim 10^4$ K) and hot ($T > 10^7$ K) components, is a direct *consequence* and *source* of feedback. The cold gas comes in two flavours (Chapter 7; see also Fig. 6.8): the extended phase (up to 20 kpc from the centre), in the form of clouds and filaments generated by thermal instabilities (and occasionally due to dredge-up by jet ram pressure), and a more spatially concentrated phase, in the form of a rotating torus due to nuclear cooling or fallen clouds. Recent Hα surveys (McDonald et al. 2009, 2010, 2011a,b,c, 2012) support both kinds of structure. Nuclear cold disks are also a common feature among ellipticals (e.g. Ford et al. 1994; Macchetto et al. 1997; Jaffe et al. 1999; Mathews & Brighenti 2003; Verdoes Kleijn et al. 2006). The generation of *extended* cold gas is dictated by an important threshold: $t_{\rm cool}/t_{\rm ff} \lesssim 10$, in agreement with the analogous observational criterion $K_0 < 30$ keV cm^2 (Sec. 7.4; Cavagnolo et al. 2008; Rafferty et al. 2008; Voit et al. 2008). Multiphase gas can exist in cool-core systems irrespectively of their initial minimum $t_{\rm cool}/t_{\rm ff}$, meaning that the core finds always a way to self-regulate toward a state of global *quasi* thermal equilibrium on large spatial and temporal scales.

8.2 Successful Feedback Characteristics

The best AGN feedback models (e.g. cl-C5m3 – cluster; cgg-C8m4 – group; iso-C3m4 – elliptical), which reproduce the above requirements and observed features, possess the following fundamental characteristics.

- **COLD FEEDBACK (primary)**

The self-regulation process is essential for preserving the cool-core structure in a state of quasi thermal equilibrium. The optimal self-regulation is provided by linking the AGN energy input to the nuclear cooling rate[3]. This is the best way to maintain the (quasi) thermal equilibrium on scales of a cooling time, for 7-10 Gyr of evolution. The multiphase simulation with inflow accretion (Chapter 7) provide the physical explanation for cold feedback. The extended cold gas condenses out of the hot phase, falls toward the black hole in roughly free fall, and boosts the feedback. These computations show that

[3]The cold feedback success does not depend on the presence of the cold gas dropout term or its parameters (like $T_{\rm cut}$, the functional form of q, or the free-fall delay).

the bulk of the 'accreted' mass is indeed the cold, and not hot, phase (by two orders of magnitude; Fig. 7.5). The cold feedback naturally produces recursive cycles and peaks of activity, promoting bubble inflation and additional (nonlinear) perturbations, as shocks and turbulence. In the cluster regime, the feedback behaviour appears more[4] explosive and impulsive, while in lighter halos the regulation is more gentle and frequent.

- **SCALING WITH THE HALO**

Groups and ellipticals are not purely scaled-down versions of clusters. In order to avoid drastic overheating and/or erasing the cool core, less bound objects require a less efficient AGN feedback. Using cold accretion, the mechanical efficiencies of the best models are: $\epsilon \sim 5\times10^{-3}-10^{-2}$ (cluster), $\epsilon \sim 5\times10^{-4}-10^{-3}$ (group) and $\epsilon \sim 10^{-4}-5\times10^{-4}$ (elliptical). I emphasise that this ϵ does not probably represent the exact BH efficiency. If the accreted mass near the Schwarzschild radius is lower, the feedback power could be maintained on the same level by increasing ϵ. On the other hand, convergence tests suggest that the trend of the increasing efficiency with system mass is real. The cluster evolution requires indeed much higher total injected energies (few 10^{62} erg), compared to the group ($\sim 10^{61}$ erg) or elliptical ($\sim 10^{60}$ erg). Even if rescaled, the same feedback in lighter halos has still more profound consequences on the T and ρ profiles, with the stronger outbursts easily perturbing the central region[5]. This can certainly contribute to the (observed) break in the self-similar scaling relations at lower masses. The physical reason for the mechanical efficiency to be linked to the environment/potential well, besides the core survival, is not clear and needs to be clarified with future investigations; the fact that the most massive BHs reside at the centre of clusters (McConnell et al. 2011) could play a crucial role.

- **HOT BONDI-LIKE FEEDBACK (secondary)**

It is not excluded that an almost continuous very low-power feedback activity may be complementary to the cold accretion mode. This mode is mainly associated with the accretion of the hot gas, which is typically (roughly) modelled via the Bondi formula. Although it is possible to retrieve reasonable heating models, Bondi-like feedback alone requires unpalatably high efficiencies ($\epsilon \gtrsim 0.1$) to quench the cooling flow, even for groups. Another issue with hot feedback is that it is always continuous, without instantaneous powerful outbursts[6] generating the typical buoyant bubbles. Hybrid models combining Bondi and cold feedback seem to be more successful in restoring a duty cycle. Finally, from a theoretical point of view, we should not be allowed to use Bondi theory, because the flow must be steady, adiabatic, without angular momentum, unperturbed and with constant boundary conditions at infinity.

- **MECHANICAL**

A pure thermal energy injection, although very effective in stopping the cooling flow, leads to the heating catastrophe, i.e. the sustained overheating for a too long period of

[4]The numerical resolution has however a relevant role in shaping the detailed duty cycle; Section 8.3.

[5]For instance, in the isolated elliptical (Sec. 6.3), a single moderate outflow with power $\sim 10^{44}$ erg s^{-1} can easily eject the gas outside the system, stopping cooling for several tens Myr.

[6]E.g., in the cluster regime the Bondi continuous activity is always sub-Eddington, with $P_{\rm jet} \sim 10^{44}$ erg s^{-1}.

time, usually with very steep negative temperature profiles. On the contrary, mechanical outflows *gradually* thermalise their energy along their path, both in space and in time, leading to the proper self-regulated quasi thermal equilibrium.

- **ANISOTROPIC**

Anisotropic injection of energy guarantees the production of all the non-spherical observed features, previously described, like the pair of bubbles, elliptical cocoons and metals uplift. Perhaps more important, bipolar outflows allow the accretion of gas along the equatorial direction, letting the ISM/ICM to communicate with the system thermostat, the black hole.

- **MASSIVE, SUBRELATIVISTIC AND POWERFUL**

Most of the outflow properties are dictated by the self-regulation, varying in time. Typical self-regulated (initial) velocities, in the best models, are around 10^4 km s^{-1}, with rarer events reaching several 10^4 – 10^5 km s^{-1} in the strongest phases (the gas velocities after several kpc decrease rapidly). Since the velocities are always subrelativistic, the outflow must be also massive. The mean mass outflow rate decreases with the system mass: $\sim 10-100\ M_\odot$ yr^{-1} (cluster), few $M_\odot$ yr^{-1} (group), and $\lesssim 1\ M_\odot$ yr^{-1} (elliptical). The mean power shows consequently the same trend: $\sim 10^{46}$ – 10^{47} erg s^{-1} (cluster), $\sim 10^{44}$ – 10^{45} erg s^{-1} (group), $\sim$ 10^{43} – 10^{44} erg s^{-1} (elliptical). The more continuous and massive outflows tend to produce a narrow channel ($\sim$ 1 kpc), which is typically fragmented by the AGN-driven turbulence and often not revealed by the SB_x maps. It is important to realise that the computed AGN outflow values are consistent with the constraints of blue-shifted absorption lines in several bands[7] (e.g. George et al. 1998; Crenshaw et al. 2003; Kriss et al. 2003; Risaliti et al. 2005; Morganti et al. 2005, 2007; McKernan et al. 2007; Cappi et al. 2009, 2011; Pounds & Reeves 2009; Nesvadba et al. 2008, 2011; Tombesi et al. 2010a,b, 2012), and also with entrained decelerated jets (Giovannini 2004; Croston 2008).

- **OTHER PROPERTIES**

The method of injection (inside the domain or through the boundary fluxes; Sec. 3.6) does not influence the dynamics of the feedback. This means that slightly longer (or larger) outflows produce very similar results[8], as long as the massive outflow is modelled on the kpc scale (as suggested by the above observations). The bipolar jets can be consistent with precession or random wobbling, however, the half-opening angle should be $\lesssim 25°$. Wider jets produce an isotropic feedback that inhibits at some point the BH fuelling, leading to the cooling catastrophe. Finally, fixing the intermittency and jet power, ignoring the self-regulation, may lead to marginally successful models for a short transient evolution, but never for the entire life of the system (e.g. Sections 4.3.9 and 5.3.12).

[7] Higher energy bands (X-ray, UV) usually capture the fast and light component of the outflow, while in optical and radio band is revealed the more massive and slower component, very likely the product of entrainment on kpc scales (Chapter 2).

[8] E.g., cgg-C8m4 model in Sec. 6.4.1 has half the height ($\sim$ 1 kpc) of previous best models in Secs. 5.3.10-5.3.11, showing analogous cooling rates, profiles, and jet evolutionary properties.

8.3 Limitations and Future Developments

I want to conclude this work highlighting the main limitations of my investigation, which also lay the bases for the future developments.

Due to the need of a long-term evolution (7-10 Gyr), the present simulations can not resolve the region near the black hole, i.e. few Schwarzschild radii. We are thus forced to limit the resolution to few 100 pc, at best. This means that we are missing the fine details of the accretion process. Since our self-regulated feedback is linked to the computed accretion/cooling rate in the nuclear region, the fine details of the feedback could be altered by the numerical resolution. For instance, the best cluster models in Chapter 7 have 10× higher resolution compared to those in Chapter 4. Besides few setup differences (initial perturbations, injection method), the two samples can be overall considered a convergence test. As expected, the duty cycle[9] is different: in the lower resolution run the feedback is more impulsive and powerful (sometimes super-Eddington), due to the high instantaneous peaks per (larger) time step; on the other hand, the higher resolution simulation shows relatively less powerful outbursts with a larger duty cycle (more similar to that of the group, ~ 0.8). It seems that only a drastic increase in resolution leads to a somewhat different cycle. For instance, the group simulation cgg-C8m4 (Sec. 6.4.1) has 2× higher resolution than cold best models in Chapter 5, and the results are very similar, also in the AGN frequency. In general, we are not in a position to affirm what is the perfect intermittency of the feedback. However, it is important to realise that the present mechanical feedback can solve the cooling flow in *both* cases, irrespective of the duty cycle details. This is a key result, that strengthens the robustness of the adopted self-regulation.

In future, it would be interesting to carry out (non-adiabatic) simulations with extremely high resolution near the black hole influence region, linking the subpc to the several kpc scale. Assessing the fate of the falling cold clouds and filaments, along with the role of the hot Bondi-like mode on these small scales, are certainly primary objectives. Moreover, with such high resolution we could better focus on the mechanism leading to the assumed massive kpc-scale outflow, casting light on the magnetically-driven or radiatively-driven jet/wind origin. This would imply to implement magneto-hydrodynamics and/or radiative transfer, a feasible task given the modularity of FLASH code.

Strong radiation coming from the central source and accretion disc (like in a quasar phase), may play an additional role in the feedback heating process. However, preliminary simple tests with Compton heating ($T_C = 2 \times 10^7$ K; see Equation 2.5) and radiation pressure (due to electron scattering) show that the feedback is rather weak due to the low densities of the surrounding absorbing medium ($n \sim 1$ cm^{-3}). Additional elements, like a dusty medium, may increase the level of radiation pressure. If the densities of the nuclear medium are, for some reason (cold clouds near the BH?), elevated by several orders of magnitude, the radiative feedback seems to not differ from a central (isotropic) injection

[9] Note that the common duty cycle retrieved by observations can be very different from our numerical value, because the definition of an 'active' AGN strongly depends on the assumed luminosity threshold and on the property of the sample.

of pure thermal energy, leading to the classic prolonged overheating (see also Brighenti & Mathews 2002b).

Magnetic fields, not only are important for the jet launching mechanism, but they provide the suppression of thermal conduction, which is in theory supposed to drive the cold phase evaporation. Conduction may be also anisotropic (when the magnetic field lines are not tangled), transforming most of our computed clouds in longer filaments and strands, possibly more consistent with observations. Turbulence and dissipation processes can be also affected by MHD, which provides additional plasma instabilities (e.g. HBI and MRI; see Section 2.5).

Always aided by high-resolution simulations, I intend to understand better the role of the lighter relativistic (radio) jets. In particular, it is essential to clarify the exact amount of entrainment on pc and kpc scales. Even without the radio jet, it is really interesting to resimulate some of the exemplary feedback events in our best models. For instance, in Figure 8.1, I present a preliminary resimulation run of the elliptical best model, with very high resolution ($\Delta x = 18$ pc); from this analysis it is possible to study in depth the spatial and temporal details of the buoyant bubble, induced shocks and driven turbulence, especially in the nuclear region.

On the other side, i.e. the larger Mpc scales, our simulations clearly lack a fully cosmological environment. Cosmological accretion and mergers can drive additional turbulence, inducing more instabilities, although it is unclear if the inner cool core ($< 0.1\ R_{\rm vir}$) will be strongly affected. Like AGN feedback, major mergers are associated with entropy generation and strong heating (up to 10^{64} erg), raising the cooling time over the system age. Thus, mergers may be responsible for extreme non-cool-core systems. However, they are also rare with timescales much longer than the core cooling times. Therefore, AGN feedback, rather than mergers, is expected to be responsible for balancing cooling in most systems. Cosmological simulations will preciously provide an extensive sample of objects; proving the deviation from the self-similar scaling relations, like the $L_{\rm x} - T$, would be a key objective.

It would be interesting to see the effects of our mechanical feedback on high-z galaxies, the building blocks of groups and clusters. As in the isolated elliptical, the feedback is expected to be more effective, although it should not prevent the formation of the intracluster/intragroup medium at later times. The fraction of ejected baryons could form the warm-hot intergalactic medium, possibly solving the missing baryon problem.

As a concluding remark, I emphasise that the feedback engine (as other key gas physics) should be carefully tested on smaller scales, as in the present Thesis, before implementing such crucial element in the complex and delicate cosmological evolution of baryons.

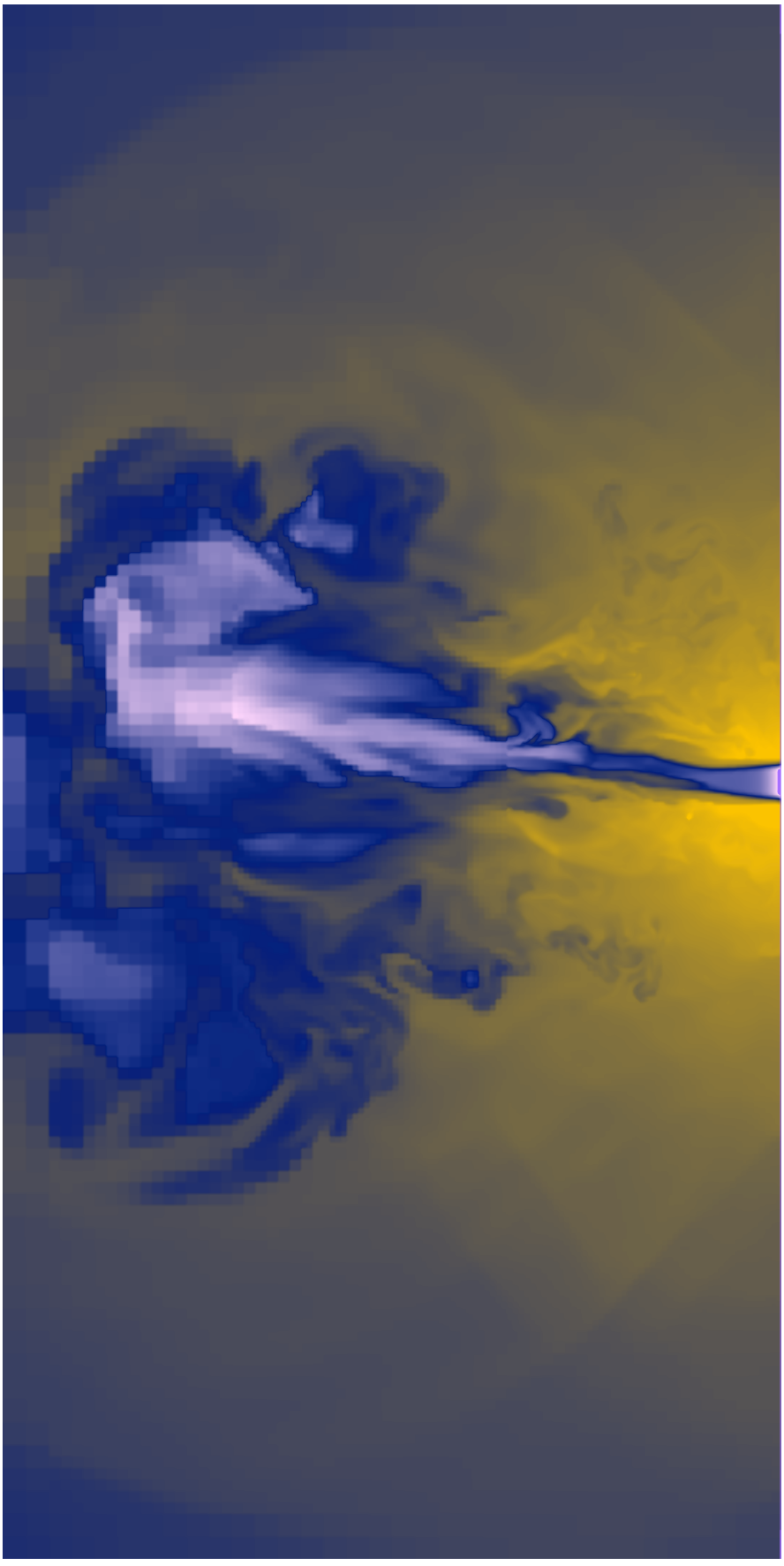

Figure 8.1. Resimulation of a feedback event, extracted from the elliptical best model (Section 6.3), with a substantial increase in resolution (Δx = 18 pc). This midplane cut of density (10 kpc × 5 kpc) provides an amazing amount of details on the buoyant bubble, shocks and driven turbulence, in the system core.

8.4 Finale

Based on the previously argued reasons and theoretical/numerical investigations carried out in the present Thesis, I conclude that the best feedback mechanism able to *solve the cooling flow problem* in every virialised system with a substantial hot gas halo, requiring

- no overcooling ($\dot{M}_{\rm cool} < 5 - 10\%\ \dot{M}_{\rm classic\,CF}$),
- no overheating (preserve the cool-core structure),

and reproducing several observational features, such as

- buoyant underdense bubbles,
- elliptical cocoons,
- weak shocks/sonic ripples (Mach $\lesssim 1.5$),
- dredge-up of metals and cold gas,
- subsonic turbulence (hundreds km s^{-1}),
- extended filamentary and nuclear cold gas,

should possess the following key characteristics:

- mechanical,
- anisotropic,
- driven by massive and subrelativistic outflows,
- self-regulated mainly by cold accretion,
- and less efficient in lighter halos.

Bibliography

Allen, S. W., Dunn, R. J. H., Fabian, A. C., Taylor, G. B., & Reynolds, C. S. 2006, MNRAS, 372, 21

Allen, S. W., & Fabian, A. C. 1997, in Astronomical Society of the Pacific Conference Series, Vol. 115, Galactic Cluster Cooling Flows, ed. N. Soker, 1

Allen, S. W., Schmidt, R. W., & Fabian, A. C. 2001, MNRAS, 328, L37

Balbus, S. A. 1988, ApJ, 328, 395

—. 2000, ApJ, 534, 420

Balbus, S. A., & Soker, N. 1989, ApJ, 341, 611

Baldi, A., Forman, W., Jones, C., et al. 2009, ApJ, 707, 1034

Balogh, M. L., Babul, A., Voit, G. M., et al. 2006, MNRAS, 366, 624

Bauer, F. E., Alexander, D. M., Brandt, W. N., et al. 2002, AJ, 123, 1163

Bender, R. 1996, in IAU Symposium, Vol. 171, New Light on Galaxy Evolution, ed. R. Bender & R. L. Davies, 181

Benson, A. J., Bower, R. G., Frenk, C. S., et al. 2003, ApJ, 599, 38

Berger, M. J., & Colella, P. 1989, Journal of Computational Physics, 82, 64

Beuing, J., Dobereiner, S., Bohringer, H., & Bender, R. 1999, MNRAS, 302, 209

Biller, B. A., Jones, C., Forman, W. R., Kraft, R., & Ensslin, T. 2004, ApJ, 613, 238

Binney, J. 2004, in The Riddle of Cooling Flows in Galaxies and Clusters of galaxies, ed. T. Reiprich, J. Kempner, & N. Soker, 233

Binney, J., & Tabor, G. 1995, MNRAS, 276, 663

Binney, J., & Tremaine, S. 1988, Galactic Dynamics (Princeton Series in Astrophysics)

Bîrzan, L., Rafferty, D. A., McNamara, B. R., Wise, M. W., & Nulsen, P. E. J. 2004, ApJ, 607, 800

Blandford, R. D., & Payne, D. G. 1982, MNRAS, 199, 883

Blanton, E. L., Randall, S. W., Douglass, E. M., et al. 2009, ApJ, 697, L95

Blanton, E. L., Sarazin, C. L., & McNamara, B. R. 2003, ApJ, 585, 227

Blanton, E. L., Sarazin, C. L., McNamara, B. R., & Wise, M. W. 2001, ApJ, 558, L15

Boehringer, H., & Hensler, G. 1989, A&A, 215, 147

Boehringer, H., Voges, W., Fabian, A. C., Edge, A. C., & Neumann, D. M. 1993, MNRAS, 264, L25

Böhringer, H., & Werner, N. 2010, A&A Rev., 18, 127

Bonafede, A., Govoni, F., Feretti, L., et al. 2011, A&A, 530, A24

Bondi, H. 1952, MNRAS, 112, 195

Booth, C. M., & Schaye, J. 2009, MNRAS, 398, 53

Borgani, S. 2006, arXiv:astro-ph/0605575

Borgani, S., Diaferio, A., Dolag, K., & Schindler, S. 2008, SSRv, 134, 269

Borgani, S., Governato, F., Wadsley, J., et al. 2001, ApJ, 559, L71

—. 2002, MNRAS, 336, 409

Borgani, S., & Guzzo, L. 2001, Nat, 409, 39

Borgani, S., & Kravtsov, A. 2009, arXiv:astro-ph/0906.4370

Borgani, S., Murante, G., Springel, V., et al. 2004, MNRAS, 348, 1078

Braginskii, S. I. 1958, Soviet Journal of Experimental and Theoretical Physics, 6, 358

Bregman, J. N., Fabian, A. C., Miller, E. D., & Irwin, J. A. 2006, ApJ, 642, 746

Bregman, J. N., Miller, E. D., Athey, A. E., & Irwin, J. A. 2005, ApJ, 635, 1031

Bregman, J. N., Miller, E. D., & Irwin, J. A. 2001, ApJ, 553, L125

Bregman, J. N., & Parriott, J. R. 2009, ApJ, 699, 923

Brighenti, F., & Mathews, W. G. 1997, ApJ, 490, 592

—. 1998, ApJ, 495, 239

—. 1999, ApJ, 512, 65

—. 2002a, ApJ, 567, 130

—. 2002b, ApJ, 573, 542

—. 2003, ApJ, 587, 580

—. 2006, ApJ, 643, 120

Brüggen, M., Heinz, S., Roediger, E., Ruszkowski, M., & Simionescu, A. 2007, MNRAS, 380, L67

Brüggen, M., & Kaiser, C. R. 2002, Nat, 418, 301

Brüggen, M., Ruszkowski, M., & Hallman, E. 2005, ApJ, 630, 740

Brüggen, M., & Scannapieco, E. 2009, MNRAS, 398, 548

Buote, D. A., Brighenti, F., & Mathews, W. G. 2004, ApJ, 607, L91

Buote, D. A., Gastaldello, F., Humphrey, P. J., et al. 2007, ApJ, 664, 123

Buote, D. A., Lewis, A. D., Brighenti, F., & Mathews, W. G. 2003, ApJ, 594, 741

Buote, D. A., & Tsai, J. C. 1996, ApJ, 458, 27

Burns, J. O., Hallman, E. J., Gantner, B., Motl, P. M., & Norman, M. L. 2008, ApJ, 675,

1125

Caon, N., Macchetto, D., & Pastoriza, M. 2000, ApJS, 127, 39

Cappi, M., Giustini, M., & Tombesi, F. 2011, in The X-ray Universe 2011, ed. J.-U. Ness & M. Ehle, 51

Cappi, M., Tombesi, F., Bianchi, S., et al. 2009, A&A, 504, 401

Cattaneo, A., Dekel, A., Faber, S. M., & Guiderdoni, B. 2008, MNRAS, 389, 567

Cattaneo, A., & Teyssier, R. 2007, MNRAS, 376, 1547

Cattaneo, A., Faber, S. M., Binney, J., et al. 2009, Nat, 460, 213

Cavagnolo, K. W., Donahue, M., Voit, G. M., & Sun, M. 2008, ApJ, 683, L107

—. 2009, ApJS, 182, 12

Cavaliere, A., & Fusco-Femiano, R. 1978, A&A, 70, 677

Chandran, B. D. G., & Cowley, S. C. 1998, Physical Review Letters, 80, 3077

Cho, J., & Lazarian, A. 2003, MNRAS, 345, 325

Churazov, E., Brüggen, M., Kaiser, C. R., Böhringer, H., & Forman, W. 2001, ApJ, 554, 261

Churazov, E., Sazonov, S., Sunyaev, R., et al. 2005, MNRAS, 363, L91

Cimatti, A. 2009, in American Institute of Physics Conference Series, Vol. 1111, American Institute of Physics Conference Series, ed. G. Giobbi, A. Tornambe, G. Raimondo, M. Limongi, L. A. Antonelli, N. Menci, & E. Brocato, 191–198

Cimatti, A., Daddi, E., Renzini, A., et al. 2004, Nat, 430, 184

Ciotti, L., D'Ercole, A., Pellegrini, S., & Renzini, A. 1991, ApJ, 376, 380

Ciotti, L., & Ostriker, J. P. 1997, ApJ, 487, L105

—. 2007, ApJ, 665, 1038

Colbert, J. W., Mulchaey, J. S., & Zabludoff, A. I. 2001, AJ, 121, 808

Colella, P., & Woodward, P. R. 1984, JCoPh, 54, 174

Combes, F., Young, L. M., & Bureau, M. 2007, MNRAS, 377, 1795

Conselice, C. J., Gallagher, III, J. S., & Wyse, R. F. G. 2001, AJ, 122, 2281

Courant, R., Friedrichs, K., & Lewy, H. 1928, Mathematische Annalen, 100, 32

Cowie, L. L., Fabian, A. C., & Nulsen, P. E. J. 1980, MNRAS, 191, 399

Cowie, L. L., & McKee, C. F. 1977, ApJ, 211, 135

Crawford, C. S., Allen, S. W., Ebeling, H., Edge, A. C., & Fabian, A. C. 1999, MNRAS, 306, 857

Crawford, C. S., Hatch, N. A., Fabian, A. C., & Sanders, J. S. 2005, MNRAS, 363, 216

Crenshaw, D. M., Kraemer, S. B., Boggess, A., et al. 1999, ApJ, 516, 750

Crenshaw, D. M., Kraemer, S. B., & George, I. M. 2003, ARA&A, 41, 117

Crocker, A., Krips, M., Bureau, M., et al. 2012, MNRAS, 2291

Croston, J. H. 2008, in ASPC, Vol. 386, Extragalactic Jets: Theory and Observation from

Radio to Gamma Ray, ed. T. A. Rector & D. S. De Young, 335

Croton, D. J., Springel, V., White, S. D. M., et al. 2006, MNRAS, 365, 11

Dalla Vecchia, C., Bower, R. G., Theuns, T., et al. 2004, MNRAS, 355, 995

David, L. P., Forman, W., & Jones, C. 1991, ApJ, 380, 39

David, L. P., Jones, C., Forman, W., & Daines, S. 1994, ApJ, 428, 544

David, L. P., Jones, C., Forman, W., et al. 2009, ApJ, 705, 624

David, L. P., Jones, C., Forman, W., Vargas, I. M., & Nulsen, P. 2006, ApJ, 653, 207

David, L. P., Nulsen, P. E. J., McNamara, B. R., et al. 2001, ApJ, 557, 546

David, L. P., O'Sullivan, E., Jones, C., et al. 2011, ApJ, 728, 162

Davis, T. A., Alatalo, K., Sarzi, M., et al. 2011, MNRAS, 417, 882

De Grandi, S., & Molendi, S. 2002, ApJ, 567, 163

de Plaa, J., Zhuravleva, I., Werner, N., et al. 2012, A&A, 539, A34

Debuhr, J., Quataert, E., & Ma, C.-P. 2011, MNRAS, 2150

Diehl, S., & Statler, T. S. 2008a, ApJ, 680, 897

—. 2008b, ApJ, 687, 986

Dong, R., Rasmussen, J., & Mulchaey, J. S. 2010, ApJ, 712, 883

Dubois, Y., Devriendt, J., Slyz, A., & Teyssier, R. 2010, MNRAS, 409, 985

Dunn, R. J. H., Allen, S. W., Taylor, G. B., et al. 2010, MNRAS, 404, 180

Dunn, R. J. H., & Fabian, A. C. 2006, MNRAS, 373, 959

Dunn, R. J. H., Fabian, A. C., & Taylor, G. B. 2005, MNRAS, 364, 1343

Edge, A. C. 2001, MNRAS, 328, 762

Ellis, S. C., & O'Sullivan, E. 2006, MNRAS, 367, 627

Elwert, G. 1952, Zeitschrift Naturforschung Teil A, 7, 432

Eskridge, P. B., Fabbiano, G., & Kim, D.-W. 1995, ApJS, 97, 141

Ettori, S., & Fabian, A. C. 1999, MNRAS, 305, 834

Ettori, S., Fabian, A. C., Allen, S. W., & Johnstone, R. M. 2002, MNRAS, 331, 635

Evrard, A. E., & Henry, J. P. 1991, ApJ, 383, 95

Faber, S. M., Willmer, C. N. A., Wolf, C., et al. 2007, ApJ, 665, 265

Fabian, A. C. 1994, ARA&A, 32, 277

Fabian, A. C., Johnstone, R. M., Sanders, J. S., et al. 2008, Nat, 454, 968

Fabian, A. C., Mushotzky, R. F., Nulsen, P. E. J., & Peterson, J. R. 2001a, MNRAS, 321, L20

Fabian, A. C., Nulsen, P. E. J., & Canizares, C. R. 1984, Nat, 310, 733

—. 1991, A&A Rev., 2, 191

Fabian, A. C., Sanders, J. S., Allen, S. W., et al. 2003, MNRAS, 344, L43

Fabian, A. C., Sanders, J. S., Ettori, S., et al. 2001b, MNRAS, 321, L33

Fabian, A. C., Sanders, J. S., Taylor, G. B., et al. 2006, MNRAS, 366, 417

Fabian, A. C., Sanders, J. S., Ettori, S., et al. 2000, MNRAS, 318, L65

Fabian, A. C., Sanders, J. S., Allen, S. W., et al. 2011, MNRAS, 418, 2154

Fakhouri, O., Ma, C.-P., & Boylan-Kolchin, M. 2010, MNRAS, 406, 2267

Faltenbacher, A., Kravtsov, A. V., Nagai, D., & Gottlöber, S. 2005, MNRAS, 358, 139

Federrath, C., Banerjee, R., Clark, P. C., & Klessen, R. S. 2010, ApJ, 713, 269

Ferrarese, L., & Merritt, D. 2000, ApJ, 539, L9

Ferrari, F., Pastoriza, M. G., Macchetto, F., & Caon, N. 1999, A&A Supp., 136, 269

Ferreras, I., & Silk, J. 2000, ApJ, 541, L37

Finoguenov, A., Böhringer, H., Osmond, J. P. F., et al. 2005, AdSpR, 36, 622

Finoguenov, A., & Jones, C. 2000, ApJ, 539, 603

—. 2001, ApJ, 547, L107

Finoguenov, A., Jones, C., Böhringer, H., & Ponman, T. J. 2002, ApJ, 578, 74

Finoguenov, A., Ruszkowski, M., Jones, C., et al. 2008, ApJ, 686, 911

Fletcher, C. A. J. 1991, Computational Techniques for Fluid Dynamics (Berlin, Springer Verlag)

Ford, H. C., Harms, R. J., Tsvetanov, Z. I., et al. 1994, ApJ, 435, L27

Forman, W., Nulsen, P., Heinz, S., et al. 2005, ApJ, 635, 894

Forman, W., Jones, C., Churazov, E., et al. 2007, ApJ, 665, 1057

Fryxell, B., Olson, K., Ricker, P., et al. 2000, ApJS, 131, 273

Fukazawa, Y., Botoya-Nonesa, J. G., Pu, J., Ohto, A., & Kawano, N. 2006, ApJ, 636, 698

Gardini, A. 2007, A&A, 464, 143

Gardini, A., Rasia, E., Mazzotta, P., et al. 2004, MNRAS, 351, 505

Gastaldello, F., Buote, D. A., Temi, P., et al. 2009, ApJ, 693, 43

Gebhardt, K., Bender, R., Bower, G., et al. 2000, ApJ, 539, L13

Geller, M. J., & Huchra, J. P. 1983, ApJS, 52, 61

George, I. M., Turner, T. J., Netzer, H., et al. 1998, ApJS, 114, 73

Ghosh, S., Mukhopadhyay, B., Krishan, V., & Khan, M. 2010, NewA, 15, 83

Giacintucci, S., O'Sullivan, E., Vrtilek, J., et al. 2011, ApJ, 732, 95

Giovannini, G. 2004, Ap&SS, 293, 1

Gitti, M., Brighenti, F., & McNamara, B. R. 2012, Adv. in Astronomy, 2012, 1

Gitti, M., Nulsen, P. E. J., David, L. P., McNamara, B. R., & Wise, M. W. 2011, ApJ, 732, 13

Gitti, M., O'Sullivan, E., Giacintucci, S., et al. 2010, ApJ, 714, 758

Godunov, S. K. 1959, Math. Sbornik, 47, 271

Goudfrooij, P., Hansen, L., Jorgensen, H. E., & Norgaard-Nielsen, H. U. 1994, A&A

Supp., 105, 341

Graves, G. J., Faber, S. M., & Schiavon, R. P. 2009, ApJ, 698, 1590

Greggio, L. 2005, A&A, 441, 1055

Greggio, L., Renzini, A., & Daddi, E. 2008, MNRAS, 388, 829

Guo, F., & Mathews, W. G. 2010, ApJ, 712, 1311

Häring, N., & Rix, H.-W. 2004, ApJ, 604, L89

Hatch, N. A., Crawford, C. S., & Fabian, A. C. 2007, MNRAS, 380, 33

Hatch, N. A., Crawford, C. S., Johnstone, R. M., & Fabian, A. C. 2006, MNRAS, 367, 433

Heckman, T. M., Baum, S. A., van Breugel, W. J. M., & McCarthy, P. 1989, ApJ, 338, 48

Heinz, S., Brüggen, M., & Friedman, S. 2011, ApJS, 194, 21

Heinz, S., Brüggen, M., Young, A., & Levesque, E. 2006, MNRAS, 373, L65

Helsdon, S. F., & Ponman, T. J. 2000, MNRAS, 315, 356

Hickson, P. 1982, ApJ, 255, 382

Hopkins, P. F., Narayan, R., & Hernquist, L. 2006, ApJ, 643, 641

Hu, E. M., Cowie, L. L., & Wang, Z. 1985, ApJS, 59, 447

Hubble, E. P. 1936, Realm of the Nebulae (New Haven: Yale University Press)

Humphrey, P. J., & Buote, D. A. 2006, ApJ, 639, 136

Humphrey, P. J., Buote, D. A., Gastaldello, F., et al. 2006, ApJ, 646, 899

Irwin, J. A., Sarazin, C. L., & Bregman, J. N. 2002, ApJ, 570, 152

Jaffe, W. 1990, A&A, 240, 254

Jaffe, W., Bremer, M. N., & Baker, K. 2005, MNRAS, 360, 748

Jaffe, W., Ford, H. C., Tsvetanov, Z., Ferrarese, L., & Dressel, L. 1999, in Astronomical Society of the Pacific Conference Series, Vol. 182, Galaxy Dynamics - A Rutgers Symposium, ed. D. R. Merritt, M. Valluri, & J. A. Sellwood, 13

Jeong, H., Yi, S. K., Bureau, M., et al. 2009, MNRAS, 398, 2028

Jetha, N. N., Hardcastle, M. J., Ponman, T. J., & Sakelliou, I. 2008, MNRAS, 391, 1052

Johnson, R., Finoguenov, A., Ponman, T. J., Rasmussen, J., & Sanderson, A. J. R. 2011, MNRAS, 413, 2467

Johnstone, R. M., Fabian, A. C., & Nulsen, P. E. J. 1987, MNRAS, 224, 75

Jones, C., Forman, W., Vikhlinin, A., et al. 2002, ApJ, 567, L115

Kaiser, N. 1986, MNRAS, 222, 323

Kato, Y., Mineshige, S., & Shibata, K. 2004, ApJ, 605, 307

Kaviraj, S., Schawinski, K., Devriendt, J. E. G., et al. 2007, ApJS, 173, 619

Khosroshahi, H. G., Jones, L. R., & Ponman, T. J. 2004, MNRAS, 349, 1240

Kim, D.-W., & Fabbiano, G. 2003, ApJ, 586, 826

King, A. 2009, ApJ, 695, L107

King, A. R., & Pringle, J. E. 2007, MNRAS, 377, L25

King, I. 1962, AJ, 67, 471

Kirkpatrick, C. C., Gitti, M., Cavagnolo, K. W., et al. 2009, ApJ, 707, L69

Kirkpatrick, C. C., McNamara, B. R., & Cavagnolo, K. W. 2011, ApJ, 731, L23

Kormendy, J., & Bender, R. 1996, ApJ, 464, L119

Kormendy, J., & Djorgovski, S. 1989, ARA&A, 27, 235

Kriss, G. A., Blustin, A., Branduardi-Raymont, G., et al. 2003, A&A, 403, 473

Krumholz, M. R., McKee, C. F., & Klein, R. I. 2005, ApJ, 618, 757

—. 2006, ApJ, 638, 369

Kuntschner, H., Emsellem, E., Bacon, R., et al. 2010, MNRAS, 408, 97

La Franca, F., Melini, G., & Fiore, F. 2010, ApJ, 718, 368

Landau, L. D., & Lifshitz, E. M. 1959, Fluid mechanics (Oxford: Pergamon Press)

Laney, C. B. 1998, Computational Gasdynamics (Cambridge UP)

Leccardi, A., & Molendi, S. 2008, A&A, 486, 359

LeVeque, R. J. 1998, Computational Methods for Astrophysical Fluid Flow (Berlin, Springer Verlag)

Liedahl, D. A., Osterheld, A. L., & Goldstein, W. H. 1995, ApJ, 438, L115

Loewenstein, M. 1989, MNRAS, 238, 15

Loewenstein, M., & Mathews, W. G. 1987, ApJ, 319, 614

—. 1991, ApJ, 373, 445

Macchetto, F., Marconi, A., Axon, D. J., et al. 1997, ApJ, 489, 579

MacDonald, J., & Bailey, M. E. 1981, MNRAS, 197, 995

Machacek, M., Nulsen, P. E. J., Jones, C., & Forman, W. R. 2006, ApJ, 648, 947

Machacek, M. E., Jerius, D., Kraft, R., et al. 2011, ApJ, 743, 15

MacNeice, P., Olson, K. M., Mobarry, C., de Fainchtein, R., & Packer, C. 2000, Computer Physics Communications, 126, 330

Mahdavi, A., Hoekstra, H., Babul, A., & Henry, J. P. 2008, MNRAS, 384, 1567

Malagoli, A., Rosner, R., & Fryxell, B. 1990, MNRAS, 247, 367

Mannucci, F., Della Valle, M., Panagia, N., et al. 2005, A&A, 433, 807

Martel, A. R., Turner, N. J., Sparks, W. B., & Baum, S. A. 2000, ApJS, 130, 267

Mathews, W. G. 1989, AJ, 97, 42

—. 1990, ApJ, 354, 468

Mathews, W. G., & Baker, J. C. 1971, ApJ, 170, 241

Mathews, W. G., & Brighenti, F. 2003, ARA&A, 41, 191

—. 2008a, ApJ, 676, 880

—. 2008b, ApJ, 685, 128

Mathews, W. G., Brighenti, F., Faltenbacher, A., et al. 2006, ApJ, 652, L17

Mathews, W. G., Faltenbacher, A., Brighenti, F., & Buote, D. A. 2005, ApJ, 634, L137

Mathews, W. G., & Loewenstein, M. 1986, ApJ, 306, L7

McCarthy, I. G., Schaye, J., Ponman, T. J., et al. 2010, MNRAS, 406, 822

McConnell, N. J., Ma, C.-P., Gebhardt, K., et al. 2011, Nat, 480, 215

McCourt, M., Sharma, P., Quataert, E., & Parrish, I. J. 2012, MNRAS, 419, 3319, [M12]

McDonald, M. 2011, ApJ, 742, L35

McDonald, M., & Veilleux, S. 2009, ApJ, 703, L172

McDonald, M., Veilleux, S., & Mushotzky, R. 2011a, ApJ, 731, 33

McDonald, M., Veilleux, S., & Rupke, D. S. N. 2012, ApJ, 746, 153

McDonald, M., Veilleux, S., Rupke, D. S. N., & Mushotzky, R. 2010, ApJ, 721, 1262

McDonald, M., Veilleux, S., Rupke, D. S. N., Mushotzky, R., & Reynolds, C. 2011b, ApJ, 734, 95

McKernan, B., Yaqoob, T., & Reynolds, C. S. 2007, MNRAS, 379, 1359

McNamara, B. R., & Nulsen, P. E. J. 2007, ARA&A, 45, 117

McNamara, B. R., Nulsen, P. E. J., Wise, M. W., et al. 2005, Nat, 433, 45

McNamara, B. R., & O'Connell, R. W. 1989, AJ, 98, 2018

McNamara, B. R., Wise, M., Nulsen, P. E. J., et al. 2000, ApJ, 534, L135

Mellier, Y., & Mathez, G. 1987, A&A, 175, 1

Merloni, A., & Heinz, S. 2008, MNRAS, 388, 1011

Mewe, R. 1999, in Lecture Notes in Physics, Berlin Springer Verlag, Vol. 520, X-Ray Spectroscopy in Astrophysics, ed. J. van Paradijs & J. A. M. Bleeker, 109

Mittal, R., Hudson, D. S., Reiprich, T. H., & Clarke, T. 2009, A&A, 501, 835

Moe, M., Arav, N., Bautista, M. A., & Korista, K. T. 2009, ApJ, 706, 525

Molendi, S., & Pizzolato, F. 2001, ApJ, 560, 194

Morganti, R., Holt, J., Saripalli, L., Oosterloo, T. A., & Tadhunter, C. N. 2007, A&A, 476, 735

Morganti, R., Tadhunter, C. N., & Oosterloo, T. A. 2005, A&A, 444, L9

Morita, U., Ishisaki, Y., Yamasaki, N. Y., et al. 2006, PASJ, 58, 719

Morsony, B. J., Heinz, S., Brüggen, M., & Ruszkowski, M. 2010, MNRAS, 407, 1277

Mościbrodzka, M., & Proga, D. 2008, ApJ, 679, 626

—. 2009, MNRAS, 397, 2087

Mulchaey, J. S. 2000, ARA&A, 38, 289

Mulchaey, J. S., Davis, D. S., Mushotzky, R. F., & Burstein, D. 1993, ApJ, 404, L9

—. 2003, ApJS, 145, 39

Nagai, D., Vikhlinin, A., & Kravtsov, A. V. 2007, ApJ, 655, 98

Nagino, R., & Matsushita, K. 2009, A&A, 501, 157

Nakamura, M., Tregillis, I. L., Li, H., & Li, S. 2008, ApJ, 686, 843

Narayan, R., & Fabian, A. C. 2011, MNRAS, 415, 3721

Narayan, R., & McClintock, J. E. 2008, NewAR, 51, 733

Narayan, R., & Medvedev, M. V. 2001, ApJ, 562, L129

Navarro, J. F., Frenk, C. S., & White, S. D. M. 1996, ApJ, 462, 563

Nesvadba, N. P. H., De Breuck, C., Lehnert, M. D., et al. 2011, A&A, 525, A43

Nesvadba, N. P. H., Lehnert, M. D., De Breuck, C., Gilbert, A. M., & van Breugel, W. 2008, A&A, 491, 407

Novak, G. S., Ostriker, J. P., & Ciotti, L. 2011, ApJ, 737, 26

Nulsen, P. E. J., David, L. P., McNamara, B. R., et al. 2002, ApJ, 568, 163

Nulsen, P. E. J., Hambrick, D. C., McNamara, B. R., et al. 2005a, ApJ, 625, L9

Nulsen, P. E. J., Jones, C., Forman, W. R., et al. 2007, in Heating versus Cooling in Galaxies and Clusters of Galaxies, ed. H. Böhringer, G. W. Pratt, A. Finoguenov, & P. Schuecker , ESO Astrophys. Symp., 210

Nulsen, P. E. J., McNamara, B. R., Wise, M. W., & David, L. P. 2005b, ApJ, 628, 629

O'Dea, C. P., Baum, S. A., Privon, G., et al. 2008, ApJ, 681, 1035

Oegerle, W. R., & Hill, J. M. 2001, AJ, 122, 2858

Omma, H., Binney, J., Bryan, G., & Slyz, A. 2004, MNRAS, 348, 1105

Oonk, J. B. R., Jaffe, W., Bremer, M. N., & van Weeren, R. J. 2010, MNRAS, 405, 898

Oosterloo, T., Morganti, R., Crocker, A., et al. 2010, MNRAS, 409, 500

Osmond, J. P. F., & Ponman, T. J. 2004, MNRAS, 350, 1511

Ostriker, J. P., Choi, E., Ciotti, L., Novak, G. S., & Proga, D. 2010, ApJ, 722, 642

O'Sullivan, E., Forbes, D. A., & Ponman, T. J. 2001, MNRAS, 328, 461

O'Sullivan, E., Giacintucci, S., David, L. P., et al. 2011a, ApJ, 735, 11

O'Sullivan, E., Giacintucci, S., David, L. P., Vrtilek, J. M., & Raychaudhury, S. 2011b, MNRAS, 411, 1833

O'Sullivan, E., Worrall, D. M., Birkinshaw, M., et al. 2011c, MNRAS, 416, 2916

Parriott, J. R., & Bregman, J. N. 2008, ApJ, 681, 1215

Pellegrini, S., Ciotti, L., & Ostriker, J. P. 2012, ApJ, 744, 21

Peres, C. B., Fabian, A. C., Edge, A. C., et al. 1998, MNRAS, 298, 416

Perley, R. A., Dreher, J. W., & Cowan, J. J. 1984, ApJ, 285, L35

Peterson, J. R., & Fabian, A. C. 2006, Phys. Rep., 427, 1

Peterson, J. R., Kahn, S. M., Paerels, F. B. S., et al. 2003, ApJ, 590, 207

Peterson, J. R., Paerels, F. B. S., Kaastra, J. S., et al. 2001, A&A, 365, L104

Piffaretti, R., & Valdarnini, R. 2008, A&A, 491, 71

Piontek, F., & Steinmetz, M. 2011, MNRAS, 410, 2625

Pizzolato, F., & Soker, N. 2005, ApJ, 632, 821

Ponman, T. J., & Bertram, D. 1993, Nat, 363, 51

Ponman, T. J., Cannon, D. B., & Navarro, J. F. 1999, Nat, 397, 135

Ponman, T. J., Sanderson, A. J. R., & Finoguenov, A. 2003, MNRAS, 343, 331

Pounds, K. A., & Reeves, J. N. 2009, MNRAS, 397, 249

Power, C., Nayakshin, S., & King, A. 2011, MNRAS, 412, 269

Press, W. H., & Schechter, P. 1974, ApJ, 187, 425

Proga, D. 2007, ApJ, 661, 693

Puchwein, E., Sijacki, D., & Springel, V. 2008, ApJ, 687, L53

Quataert, E. 2008, ApJ, 673, 758

Rafferty, D. A., McNamara, B. R., & Nulsen, P. E. J. 2008, ApJ, 687, 899

Rafferty, D. A., McNamara, B. R., Nulsen, P. E. J., & Wise, M. W. 2006, ApJ, 652, 216

Randall, S. W., Forman, W. R., Giacintucci, S., et al. 2011, ApJ, 726, 86

Rasia, E., Mazzotta, P., Bourdin, H., et al. 2008, ApJ, 674, 728

Rasia, E., Ettori, S., Moscardini, L., et al. 2006, MNRAS, 369, 2013

Rasmussen, J., & Ponman, T. J. 2009, MNRAS, 399, 239

Reale, F., Rosner, R., Malagoli, A., Peres, G., & Serio, S. 1991, MNRAS, 251, 379

Rebusco, P., Churazov, E., Böhringer, H., & Forman, W. 2005, MNRAS, 359, 1041

Renzini, A., & Ciotti, L. 1993, ApJ, 416, L49

Revaz, Y., Combes, F., & Salomé, P. 2008, A&A, 477, L33

Reynolds, C. S., Heinz, S., & Begelman, M. C. 2001, ApJ, 549, L179

—. 2002, MNRAS, 332, 271

Risaliti, G., Bianchi, S., Matt, G., et al. 2005, ApJ, 630, L129

Roache, P. 1998, Fundamentals of Computational Fluid Dynamics (Hermosa)

Rosati, P., Borgani, S., & Norman, C. 2002, ARA&A, 40, 539

Ruszkowski, M., Brüggen, M., & Begelman, M. C. 2004a, ApJ, 611, 158

—. 2004b, ApJ, 615, 675

Ruszkowski, M., Ensslin, T. A., Brüggen, M., Begelman, M. C., & Churazov, E. 2008, MNRAS, 383, 1359

Ruszkowski, M., & Oh, S. P. 2010, ApJ, 713, 1332

—. 2011, MNRAS, 414, 1493

Salomé, P., & Combes, F. 2003, A&A, 412, 657

—. 2004, A&A, 415, L1

Salomé, P., Combes, F., Revaz, Y., et al. 2008, A&A, 484, 317

Salomé, P., Combes, F., Edge, A. C., et al. 2006, A&A, 454, 437

Samuele, R., McNamara, B. R., Vikhlinin, A., & Mullis, C. R. 2011, ApJ, 731, 31

Sanders, J. S., Fabian, A. C., & Smith, R. K. 2011, MNRAS, 410, 1797

Sanderson, A. J. R., Ponman, T. J., & O'Sullivan, E. 2006, MNRAS, 372, 1496

Sansom, A. E., O'Sullivan, E., Forbes, D. A., Proctor, R. N., & Davis, D. S. 2006, MNRAS, 370, 1541

Sarazin, C. L. 1986, Reviews of Modern Physics, 58, 1

—. 1999, ApJ, 520, 529

Sarazin, C. L., & Ashe, G. A. 1989, ApJ, 345, 22

Sarazin, C. L., Irwin, J. A., & Bregman, J. N. 2001, ApJ, 556, 533

Sarazin, C. L., & White, III, R. E. 1988, ApJ, 331, 102

Sazonov, S. Y., Ostriker, J. P., & Sunyaev, R. A. 2004, MNRAS, 347, 144

Schneider, D. P., Hall, P. B., Richards, G. T., et al. 2005, AJ, 130, 367

Sharma, P., McCourt, M., Quataert, E., & Parrish, I. J. 2012, MNRAS, 420, 3174, [S12]

Sharma, P., Parrish, I. J., & Quataert, E. 2010, ApJ, 720, 652

Sijacki, D., Springel, V., Di Matteo, T., & Hernquist, L. 2007, MNRAS, 380, 877

Smith, D. A., Wilson, A. S., Arnaud, K. A., et al. 2002, ApJ, 565, 195

Smith, R. K., Brickhouse, N. S., Liedahl, D. A., & Raymond, J. C. 2001, ApJ, 556, L91

Soker, N. 2008, NewA, 13, 296

Soker, N., & Pizzolato, F. 2005, ApJ, 622, 847

Spitzer, L. 1962, Physics of Fully Ionized Gases, New York: Interscience (Wiley)

Springel, V., Di Matteo, T., & Hernquist, L. 2005, MNRAS, 361, 776

Sternberg, A., Pizzolato, F., & Soker, N. 2007, ApJ, 656, L5

Stone, J. M., & Norman, M. L. 1992, ApJS, 80, 753

Strang, G. 1968, JNA, 5, 506

Sun, M. 2009, ApJ, 704, 1586

Sun, M., Jones, C., Forman, W., et al. 2007, ApJ, 657, 197

Sun, M., Vikhlinin, A., Forman, W., Jones, C., & Murray, S. S. 2005, ApJ, 619, 169

Sun, M., Voit, G. M., Donahue, M., et al. 2009, ApJ, 693, 1142

Sunyaev, R. A., & Zeldovich, Y. B. 1972, Comments on Astrophysics and Space Physics, 4, 173

Sutherland, R. S., & Dopita, M. A. 1993, ApJS, 88, 253

Szuszkiewicz, E. 2004, in Carnegie Observatories Astrophysics Series, Vol. 1, Coevolution of Black Holes and Galaxies, ed. L. C. Ho

Tamura, T., Kaastra, J. S., den Herder, J. W. A., Bleeker, J. A. M., & Peterson, J. R. 2004, A&A, 420, 135

Tamura, T., Kaastra, J. S., Makishima, K., & Takahashi, I. 2003, A&A, 399, 497

Tamura, T., Kaastra, J. S., Peterson, J. R., et al. 2001, A&A, 365, L87

Temi, P., Brighenti, F., & Mathews, W. G. 2007, ApJ, 666, 222

—. 2009, ApJ, 707, 890

Tombesi, F., Cappi, M., Reeves, J. N., & Braito, V. 2012, MNRAS, L413

Tombesi, F., Cappi, M., Reeves, J. N., et al. 2010a, A&A, 521, A57

Tombesi, F., Sambruna, R. M., Reeves, J. N., et al. 2010b, ApJ, 719, 700

Tornatore, L., Borgani, S., Springel, V., et al. 2003, MNRAS, 342, 1025

Toro, E. F. 1997, Riemann Solvers and Numerical Methods for Fluid Dynamics (Berlin, Springer Verlag)

Townsend, R. H. D. 2009, ApJS, 181, 391

Trager, S. C., Faber, S. M., Worthey, G., & González, J. J. 2000, AJ, 119, 1645

Tran, H. D., Tsvetanov, Z., Ford, H. C., et al. 2001, AJ, 121, 2928

Trinchieri, G., Fabbiano, G., & Canizares, C. R. 1986, ApJ, 310, 637

Trinchieri, G., Pellegrini, S., Fabbiano, G., et al. 2008, ApJ, 688, 1000

van Leer, B. 1979, Journal of Computational Physics, 32, 101

Vazza, F., Brunetti, G., Gheller, C., Brunino, R., & Brüggen, M. 2011, A&A, 529, A17

Veilleux, S., Cecil, G., & Bland-Hawthorn, J. 2005, ARA&A, 43, 769

Verdoes Kleijn, G. A., Baum, S. A., de Zeeuw, P. T., & O'Dea, C. P. 2002, AJ, 123, 1334

Verdoes Kleijn, G. A., van der Marel, R. P., & Noel-Storr, J. 2006, AJ, 131, 1961

Vernaleo, J. C., & Reynolds, C. S. 2006, ApJ, 645, 83

Vikhlinin, A. 2006, ApJ, 640, 710

Voigt, L. M., & Fabian, A. C. 2004, MNRAS, 347, 1130

Voit, G. M. 2005, RevModPhys, 77, 207

Voit, G. M., Bryan, G. L., Balogh, M. L., & Bower, R. G. 2002, ApJ, 576, 601

Voit, G. M., Cavagnolo, K. W., Donahue, M., et al. 2008, ApJ, 681, L5

Voit, G. M., & Donahue, M. 2005, ApJ, 634, 955

Warren, M. S., & Salmon, J. K. 1993, in Proc. SuperComputing, Washington DC: IEEE Comput. Soc., 12

Welch, G. A., & Sage, L. J. 2003, ApJ, 584, 260

Werner, N., Zhuravleva, I., Churazov, E., et al. 2009, MNRAS, 398, 23

Wise, M. W., McNamara, B. R., Nulsen, P. E. J., Houck, J. C., & David, L. P. 2007, ApJ, 659, 1153

Xu, H., Kahn, S. M., Peterson, J. R., et al. 2002, ApJ, 579, 600

Yoshida, T., Habe, A., & Hattori, M. 1991, MNRAS, 248, 630

Young, L. M., Bureau, M., Davis, T. A., et al. 2011, MNRAS, 414, 940

Younger, J. D., & Bryan, G. L. 2007, ApJ, 666, 647

Zabludoff, A. I., & Mulchaey, J. S. 1998, ApJ, 496, 39

Zanni, C., Murante, G., Bodo, G., et al. 2005, A&A, 429, 399

PhD Production

The extensive work carried out during this PhD period produced the following publications, on which the Chapters 4-7 are mostly based.

1. *The Dance of Heating and Cooling in Galaxy Clusters: 3D Simulations of Self-Regulated AGN Outflows*, Gaspari M., Melioli C., Brighenti F., D'Ercole A., 2011a, MNRAS, 411, 349 (astro-ph/1007.0674)

2. *AGN Feedback in Galaxy Groups: the Delicate Touch of Self-Regulated Outflows*, Gaspari M., Brighenti F., D'Ercole A., Melioli C., 2011b, MNRAS, 415, 1549 (astro-ph/1103.5351)

3. *Cause and Effect of Feedback: Multiphase Gas in Cluster Cores Heated by AGN Jets*, Gaspari M., Ruszkowski M., Sharma P., 2012a, ApJ, 746, 1 (astro-ph/1110.6063)

4. *Mechanical AGN Feedback: Controlling the Thermodynamical Evolution of Elliptical Galaxies*, Gaspari M., Brighenti F., Temi P., 2012b, recently submitted to MNRAS (astro-ph/1202.6054)

5. *3D Numerical Simulations of AGN Outflows in Clusters and Groups*, Gaspari M., Melioli C., Brighenti F., D'Ercole A., 2009, in Heinz S., Wilcots E., eds., AIPC 1201, 'The Monster's Fiery Breath: Feedback in Galaxies, Groups, and Clusters', 309 (astro-ph/0909.1282)

The first article caught the attention of the main newspapers (e.g. Corriere della Sera; La Repubblica), magazines (National Geographic), radio and TV programs (e.g. 'Parla con me'; RCDC), usually with the quite funny title 'Buchi neri: contraccettivi del cosmo' ('Black holes: contraceptives of the cosmos').
More important, during this three-year period we won several computational grants, fundamental to execute the massively parallel HPC simulations. From the latest:

1. Grant NASA *Pleiades* (2011-2013), SMD-11-2507: 1,080,000 CPU-hours.

2. Grant NASA *Pleiades* (2011-2012), SMD-11-2209: 512,000 CPU-hours.

3. Grant NASA *Pleiades* (2010-2011), SMD-10-1609: 200,000 CPU-hours.

4. Grant CINECA-ISCRA *SP6* (2011-2012), HP10BOB5U6: 150,000 CPU-hours.
5. Grant CINECA-ISCRA *SP6* (2010-2011), HP10BPTM62: 120,000 CPU-hours.
6. Grant CINECA-INAF *SP6* (2009-2010), AGN FEEDBACK: 100,000 CPU-hours.

Finally, besides having the pleasure to assist Prof. Brighenti for the courses of 'Numerical Calculus' and 'Elements of Programming II', the PhD production includes also several talks and student lectures. For any request and comment on the present work, or if you want to discuss other scientific topics, feel free to write me an email at massimo.gaspari4@unibo.it.

Acknowledgments

During these 3 years, I have dedicated most of my life to grow as a scientist, pursuing with passion and dedication the astrophysical research, whose (numerous) fruits are presented in this Thesis. During this journey, I have learnt that the research can be as rewarding as frustrating. You try always to improve, continuously pushing your limits and challenging yourself. Sometimes, you build such a solid building, and in no time you may end up razing it almost completely to the ground. And then you start again, trying to find new solutions.

This circle can be virtuous. You may find much strength in yourself, however, I do not think that I would have sustained the difficulties without the support of fundamental people. It is impossible to begin the research path without a great family behind your back, both from a human and material point of view. For this reason, my first acknowledgments go to them, in particular my mother and my father. Thank you. Without the continuous encouragement of my little Sveta, I don't know where I would be now. Thank you for the love you show me every day; even if we are often so distant, I still feel you are always beside me. I want then to thank much Bianca (and the little bastard, Zeus!). A better friend is impossible to find. My two grandmothers have left me, in the present, but not in the hearth and mind. Thanks also to my grandfather Giuseppe, for his support and interest in astrophysics, out of common.

Among the astronomers, I would like to thank in particular Fabrizio, for having often clarified my numerous scientific doubts, and whose comments and critiques have certainly improved the work done during the PhD. I hope to have made you proud of me. Thank you Annibale, an excellent officemate, as well as scientist and person with whom talking about life. Thanks to all the other researchers who supported me, like Pasquale (at NASA), Mateusz and Prateek. From all of you I have learnt much.

Ringraziamenti

Durante questi 3 anni ho dedicato gran parte della mia vita a formarmi come scienziato, perseguendo con passione e dedizione la ricerca astrofisica, i cui (numerosi) frutti sono presentati in questa Tesi. Durante questo percorso ho imparato che la ricerca può essere tanto gratificante quanto frustrante: è un continuo superare i propri limiti, mettersi in discussione e migliorarsi. Edifichi una buona costruzione che sembra solida, e in breve tempo puoi giungere a raderla quasi del tutto al suolo. Si riparte di nuovo, cercando di trovare una nuova soluzione.

Questo circolo può essere virtuoso. Molta forza la puoi trovare in te stesso, tuttavia, non credo che avrei retto le diverse difficoltà, senza il supporto di persone fondamentali. Iniziare a fare il ricercatore è impossibile farlo senza un'ottima famiglia alle spalle, sia dal punto di vista umano che materiale. Per questo, i miei primi ringraziamenti vanno a loro, in particolare a mia madre e a mio padre. Grazie. Senza il continuo ascoltarmi ed aiutarmi della mia piccola Sveta, non so dove sarei in questo momento. Grazie per tutto l'amore che mi mostri ogni giorno; anche se spesso così distanti, io ti sento sempre accanto. Non posso inoltre che ringraziare Bianca (ed il bastardo Zeus!), un'amica così è impossibile da trovare. Le mie due nonne mi hanno lasciato, nel presente, ma nel cuore e nella testa ci sono sempre. E grazie anche a mio nonno Giuseppe, per il sostegno ed il suo continuo interesse nell'astrofisica, fuori dal comune.

Tra gli astronomi, vorrei ringraziare in particolare Fabrizio, per aver spesso chiarito i miei numerosi dubbi scientifici, i cui commenti e critiche hanno sicuramente migliorato il lavoro svolto durante il dottorato. Spero di averti reso orgoglioso. Grazie ad Annibale, un ottimo compagno di ufficio, nonché scienziato e persona con cui dialogare della vita. Grazie a tutti gli altri ricercatori che mi hanno supportato, come Pasquale (alla NASA), Mateusz e Prateek. Da voi tutti ho imparato molto.